UNIVERSIDAD DE CHILE
FACULTAD DE CIENCIAS FÍSICAS Y MATEMÁTICAS
DEPARTAMENTO DE INGENIERÍA CIVIL

ANALYSIS OF BEAMS WITH TRANSVERSE OPENING USING A SHEAR-FLEXURE INTERACTION MODEL AND VALIDATION WITH EXPERIMENTAL DATA

MEMORIA PARA OPTAR AL TÍTULO DE INGENIERO CIVIL

MAXIMILIANO HERNÁN BARRA CORTÉS

PROFESOR GUÍA:
LEONARDO MASSONE SÁNCHEZ

MIEMBROS DE LA COMISIÓN:
ANNE LEMNITZER
FABIÁN ROJAS BARRALES

SANTIAGO DE CHILE
2015

RESUMEN DE LA MEMORIA PARA OPTAR AL
TÍTULO DE: Ingeniero Civil
POR: Maximiliano Hernán Barra Cortés
FECHA: 13/07/2015
PROFESOR GUÍA: Leonardo Massone Sánchez

ANÁLISIS DE VIGAS CON ABERTURA TRANSVERSAL UTILIZANDO UN MODELO DE INTERACCIÓN CORTE-FLEXIÓN Y VALIDACIÓN CON DATOS EXPERIMENTALES

Un modelo que combina las respuestas de corte y flexión fue desarrollado por Massone et al. (2006). Este modelo ha sido validado para muros esbeltos y muros cortos (Massone et al., 2009). El modelo fue adaptado para su uso en vigas simplemente apoyadas con ciertas particularidades, como fibras de acero en la mezcla de hormigón o la utilización de hormigón de auto consolidación (Galleguillos, 2010 y Gotschlich, 2011 respectivamente).

El modelo de interacción corte-flexión fue adaptado para simular vigas de hormigón armado en cantiléver con una abertura rectangular en la dirección transversal horizontal al centro de su luz. El objetivo era el de validar el modelo para su uso en elementos de esta naturaleza, que son comunes en edificios modernos, en donde se busca aprovechar la altura completa de pisos. Las aberturas se utilizan para el paso de conductos y tuberías.

Los resultados obtenidos mediante el modelo de interacción fueron comparados con resultados experimentales, descritos por Lemnitzer et al. (2013). La respuesta global predicha se acerca considerablemente a la respuesta experimental, mostrando curvas de carga desplazamiento razonables. Las limitaciones del modelo fueron evidentes al estimar la zona de falla del Espécimen 1, que presenta daño en su abertura. Otras discrepancias son la alta ductilidad que entrega el modelo analítico, retrasando la degradación por la contribución de corte, así como la alta rigidez inicial que presentan las simulaciones. La acumulación de daño por corte en ciertas zonas fue bien capturada mediante el modelo para los tres especímenes que fallaron en su interfaz con el bloque de reacción, pero no así la acumulación de daño por flexión. La máxima capacidad de los especímenes fue bien predicha, con discrepancias iguales o menores a un 10%.

Una variación en la discretización inicial de las vigas junto a una baja en las resistencias de los elementos en el modelo permite inducir la falla en la zona de la abertura. Esta última discretización es recomendada para estudios a futuro.

ABSTRACT

A model that combines the shear and flexural responses was developed by Massone et al. (2006). This model has been validated for slender walls and short walls (Massone et al., 2009). The model was adapted for its use in simply supported beams with certain peculiarities, such as steel fibers present in the concrete mix or the utilization of self-consolidating concrete (Galleguillos, 2010 and Gotschlich, 2011 respectively).

The shear-flexure interaction model was adapted in order to simulate reinforced concrete beams in cantilever with a rectangular opening in the horizontal transverse direction located at the center of their length. The objective was the validation of the model for its use in elements of this nature, which are common in modern buildings, where the intention is to utilize the entire floor height. The openings are used for the passage of ducts and pipes.

The results obtained through the interaction model were compared with experimental results, provided by Lemnitzer et al. (2013). The predicted global response approaches considerably to the experimental response, showing reasonable load displacement curves. The limitations of the model were evident when estimating the failure zone of Specimen 1, which presents damage in its opening. Other discrepancies are the high ductility that the analytical model gives, retarding the degradation due to the shear contribution, as well as the high initial stiffness that the simulations present. The accumulation of shear damage in certain zones was well captured through the model for the three specimens that failed at their interface with the reaction block, but that was not the case with the accumulation of flexural damage. The maximum capacity of the specimens was accurately predicted, with discrepancies equal or lesser than 10%.

A variation in the initial beam discretization together with a decrease in the strength of the materials in the model enables to induce the failure at the opening zone. This last discretization is recommended for future studies.

AGRADECIMIENTOS

Agradezco, en general, a quienes me han acompañado, apoyado, ilustrado (deliberadamente o no) o han compartido (algo) conmigo.

A mis padres por ser mi sostén incondicional. A mis hermanos, por ser parte de mi historia y por la familiaridad. Especialmente a mi pequeña hermana, por ser mi vida.

A mi tía M.B., por su calidez y su admirable resiliencia.

A mi prima G.P., por aparecer en mi vida con su hermosa conciencia.

A mi amigo J.P.C., por ser imprescindible y por ser un hombre bueno.

A mi amigo V.M., por tantos años (y por los que aún faltan por escribir).

A mi amigo y compañero Juan Antonio C., Juglar, por todo lo del primer párrafo y por su carisma inigualable.

A mi amigo Álvaro J., por intercambiar perspectivas conmigo.

A mi amigo Edgardo M., por ser un ejemplo de integridad.

A la familia Murúa Vial, por sus valores y por su apoyo.

A Aníbal P., por las horas de estudio juntos y por ser otro ejemplo de integridad.

Al resto de mis amigos del colegio, universidad y otros pasajes de mi vida.

A mi Profesor Guía, Leonardo Massone, por la atención dedicada, por la oportunidad concedida y, especialmente, por la paciencia y comprensión hacia mi persona.

A la pequeña mujer que me acompaña desde hace un tiempo, por su cariño, su apoyo y por cruzar en mi camino.

CONTENTS

INDEX OF TABLES

INDEX OF FIGURES

CHAPTER 1. Introduction

1.1. Introduction

Reinforced Concrete elements are commonly used in structures because of their mechanic and economic features. Due to their high demand in modern structures, it becomes necessary to count on analytical models which enable the accurate prediction of their behavior, given by parameters such as resistance, deformations, stiffness, failure mode and others.

An analytical model that combines the shear and flexure responses was proposed by Massone et al. (2006), based on studies by Petrangeli et al. (1999). The model was originally validated for slender elements and then obtained satisfactory results for short walls (Massone et al., 2009). Later studies (Massone et al., 2010), (Massone et al., 2012) validated the model for its use in “steel fiber-reinforced concrete beams” and “pre-stressed self-consolidating reinforced concrete beams” respectively.

The proposed shear-flexure interaction model incorporates reinforced concrete panel behavior in each fiber or uniaxial element. Each fiber presents membrane actions, i.e., uniform normal and shear stresses applied in the in-plane direction. Therefore, the model incorporates the interaction between flexure and shear for each uniaxial element. Constitutive models for concrete and steel are incorporated in the model to simulate their behavior under different load conditions.

The development of this work seeks to extend the applicability of the model for its use in cantilever reinforced concrete beams with rectangular transverse openings. These features are used for economic and aesthetic purposes in modern buildings. Results of a series of tests performed to four specimens (three with openings) subjected to cyclic loading until complete structural failure (Lemnitzer et al., 2013) are available. The results are used in order to be compared with the model results, for the eventual validation of the latter.

1.2. Objectives

The main objective of this study is to validate the shear-flexure interaction model for reinforced concrete cantilever beams with rectangular transverse openings.

1.3. Methodology

The following steps outline the development of the work carried out:

- Collect information related to the background of models for reinforced concrete elements that consider shear deformations.
- Study the available literature that explains the shear-flexure interaction model and get to understand it.
- Model the response of beams with transverse openings according to the interaction model (Massone et al., 2006). Variants in order to represent the opening are incorporated. As modeling tool, the finite element software OpenSees is used.
- Review the “Beams with and without openings” report conducted by Lemnitzer et al. (2013). The important aspects to be researched are the characteristics of each tested specimen and their results.
- Estimate the flexure and shear deformations using the instrumentation readings from the tests. It is essential to verify the existence of any important shear deformation.
- Compare the response for beams with transverse openings using the interaction model with the experimental behavior.

1.4. Scope

- **Chapter 1: Introduction**

  Includes a motivation/introduction for the research theme to be developed. Additionally, the main objective of the study is presented and a methodology is detailed.

- **Chapter 2: Shear-Flexure Interaction Model**

  A description of the materials that compose the elements and its constitutive models is provided. The flexural model which serves as base for the interaction model is described. Afterwards, a detailed explanation of the latter is provided with each assumption made in its formulation.

- **Chapter 3: Estimation of Deformations using Experimental Results**

  The tests conducted by Lemnitzer are described. This chapter includes the specimens description, loading conditions and instrumentation used. The flexure and shear deformations are estimated from the results of the four tested specimens.

- **Chapter 4: Implementation of Beams with Transverse Openings in the Flexure and Shear-Flexure Interaction Models**

  The implementation of the beams in the analytical models is detailed. The assumptions and variations used in order to incorporate the openings and to accurately represent the tested specimens are described.

- **Chapter 5: Analysis of Results**

  The results from the tests and the model are analyzed and compared for the validation of the latter. Results of interest are both the global response of the specimens and their local deformations.

- **Chapter 6: Summary and Conclusions**

  The conclusions and relevant comments of the work are presented.

CHAPTER 2. Shear-Flexure Interaction Model

2.1. Constitutive Models of Materials

2.1.1. Constitutive Model for Concrete in Compression

To describe the behavior of concrete in compression, the stress-strain base curve by Thorenfeldt et al. (1987) is used. This base curve, calibrated by Collins and Porasz (1989), Wee et al. (1996) and Carreira and Kuang-Han (1985) was updated with the introduction of the compression softening parameter β, proposed by Vecchio and Collins (1993).

The aforementioned parameter considers the effect of biaxial compression softening (reduction in principal compressive stresses in concrete due to cracking under tensile strains in the orthogonal direction). With the addition of this parameter, the panel behavior represented by the model is more reliable.

The equation 2.1.1.1 shows the Thorenfeldt base curve definition:

$$\sigma_c = f_c' \cdot \frac{n\left(\frac{\varepsilon_c}{\varepsilon_0}\right)}{n-1+\left(\frac{\varepsilon_c}{\varepsilon_0}\right)^{nk}} \qquad (2.1.1.1)$$

where σ_c is the stress of the concrete in compression at any given compressive strain ε_c. Parameters f_c' and ε_0 are the peak compressive stress (maximum capacity) and peak compressive strain respectively. The remaining parameters n and k are given by expressions proposed by Collins and Porasz (1989), which are valid for relatively high-strength concrete:

$$n = 0.8 + \frac{f_c'(MPa)}{17} \qquad (2.1.1.2)$$

$$k = 1 \quad \text{when} \quad 0 \leq \varepsilon \leq \varepsilon_0 \qquad (2.1.1.3)$$

$$k = 0.67 + \frac{f_c'(MPa)}{62} \quad \text{when} \quad \varepsilon_0 \leq \varepsilon \qquad (2.1.1.4)$$

In order to incorporate the compression softening effect, an important consideration to represent the behavior of a reinforced concrete panel element under membrane actions, a reduction factor is used. This factor was proposed by Vecchio and Collins (1993), whom used a large experimental database to calibrate an expression for the compression softening effect. The reduction factor to be applied to the peak compressive stress is given by the expression 2.1.1.5:

$$\beta = \frac{1}{0.9+0.27\frac{\varepsilon_1}{\varepsilon_0}} \qquad (2.1.1.5)$$

where ε_1 is the principal tensile strain, and ε_0 represents the same strain mentioned before. The ratio $\varepsilon_1/\varepsilon_0$ is considered positive.

The Thorenfeldt base curve, adjusted by Collins and Porasz (1989), including the compression softening factor is shown in Figure 2.1:

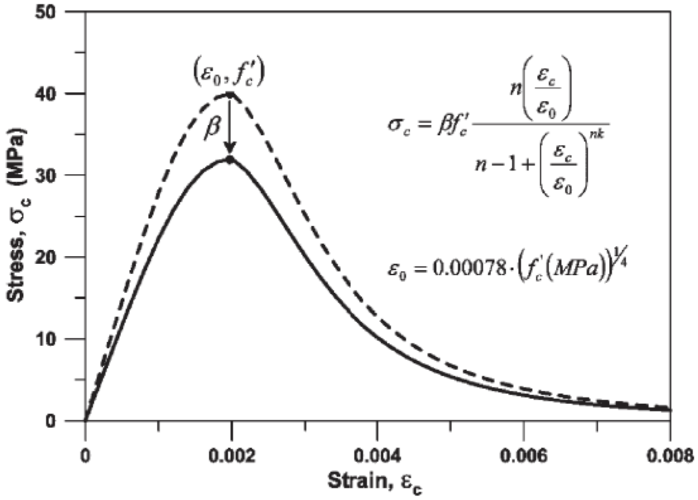

Figure 2.1: Constitutive model for concrete in compression (Massone et al., 2006).

2.1.2. Constitutive Model for Concrete in Tension

The constitutive laws for concrete in tension used in the model are the analytical expressions determined by Belarbi and Hsu (1994). The formulation of the average stress-strain relationship of concrete in tension was derived from tests performed on reinforced concrete panels.

The relations of the concrete in tension determined by Belarbi and Hsu (1994) consider the effect of tension stiffening (average post-peak tensile stresses in concrete due to the bonding of concrete and reinforcing steel between cracks).

To describe the behavior of concrete in tension, the expressions 2.1.2.1 and 2.1.2.2 are implemented in the model:

$$\sigma_c = \left(\frac{f_{cr}}{\varepsilon_{cr}}\right)\varepsilon_c \qquad \text{when} \quad \varepsilon_c \le \varepsilon_{cr} \qquad (2.1.2.1)$$

$$\sigma_c = f_{cr}\left(\frac{\varepsilon_{cr}}{\varepsilon_c}\right)^b \qquad \text{when} \quad \varepsilon_c > \varepsilon_{cr} \qquad (2.1.2.2)$$

where σ_c and ε_c are the concrete tensile stress and strain respectively.

While f_{cr} is the tensile strength and ε_{cr} is the strain at tensile strength. Recommended values for the modulus of elasticity, f_{cr} and ε_{cr} are (Belarbi and Hsu, 1994):

$$E_c = 3917\sqrt{f_c'(MPa)} \qquad (2.1.2.3)$$

$$f_{cr} = 0.313\sqrt{f_c'(MPa)} \qquad (2.1.2.4)$$

$$\varepsilon_{cr} = 0.00008 \qquad (2.1.2.5)$$

The parameter b controls the ability to redistribute the stresses in the concrete after cracking. The condition for this redistribution to be possible is to have longitudinal reinforcing bars, which is the case of the tests conducted by Belarbi and Hsu (1994). The best fit found after the tests was $b = 0.4$.

Figure 2.2 sums up the model used for Concrete in Tension.

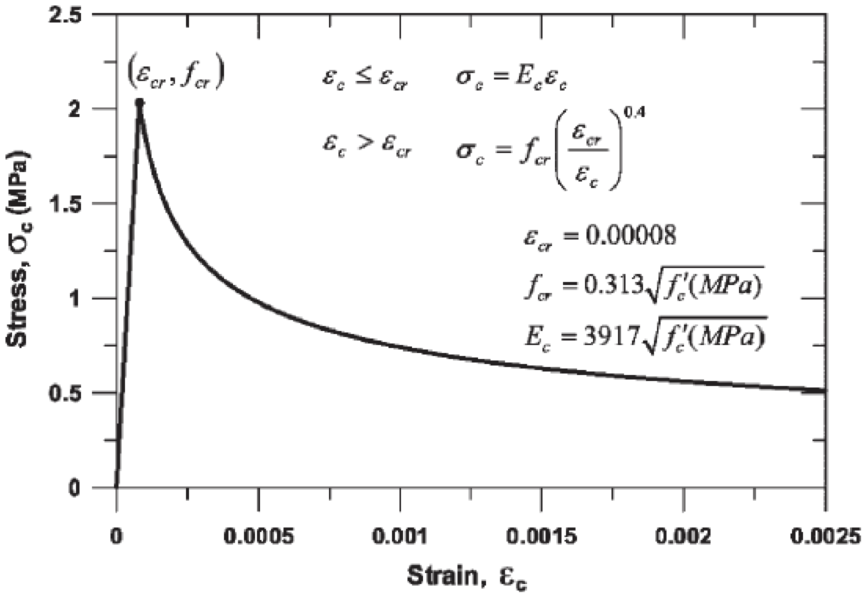

Figure 2.2: Constitutive model for concrete in tension (Massone et al., 2006).

2.1.3. Constitutive Model for Confined Concrete

The confined concrete's behavior differs from that of the unconfined concrete. An analytical model developed by Saatcioglu and Razvi (1992) is used to derive a stress-strain relationship for confined concrete from the parameters that rule the behavior of unconfined concrete.

The model proposes a stress-strain curve consisting of a parabolic ascending branch followed by a linear descending segment. The curve was calibrated from a large number of tests, including different cross sections and amounts of confinement.

For the peak stress (strength) of the confined concrete, the expression 2.1.3.1 is used:

$$f'_{CC} = f'_{CO} + k_1 f_{le} \qquad (2.1.3.1)$$

where

f'_{CO} is the unconfined concrete strength

$$f_{le} = k_2 \cdot f_l \qquad (2.1.3.2)$$

f_{le} is the equivalent uniform pressure

$$f_l = \frac{\sum A_s f_{yt} sin\alpha}{s \cdot b_c} \tag{2.1.3.3}$$

f_l: average lateral pressure

A_s : area of transverse reinforcement

f_{yt} : yield strength of the transverse reinforcement

b_c : distance center to center of perimeter hoop

s : distance center to center of tie spacing

α : takes value of 90º if the transverse reinforcement is perpendicular to b_c

k_2 is a reduction factor, function of the average lateral pressure f_l, given by the equation 2.1.3.4:

$$k_2 = 0.26\sqrt{\left(\frac{b_c}{s}\right)\left(\frac{b_c}{s_l}\right)\left(\frac{1}{f_l}\right)} \leq 1.0 \tag{2.1.3.4}$$

where f_l is in MPa.

s_l is the maximum spacing of laterally supported longitudinal reinforcement

k_1 is a function of the Poisson ratio that varies with the lateral pressure. The expression 2.1.3.5 is obtained from regression analysis of test data (Saatcioglu and Razvi, 1992):

$$k_1 = 6.7(f_l)^{-0.17} \tag{2.1.3.5}$$

For rectangular confinement, which is the case of this study, the estimation of the equivalent uniform pressure must be made for both directions (x and y), therefore the final value of f_l should be:

$$f_{le} = \frac{f_{lex} b_{cx} + f_{ley} b_{cy}}{b_{cx} + b_{cy}} \tag{2.1.3.6}$$

where f_{lex} and f_{ley} are the effective lateral pressures acting perpendicular to core dimensions b_{cx} and b_{cy} respectively.

The peak stress is already defined. For the strain at this peak stress ε_1, the expression 2.1.3.7 is proposed:

$$\varepsilon_1 = \varepsilon_{01}(1 + 5K) \tag{2.1.3.7}$$

where

$$K = \frac{k_1 f_{le}}{f'_{CO}} \tag{2.1.3.8}$$

and ε_{01} is the strain at peak stress for unconfined concrete. For this value, in the absence of experimental data, 0.002 is considered appropriate under slow rate of loading.

The parabolic ascending branch for the stress-strain curve of the confined concrete is given by the relation:

$$f_c = f'_{CC}\left[2\left(\frac{\varepsilon_c}{\varepsilon_1}\right) - \left(\frac{\varepsilon_c}{\varepsilon_1}\right)^2\right]^{1/(1+2K)} \leq f'_{CC} \tag{2.1.3.9}$$

where f_c and ε_c are the stress and strain for confined concrete respectively.

Beyond the peak of the stress-strain curve, follows a linear descending branch, defined by the strain at 85% strength level. This strain is given by the expression 2.1.3.10:

$$\varepsilon_{85} = 260\rho\varepsilon_1 + \varepsilon_{085} \tag{2.1.3.10}$$

where

ε_{085} : strain at 85% strength level beyond the peak stress for unconfined concrete,

In the absence of test data, a value of 0.0038 is considered appropriate for ε_{085} under slow rate of loading (Saatcioglu and Razvi, 1992).

ρ : reinforcement ratio

$$\rho = \frac{\sum A_S}{s(b_{cx}+b_{cy})} \tag{2.1.3.11}$$

the summation ($\sum$) in the numerator of eq. (2.1.3.11) indicates the total area of transverse reinforcement in the two directions, crossing b_{cx} and b_{cy}.

At the end of the linear descending branch a constant residual strength is assumed at 20% strength level. The effect of the confinement on the stress-strain curve of the concrete is shown in Figure 2.3, proposed by Saatcioglu and Razvi (1992):

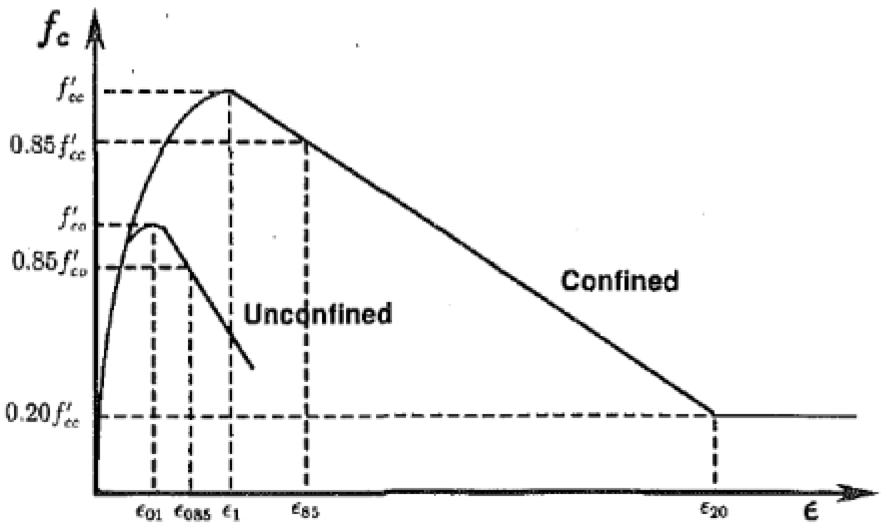

Figure 2.3: Stress-Strain Relationship for Confined Concrete (Saatcioglu and Razvi, 1992).

In order to input the parameters for the unconfined concrete in the model, the stress-strain curve obtained by the procedure proposed by Saatcioglu and Razvi (1992), has to be adjusted so it fits the Thorenfeldt base curve expression (2.1.1.1). In this last equation, for the confined concrete, new values for n and k are determined for each specimen to be modeled and f_c' takes the value of the respective confined strength f_{CC}'.

2.1.4. Constitutive Model for Reinforcing Steel

The stress-strain relationship for the reinforcing steel implemented in the model is the constitutive model of Menegotto and Pinto (1973). The curve takes its shape from two straight lines in the form of curved transitions. The first straight line asymptote has a slope of E_0 (modulus of elasticity), and the second asymptote has a slope of $E_1 = bE_0$. The parameter b is the strain hardening ratio. A transition between the two asymptotes is governed by the parameter R_0. The cyclic behavior (which can be seen in Figure 2.4) is not incorporated in the model, only the monotonic branch is considered, since the model can only reproduce monotonic behavior.

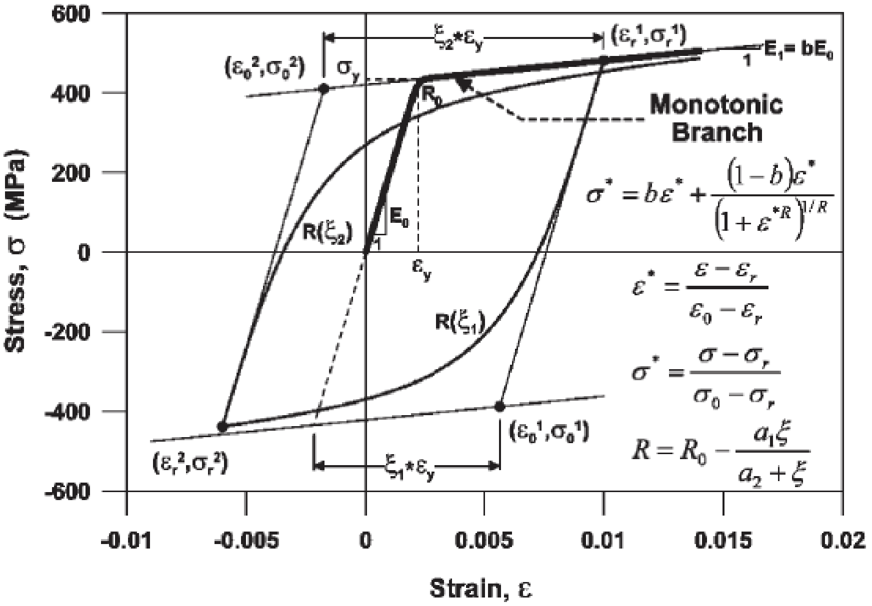

Figure 2.4: Constitutive Model for Reinforcing Steel (Massone et al., 2006).

Belarbi and Hsu (1994), developed studies to consider the effects of tension stiffening on reinforcement (a result of the stress redistribution between steel and concrete after cracking). They propose a reduction on the effective yield stress and strain (intersection of the elastic and yield asymptotes), resulting in the consideration of only 91% of the yield stresses and strains of bars embedded in concrete.

The monotonic curve parameter R_0 is described by the relation 2.1.4.1, empirically determined:

$$R_0 = \frac{1}{9B - 0.2} \leq 25 \tag{2.1.4.1}$$

where

$$B = \frac{1}{\rho}\left(\frac{f_{cr}}{\sigma_y}\right)^{1.5} \tag{2.1.4.2}$$

f_{cr} is the concrete cracking stress, ρ is the cross-sectional area ratio of the longitudinal steel bars and σ_y is the yielding stress of the steel.

2.2. Flexural Model Description

A fiber model able to capture the flexural response of reinforced concrete elements has been implemented in OpenSees. It is used in this study to compare the response of the beams with this model first and then with the interaction model, which takes into account the shear deformations together with the flexural deformations. It consists of a nonlinear fiber model analysis where the beam is divided into several elements through its length. Each one of these elements is also subdivided into a certain number of horizontal fibers. One fiber is represented with a single spring in the longitudinal direction of the beam (Figure 2.5). In case of two-dimensional deformations, each element is characterized by three degrees of freedom at each end of it (axial deformation, transverse deformation and rotation). The beam discretization is shown in Figure 2.5 for the flexure model:

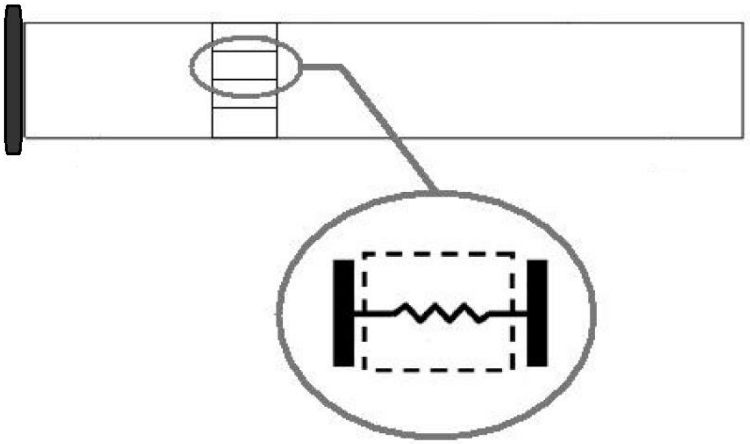

Figure 2.5: Beam discretization (Fiber Model), (Massone et al., 2012).

In order to determine the stresses and strains of the beam, the model performs the following procedure: at a certain deformations level for the aforementioned degrees of freedom and assuming the Bernoulli hypothesis (plane sections remain plane after loading), the axial strain ε_x can be estimated for each fiber. Then, using the constitutive models of materials (concrete and steel) and the fiber dimensions, the stresses can be determined. The moment and axial forces can be determined from the stresses and fiber geometry, and the shear force is estimated from the equilibrium. At global level, the model imposes a certain displacement (in this case at the tip of the beam). Subsequently the deformations of each element are adjusted to reproduce the global displacement at a fixed tolerance and finally it returns the load needed for the given displacement.

The flexural model serves as a base for the implementation of the shear-flexure interaction model.

2.3. Shear-Flexure Interaction Model Description

The shear-flexure interaction model corresponds to a bi-directional fiber model. This model is quite similar to the flexural model detailed in Section 2.2, with the improvement provided by the addition of a vertical spring in each fiber, which enables the representation of the shear response of the elements. The Beam is discretized in several elements through its length as in the flexure model. Every element is also subdivided into a certain number of horizontal fibers. The difference with the flexural model, as already mentioned, comes with the addition of a vertical spring, in each fiber, together with the horizontal spring (as seen in Figure 2.5). The discretization of the beam is now represented by Figure 2.6:

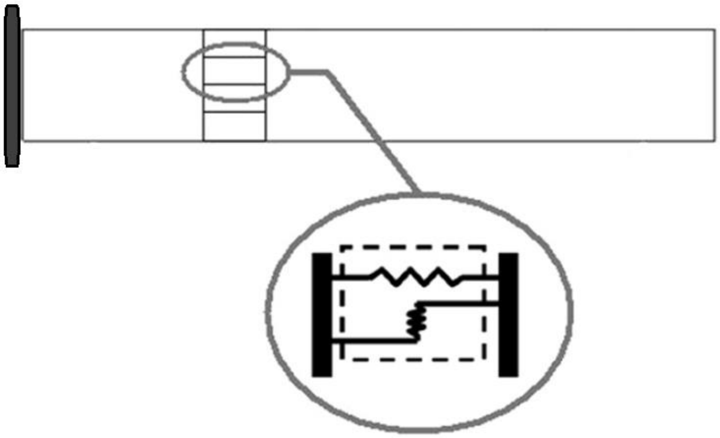

Figure 2.6: Beam discretization (Interaction Model), (Massone et al., 2013).

The first assumption made for the interaction model is that the rotation due to flexure of each element occurs at a specific intermediate point located at a distance $c \cdot h$ from the beginning of the element, where h is the length of the element and c is a constant between 0 and 1, seeking to locate the center of rotation at a fraction c of the length h. Studies by Massone and Wallace (2004), showed that a value of $c = 0.4$ is appropriate for cantilever walls. For beams, studies by Galleguillos (2010), and Gotschlich (2011), showed satisfactory results when imposing a value of $c = 0.5$ to locate the center of rotation of an element. This center is also used to locate the vertical spring. Now a shear-flexure interaction model element is represented by Figure 2.7.

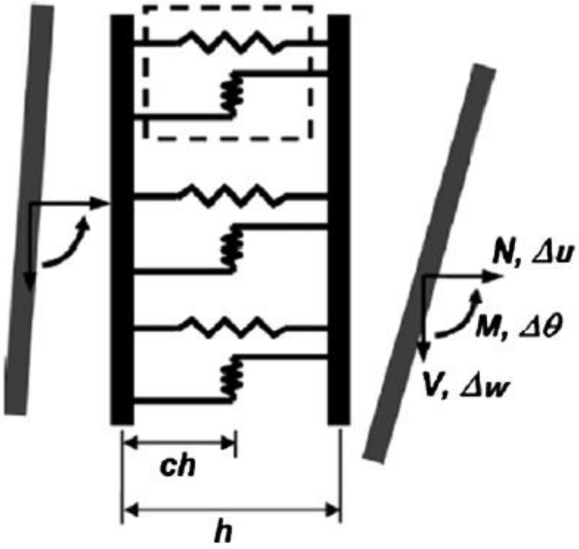

Figure 2.7: Element representation for the Shear-Flexure Interaction Model, (Massone et al., 2013).

Each element has the same three degrees of freedom (u_x, u_y, θ) at each end, as in the flexural model. For a prescribed deformations level for the degrees of freedom and through a similar procedure as in the flexural model (using the given deformations and the Bernoulli hypothesis of plain sections remain plane after loading), the axial strain (ε_x) and the shear distortion (γ_{xy}) can be obtained for each fiber (or panel). A second assumption is made at this point, the shear distortion is assumed to be uniform in the section. The horizontal spring is associated to the axial strain (ε_x), and the vertical spring is modeled to capture the shear distortion (γ_{xy}). The panel behavior with interaction between flexure and shear deformations is shown in Figure 2.8.

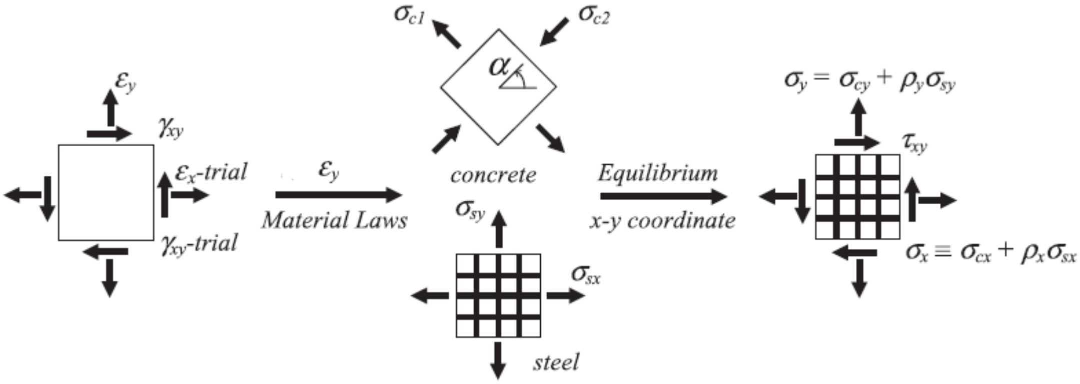

Figure 2.8: Panel strain to stress determination, (Massone, 2010).

The transverse normal strain (ε_y) is unknown up to this point. Three options emerge for the determination of its value: (1) assuming zero transverse normal strain ($\varepsilon_y = 0$), (2) using an experimentally calibrated expression for the transverse normal strain (ε_y) or (3) assuming zero resultant transverse normal stress ($\sigma_y = 0$) along the entire beam length. The first option is not quite compatible with the tests configuration studied, for whom the transverse deformations are not restrained along the beam. The second option showed satisfactory results for load-displacement prediction of squat structural walls (Massone et al., 2009) and was later used in the modeling of reinforced concrete beams (studies by Galleguillos (2010) and Gotschlich (2011)), showing relatively good results. For this study, the third option is used (third assumption made).

The assumption of zero resultant transverse normal stress ($\sigma_y = 0$) is compatible with the boundary conditions of the tested beams, as no transverse load is applied through its length. In order to obtain the transverse normal strain (ε_y), iterations are made to achieve the transverse equilibrium, where (ε_y) is the varied parameter.

In order to obtain the stress field of the panel from the known strain field, the procedure seen in Figure 2.8 is followed. The fourth assumption of the model is made, assuming that the principal directions of the strain and stress fields coincide. The reinforcing steel stresses can be determined directly for the coordinate directions x and y using the known strains, because an uniaxial stress-strain model is used for the steel and the beams are reinforced in the longitudinal and transverse directions (x and y respectively). For the concrete, the stresses have to be transformed from the principal directions (angle α in Figure 2.8) to the coordinate directions. A rotating-angle modeling approach is used, as provided by the studies of Vecchio and Collins (1986) or Pang and Hsu (1995). Finally the stress field for the coordinate directions (x and y) is obtained, representing the coupled response of flexure and shear for the concrete and steel together.

When obtaining the stress field of the panel, the model verifies the assumption of $\sigma_y = 0$ for the prescribed tolerance. Each element is verified so they satisfy the equation, if not, ε_y is re-estimated and the process is repeated.

As in the flexural model, the procedure steps are the following: impose a displacement, estimate the strains, estimate the stresses and obtain the load needed for the imposed displacement.

CHAPTER 3. Estimation of Deformations using Experimental Results

3.1. Tests Description

3.1.1. General Description

Between March 1st and June 2nd, 2013, four reinforced concrete cantilever specimens were tested in the Structural Engineering Testing Hall Laboratory at the University of California, Irvine. The tests, conducted by Lemnitzer et al. (2013), were part of the Metropolitan Water District's seismic beam evaluation program.

The specimens, constructed as cantilever beams as a simplification, intended to replicate existing moment frame beams located at the Metropolitan Water District's Headquarter building in Los Angeles, California. The typical Special Moment Frame beam under vertical loading fixed between two columns can be seen in Figure 3.1:

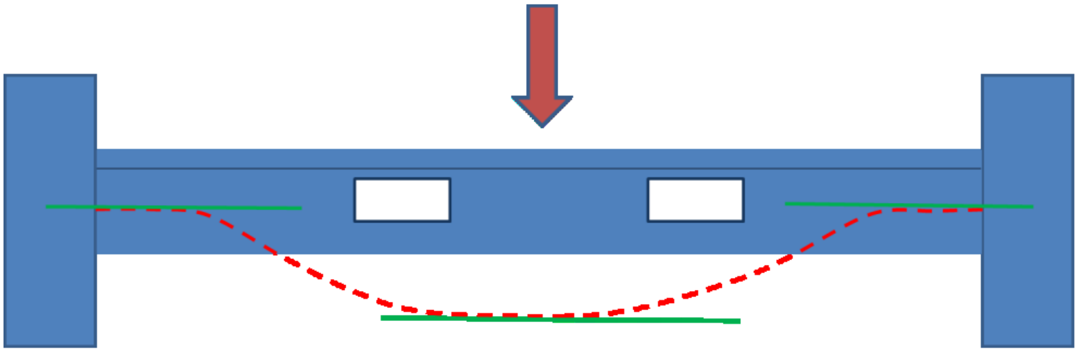

Figure 3.1: Typical SMF beam under vertical loading (Lemnitzer et al., 2013).

Only one half of the length of the in-situ beams was constructed as specimens for practical reasons (therefore built as cantilever specimens). Also, each specimen was constructed in a 4/5th scale of the beam's in-situ condition, adjusting the steel reinforcing bars diameters to faithfully represent the full scale beams.

The basic test setup consisted of the cantilever beam fixed to a reaction block. The reaction block is anchored to a strong wall and to a strong floor. The load application system consists of a vertical actuator fixed to a high capacity loading frame and anchored to the specimen, ready to produce quasi static reverse cyclic loading. The basic setup can be seen in Figure 3.2.

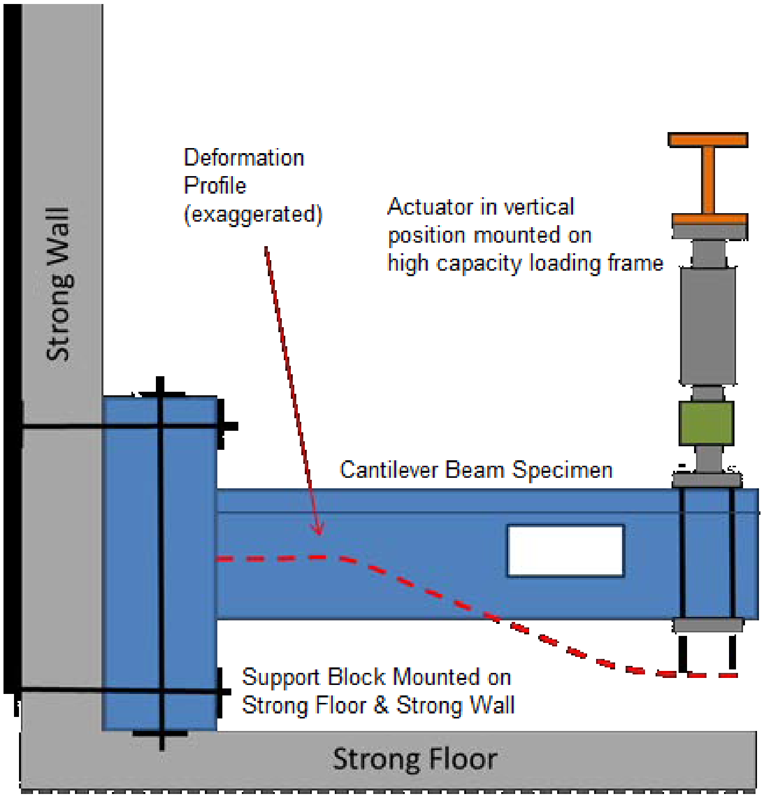

Figure 3.2: Basic test setup (Lemnitzer et al., 2013).

The load application system is not able to fully constrain the rotation of the specimen at its loaded end, because of the massiveness of the specimens. However, the rotation might be restrained into a certain amount, therefore, some assumptions are made for the model in order to represent a certain restriction in the rotation (detailed in section 4.4).

Four specimens were built for the tests. Three of them had a transverse opening and the remaining one had no opening. The latter was the first built specimen, and was useful to verify and validate the test setup, instrumentation scheme, cyclic loading protocol and provided a good overall basis for the more demanding tests with specimens that had openings.

All material testing was conducted according to ASTM Standards and the structural testing was conducted according to ASCE 41-06 S1, under reverse cyclic loading applied at the beam tip with three cycles per displacement level. More information related to the followed standards and supervisions made can be found in the “Cyclic Behavior of SMRF RC Beams with and without openings – Phase 1” report (Lemnitzer et al., 2013).

3.1.2. Specimen Description

All the specimens had a common cross section, consisting of a web of 24 $[inches]$ in width and 33.6 $[inches]$ in height and a top slab with dimensions of 62.4 $[inches]$ width and 4.8 $[inches]$ in height. The common cross section is shown in Figure 3.3.

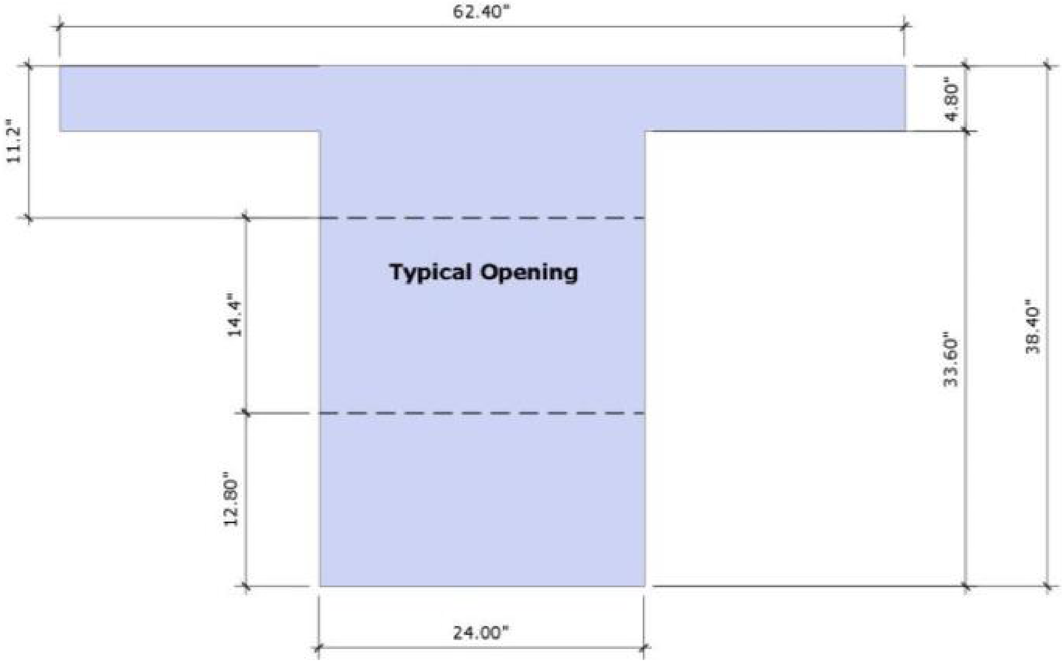

Figure 3.3: Typical cross section (Lemnitzer et al., 2013).

The transverse opening, which can be found in three of the specimens, is also shown in Figure 3.3, located 12.8 $[inches]$ higher than the bottom edge of the beam and extends for 14.4 $[inches]$ through the height of the web. As it was mentioned in Chapter 2, the longitudinal reinforcing condition varies from one specimen to another and also through the length of one particular specimen. Therefore, Figure 3.3 only shows the common dimensions of the cross section.

3.1.2.1. Specimen 1

Specimen 1 had a total length of $158\ [inches]$ and a length of $134\ [inches]$ up to the load application point.

The steel reinforcing conditions for Specimen 1 were the following:

Top reinforcement:

- *4 #9* Main U bars.
- *2 #9* and *2 #7* Added L bars (embedded into the reaction block, extend into the beam 76.8'').
- *4 #8* and *2 #7* Jamb bars (do not go into the reaction block, began 9.6'' away from the block, extend up to the end of the beam).
- *4 #9* Lap bars
  (There was a gap of 9.6'' between the added bars and the lap bars).

Bottom reinforcement:

- *4 #9* Main U bars.
- *2 #9* Added L bars.
- *4 #8* and *2 #7* Jamb bars (identical to top jamb reinforcement).
- *4 #9* Lap bars (identical to top lap reinforcement).

  All flexural reinforcement had a development length of 35.2'' into the reaction block with standard hooks.

Transverse reinforcement:

- *#4* stirrups spaced 4.75'' for 86.3'' from the reaction block to the inside of the opening.
- *#4* stirrups spaced 3.25'' after wards until end of the beam.

Top flange reinforcement:

4 #4 longitudinal bars distributed along the width of the flange.

Side reinforcement:

4 #3 side reinforcement was placed on both sides of the opening and extended $2\ [feet]$ into the reaction block.

A side look of Specimen 1 is shown in Figure 3.4.

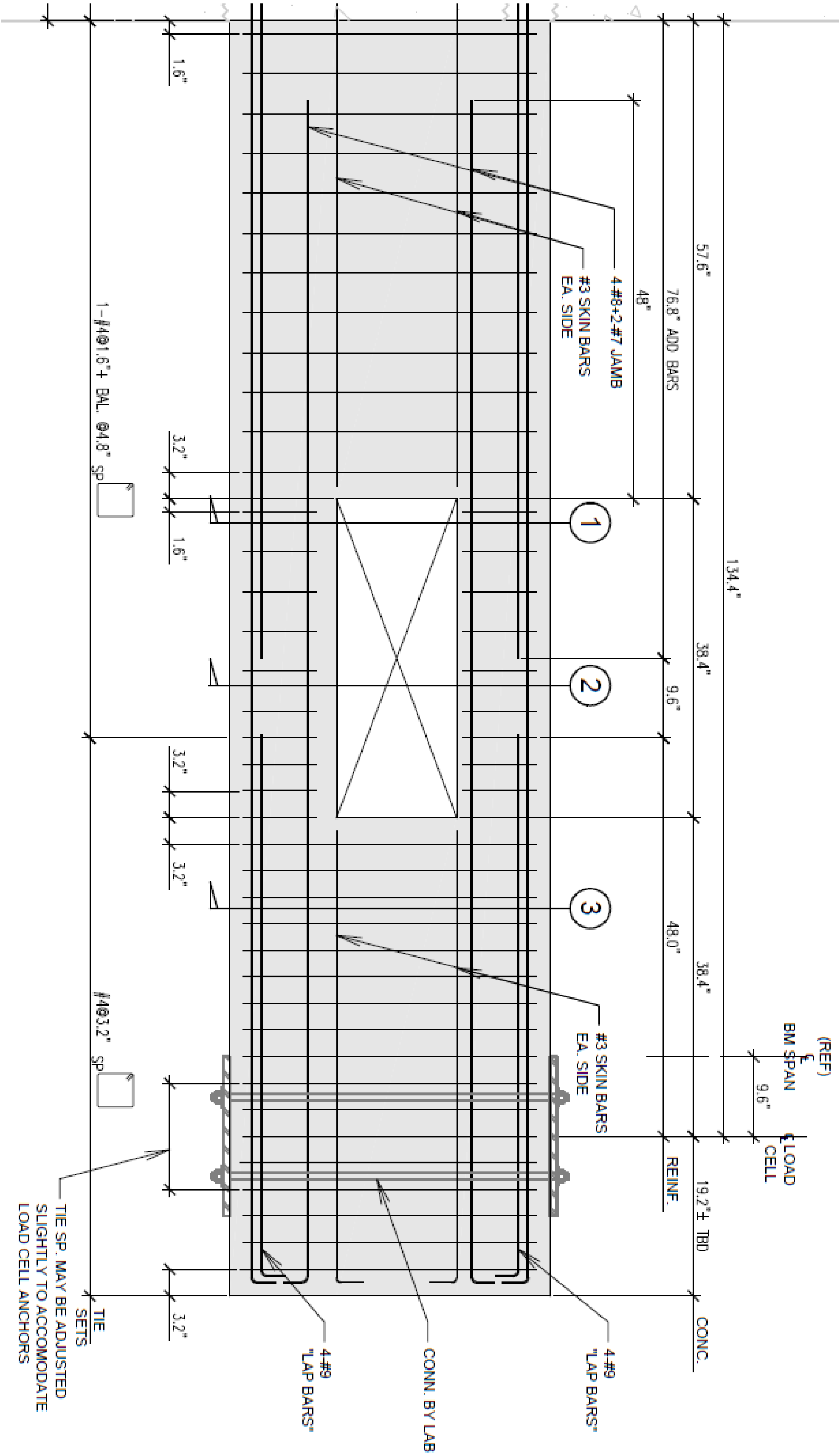

Figure 3.4: Side elevation of Specimen 1 (Lemnitzer et al., 2013).

3.1.2.2. Specimen 2

Specimen 2 had a total length of $173\ [inches]$ and a length of $149\ [inches]$ up to the load application point.

The steel reinforcing conditions for Specimen 2 were the following:

Top reinforcement:

- *6 #9* Main U bars.
- *6 #9* Added L bars (end after 81.6’’ from the reaction block).
- *6 #9* Jamb bars (began 12.8’’ from the reaction block and extended up to the end of the beam).

Bottom reinforcement:

- *4 #8* Main U bars.
- *2 #8* Added L bars.
- *6 #9* Jamb bars (identical to top jamb reinforcement).
- *4 #9* Lap bars (identical to top lap reinforcement)*.

  *All lapped bars were paired together with the main top and bottom bars at the tip of the beam and extended 57’’ toward the reaction block.

  There was a 28.8’’ gap between the added bars and lapped bars.

  Longitudinal reinforcement extended into the reaction block by a length of 35.2’’ with a standard hook at 90°.

Transverse reinforcement:

- Two sets of *15 #4* stirrups spaced at 4.75’’.
- Two sets of *29 #4* stirrups spaced at 3.25’’.

Top flange reinforcement (identical to Specimen 1):

4 #4 longitudinal bars distributed along the width of the flange.

Side reinforcement:

4 #3 side reinforcement was placed on both sides of the opening and extended $2\ [feet]$ into the reaction block.

A side elevation of Specimen 2 is shown in Figure 3.5.

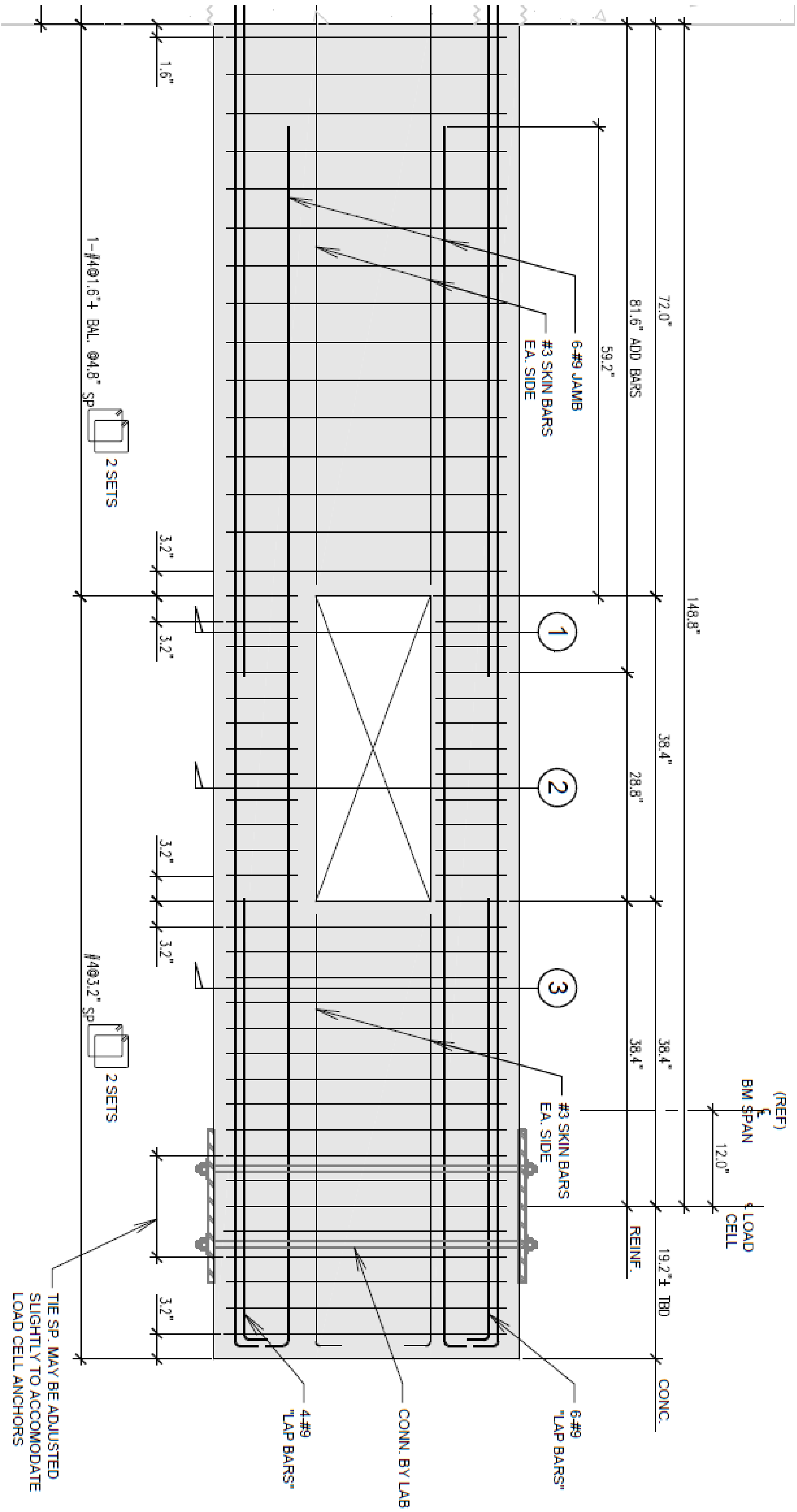

Figure 3.5: Side elevation of Specimen 2 (Lemnitzer et al., 2013).

3.1.2.3. Specimen 6

Specimen 6 had a total length of $209.6\ [inches]$ and a length of $185.6\ [inches]$ up to the load application point.

The steel reinforcing conditions for Specimen 6 were the following:

Top reinforcement:

- *6 #9* Main U bars (embedded 35.2'' into the reaction block).
- *2 #9* Added L bars (extended 105.6'' from the reaction block).
- *6 #7* Jamb bars*.

Bottom reinforcement:

- *4 #8* Main U bars.
- *2 #8* Added L bars.
- *6 #7* Jamb bars*.

  *Jamb bars were placed in order to coincide with the center of the opening and extended 38.4'' in both directions.

Transverse reinforcement:

- From reaction block: *18 #4* stirrups placed at 4.75''.
- At the opening: *9 #4* stirrups at 4.5''.
- Remainder: *12 #4* stirrups at 8.75''.

Top flange reinforcement (identical to Specimens 1 and 2):

4 #4 longitudinal bars distributed along the width of the flange.

Side reinforcement:

4 #3 side reinforcement was placed on both sides of the opening and extended $2\ [feet]$ into the reaction block.

A side elevation of Specimen 6 is shown in Figure 3.6.

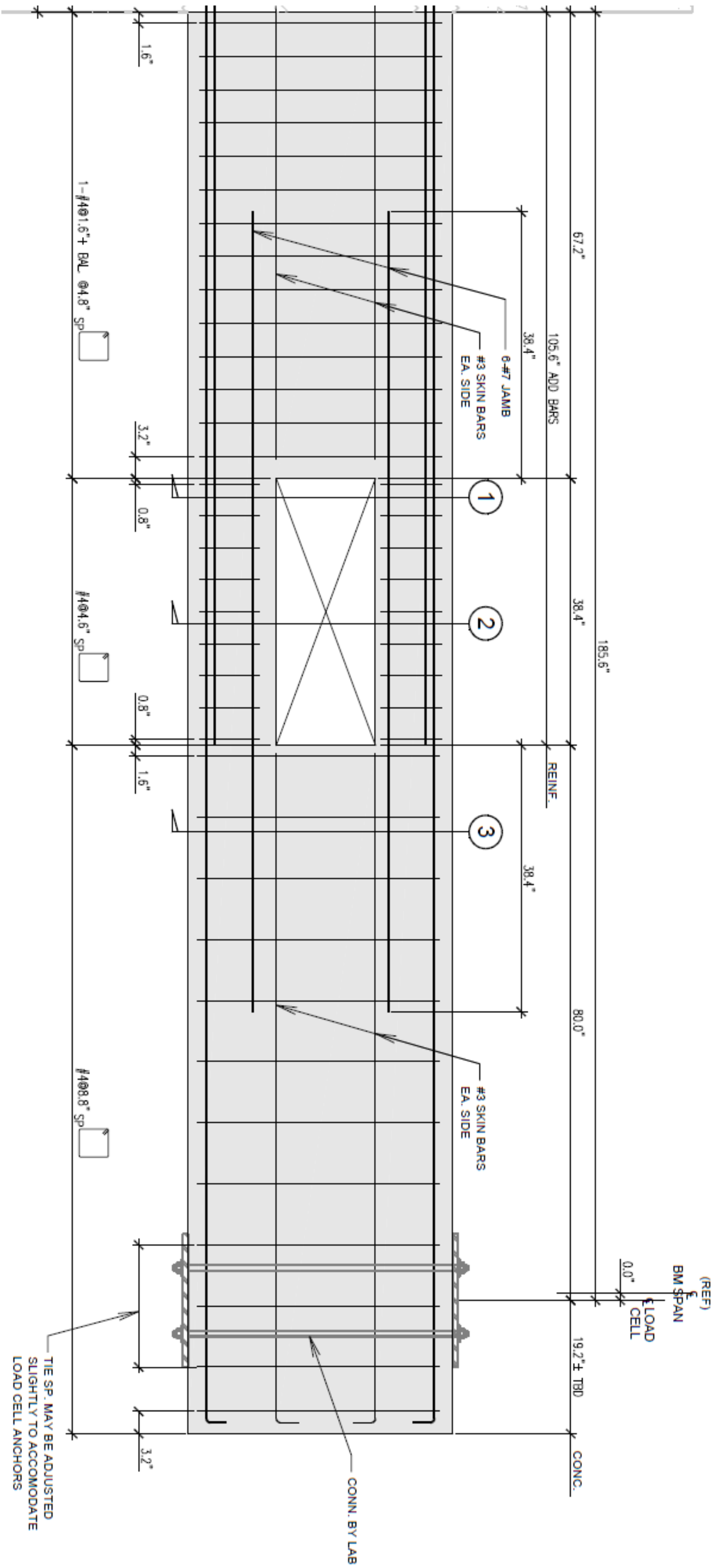

Figure 3.6: Side elevation of Specimen 6 (Lemnitzer et al., 2013).

3.1.2.4. Specimen 7

Specimen 7 had a total length of $148.8\ [inches]$ and a length of $124.8\ [inches]$ up to the load application point.

The steel reinforcing conditions for Specimen 7 were the following:

Top reinforcement:

- *4 #9* Main U bars.
- *2 #9* and *2 #8* Added L bars (extended 96'' away from the face of the reaction block).

Bottom reinforcement:

- *4 #8* Main U bars.
- *2 #8* Added L bars (identical specification as top added bars).

  All longitudinal reinforcement extended 35.2'' into the reaction block with standard hooks.

Transverse reinforcement:

- *17 #4* stirrups equally spaced at 4.75'' starting at the beam block interface.
- *10 #4* stirrups spaced 6.5'' for the remainder of the beam.

Top flange reinforcement (identical to the previous specimens):

4 #4 longitudinal bars distributed along the width of the flange.

Side reinforcement:

4 #3 side reinforcement was placed on both sides of the opening and extended $2\ [feet]$ into the reaction block.

A side elevation of Specimen 7 is shown in Figure 3.7.

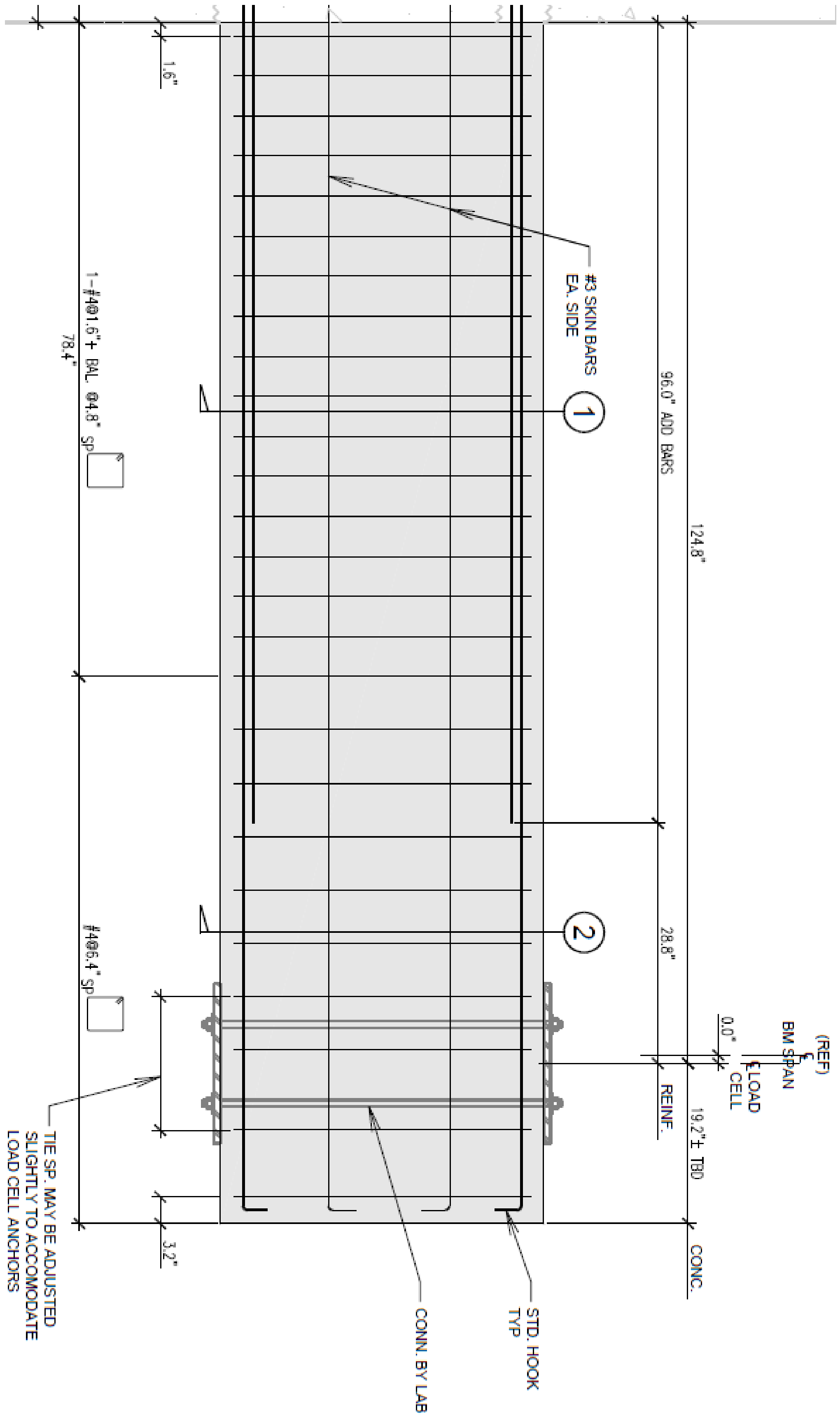

Figure 3.7: Side elevation of Specimen 7 (Lemnitzer et al., 2013).

3.1.3. Material Properties

3.1.3.1. Concrete

The concrete used for the specimens intended to provide a compressive strength similar to the in-situ conditions. Some important considerations were made (regarding the aggregates, slump tests, void ratio, etc.) in order to achieve the desired concrete mix. For this report, the only important parameter is the concrete compressive strength at the day of testing for each specimen, useful to be incorporated in the models described in Chapter 2. These parameters are shown in Table 3.1.

Table 3.1: Concrete compressive strengths at the day of testing.

Specimen	f'_c [ksi]
S1	7.7
S2	7.6
S6	7.83
S7	7

3.1.3.2. Steel

The steel reinforcing bar diameters were carefully picked in order to faithfully represent the in-situ beams in the mentioned 4/5th scale. Grade 60 reinforcing steel was used, reaching yield strength of about $66\ [ksi]$. Tests were performed to one bar of each size to determine the estimated yield strength, which is the relevant parameter for the model. Table 3.2 shows the test results.

Table 3.2: Reinforcing bars test results.

Size #	Yield Strength [ksi]	Ultimate Tensile [ksi]
#3	65.4/65.6	98.55/95.5
#4	69.6	108
#7	66.7	108.3
#8	66.5	110.3
#9	64.3	105.94

For more information about the concrete mix, the steel reinforcing bars and the followed standards with regard to the material tests, the report developed by Lemnitzer et al. (2013) can be reviewed (Section 2.4 of the report).

3.1.4. Instrumentation

The instrumentation, in order to monitor the beam displacements, rotations and internal strains consisted of strain gauges, linear variable differential transducers (LVDTs) and string potentiometers.

Strain gauges were installed on the reinforcing bars before the concrete pouring.

LVDTs were installed at both sides of the specimens. Horizontal LVDTs were used on one side of each specimen in order to capture the flexural deformations and diagonal LVDTs were placed on the other side of each specimen, used to capture the shear deformations. These instruments had both ends fixed on the surface of the specimens and because of that reason they can be referred to in this report as “internal instrumentation” at some point.

String potentiometers were installed to capture the total displacements of the specimens at certain lengths (in particular at the length of the load application point) and the eventual rotations of the reaction block. These instruments had one end fixed to the surface of the specimens (or the reaction block) and the other end fixed to a strong member (such as the strong floor or the strong wall). Therefore, they can be referred to as “external instrumentation” in counter position to the LVDTs (internal instrumentation).

An exemplification of the instrumentation is shown in Figures 3.8 to 3.11, where the layout of the instruments installed in Specimen 1 can be seen.

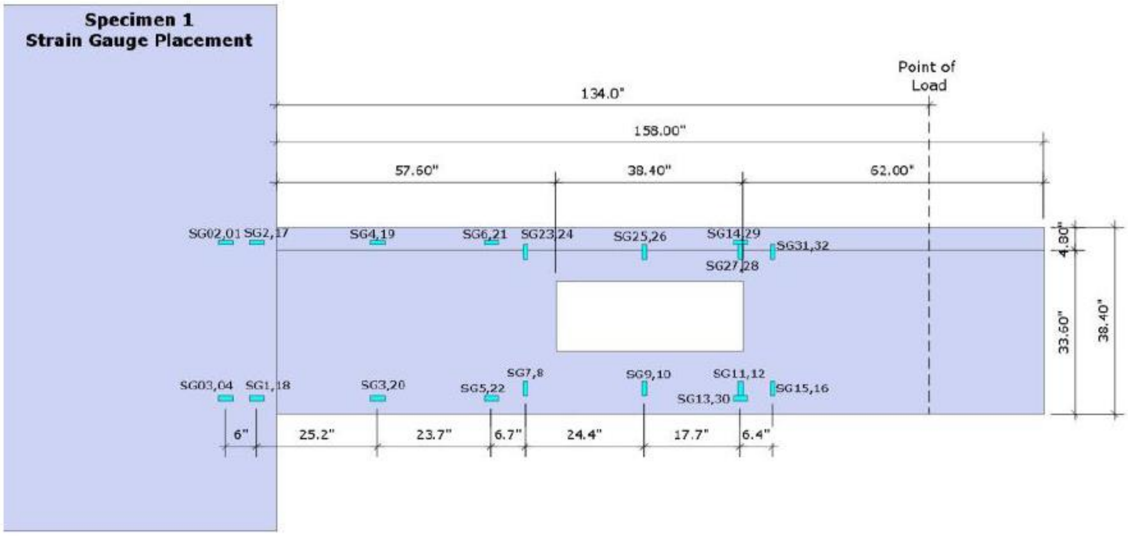

Figure 3.8: Layout of Strain Gauges on Specimen 1 (Lemnitzer et al., 2013).

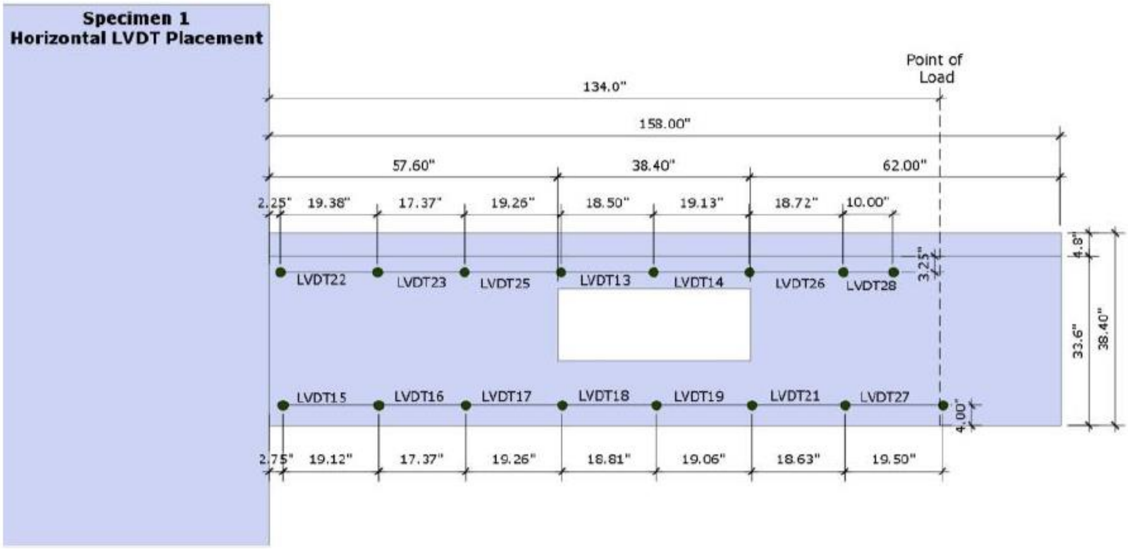

Figure 3.9: Layout of horizontal LVDTs on Specimen 1 (Lemnitzer et al., 2013).

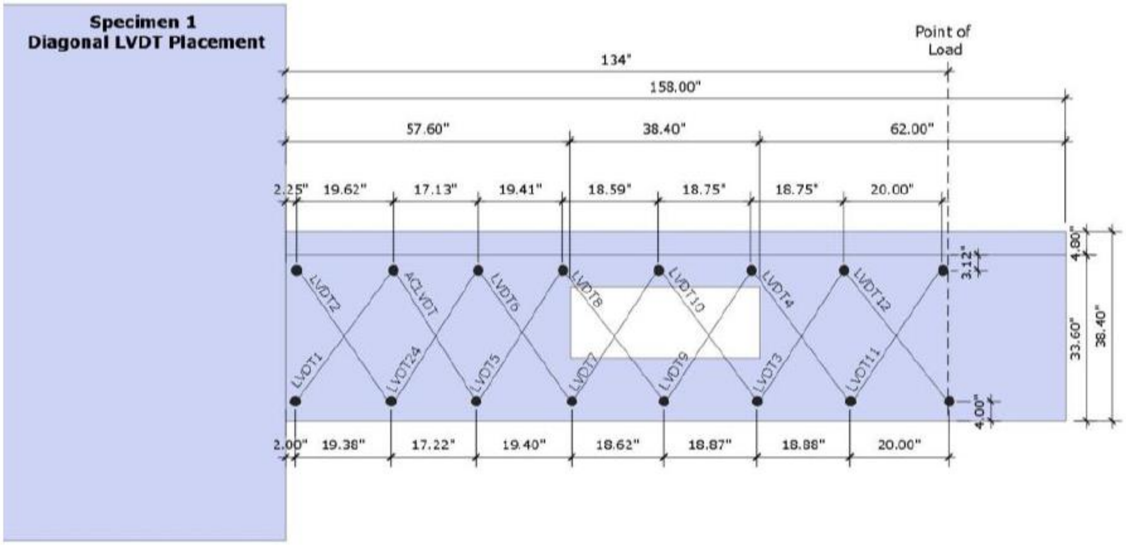

Figure 3.10: Layout of diagonal LVDTs on Specimen 1 (Lemnitzer et al., 2013).

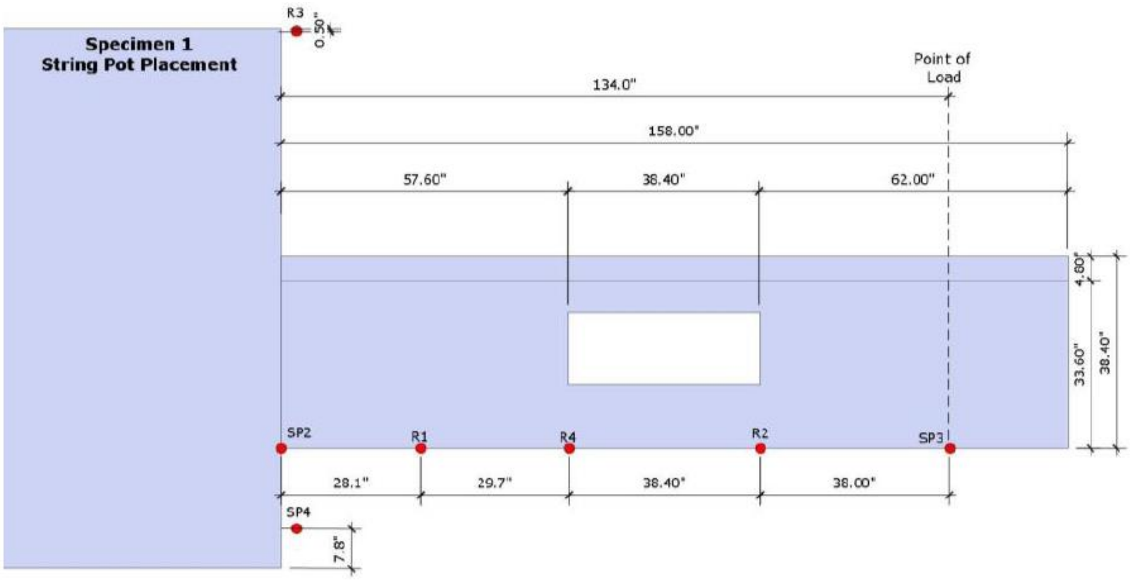

Figure 3.11: Layout of String Potentiometers on Specimen 1 (Lemnitzer et al., 2013).

The layout of the LVDTs for each specimen is available in Appendix B. For more details about the instrumentation and the remaining placement schemes can be found in the "Cyclic Behavior of SMRF RC Beams with and without openings – Phase 1" report (Lemnitzer et al., 2013).

3.1.5. Load Application

The load application system consisted of a vertical point load applied at the non-fixed end of the specimen. A hydraulic actuator with a capacity of $300\,[kips]$ in compression (downward push) and $270\,[kips]$ in tension (upward pull) was used. The actuator was attached to a loading frame with a maximum capacity of $270\,[kips]$, which was anchored to the strong floor and chained to both the strong wall and the strong floor in order to prevent possible rotations of the frame.

A u-shaped three plate system was anchored to the specimen at its end, in order to apply the load from the actuator. Figure 3.12 shows the loading frame with the actuator already anchored and chained and Figure 3.13 shows the plate system at the load application point.

Figure 3.12: Loading Frame with Actuator (Lemnitzer et al., 2013).

Figure 3.13: Plate system anchored to the specimen (Lemnitzer et al., 2013).

The actuator applied a quasi-static reverse cyclic loading with displacement control.

A testing protocol was developed, and it is available in Appendix 4 of the report by Lemnitzer et al. (2013). In general, it can be mentioned that in accordance with ASCE 41-06 S1, three cycles per displacement level were applied for the first part of the tests and just two cycles were applied later, when plastic rotation was exceeded.

3.2. Preliminary Tests Results

The preliminary test results are available in Section 3 of the report by Lemnitzer et al. (2013). Those results include the time histories directly from the instruments data, force-deformation curves and beam deflection profiles. However, the most important information available directly in the mentioned report is the description of the failure modes and the photographs showing the final state of each specimen.

Figures 3.14 to 3.21 show the failure mode of each specimen and a brief description of its nature.

Specimen 1

Specimen 1 failed due to the development of a plastic hinge at the opening. Early crack development was observed around the opening according to the reference (Lemnitzer et al., 2013). Figures 3.14 and 3.15 show the plastic hinge at the opening.

Figure 3.14: Plastic hinge at 4.5% drift level (Specimen 1), (Lemnitzer et al., 2013).

Figure 3.15: Opening section at test termination (Specimen 1), (Lemnitzer et al., 2013).

Specimen 2

In contrast to Specimen 1, in this case the opening remained undamaged. The failure occurred at the beam/block interface with the formation of a plastic hinge accompanied with concrete spalling and buckling of reinforcing bars. Figure 3.16 shows the plastic hinge at the interface and Figure 3.17 shows the undamaged opening section after test completion.

Figure 3.16: Plastic hinge with rebar buckling (Specimen 2), (Lemnitzer et al., 2013).

Figure 3.17: Specimen 2 at test completion with plastic hinge at the left of the picture and the undamaged opening at the center, (Lemnitzer et al., 2013).

Specimen 6

Similar to Specimen 2, Specimen 6 failed at the beam/block interface due to the formation of a plastic hinge and the opening section remained undamaged. Figure 3.18 shows a close up of the plastic hinge region and Figure 3.19 shows the entire specimen after test completion with emphasis on the undamaged opening.

Figure 3.18: Plastic hinge at beam/block interface (Specimen 6), (Lemnitzer et al., 2013).

Figure 3.19: Undamaged opening at Specimen 6 after test completion and plastic hinge at the far left of the picture, (Lemnitzer et al., 2013).

Specimen 7

Specimen 7, the only one without an opening, developed a plastic hinge at the beam/block interface, similar to Specimens 2 and 6. Figures 3.20 and 3.21 show the development of the hinge first at certain displacement level and then after test completion.

Figure 3.20: Early plastic hinge with separation of the top slab (Specimen 7), (Lemnitzer et al., 2013).

Figure 3.21: Specimen 7 after test completion, plastic hinge accompanied with rebar buckling, (Lemnitzer et al., 2013).

3.3. Estimation of Deformations

The deformations can be estimated from the tests data, derived from the instruments time histories using appropriate relations that are detailed in this section. The main interest is to estimate the shear and flexure deformations of the specimens, which is essential in order to compare the experimental and the analytical results.

As mentioned in Section 3.1.4, a difference is made when referring to the instruments. Taking account of that consideration, it should be noted that the "internal instrumentation" is useful to estimate the shear and flexural deformations independently and the "external instrumentation" is useful to determine the total deformations of the specimens. It is worth to mention that the internal instrumentation may experience difficulties in capturing the total deformations because of limitations given by its own configuration, but it is a reliable way to estimate the shear and flexure deformations independently.

3.3.1. Shear deformations

The shear deformations are estimated using the readings from the diagonal LVDTs. The general case is presented, showing the procedure.

The generic specimen is divided into several levels through its length. One level is represented by each "X" configuration consisting of a pair of LVDTs. Deformations are estimated using the relation 3.3.1.1 for each level. The situation described is shown in Figure 3.22.

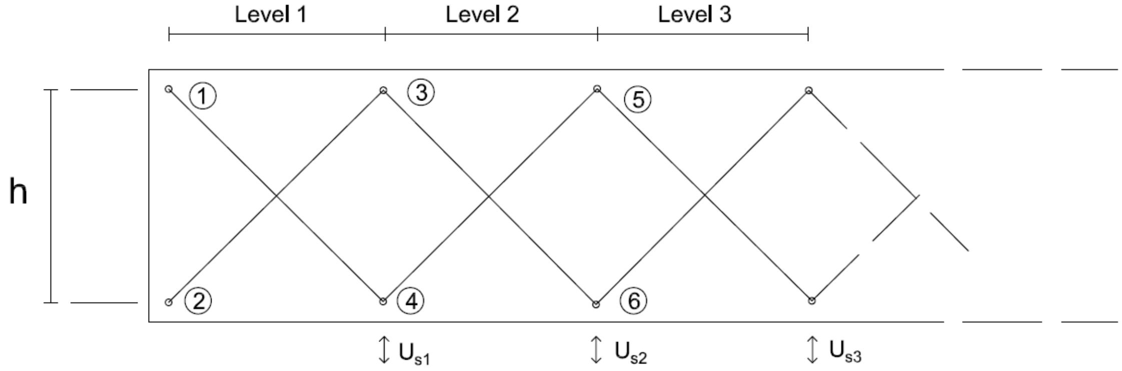

Figure 3.22: Levels for shear deformations.

Each level contributes with a vertical displacement that adds to the total tip displacement. To exemplify and detail how each level displacement is estimated, Figure 3.23 is introduced, with level 1 as generic example.

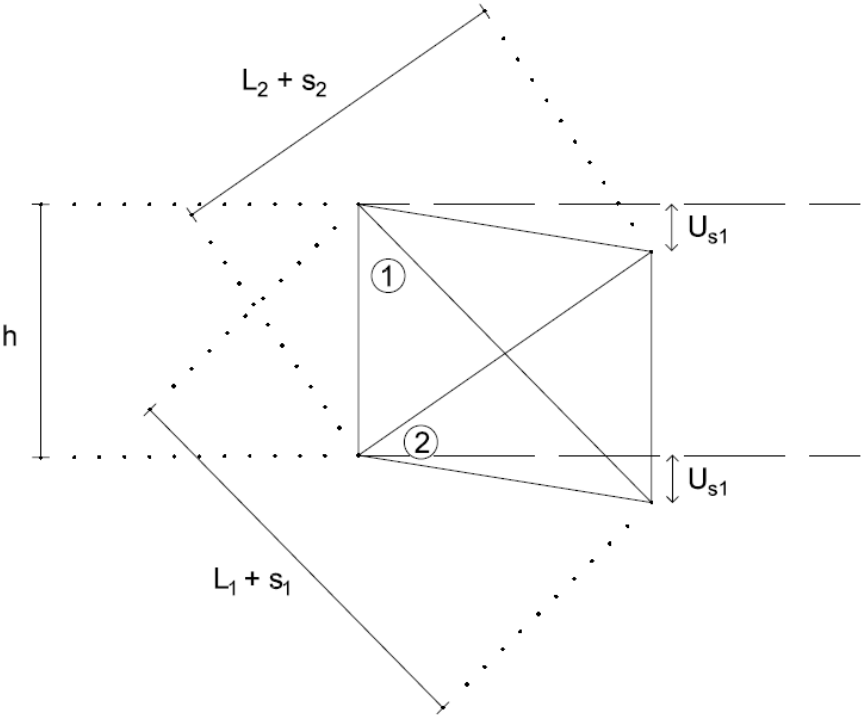

Figure 3.23: Shear displacement determination for one level.

In Figure 3.23, level 1 is represented by its two diagonal LVDTs, identified with numbers 1 and 2 inside a circle. The situation represented is a particular deformation, where LVDT 1 extends and LVDT 2 shortens. The lengths of the LVDTs in that state are the sum of its original lengths (L_1 and L_2 respectively) and the readings at that moment (s_1 and s_2 respectively). The shear displacement at any given displacement control level is obtained using the relation 3.3.1.1 (Massone and Wallace, 2004).

$$\boldsymbol{U_{s1} = L_0 \cdot \frac{(s_1 - s_2)}{2h}} \tag{3.3.1.1}$$

where,

$\boldsymbol{U_{s1}}$: shear displacement for level 1.

$\boldsymbol{s_1, s_2}$: readings of the LVTDs.

$$\boldsymbol{L_0 = \frac{L_1+L_2}{2}}$$,(average length of the LVDTs).

$\boldsymbol{h}$: height of the “X” configuration.

The total shear displacement at the tip of the specimen (load application point) is estimated as the sum of the shear displacements of all levels along the beam:

$$\overline{\boldsymbol{U}}_{\boldsymbol{s}} = \sum \boldsymbol{U}_{\boldsymbol{si}} \tag{3.3.1.2}$$

The results are available in Chapter 5.

3.3.2. Flexural deformations

For the flexural deformations, the readings from the horizontal LVDTs are used.

In order to estimate the flexural deformations, a similar procedure to the shear deformations is followed. The specimen is divided into several levels (not necessary the exact same lengths as the shear levels) and a vertical displacement is estimated for each level. The situation is presented in Figure 3.24.

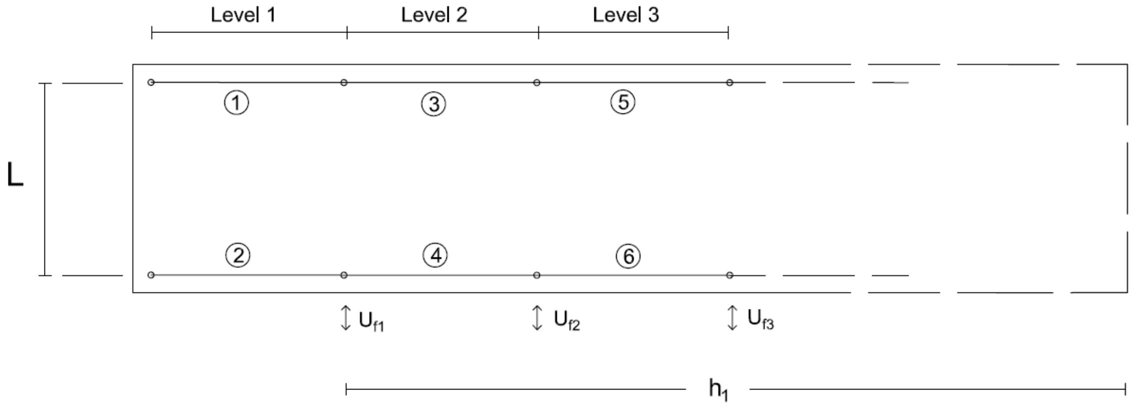

Figure 3.24: Levels for flexural deformations.

Level 1 is now used as example on how to estimate the flexural deformation for one level in Figure 3.25.

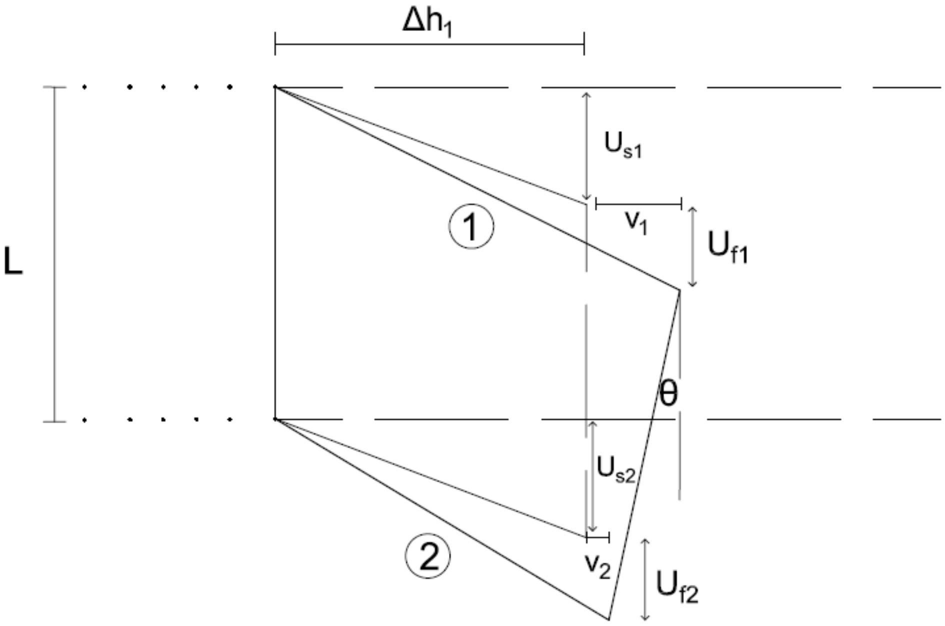

Figure 3.25: Flexural deformation for one level.

Figure 3.25 shows the combined shear and flexural deformations for level one. The horizontal LVDTs (LVDT 1 and LVDT 2), used to estimate the flexural contribution, are labeled with numbers 1 and 2 inside a circle. Those LVDTs present extensions of v_1 and v_2 respectively. The flexural contribution U_{f1} is estimated following the relation 3.3.2.1 (Massone and Wallace, 2004).

$$\boldsymbol{U_{f1} = \theta_1 \cdot (\alpha \cdot \Delta h_1 + h_1)} \qquad (3.3.2.1)$$

where,

$\boldsymbol{U_{f1} = U_{f2}}$: flexural deformation for level 1 (level 2 adopts the notation U_{f2} as its flexural deformation).

$\boldsymbol{\theta_1 = \frac{v_1 - v_2}{L}}$

$\boldsymbol{L}$: height of the horizontal bi-LVDT configuration.

$\boldsymbol{v_1, v_2}$: readings of the horizontal LVDTs.

$\boldsymbol{\alpha}$: center of rotation for the level due to flexural deformation (assumption: $\alpha = 0.5$).

$\Delta \boldsymbol{h_1}$: average original length of the LVDTs.

$\boldsymbol{h_1}$: distance between the right end (loaded end) of the specimen and the right original border of level 1 (shown in Figure 3.24).

The total flexural displacement at the tip of the specimen (load application point) is estimated as the sum of each level displacement:

$$\boldsymbol{\overline{U}_f = \sum U_{fi}} \tag{3.3.2.2}$$

The results are available and analyzed in Chapter 5.

3.3.3. Further relevant data

Other estimations that can be made from the instrumental data, in order to capture the behavior of the specimens are: the beam deflection profiles and the eventual rotations of the reaction block (both from the string potentiometers), the load-displacement curves and internal strains from the strain gauges. The totality of the results including those mentioned here are available in Chapter 5.

CHAPTER 4. Implementation of Beams with Transverse Openings in the Flexure and Shear-Flexure Interaction Models

4.1. Beam Discretization

The beam discretization is the same for the flexural model and the interaction model. Four cantilever beams were modeled, according to the four specimens tested (description of the tests in Chapter 3).

As described in Sections 2.2 and 2.3, a beam is first divided into several elements through its length, and then, the cross section is divided horizontally into several fibers or panels.

Some aspects to be kept in consideration are:

- Beams are cantilever specimens fixed to a reaction block on one end and loaded through an actuator on the free end.
- Beams have a common cross section but differ in length and reinforcement.
- The beam has a top slab of 4.8 [inches] in thickness, giving the appearance of a T shaped beam.

4.1.1. Element Discretization

The main criteria in order to determine the length of the elements for discretization is to give similar lengths to the elements for each specimen in particular. The second aspect to be kept in consideration is the transverse reinforcement: one element cannot be defined with two or more different spacings for the stirrups. As consequence: where the stirrups spacing changes, there has to be an interface between elements.

Specimen 1 was discretized into 14 elements, the first 13 are 9.6 [inches] in length and the last one is 9.2 [inches] long. The discretization can be seen on the Appendix A, Figure A.1.

Specimen 2 was initially discretized into 11 elements of reasonable similar length. Two nodes were added after, increasing the number of elements up to 13. The first node was added as a consequence of the emergence of the opening inside one of the former elements, obliging to divide the one element that incorporated both section types: without opening and with opening. The second node is added in order to count with a reference node for the center (longitudinal) of the beam. This node is used to incorporate a self-weight load into the model, and it is located inside the same previously mentioned element (For Specimen 1, the addition of an extra node was not required, because one of the base nodes was located reasonably at the center of the beam). The result is that the former element of length 13.76 [inches] was divided into 3 shorter elements. The discretization described is shown in Figure A.2 of Appendix A.

Specimen 6 was divided into 14 elements. The first two elements are 14.4 [inches] long, the next nine elements are 12.8 [inches] long and the last three elements are 13.86 [inches] long. No initial element was modified in order to include nodes for self-weight load or due to transverse reinforcement properties. The discretization scheme for specimen 6 can be seen in Figure A.3 of Appendix A.

Specimen 7 is the only one without an opening. It was initially discretized into 8 elements, the first six elements were 16 [inches] long and the last two were 14.4 [inches] long. An additional node was necessary in order to have the reference node for the application of the self-weight load at the center of the beam. As a result of the addition of the reference node, element 4 (originally 16’’ long) was divided into two elements of shorter length. The number of elements increases to 9. The discretization of Specimen 7 is shown in Appendix A, Figure A.4.

4.1.2. Fiber Discretization

The dimensions of the cross section are common to all of the specimens. This reason gives the possibility of discretizing the cross section into the same 18 fibers for the four specimens. Each fiber, with its respective identification number, is located at the same height for every modeled specimen. The difference between specimens comes when assigning the tributary areas of concrete and steel to each fiber, because the reinforcement ratios vary from one to another. The flange was divided into 4 fibers of 1.2 [inches] thick, while the web was divided into 14 fibers of 2.4 [inches] thick. The common cross section and its dimensions is presented in Figure A.5 and the discretized section is shown in Figure A.6, both available in Appendix A.

As briefly mentioned, for each fiber it is necessary to assign a tributary area for both concrete (confined and unconfined independently) and steel, depending on the reinforcing ratio of the specimen that is being studied. The longitudinal reinforcement varies through the specimen’s length, thus, for any given specimen, several sections must be declared and later assigned to the elements according to the longitudinal position being considered. For example, Figure 4.1 shows the reinforcing condition for Specimen 1 at Element 1 (as seen on Figure A.1).

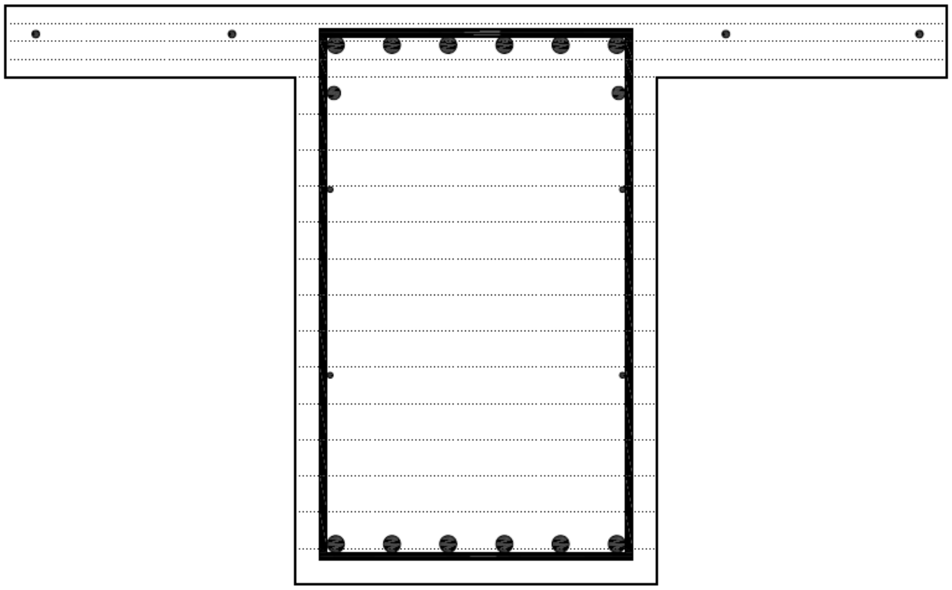

Figure 4.1: Cross Section for Specimen 1 at Element 1.

Figure 4.2 illustrates the reinforcing condition for Specimen 1 at the level of Elements 2,3,4,5 and 6 (from Figure A.1):

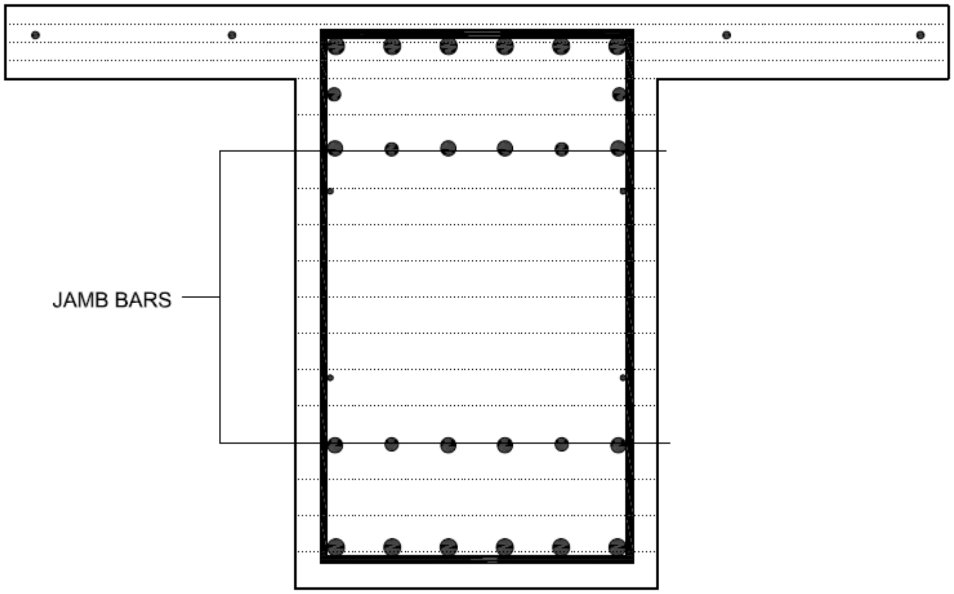

Figure 4.2: Cross Section for Specimen 1 at Elements 2,3,4,5 and 6.

It is clear that the addition of the Jamb Bars changes the cross section. Now some fibers that did not have steel tributary area (Figure 4.1) will do (Figure 4.2), and those same fibers will decrease their confined concrete tributary area because of the presence of the steel bars. Therefore, more than one section can be declared for one specimen, all depending on which element the section is used.

In order to exemplify the assignation of the tributary areas for a fiber, Figure 4.3 is introduced:

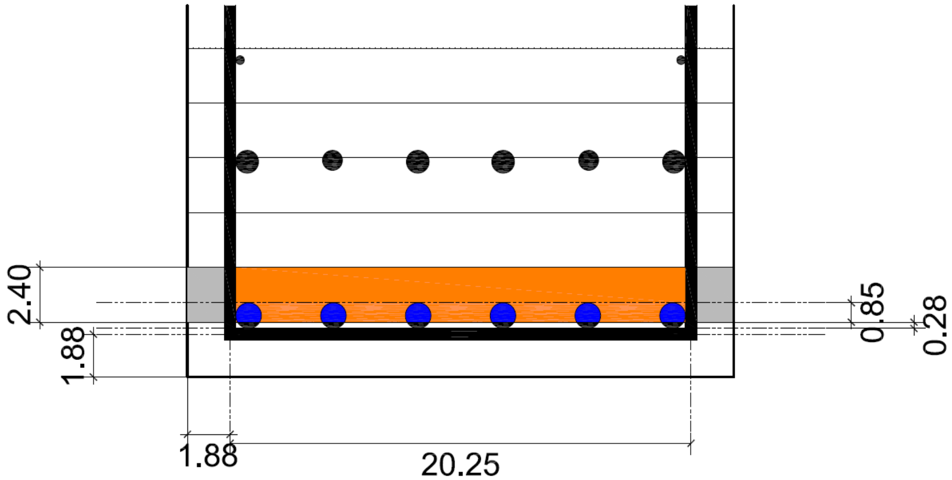

Figure 4.3: Tributary area assignment.

Figure 4.3 shows the lower portion of the cross section for Specimen 1 at the level of Elements 2,3,4,5 and 6 (same cross section as in Figure 4.2). The assignation of tributary areas for Fiber 2 is analyzed. This fiber is the second one from bottom to top and it has a thickness of 2.4 [inches]. The confined concrete is taken as the concrete inside the transverse reinforcement (which is presented as the thickest continuous line in Figure 4.3) from center to center of the stirrups and it is colored with orange. The unconfined concrete is colored with gray and it is the concrete from the center of the stirrups up to the end of the web. There is also a portion of the #9 bars that belong to Fiber 2, shown in blue color in Figure 4.3.

The tributary areas must be estimated as follows:

Steel:

> The steel area for Fiber 2 will be the area in blue, seen in Figure 4.3, associated with the material model of reinforcing steel detailed in Section 2.1.4.

Confined Concrete:

> The area of confined concrete for Fiber 2 is estimated as the difference between the total area inside the confinement and the area of steel inside the confinement. Associated with the material model for confined concrete, described in Section 2.1.3.

Unconfined Concrete:

> The remaining area of the fiber is the unconfined concrete, estimated as the difference of the total area of the fiber and the areas previously estimated. This area is associated with the material model of unconfined concrete (in case of compression of the lower part of the section) or the material model for concrete in tension (when the lower part is in tension).

4.1.3. Tributary Areas Assignment

As mentioned before, each specimen has different cross sections through its length, depending on the steel longitudinal reinforcement and the eventual presence of the transverse opening. A detailed description of each section found in each specimen is available in Appendix A, Section A.2.

The Figures A.7 to A.12 show the different cross sections that compose Specimen 1 in order of appearance, related to the elements into which Specimen 1 is divided (according to Figure A.1). These sections are described in Section A.2.1. If a cross section has some reinforcing bar in the figure, this is an indicator of the presence of the reinforcing bar where the cross section in question is located, does not indicate that the bar is effectively acting as reinforcement (development length might not yet have been reached within certain sections). Table A.1 shows the assignments of tributary areas for Specimen 1, following the procedure described in Section 4.1.2. Each section found through the length of Specimen 1 has 18 fibers. Each one of those fibers is assigned a tributary area for: unconfined concrete, confined concrete and steel. This detailed table is useful in order to create the sections in the Models (Flexure and Interaction). Several assumptions described in Section 4.3 are incorporated into the tributary area assignment that is seen in Table A.1 (as well as in Tables A.2, A.3 and A.4 that are yet to be mentioned).

The detailed tributary areas assigned per fiber according to their respective section for Specimen 2 are shown in Table A.2, in accordance to Figures A.13 to A.17 and to the description in Section A.2.2.

Analogously, the information for Specimen 6 is available in Section A.2.3 and for Specimen 7 in Section A.2.4, both found in Appendix A.

4.1.4. Transverse reinforcement

In order to incorporate the transverse reinforcement, a particular ratio must be associated with each section defined (as those mentioned in Section 4.1.3 and described in Section A.2). Where the ratio represents the transverse reinforcement for each element defined using a particular section. The ratio in question is the parameter required by the analytical model to incorporate the transverse reinforcement.

As an example, Specimen 1 is used. There are two different transverse reinforcement spacings along Specimen 1. For the first $86.4\ [inches]$, $\#4$ stirrups spaced $4.75\ [inches]$ are found. The remaining of the specimen has $\#4$ stirrups spaced $3.25\ [inches]$.

The spacing of $4.75\ [inches]$ covers the first 9 elements of the specimen (elements are shown in Figure A.1 and stirrups for each specimen can be appreciated in Figures B.1 to Figure B.4). A total of 18 stirrups are reinforcing those 9 elements, giving an average per Element of:

$$Stirrups\ per\ Element = \frac{18}{9} = 2\ \left[\frac{stirrups}{element}\right]$$

Each element contains two stirrups. The transverse cross section of one element looks like Figure 4.4 (plan view).

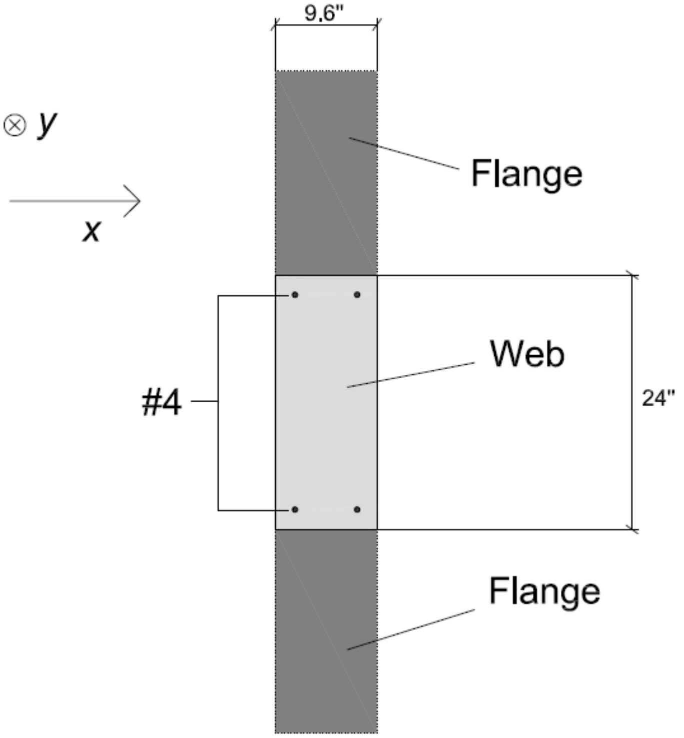

Figure 4.4: Transverse reinforcement example (Specimen 1).

Four $\#4$ reinforcing bars appear in the transverse cross section of one elements given the first stirrups spacing on Specimen 1. The total area of transverse reinforcement per element is:

$$A_{st} = 4 \cdot \frac{\pi}{4} \cdot \left(\frac{4}{8}\right)^2 = 0.7854\ [in^2]$$

Therefore, the sections for the first 9 elements of Specimen 1, must be assigned with $0.7854\ [in^2]$ of transverse steel.

An analog procedure is carried out for the remaining elements of Specimen 1 and to the entire remaining specimens. Table A.5 contains the areas of transverse steel assigned to the four specimens. The elements referred to in Table A.5 are the elements detailed in the discretizations shown in Figures A.1 to A.4, according to the particular specimen that is being studied.

4.2. Relevant parameters to be included in the models

The relevant parameters that are incorporated in the model to represent the materials have been mentioned in Section 2.1. A summary of those parameters is available in Appendix C, Table C.3. The yield strengths of the steel reinforcing bars can be seen in Table 3.2.

4.3. Further Assumptions

4.3.1. Incorporating the Transverse Opening

In order to incorporate the transverse rectangular opening to the three specimens that contain this feature, the procedure is simple, but a slight assumption is made. The procedure consists of assigning a tributary area small enough to be negligible in the fibers that coincide with the opening. Figure 4.5 shows the cross section for Specimen 1 at the level of Elements 7 and 8 (as seen in Figure A.1), where the opening appears.

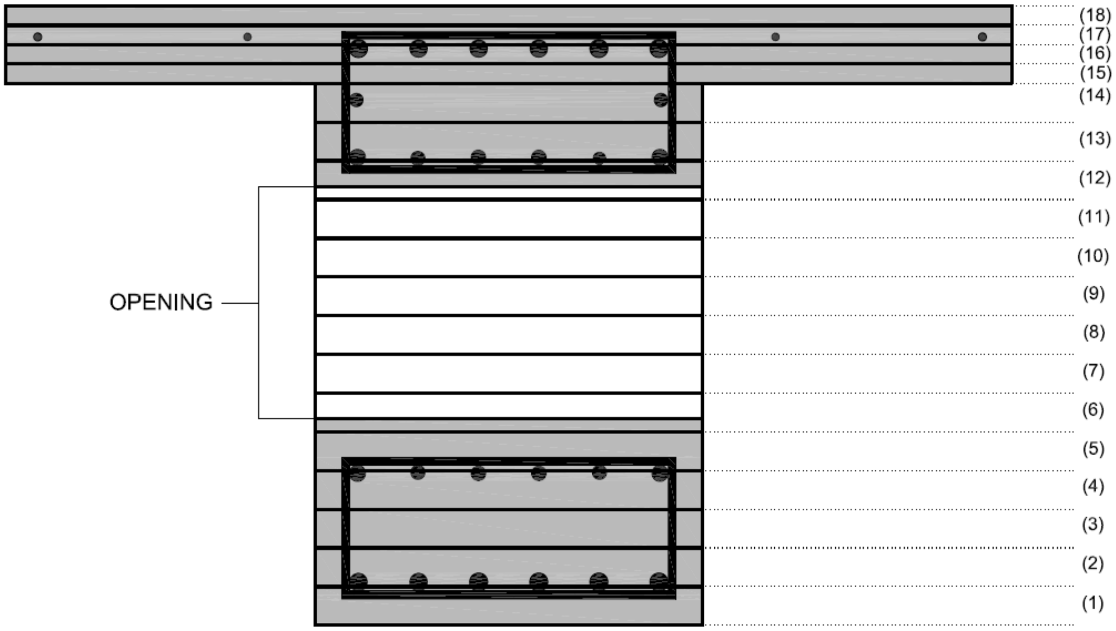

Figure 4.5: Cross Section with transverse opening.

For the fibers 7, 8, 9, 10 and 11 there is no concrete nor steel at all, making possible to assign minimum (negligible) tributary area in them. There is a small complication for the fibers 6 and 12. For fiber 6, there is a portion of unconfined concrete present, making more challenging to assign minimum tributary area. For fiber 12, there is a smaller portion of opening on a fiber more than half filled with unconfined concrete, resulting in the same problem just mentioned. The solution proposed consists in different approaches for the two fibers with problems. For Fiber 6, the solution is to assign the minimum area to it, but the portion of unconfined concrete is added to the Fiber 5, seeking to not underestimate the total area of concrete for the whole section. In the case of Fiber 12, an equivalent concrete area just as the one seen in Figure 4.5 is assigned, therefore considering the opening portion present. Figure 4.6 is shown in order to clarify the described procedure.

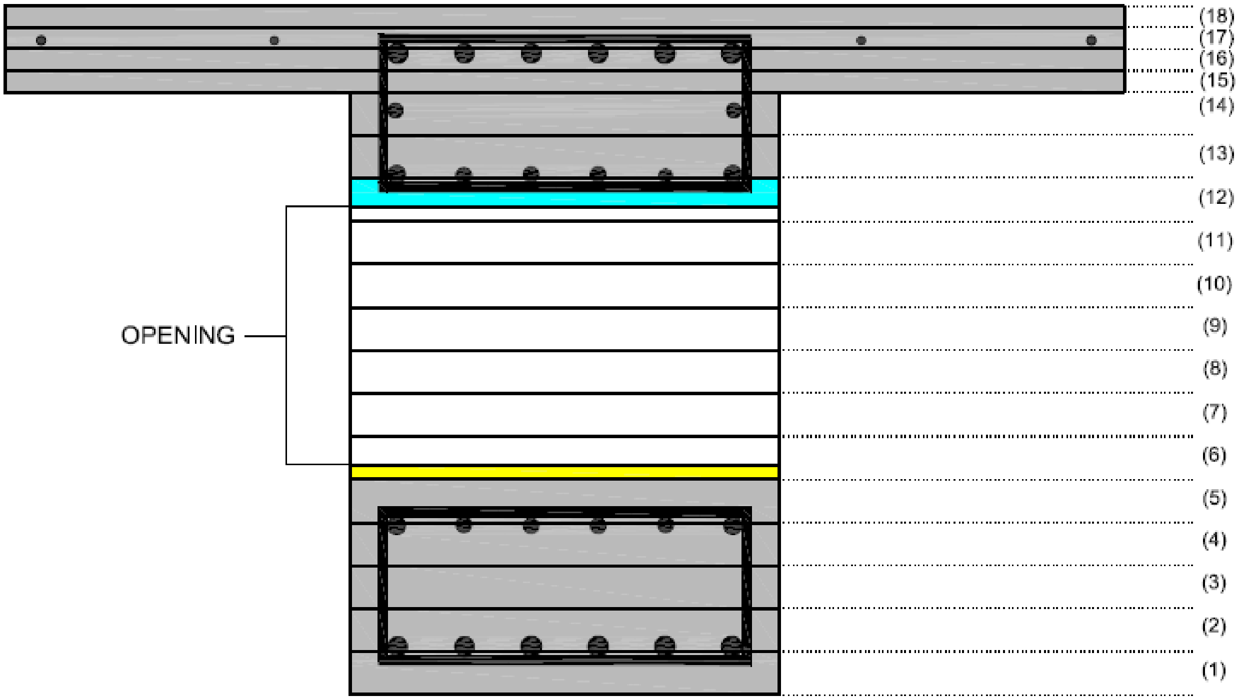

Figure 4.6: Tributary areas assignation with transverse opening.

The yellow portion seen in Fiber 6 of Figure 4.6 contains a certain area of unconfined concrete, but because this fiber is assigned with minimum tributary area, the yellow area of unconfined concrete is added to Fiber 5. In Fiber 12, the total area of unconfined concrete assigned is the one colored in cyan, without considering the opening portion.

4.3.2. Rotational Spring at Beam/Block Interface due to Strain Penetration

Some important discrepancies were observed in the first responses obtained through both the flexural and interaction models in the initial stiffness of the global load-displacement behavior of the specimens. Compared with the experimental results (available in Chapter 4), the stiffness is over predicted when the constraint at the beam-block interface is that of zero rotation. While the intention of the tests configuration is to give a constraint of zero rotation in that interface, in practice some inconveniences can occur.

As investigated and implemented in studies by Massone et al. (2009), there may be an unexpected rotation happening in the beam-block interface. This study investigated the presence of this rotations in walls anchored to a pedestal with no axial load but subjected to lateral cyclic loading, therefore it can be extended for its use in cantilever beams. The potential rotations may be caused by the extension of the longitudinal reinforcing bars.

A slipping of the longitudinal reinforcing bars extending into the reaction block is possible. Tensile forces are transferred from the steel rebar to the reaction block concrete because of the bond stresses between the rebar and its surrounding concrete. As a result, the stress on the rebar is reduced, and consequently the strain is also reduced as it extends deeper into the embedment. Along the development length (l_d), the force corresponding to yielding of the rebar is required to be fully transferred to the concrete. Longitudinal deformations of the rebar are caused by the strains along the development length, inducing the rotations at the beam-block interface. Slip of the rebar can be expected if the development length is not enough, degrading the bond between steel and concrete in the embedment.

In the present study, #3, #4, #7, #8 and #9 reinforcing bars are used in the tested specimens. However, main bars for top and bottom reinforcement consist of #8 and #9 bars for all the specimens. The recommended development length for these sizes can be estimated using the expression from ACI 318-2011 (Section 12.5.2), recommended for reinforcing bars in tension terminating in a standard hook, as it is the case with the main bars of the specimens. The equation is 4.3.2.1.

$$l_{dh} = \frac{0.02\,\psi_e f_y}{\lambda\sqrt{f_c'}} \cdot d_b \qquad (4.3.2.1)$$

where:

l_{dh} : development length with standard hook end.

d_b : reinforcing bar diameter.

f_y : yield strength of steel.

f_c' : compressive strength of concrete.

ψ_e = 1.0 for not epoxy-coated reinforcement.

λ = 1.0 for normal weight concrete.

The development length for sizes #8 and #9 bars terminating in a standard hook are shown in Table 4.3.

Table 4.1: Yield strength of reinforcing main bars (common for all specimens).

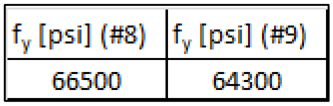

f_y [psi] (#8)	f_y [psi] (#9)
66500	64300

Table 4.2: Concrete compressive strength for each specimen.

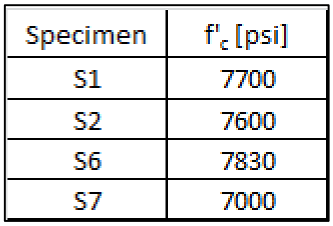

Specimen	f'_c [psi]
S1	7700
S2	7600
S6	7830
S7	7000

Table 4.3: Development length for main reinforcing bars.

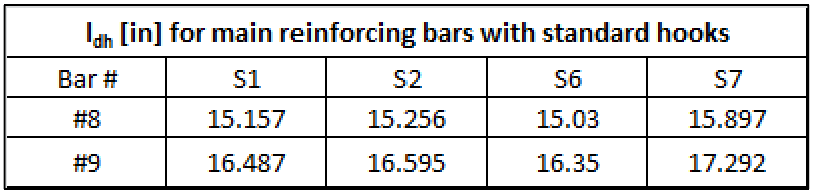

l_{dh} [in] for main reinforcing bars with standard hooks				
Bar #	S1	S2	S6	S7
#8	15.157	15.256	15.03	15.897
#9	16.487	16.595	16.35	17.292

The tested specimens had their longitudinal reinforcing main bars embedded 35.2 [inches] into the reaction block. Given the required development lengths shown in Table 2.3, it is clear that the extension of the bars into the reaction block is more than enough according to ACI 318-2011. Considering this last proposition, bond slip is not expected for the reinforcing bars, only the extension of them within the reaction block is considered.

Potential reinforcing bar extension can be analytically modeled. It is assumed that a crack forms at the beam-block interface. The interface cracks are formed during the post-tensioning of anchor bars or by micro-cracking caused by differential shrinkage of concrete at the interface. These cracks can cause rotations in the interface, and therefore reduce the rigidity for the load-displacement response for the modeled specimens. As mentioned in studies by Massone (2009), the contact in concrete can be restored after the application of a vertical load that creates a moment at the interface and the entire interface may not be fully cracked. However, the assumption described is used in order to predict a lower-bound vertical stiffness that takes into account the bar extension, and contact of concrete is considered within the compressive zone. The situation described and the solution proposed can be seen in Figure 4.7.

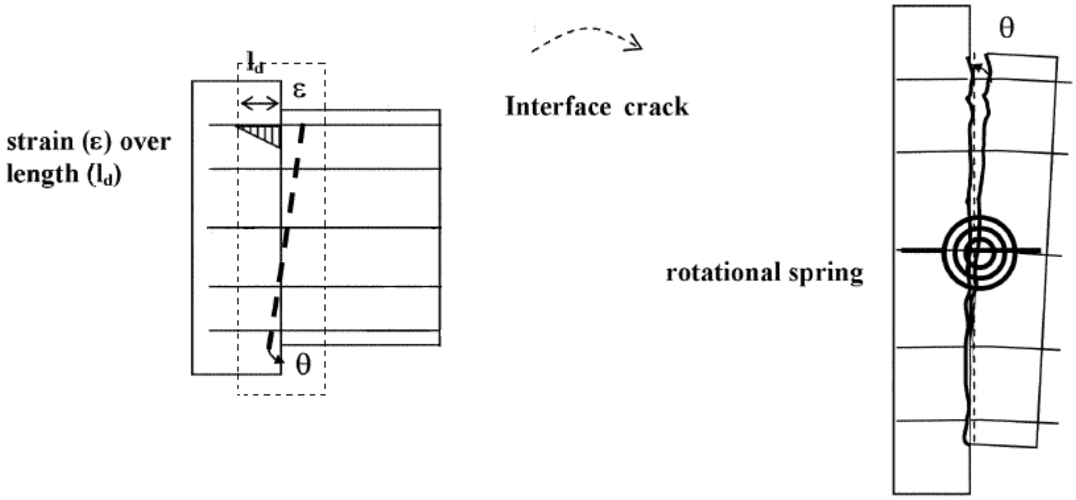

Figure 4.7: Reinforcing bar extension and interface cracking.

A rotational spring is considered in the model as a zero length element, where the stiffness is derived from a basic moment-curvature diagram of the cross section at the beam-block interface obtained using ETABS. The bending moment to curvature stiffness is determined directly from the moment-curvature diagrams.

The bending moment to curvature stiffness ($k_{m-\varphi}$) is estimated as the slope of the linear ascending portion (up to yielding point) of the moment-curvature diagram:

$$k_{m-\varphi} = \frac{M_y}{\varphi_y} \tag{4.3.2.2}$$

where M_y is the yield moment and φ_y is the yield curvature.

As the elongation of the reinforcing bars in the reaction block occurs, a cumulative rotation at the beam-block interface is expected as a result of the linear distribution of the longitudinal strains over the development length. The cumulative rotation (θ) is related to the curvature (φ), as it can be seen in Figure 4.8.

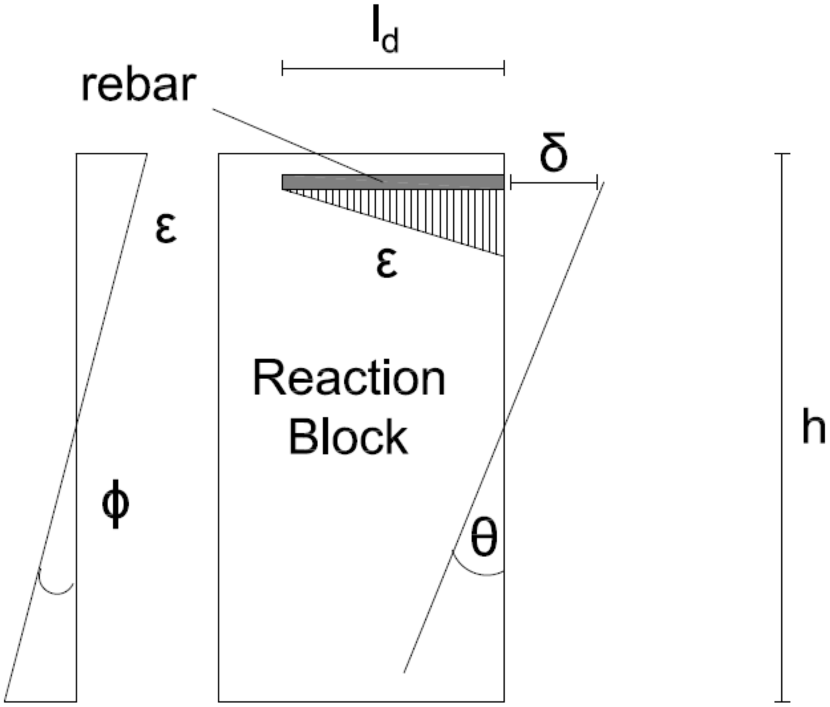

Figure 4.8: Bar extension and its relation with the rotation.

the bar (δ) extension is given by (considering maximum strain at the interface and zero strain when the development length is reached):

$$\delta = \frac{l_d}{2} \cdot \varepsilon$$

while the bar deformation (ε) can be estimated using the curvature (φ) and the beam height (h), (assuming rotation occurs at the center of the height of the beam):

$$\varepsilon = \frac{h}{2} \cdot \varphi$$

using both previous equations:

$$\delta = \frac{l_d}{2} \cdot \frac{h}{2} \cdot \varphi$$

but using the cumulative rotation:

$$\delta = \frac{h}{2} \cdot \theta$$

equaling the last two relations, expression 4.3.2.3 is obtained.

$$\Rightarrow \qquad \theta = \frac{l_d}{2}\varphi \tag{4.3.2.3}$$

The stiffness of the rotational spring is determined combining equations 4.3.2.2 and 4.3.2.3:

$$k_{m-\theta} = \frac{2}{l_d} \cdot k_{m-\varphi} \tag{4.3.2.4}$$

With the rotational spring at the beam-block interface, a lower bound-prediction of the rotational stiffness is used to the detriment of the zero rotation constraint at the interface. The estimated stiffness depends on whether the moment applied for the moment-curvature analysis is positive or negative. Both analyses must be made in order to simulate the load application on a cantilever beam upwards (positive moment) and downwards (negative moment) as the experimental program involves reverse cyclic loading. The results are in Table 4.4, showing the values used for the stiffness of each zero length element implemented in the model, depending on the direction of analysis.

Table 4.4: Rotational stiffness for the specimens.

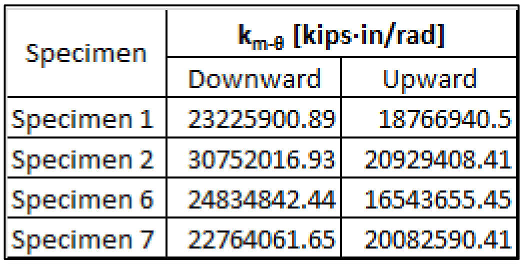

Specimen	$k_{m\text{-}\theta}$ [kips·in/rad]	
	Downward	Upward
Specimen 1	23225900.89	18766940.5
Specimen 2	30752016.93	20929408.41
Specimen 6	24834842.44	16543655.45
Specimen 7	22764061.65	20082590.41

4.3.3. Assignment of Self-Weight Load

A slight modification was implemented to the original model responses. An initial static load, equal to the total self-weight of each specimen was applied to the models respectively. This assumption accounts for the possible omission of the initial vertical displacements that a tested specimen can experiment prior to the test itself. If omitted, these displacements cannot be captured by the external instrumentation that measures the tip displacement of the beam. These sensors are calibrated and brought to a zero value prior to the beginning of the tests, but is possible that this calibration, without considering the self-weight load, induced displacements.

The procedure consists of estimating the self-weight of each specimen given their dimensions and assuming a unit weight of $2.5\ \left[\frac{ton}{m^2}\right]$ for the reinforced concrete. Table C.2 in Appendix C contains the estimated values of the self-weights for each specimen, and these values are applied as a downward static vertical load at the center length of the specimens in the model (as seen in Figure 4.9). The self-weights of the specimens range between 12 and 17 [kips].

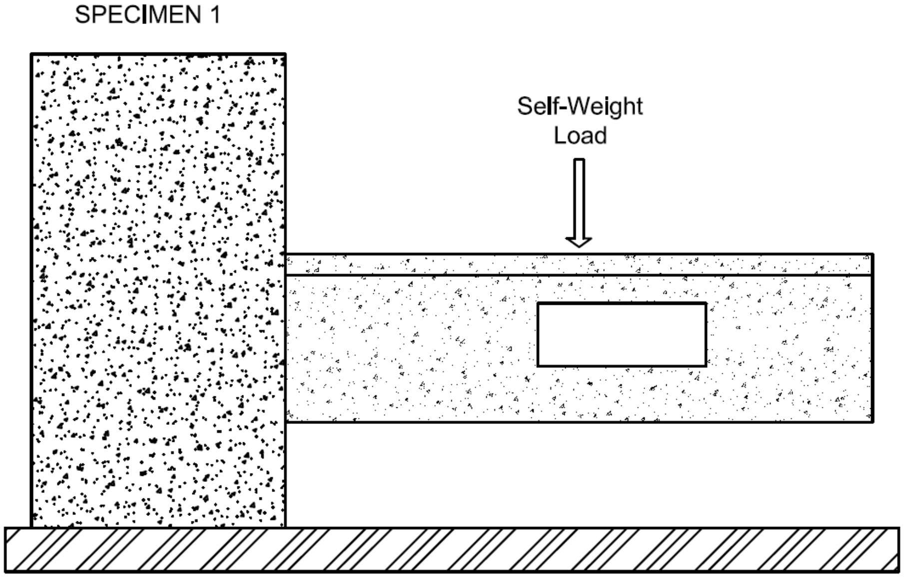

Figure 4.9: Self-weight load application at the center of the specimen.

4.3.4. Consideration of the Development Length when modeling Reinforcing Bars

The specimens had some of its reinforcing bars discontinuous along its length. This implicates that the development length of those bars is located inside the beam. For modeling purposes, the yield strength of those bars should not be taken as the 100% of the tested strength (f_y: as seen in Table 3.2) in some sections of the specimens.

In order to reach its effective yield strength, a reinforcing bar requires a minimum extension beyond the point where the peak stress is needed. This extension is the *development length*, which can be estimated for each bar size through the general relation (12-1) from ACI 318-2011:

$$l_d = \frac{3}{40} \cdot \frac{f_y}{\sqrt{f_c'}} \cdot \frac{\psi_t \psi_e \psi_s \lambda}{\left(\frac{c_b + k_{tr}}{d_b}\right)} \cdot d_b \qquad (4.3.4.1)$$

where,

l_d : development length

d_b : reinforcing bar diameter (inches)

f_y : yield strength of steel.

f_c' : compressive strength of concrete.

ψ_t = 1.0 when less than 12 [in] of fresh concrete is cast below the development length.

ψ_e = 1.0 for uncoated and galvanized reinforcement.

ψ_s = 1.0 for number 7 and larger reinforcing bars.

λ = 1.0 for normal weight concrete.

C_b : one half of the center to center spacing between bars.

k_{tr} = 0 as a simplification permitted by the code ACI 318-2011.

An approximation is made in order to account for the development length of the discontinuous reinforcing bars in the specimens. For the model, just 50% of the yield strength is considered along the development length of the bars. This is effective, assigning the 50% of f_y to the bars in the elements (as seen in Figures A.1 to A.4) where the development length is being reached. If one element combines a portion of the bar where the development length is yet to be reached and a portion where it is already completed, then 100% of f_y is assumed. Figure 4.10 sums up the described assumption.

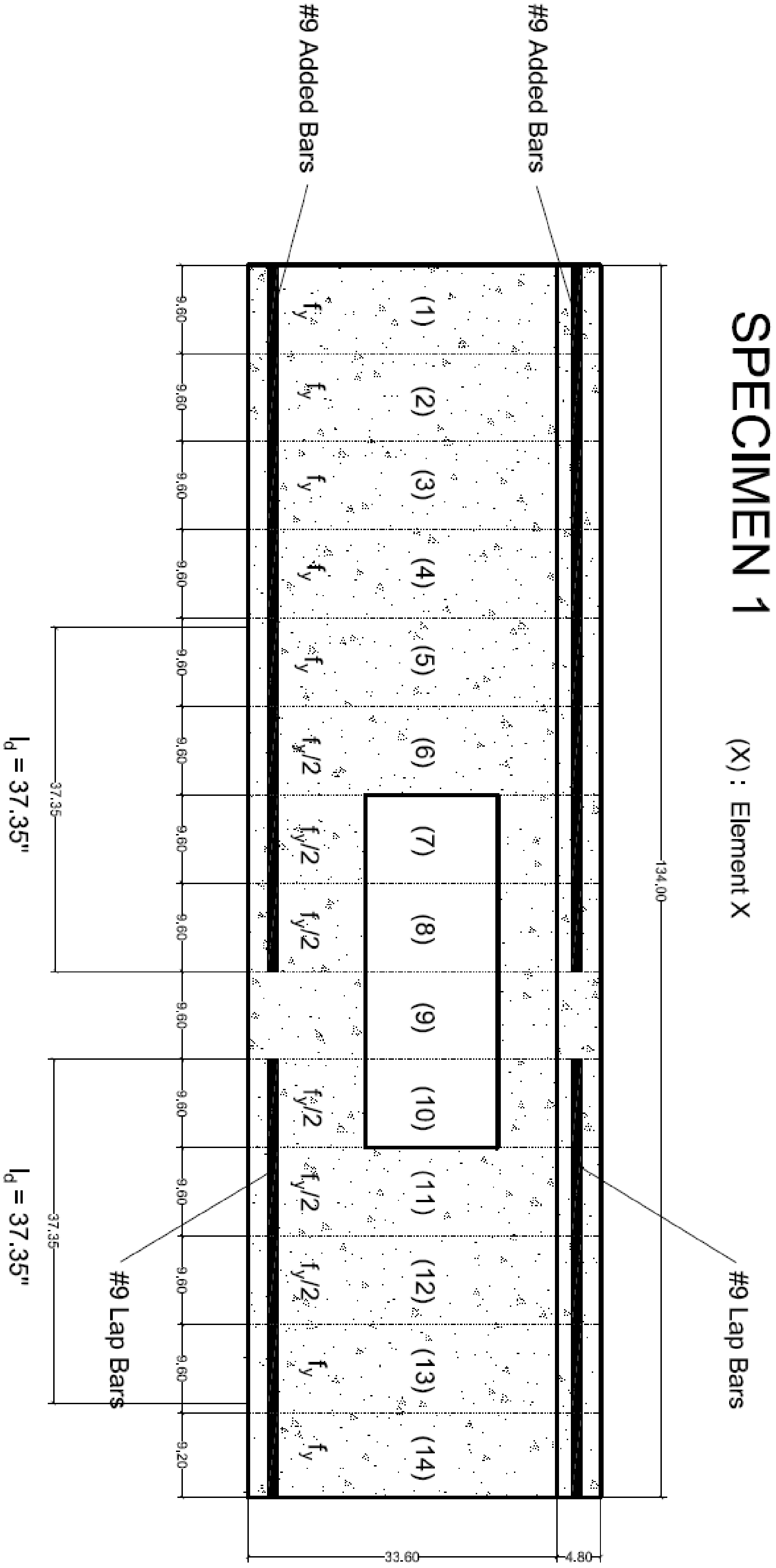

Figure 4.10: Example for the consideration of the Development Length.

The development length for a #9 reinforcing bar through equation 4.3.4.1 is 37.345 [inches]. Figure 4.10 shows the #9 added and lapped bars of Specimen 1, which are located at the same height of the main bars. The added bars count with the development length provided by the embedded portion of the bars at the left of the figure, assuring that the bars can take maximum stress for the first four elements. Elements (6), (7) and (8) are located along the development length, therefore 50% of the yield strength (f_y) is assigned to those elements. Element (5) combines segments of development length and 'reached development length', and taking into consideration the assumption described in the aforementioned paragraph, 100% of f_y is assigned. Similar analysis is made to the lapped bars, where the elements (10), (11) and (12) fall into 'development length portions'. The far right end of the specimens (beyond element 14 in Figure 4.10) is not considered in the model, because a specimen is modeled until the load application point. For this reason, element (14) can take 100% of f_y because the lapped bars of the real specimen had standard hooks at the right end and at the level of element (14), the development length is already reached.

Note: the reduction detailed in Section 2.1.4 is considered after the assignment of either 100% or 50% of f_y.

4.4. Alternative Beam Discretization

An alternative beam discretization was implemented for the specimens with openings (Specimens 1, 2 and 6). The main reason for this proposition is the inability to make Specimen 1 to fail at the opening through the interaction model using all the assumptions described up to Section 4.3.4. Specimen 1 was the only one that failed at the opening section during the tests described in Chapter 3.

The beam discretization proposed as an alternative consists in dividing the opening section in independent elements for the upper stretch and the lower stretch, as opposed to defining just one section through the height of the beam and assigning negligible area on the opening portion. Figure 4.11 shows the difference between the former assumption (original discretization) and the alternative discretization.

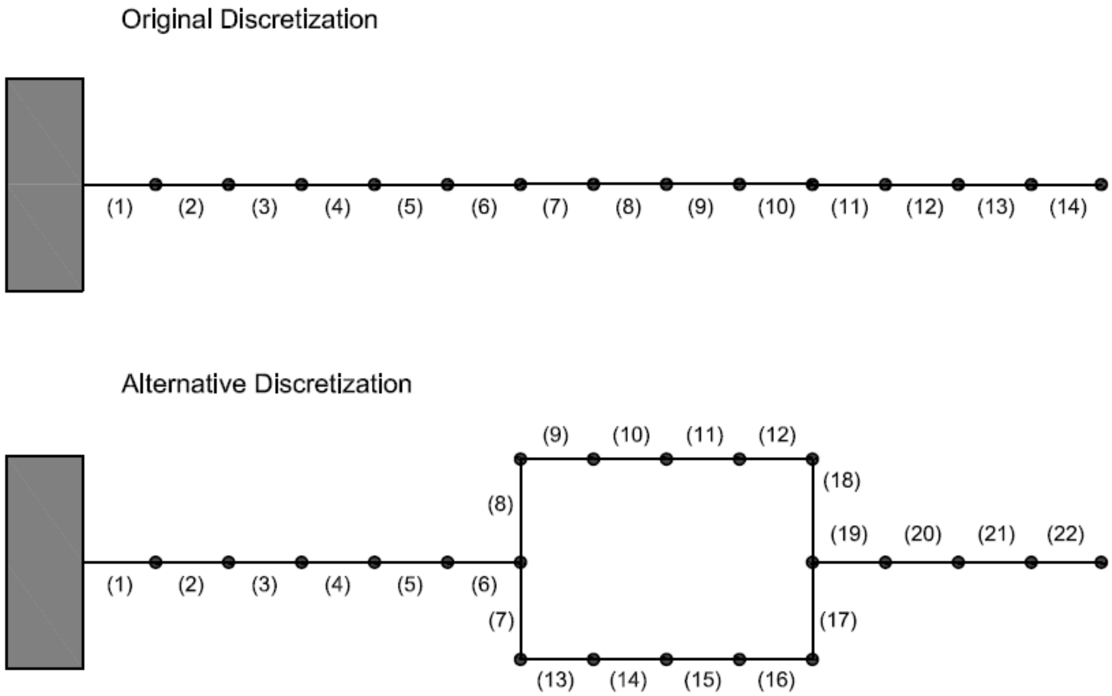

Figure 4.11: Difference between specimen discretizations.

Specimen 1 is used as example in Figure 4.11. With the original discretization, elements 7, 8, 9 and 10 composed the opening portion. The alternative discretization increases the number of elements from 14 to 22. Elements 7 and 8 are now vertical rigid elements (analog to elements 17 and 18) at the end of the specimen. Elements 9 to 12 now compose the upper stretch of the opening section and elements 13 to 16 compose the lower stretch of the opening section.

It is important to mention that only the elements that compose the opening are modified. Rigid elements are located at both ends of the opening (as seen in Figure 4.12), and independent elements are located over and beneath the opening. With this discretization, the negligible area used before is not necessary, because with this alternative there are no fibers composing the opening. The opening is modeled as a void between elements. With the rigid vertical elements at both extremes of the specimen, the model would look like Figure 4.12.

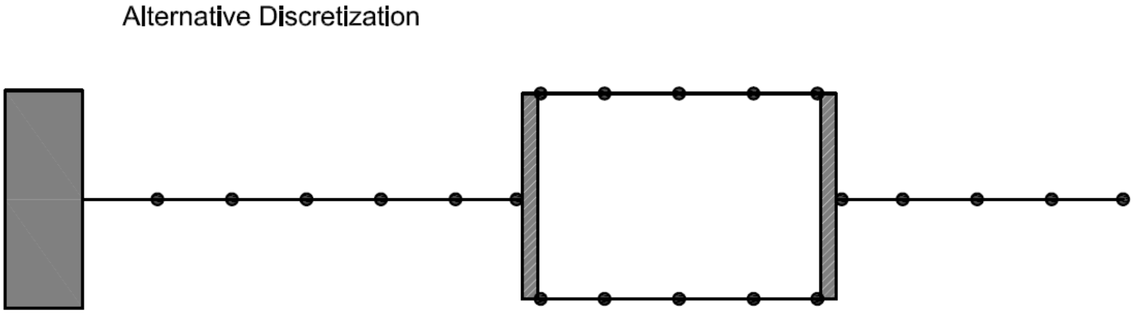

Figure 4.12: Alternative discretization with rigid elements.

For one particular specimen with opening, the sections that compose the opening stretch are originated from the sections declared for the former discretization. A section that is located over the opening is the same section as if in Figure 4.6 only fibers 12 to 18 were considered. Similarly, a section located beneath the opening would consider only fibers 1 to 6 of Figure 4.6. Therefore, reinforcement conditions are not modified, nor the tributary areas, just the positions of fibers 12 (for the upper stretch) and fiber 6 (for the lower stretch) are slightly modified with the intention of locating those fibers in the correct position for their centroid.

Figure 4.13 shows an example of how an original section is divided in two sections in this alternative specimen discretization.

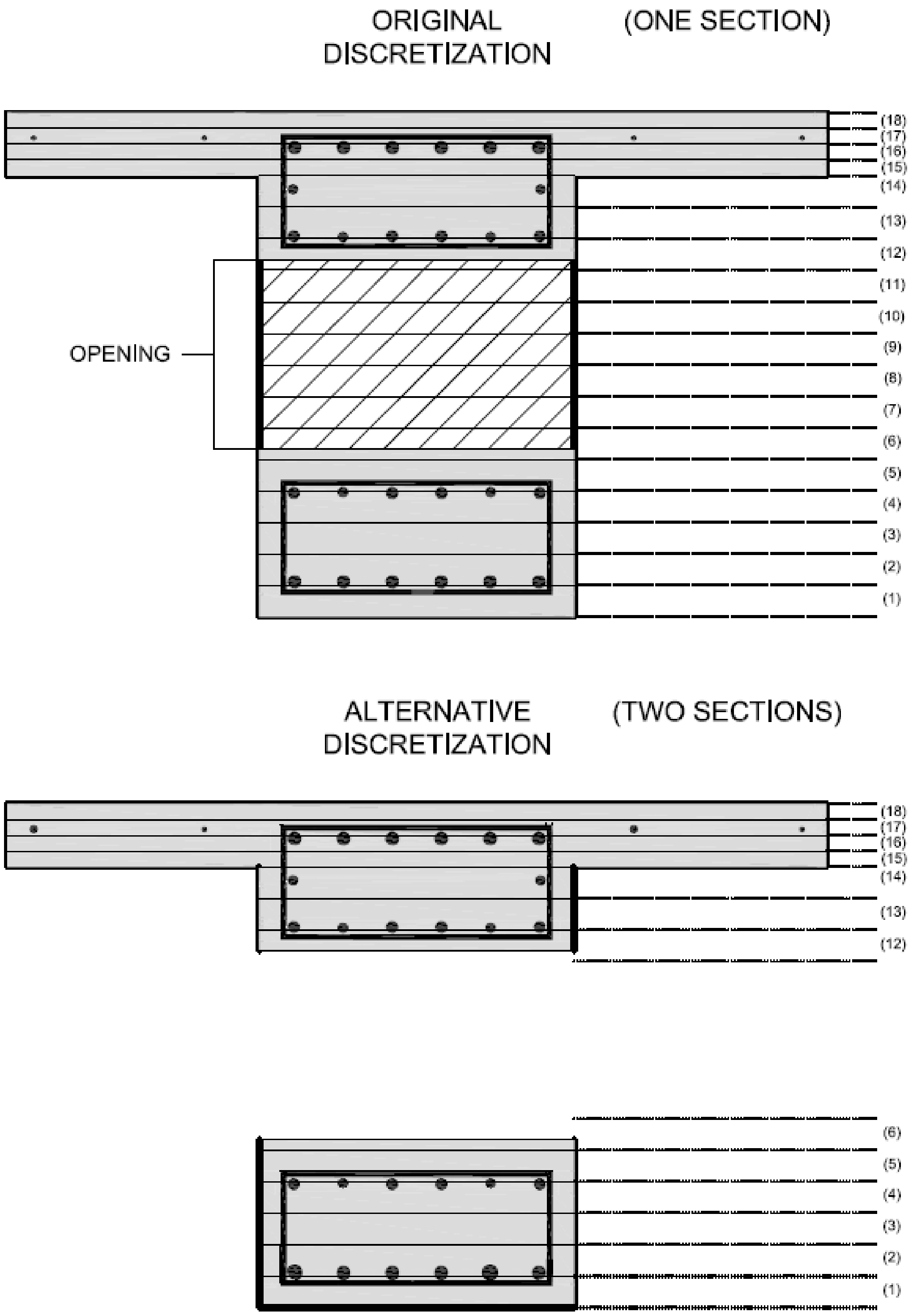

Figure 4.13: Section origin for the alternative specimen discretization.

Schemes of the alternative specimen discretization for each of the three specimens with openings are available at the end of Appendix A (Figures A.25, A.26 and A.27).

CHAPTER 5. Analysis of Results

5.1. Global Response

The global response is compared showing three curves for each Specimen, two of them are analytical (Flexural and the Interaction models) and the third curve shows the cyclic experimental response.

5.1.1. Signs and Quadrants clarification

First of all must be clarified that following the rule used in the report by Lemnitzer et al. (2013), a downward push produced on a specimen was recorded as a positive force. But a slight difference is made in this report. While the downward push is also plotted in the first quadrant, its displacement is noted with positive sign for the load-displacement curves, as opposed to the report by Lemnitzer et al. (2013), where the downward push is plotted with a negative displacement but in reversed x-axis, seeking to locate the downward push in the first quadrant. The idea is to utilize positive forces with positive displacements.

Without further confusion, a downward push produced by a positive force is shown with a positive displacement in the load-displacement responses (first quadrant). That forces to represent the upward pull with a negative force that produces a negative displacement (third quadrant).

5.1.2. Load-Displacement Curves

The following load-displacement curves consider the flexural and interaction models with all the assumptions made up to section 4.3.4. A comparison between the responses of the interaction model prior to and then after the assumption made in 4.3.4 (considering 50% of f_y during the development length of reinforcing bars) was made. Figures D.1, D.2, D.3 and D.4 show this comparison for each specimen. It can be appreciated that the load-displacement responses barely change for Specimens 1 and 7, while some discrepancies can be appreciated for Specimens 2 and 6. Specimen 2 proves to be more ductile for the upward pull with the assumption and Specimen 6 slightly approaches the experimental response with the assumption.

The assumption of 50% of f_y during the development length of reinforcing bars barely produces improvement in the load-displacement response, which is the only parameter where the difference is studied. However, the assumption is made for the remainder of the study, as it resembles the empirical situation in a better way than assuming reinforcing bars with their full yield strength before reaching their development length.

Specimen 1

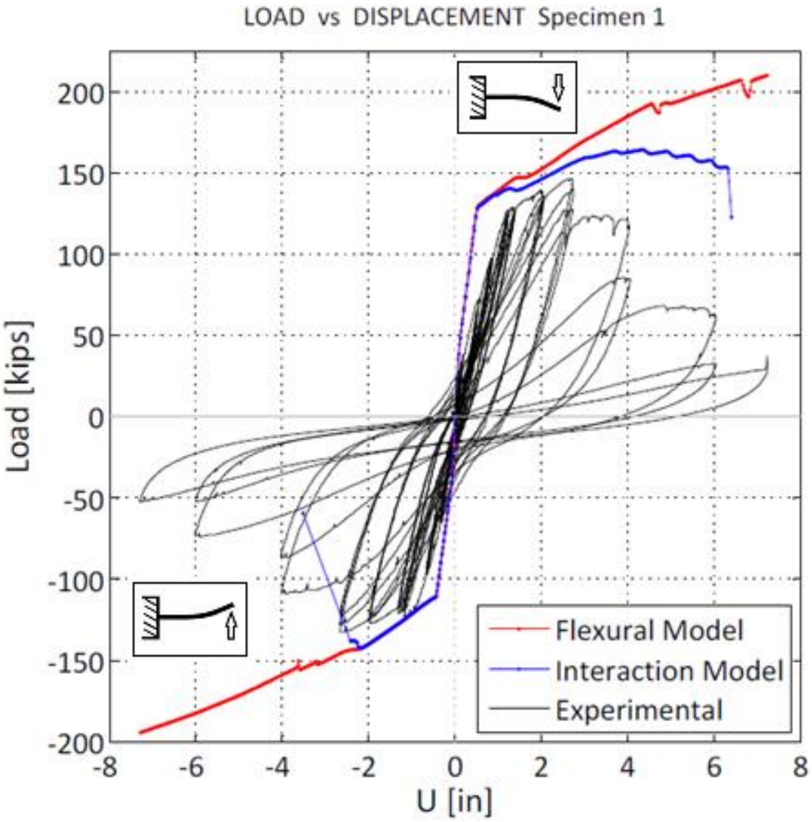

Figure 5.1: Load - Displacement Curves for Specimen 1.

The flexural model fails to reach degradation zone (as with all the other specimens) in both directions, because of its impossibility to consider the shear contribution to the displacements. It behaves identical to the interaction model in terms of initial stiffness and for the upward pull it behaves identical to the interaction model even after the initial elastic stretch.

The interaction model (as the flexural model) presents higher initial stiffness compared to the experimental response, with an estimated initial stiffness in the range of 140% higher than the experimental (initial stiffness estimations are shown in Table D.2 of Appendix D.). The assumption of rotational spring at the beam/block interface described in Section 4.3.2 is insufficient in order to fix the stiffness problem by itself.

At the end point of their respective elastic stretch (when the yield point of the reinforcing bars is expected), the displacements of the interaction model are less than 40% of the experimental displacements (Table D.2), as a consequence of the higher initial stiffness of the interaction model. The experimental load at this point is slightly higher for the downwards direction and 13% higher for the upwards direction (Table D.2).

As Table D.3 shows, the experimental ultimate strength or maximum capacity is $146.65\,[kips]$ in the downwards direction, at a displacement of $2.7\,[inches]$ ($2.0\,\%$ drift) and $132.613\,[kips]$ in the upwards direction, at a displacement of $2.6\,[inches]$ ($2.0\,\%$ drift). The maximum capacity for the interaction model is $164.28\,[kips]$ downwards, at a displacement of $4.33\,[inches]$ ($3.2\,\%$ drift) and $142.36\,[kips]$ in the upwards direction, at a displacement of $2.19\,[inches]$ (1.6% drift). Both maximum capacities are overestimated in the range of $\sim 10\%$, while the displacements do not follow analog behavior, as the displacement is considerably higher in the downwards direction and it is lower upwards, but nearer to the experimental response.

The maximum capacity is higher in the downwards direction as a result of the reinforcing condition. The top part of the specimen has a higher reinforcement ratio than the lower part in all of the specimens.

The beginning of degradation (when the element evidently fails to take load) occurs at a displacement of $2.74\,[inches]$ ($2.0\,\%$ drift) for the experimental downwards direction and $6.33\,[inches]$ ($4.7\,\%$ drift) for the interaction model (results available in Table D.4). The interaction model proves to represent the specimen more than twice as ductile as the tested specimen for the downward push. For the upward pull, the beginning of degradation occurs at a displacement of $2.67\,[inches]$ ($2.0\,\%$ drift) according to the experimental response and at $2.42\,[inches]$ ($1.8\,\%$ drift) for the interaction model (Table D.4). The upward pull is represented more accurately by the interaction model than the downward push in terms of ductility.

For the global response judged by the load-displacement curves, overall, the interaction model resembles the experimental results in higher amount for the upward pull than the downward push, as it was verified quantitatively for the maximum capacity and the ductility of the specimen. This assessment is evident when Figure 5.1 is seen, as the interaction model approaches better the experimental results in the third quadrant, which shows the upward pull.

Specimen 2

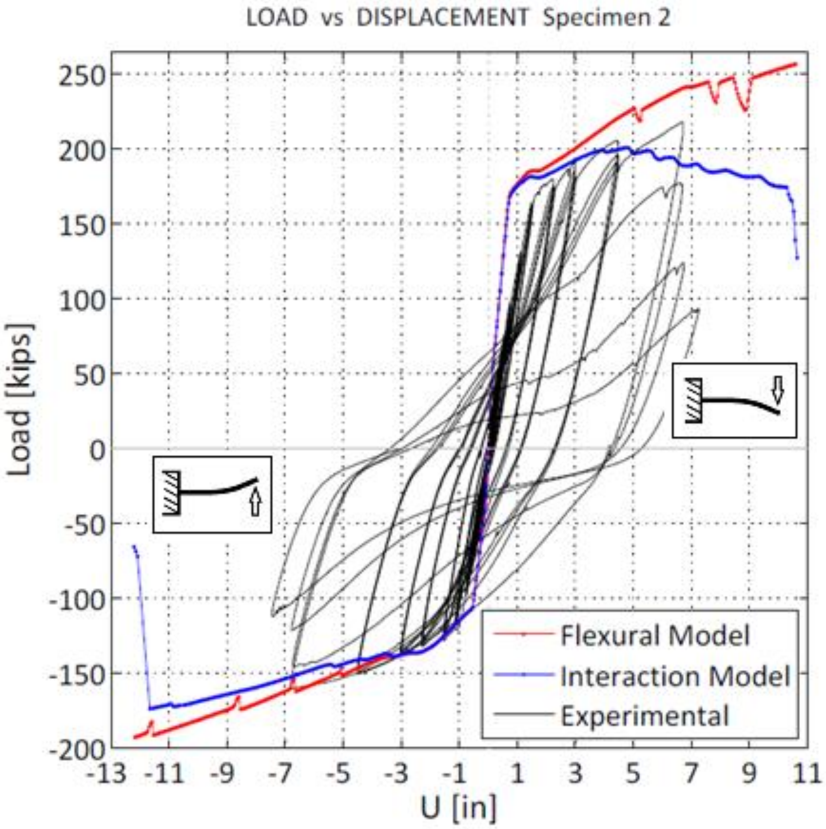

Figure 5.2: Load - Displacement Curves for Specimen 2.

The flexural model, with its limitations mentioned in the analysis of Specimen 1, behaves analogously to that specimen. In the elastic stretch, the flexural model follows the same curve as the interaction model. For the upward pull, the flexural model approaches the interaction model even after the initial elastic stretch, but drifts away from the interaction model curve after the elastic stretch for the downwards direction.

The initial stiffness for the interaction model is two times the initial stiffness of the experimental curve for the downward push and is $80\ \%$ higher for the upward pull. In this case, the estimated results (available in Table D.2) improve when compared to Specimen 1, but differ significantly from the expected results again.

At the end of the initial elastic stretch, the experimental displacements are $1.51\ [inches]$ and $1.11\ [inches]$ (as seen in Table D.2) for the downwards push and the upwards pull respectively. The interaction model computes displacements of $0.71\ [inches]$ and $0.53\ [inches]$ respectively. These results are to be expected, considering the initial stiffness for the experimental results that are found to be in the range of $\sim 50\%$ of the initial stiffness of the interaction model. The loads at this point are relatively similar for the experimental case and the interaction model.

Using the results from Table D.3, the experimental maximum capacity is $218.01\ [kips]$ for the downward push, at a displacement of $6.7\ [inches]$ (4.5% drift) and $160.47\ [kips]$ for the upward pull, at a displacement of $6.8\ [inches]$ (4.6% drift). For the interaction model the maximum capacity is $200.74\ [kips]$ for the downward push, at a displacement of $4.75\ [inches]$ (3.2% drift) and $174.02\ [kips]$ for the upward pull, at a displacement of $11.66\ [inches]$ (7.8% drift). The maximum capacities are in similar ranges experimentally and analytically, but as Figure 5.2 shows, the interaction model is too ductile in the upwards direction, reproducing a higher capacity than expected. In the downwards direction, the interaction model is also ductile, but the load that it can take reaches its maximum before reaching the degradation point.

The experimental beginning of degradation occurs at a displacement of $6.72\ [inches]$ (4.5% drift) for the downward push and $6.82\ [inches]$ (4.6% drift) for the upward pull (Table D.4). It presents almost identical ductility in both directions. The interaction model degradation begins at a displacement of $10.31\ [inches]$ (6.9% drift) downwards and at a displacement of $11.66\ [inches]$ (7.8% drift) upwards (same values of displacement and drift than for the maximum capacity in this direction). In terms of ductility, both directions present non satisfactory results, as the interaction model is considerably more ductile compared to the experimental results.

For Specimen 2, the interaction model fails to accurately represent the experimental results of the load-displacement curve. At global scale, the only parameter that approaches the desired results is the maximum capacity. The initial stiffness and the ductility are deficiently represented by the interaction model. Visually, the results are confirmed, approaching the experimental results just for the maximum capacity.

Specimen 6

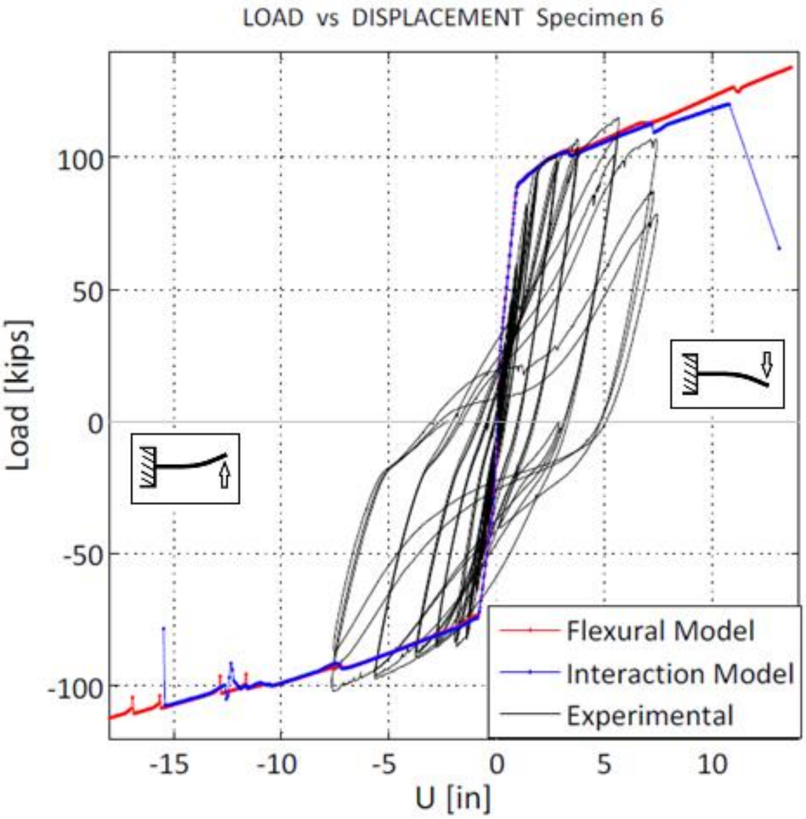

Figure 5.3: Load - Displacement Curves for Specimen 6.

The flexural model approaches the interaction model for the majority of each curves, drifting away from the interaction model in the downward push just before the latter reaches the beginning of degradation.

Estimated results for initial stiffness (available in Table D.2) indicate that the interaction model presents 75% higher initial stiffness for the downward push and 52% higher initial stiffness for the upward pull when compared to the experimental results. These results represent an improvement when compared with the results for Specimens 1 and 2, but are not entirely satisfactory.

The end of the elastic stretch occurs at displacements in the range of 50% higher for the experimental case, which is expected because of its lower initial stiffness, compared to the analytical initial stiffness. The load magnitudes at these points are similar between experimental and interaction model results, in the range of $\sim 10\%$ lower for the latter. (Results available in Table D.2).

Similar results are obtained for the maximum capacity between the experimental and the interaction model results (Table D.3). With differences in the range of 5%. The experimental maximum capacity is $114.94\ [kips]$ (at 3.0% drift) for the downward push and $102.01\ [kips]$ (at 4.1% drift) for the upward pull. The maximum capacity for the downward push of the interaction model is $120.05\ [kips]$ (at 5.8% drift) and $107.31\ [kips]$ (at 8.3% drift) for the upward pull. It is evident that while the maximum capacities are similar, the displacements at which those occur are two times higher for the interaction model. This is a consequence of the ductility that the interaction model tends to reproduce.

The beginning of degradation occurs at a displacement of $7.4\ [inches]$ (4.0% drift) in the experimental downward push (as seen in Table D.4), compared to $10.81\ [inches]$ and (5.8% drift) for the interaction model. For the upward pull, the experimental displacement is $7.64\ [inches]$ (4.1% drift) and it is $15.39\ [inches]$ (8.3% drift) for the interaction model. The ductility of the interaction model is noticeable again.

Specimen 6 is more accurately represented by the interaction model than Specimens 1 and 2 when considering the initial stiffness, maximum capacity and the overall response. The ductility is the main problem with the representation of Specimen 6, when considering just the global response given by the load-displacement curves.

Specimen 7

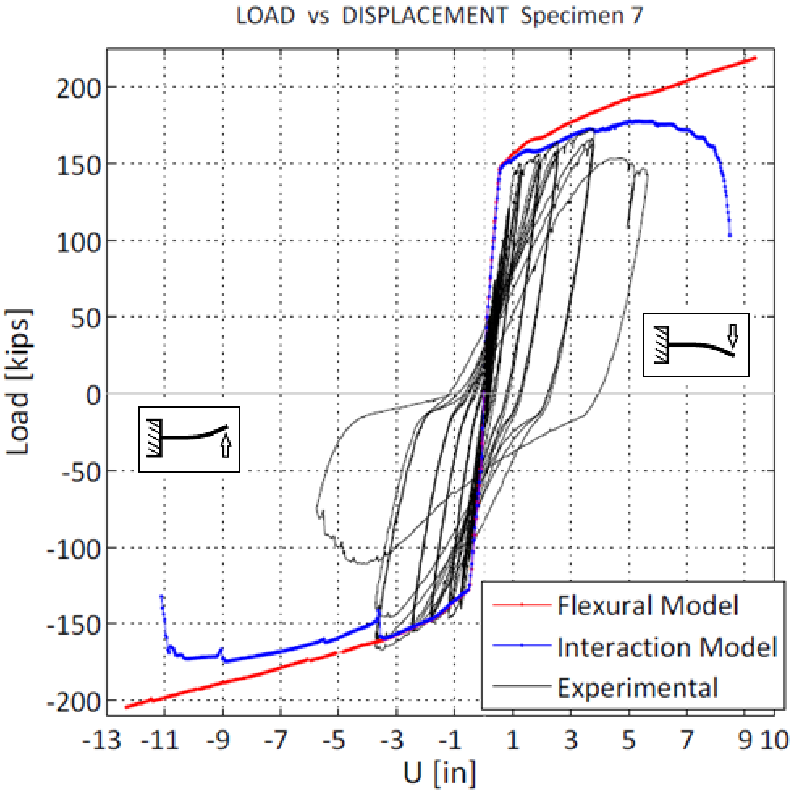

Figure 5.4: Load - Displacement Curves for Specimen 7.

Specimen 7 is the only specimen without the transverse opening.

The flexural model approaches the interaction model during the initial elastic stretch in both directions and for a further stretch after for the upward pull. For the downward push, the flexural model drifts from the interaction model after the end of the initial elastic stretch.

In the upwards direction, the initial stiffness is similar between the interaction model and the experimental case (just 7.6% higher for the interaction model, according to the estimated results shown in Table D.2). In the downwards direction, the initial stiffness is almost two times higher for the interaction model when compared to the experimental results.

The end of the initial elastic stretch occurs at similar displacements for the upward pull because of the similarity in the initial stiffness in that direction. For the downward push, the experimental displacement is two times the displacement of the interaction model at the end of the initial elastic stretch because of its lower initial stiffness (estimated results available in Table D.2).

Specimen 7 presents satisfactory results in maximum capacity, as the interaction model results are just ~4% higher than the experimental results (Table

D.3). In the downwards direction, the maximum capacity is $177.42\ [kips]$ for the interaction model and $172.147\ [kips]$ for the experimental case. In the opposite direction, the maximum capacity is $174.57\ [kips]$ for the interaction model and $167.36\ [kips]$ for the experimental response. It can be noted that the maximum capacity is similar in both directions. The main difference is that because of the ductility of the interaction model, the maximum capacities are reached at higher displacements than in the experimental case.

An observation can be made at this point, as Specimen 1 and 7 are the most similar ones, in length and reinforcing condition, but with the difference of the presence of an opening in Specimen 1. As it was studied by Aykac et al. (2014), the presence of openings in a reinforced concrete beam reduces its load-carrying capacity. This is confirmed when comparing the maximum capacities of Specimen 1 and Specimen 7, as the first (with opening) presents lower capacities in both directions. Figure 5.5 shows the experimental responses of Specimen 1 and Specimen 7. It can be appreciated that the blue curve (Specimen 1, with opening) reaches lower values for capacity in both directions, when compared to Specimen 7.

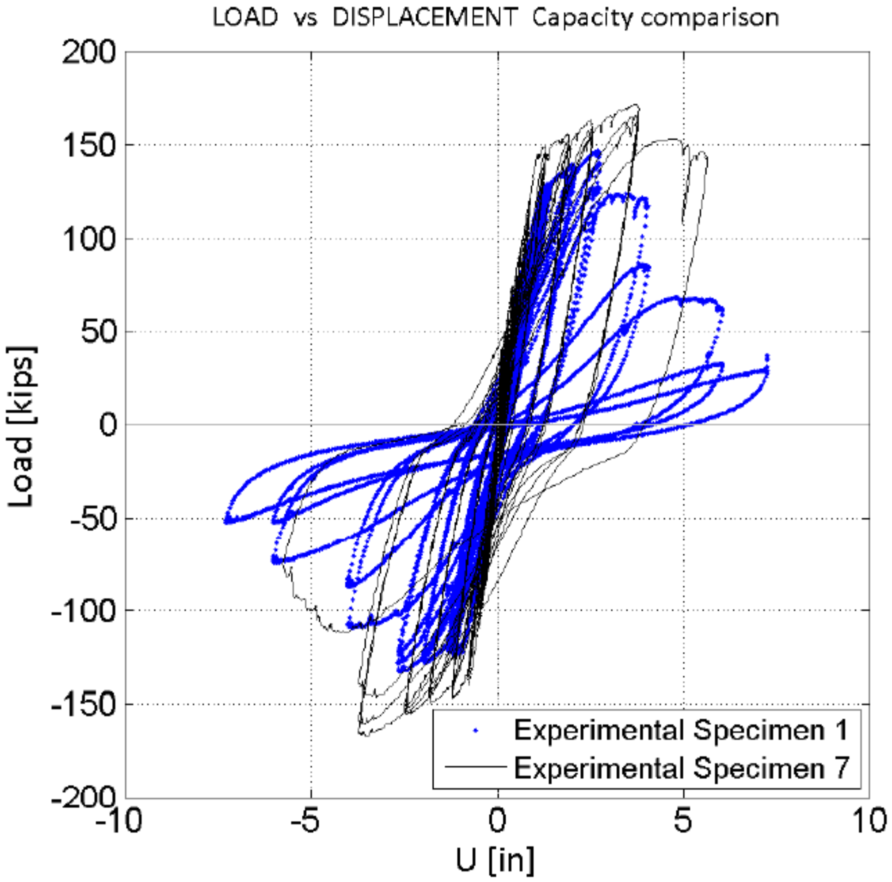

Figure 5.5: Capacity comparison between Specimens 1 and 7.

The beginning of degradation occurs at a displacement three times higher for the interaction model in the upward pull when compared to the experimental case. In the downwards direction, the result is not as unsatisfying, with a displacement 50% higher for the interaction model.

The interaction model, resembles visually and quantitatively the load-displacement behavior of Specimen 7 in the upwards direction. A slight inconvenient is appreciable in that curve, because although the interaction model appears to initially begin to degrade identically to the experimental case, the degradation stops suddenly, and the model continues to take significant load until a drift of 8.7%. In the downwards direction, the only satisfactory parameter is the maximum capacity.

As a general comment, it can be noted that the discrepancies in ductility between the experimental and the analytical results could be improved with the use of a cyclic model. When the degradation appears in one direction, this immediately affects the load-carrying capacity in the opposite direction, in which the ductility should decrease considerably. A cyclic model could show better prediction of the ductility.

5.1.3. Deflection Profiles

The deflection profiles are presented for each specimen in Figures 5.6 to 5.22. Each figure contains three plots that show the deflection profiles of the specimens at certain level of deformations. The first plot shows the estimated shear deformations by level (as explained in Section 3.3.1), compared to the analytical shear deformations by element. The second plot shows the flexural deformations, compared between the experimental estimations detailed in Section 3.3.2 and the analytical results. The third plot contains three curves: the first one shows the total deformations estimated using the external instrumentation (for “external instrumentation”, an explanation is provided in Section 3.1.4), the second curve is the experimental deflection profile estimated as the addition of the flexural and the shear deformations estimated using the internal instrumentation (the expression “internal instrumentation” is also explained in Section 3.1.4) and the third curve is the total analytical deformation along the specimen. The second and third curves are the sum of their respective shear and flexure curves from the first two plots.

It must be mentioned that adding the experimental estimated shear and the flexural deformations does not warrant getting the total deformations of each specimen. As it is shown in Figures D.5 to D.8 of Appendix D, the sum of the estimated shear and flexural deformations underestimate the total deformations (captured with the external instrumentation) in the range of 33-39%. The reason for this underestimation can be the fact that, as Figures 3.9 and 3.10 show, at the left of the specimens there is a slight gap that remains uncovered by the instrumentation (LVDTs) between the reaction block and the first end of these sensors, where important part of the flexural deformation might be developing.

The total deformations obtained using the external instrumentation are shown just as reference, but are not object of a thorough analysis. The shape of these curves indicates some deficiencies or limitations in the instrumentation. As the shape described is not always that of a cantilever specimen. Part of this can be attributed to the deterioration of the external instrumentation when each test reaches large displacements and not to a deficient configuration.

Specimen 1

The first specimen shows a reasonable accurate representation in both directions for the absolute displacements until the yield point (end of the initial elastic stretch), when compared with the value given by the sum of the estimated shear and flexure displacements. Beyond the yield point, in general, the interaction model underestimates the displacements at global scale.

The shear displacements are underestimated by the interaction model, being unable to represent the accumulation of damage at certain levels of the specimen (at certain lengths), this is evident through Figures 5.6 to 5.9. For example, Figures 5.8 and 5.9, show that Specimen 1 begins to accumulate shear displacement at the point of maximum capacity, especially between levels 3, 4 and 5. This is expected, as Specimen 1 failed at the opening, located at those three levels (as Figures 3.14 and 3.15 show).

Experimentally, the flexural displacement is concentrated at the first level, when reaching the maximum capacity and beyond. The interaction model shows a different approach, incrementing the flexural displacements almost linearly along the elements (elements would be the analog of levels used for the analytical case).

The behavior of Specimen 1 is not accurately represented with the interaction model, using the assumptions made up to Section 4.3.4, mainly because of the underestimation of the shear displacements at global scale, and particularly, because it is not able to accumulate the displacements in the correct elements. Specimen 1 fails at the opening, mainly because of the accumulation of the shear displacements at that level, what is not represented by the model. Some further assumptions are made in order to capture the behavior of Specimen 1 more accurately. The results with those assumptions are analyzed in Section 5.2.

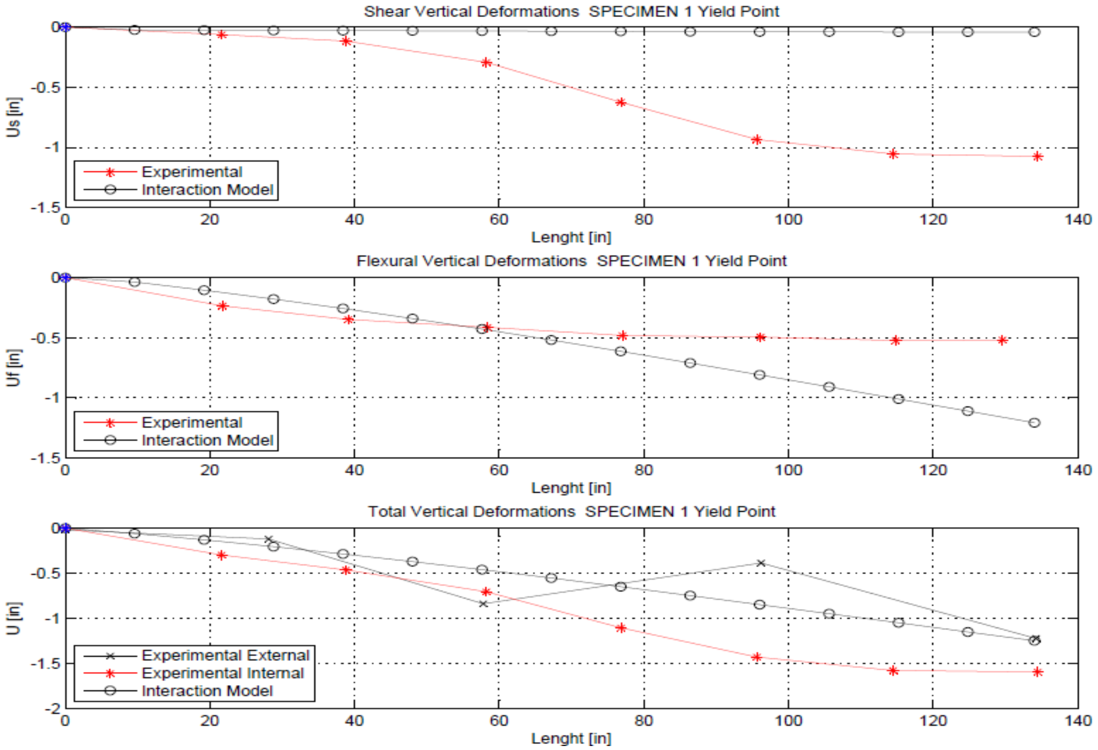

Figure 5.6: Experimental and analytical deflection profiles for Specimen 1 at Yield Point (end of the initial elastic stretch of the Load-Displacement curve) of the downward push. The fixed end is shown with a blue asterisk. (Analytical refers to the Interaction Model). Drift level 0.91%.

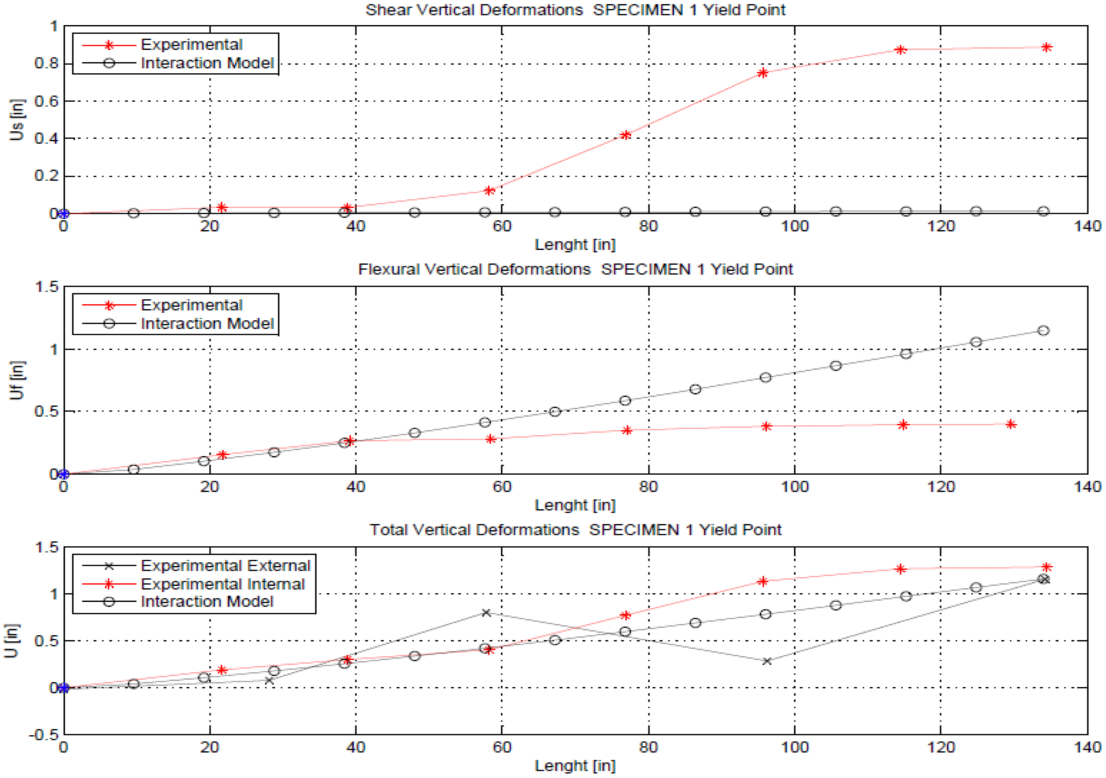

Figure 5.7: Experimental and analytical deflection profiles for Specimen 1 at Yield Point (end of the initial elastic stretch of the Load-Displacement curve) of the upward pull. The fixed end is shown with a blue asterisk. (Analytical refers to the Interaction Model). Drift level 0.86%.

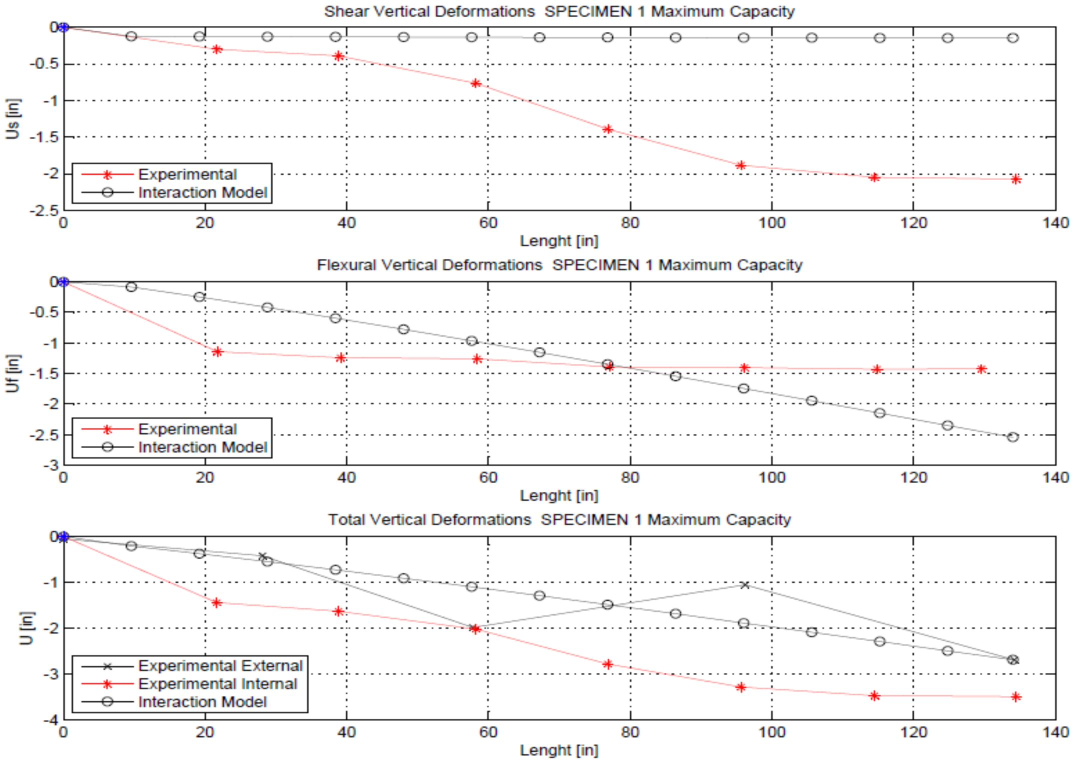

Figure 5.8: Experimental and analytical deflection profiles for Specimen 1 at Maximum Capacity level of the downward push. The fixed end is shown with a blue asterisk. (Analytical refers to the Interaction Model). Drift level 2.0%.

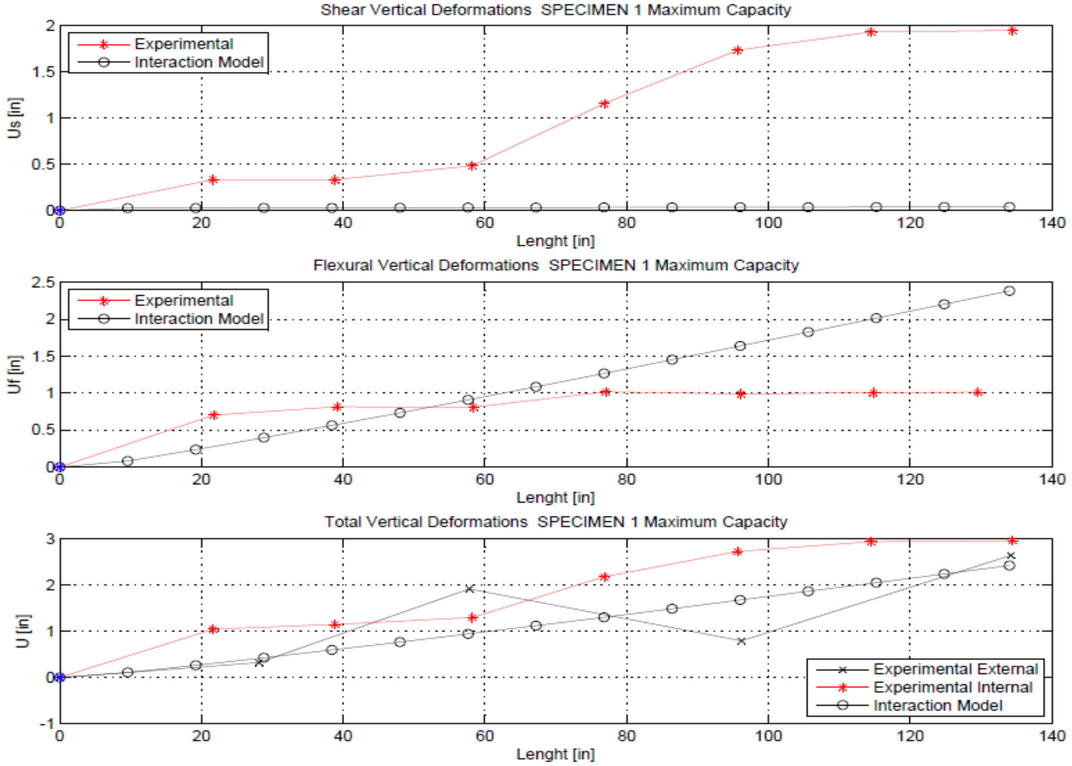

Figure 5.9: Experimental and analytical deflection profiles for Specimen 1 at Maximum Capacity level of the upward pull. The fixed end is shown with a blue asterisk. (Analytical refers to the Interaction Model). Drift level 1.97%.

Specimen 2

The total vertical deformations are reasonably well predicted by the analytical model until reaching the yield point when the tip displacement is seen in Figures 5.10 and 5.11, with slight discrepancies in the distribution.

The flexural displacement is overestimated at the tip of the specimen at the moment when the elastic loading stretch concludes (Figures 5.10 and 5.11), which occurs at a drift level of ~1% as well as at the drift of maximum capacity ~4.5% (Figures 5.12 and 5.13). Regarding the distribution of the flexural deformations, those should be accumulated in the first level, according to the experimental deflection curves shown in Figures 5.12 and 5.13, but the model seems to increase the flexural deformations almost linearly along the length of the specimen, as a cantilever beam. The failure of Specimen 2, as Figures 3.16 and 3.17 can validate, was at the beam/block interface, in accordance with the accumulation of flexural deformations in the first level.

Important shear deformations are also accumulated in the first level, according to the experimental curves, a behavior that is accurately represented by the interaction model. Although this situation can barely be appreciated in Figures 5.12 and 5.13, because at the 4.5% drift (when the experimental maximum capacity is reached) the shear deformations are just beginning to accumulate in the first element for the analytical response. The interaction model tends to accumulate damage in the first element, beyond reaching its maximum capacity. The shear damage present in the first level shows an important contribution of the shear deformations to the failure of Specimen 2, coupled with the earlier mentioned flexural damage accumulated at the failure zone. Figures 5.10 to 5.13 show a considerable accumulation of shear displacements at the levels where the opening is located for the experimental response. Although the deformations are notorious in the deflection curves, those do not accumulate enough damage to cause the failure of the specimen, since the failure occurs at the beam/block interface.

As final commentary for Specimen 2, the interaction model accurately predicts the accumulation of shear damage in the first level, but underestimates its magnitude. The flexural displacements are not accurately predicted in location and in magnitude, as the analytical flexural displacements are overestimated.

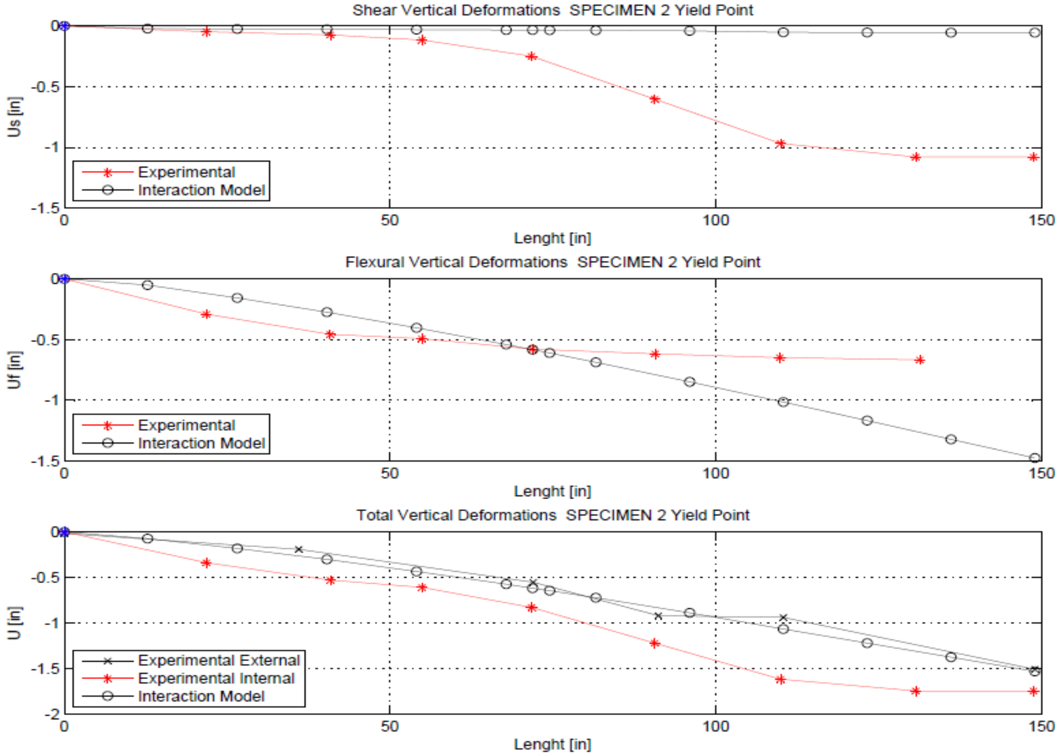

Figure 5.10: Experimental and analytical deflection profiles for Specimen 2 at Yield Point (end of the initial elastic stretch of the Load-Displacement curve) of the downward push. The fixed end is shown with a blue asterisk. (Analytical refers to the Interaction Model). Drift level 1.01%.

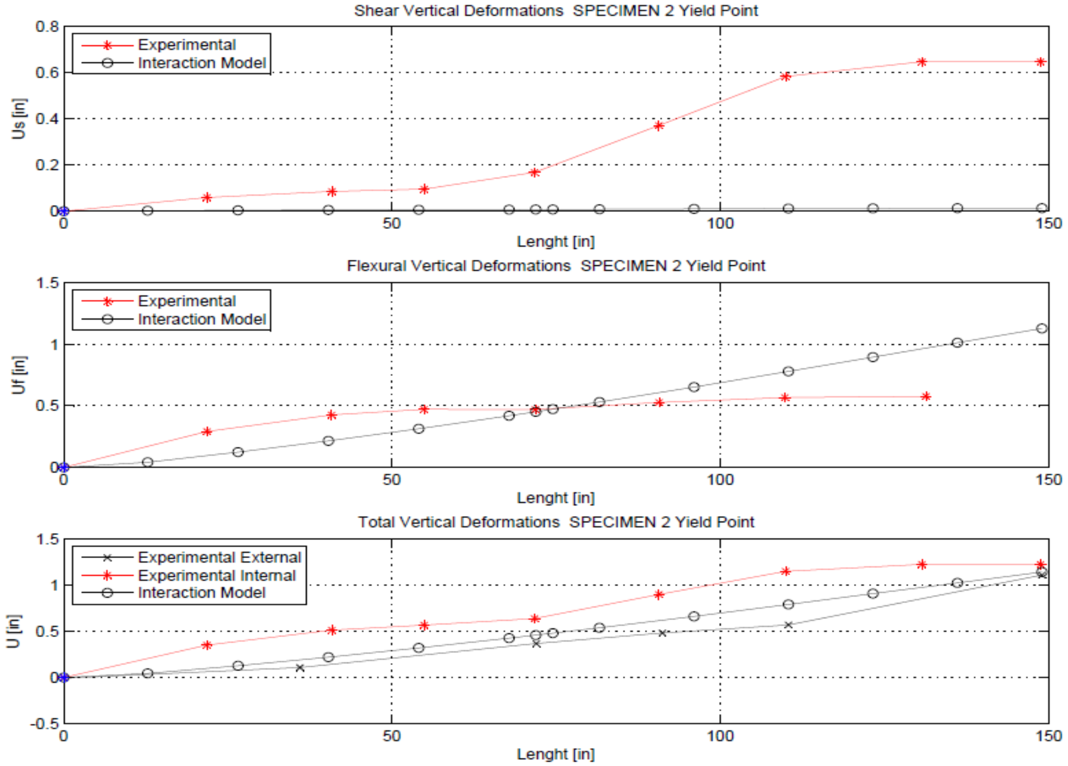

Figure 5.11: Experimental and analytical deflection profiles for Specimen 2 at Yield Point (end of the initial elastic stretch of the Load-Displacement curve) of the upward pull. The fixed end is shown with a blue asterisk. (Analytical refers to the Interaction Model). Drift level 0.74%.

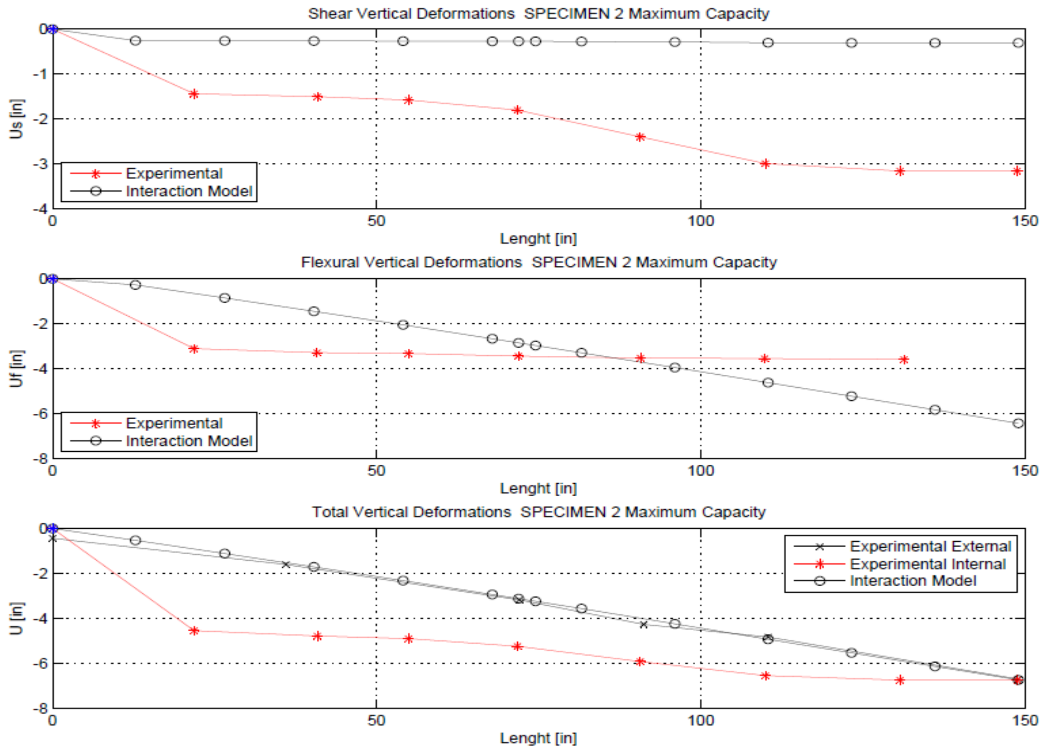

Figure 5.12: Experimental and analytical deflection profiles for Specimen 2 at Maximum Capacity level of the downward push. The fixed end is shown with a blue asterisk. (Analytical refers to the Interaction Model). Drift level 4.49%.

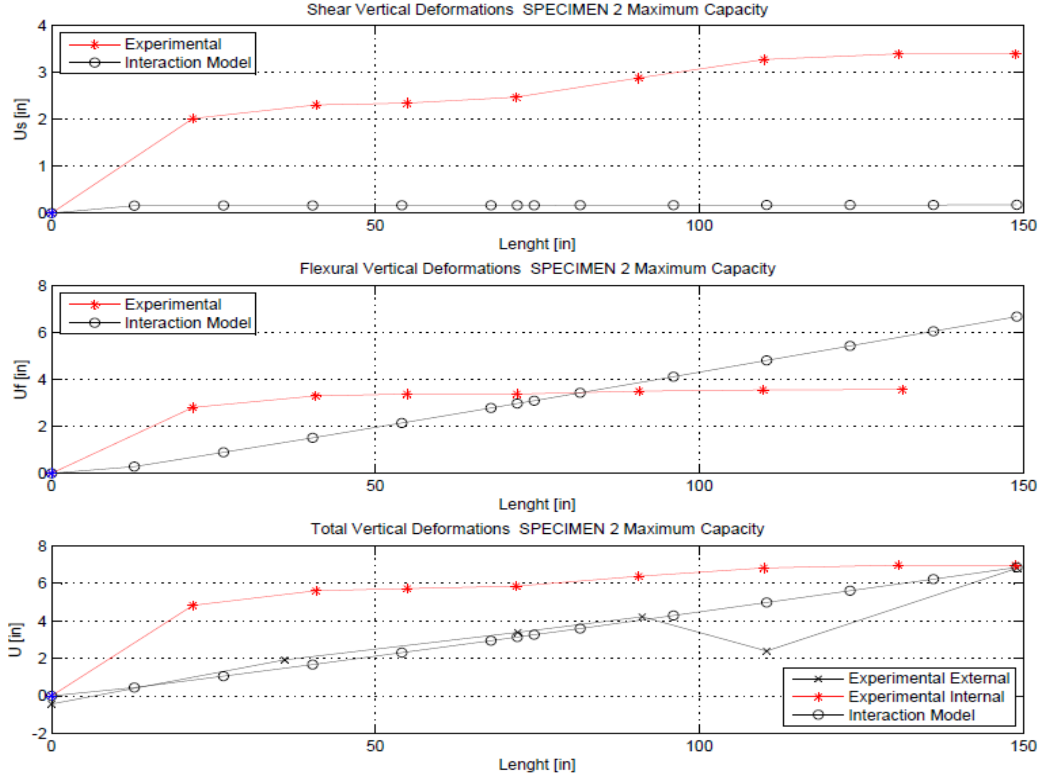

Figure 5.13: Experimental and analytical deflection profiles for Specimen 2 at Maximum Capacity level of the upward pull. The fixed end is shown with a blue asterisk. (Analytical refers to the Interaction Model). Drift level 4.57%.

Specimen 6

The total displacements present evident discrepancies in distribution for the drift levels shown if Figures 5.14 to 5.17. Those figures show the deflection profiles at the drifts where the end of the initial elastic stretch (of the load-displacement curve) ends, called yield point, and at the drift level where the experimental maximum capacity is reached.

When the end of the initial elastic stretch is reached, the flexural deformations at the tip of the specimen are overestimated (Figures 5.14 and 5.15), and the distribution of these deformations along the length of the specimen is not accurately captured. At the same point mentioned, the shear deformations are underestimated, as it occurs for the remainder of the simulation (the analytical shear deformations are much smaller than the experimental shear deformations, as it can be seen in Figures 5.14 to 5.17).

The flexural deformations are once again overestimated at the drift levels of maximum capacity, presented in Figures 5.16 and 5.17. Experimentally, flexural deformations accumulate in the first two levels, in accordance with the failure appearance of Specimen 6 (Figures 3.18 and 3.19), developing a plastic hinge in the levels closer to the beam/block interface. The experimental shear displacements also concentrate the higher values in the first two levels (once again in accordance with the failure of the Specimen) and some lower accumulated displacement in levels 4 and 5, as Figures 5.14 to 5.17 show. A similar behavior to that of Specimen 2. The accumulated shear deformations in the central levels are not enough to cause the failure.

As mentioned before, shear displacements are underestimated, but regarding the accumulation of these displacements, Figure 5.18 shows that the shear deformations begin to accumulate in the first two elements of the analytical response, at a drift level slightly higher than the one shown in the deflection curves of Figure 5.16. The magnitude of the accumulated shear displacement is very low, but gives an insight about the location of the shear damage that the model predicts. The accumulation of shear displacements in the first elements (albeit at lower magnitudes than the experimental case), is in accordance with the failure mode of the Specimen 6. But it has to be clarified that the flexural deformations contribute almost the totality of the displacements seen at the drift levels shown in Figures 5.14 to 5.17.

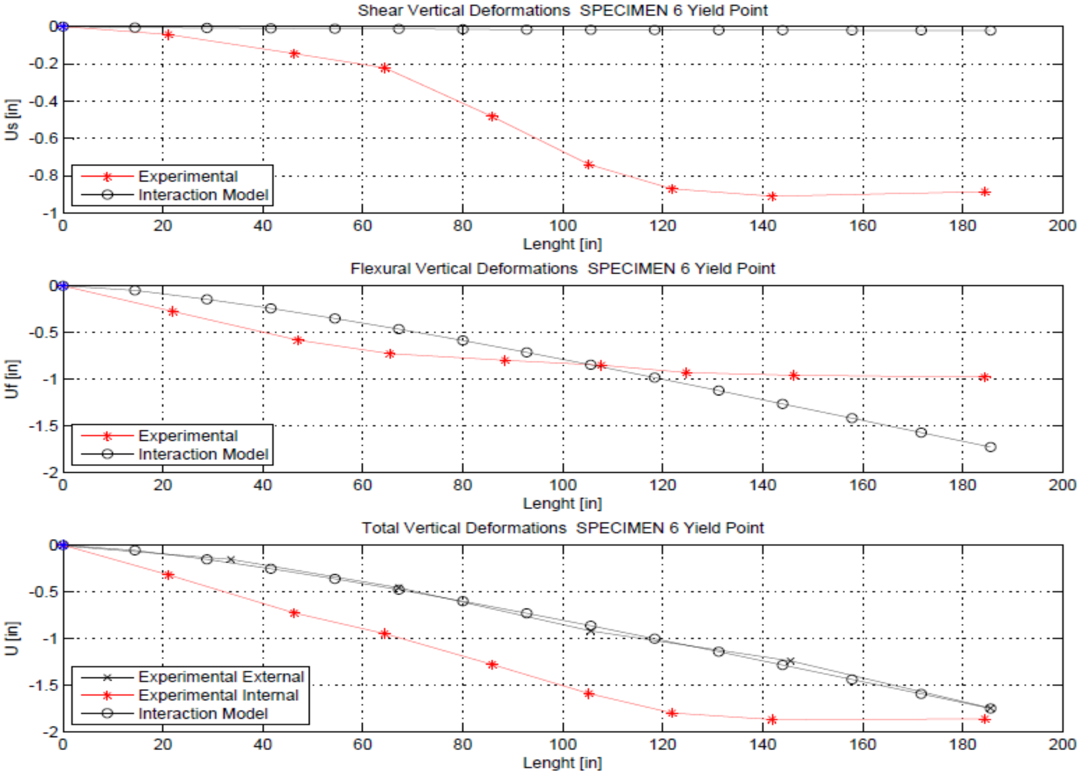

Figure 5.14: Experimental and analytical deflection profiles for Specimen 6 at Yield Point (end of the initial elastic stretch of the Load-Displacement curve) of the downward push. The fixed end is shown with a blue asterisk. (Analytical refers to the Interaction Model). Drift level 0.94%.

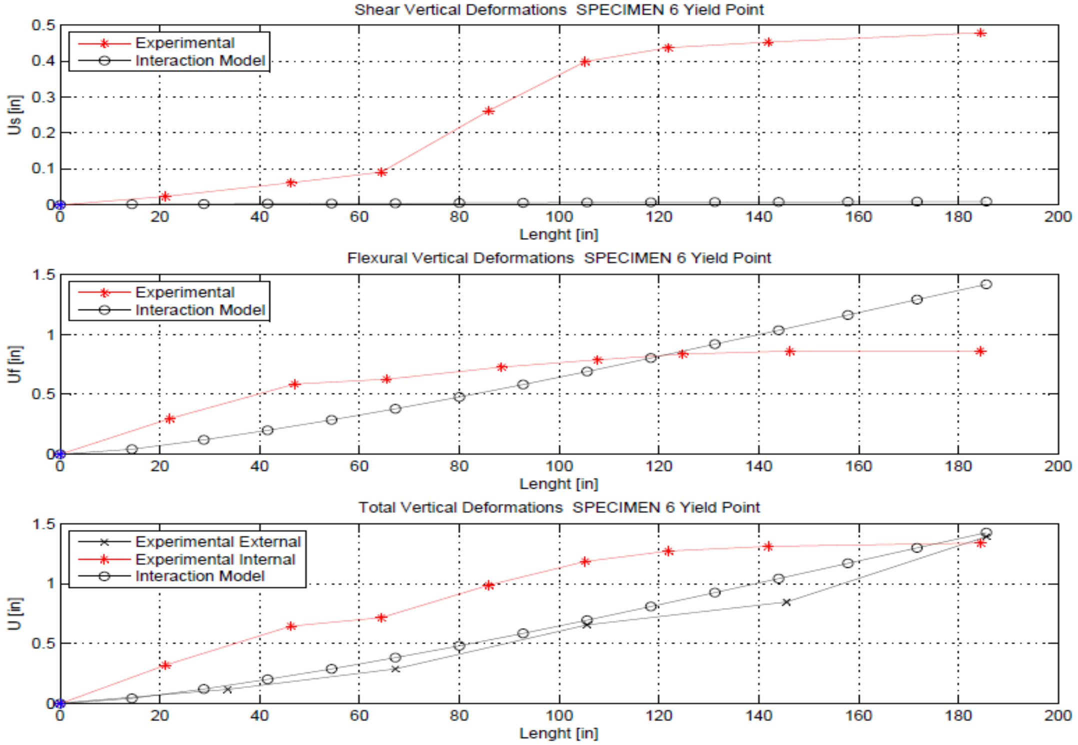

Figure 5.15: Experimental and analytical deflection profiles for Specimen 6 at Yield Point (end of the initial elastic stretch of the Load-Displacement curve) of the upward pull. The fixed end is shown with a blue asterisk. (Analytical refers to the Interaction Model). Drift level 0.75%.

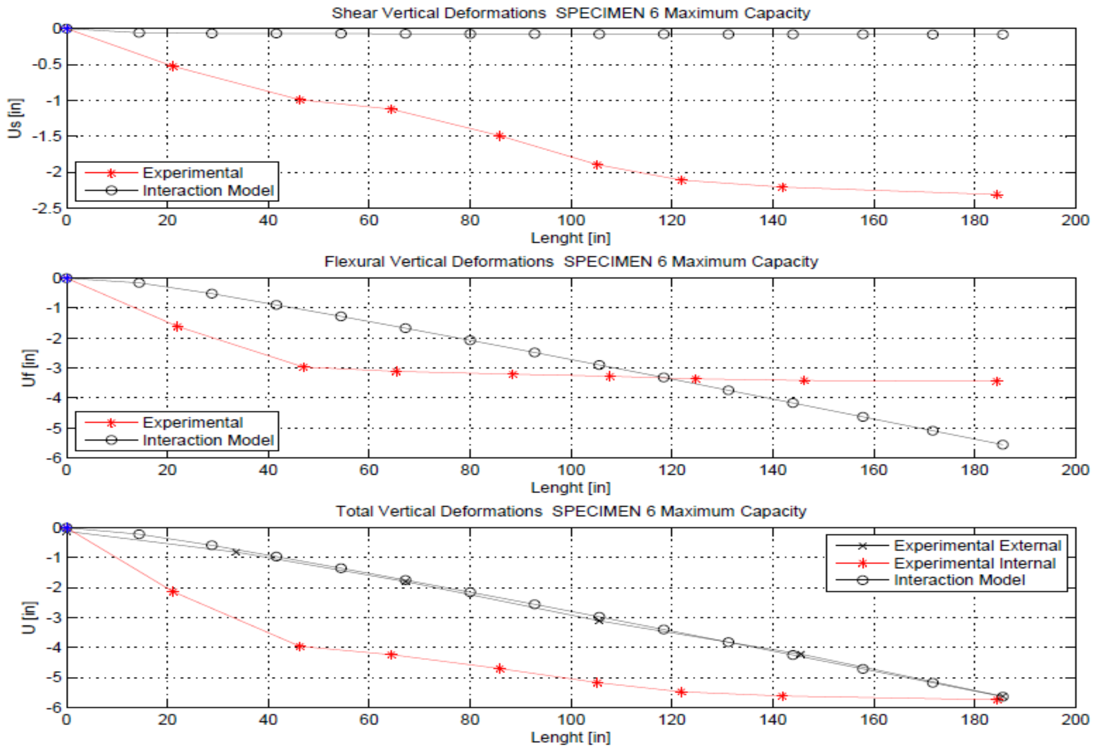

Figure 5.16: Experimental and analytical deflection profiles for Specimen 6 at Maximum Capacity level of the downward push. The fixed end is shown with a blue asterisk. (Analytical refers to the Interaction Model). Drift level 3.03%.

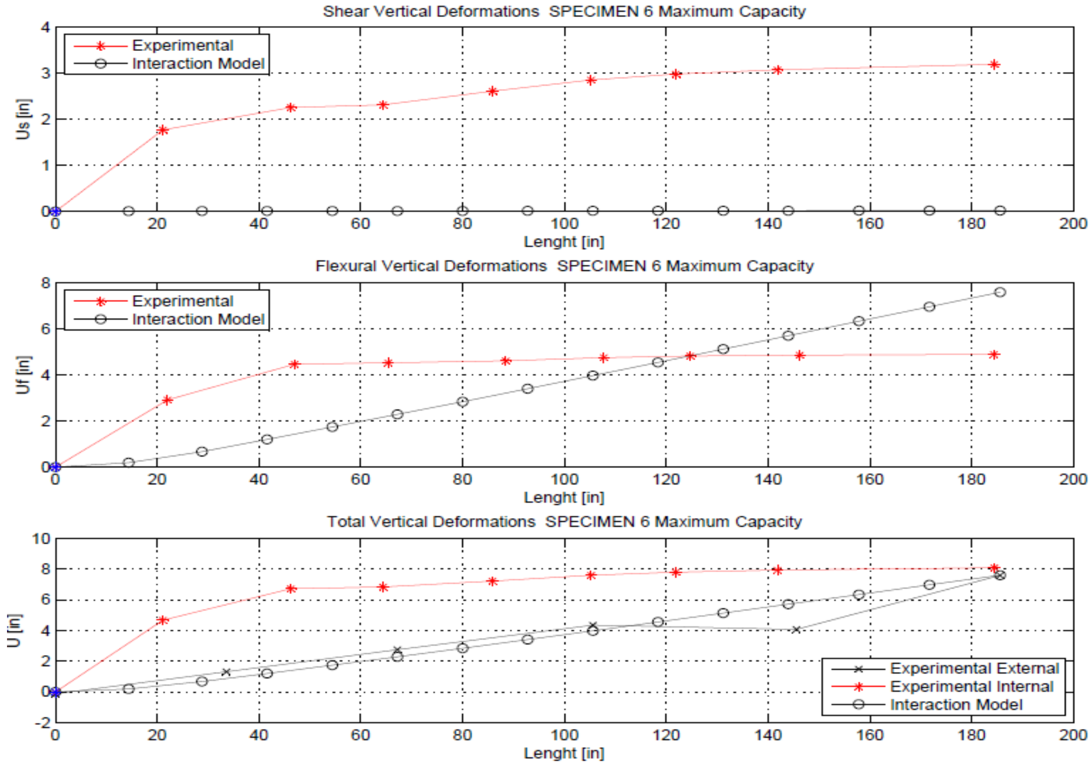

Figure 5.17: Experimental and analytical deflection profiles for Specimen 6 at Maximum Capacity level of the upward pull. The fixed end is shown with a blue asterisk. (Analytical refers to the Interaction Model). Drift level 4.09%.

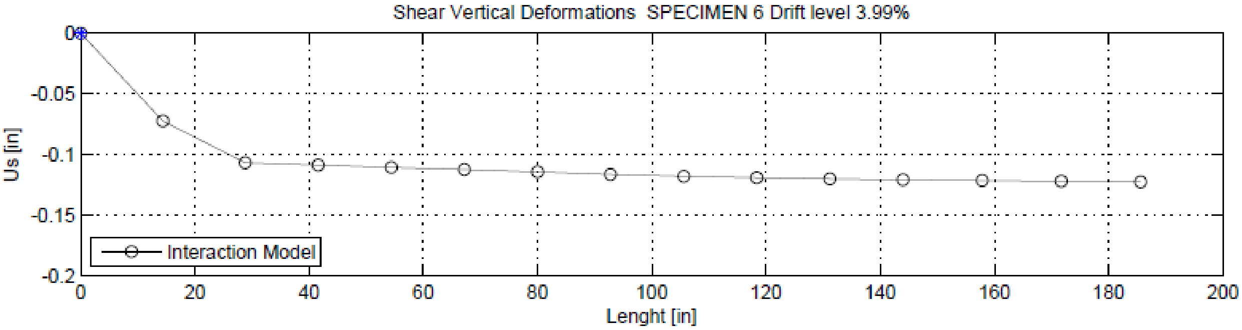

Figure 5.18: Analytical shear deflections profile for Specimen 6 in the downwards direction. Drift level 3.99%.

Specimen 7

The only specimen without opening exhibits an overall underestimation of the shear displacements according to the interaction model (Figures 5.19 to 5.22).

In the case of the flexural deformations, these are overestimated at the drift levels shown in Figures 5.19 to 5.22. The experimental accumulation of the flexural displacements occurs in the first two levels, which is expected looking at Figures 3.20 and 3.21, showing the failure of Specimen 7 in the zone composed by the first two elements. Analytically, the flexural deformations tend to increase gradually from fixed end to tip of specimen.

The shear contribution seems to be similar to the flexural contribution, in terms of total displacements (estimated at the tip of the specimen). The shear displacements are also accumulated in the first two levels, with considerable contribution to the tip displacement and eventually (and more importantly), to the failure of the specimen. This accumulation of shear displacements in the first two levels is satisfyingly represented by the interaction model, but with lesser magnitude (lower shear displacements), at least for the downwards direction, as Figure 5.21 shows.

Overall, the total deformations predicted by the interaction model along Specimen 7 are similar in shape to the experimental response (at the drift levels shown, which are ruled by the end of the elastic stretch and the maximum capacity points in the experimental load-displacement curve). The flexural displacements reach exaggerated values in the analytical case, what could be attributed to the lack of instrumentation over a small stretch between the reaction block and the first end of the LVDTs (Figures B.7 and B.8 of Appendix B). That non-instrumented stretch could present considerable flexural deformations that are not captured, explaining the discordance between the analytical and the experimental deformations.

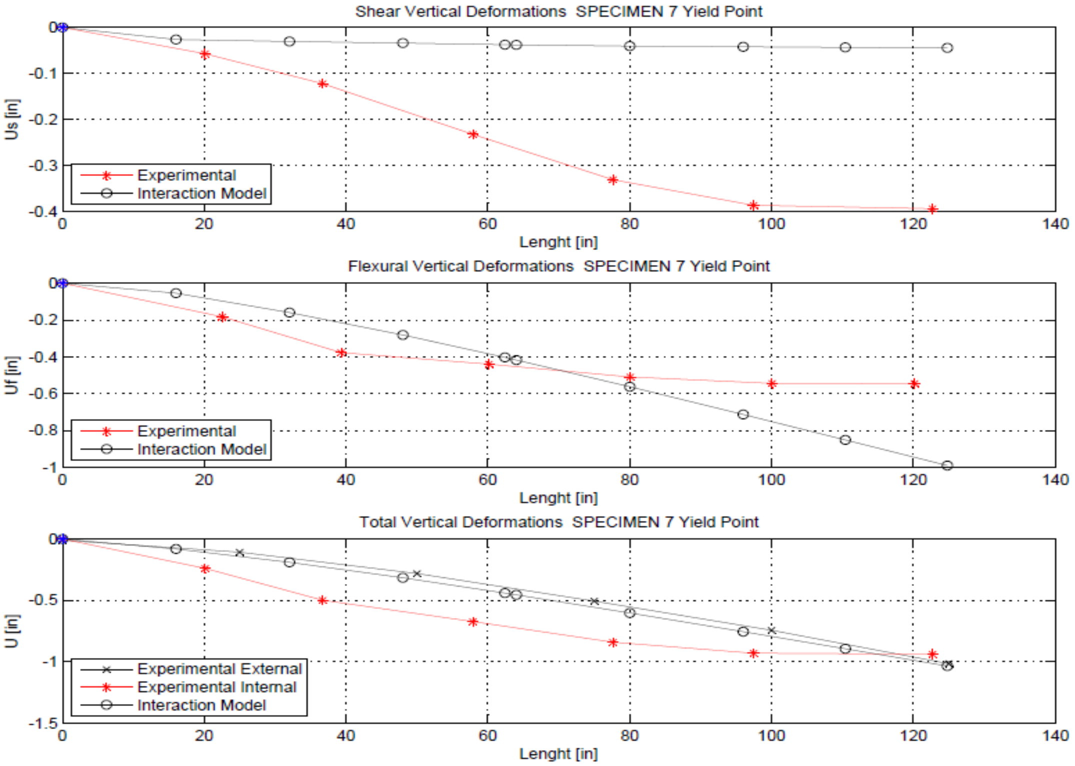

Figure 5.19: Experimental and analytical deflection profiles for Specimen 7 at Yield Point (end of the initial elastic stretch of the Load-Displacement curve) of the downward push. The fixed end is shown with a blue asterisk. (Analytical refers to the Interaction Model). Drift level 0.81%.

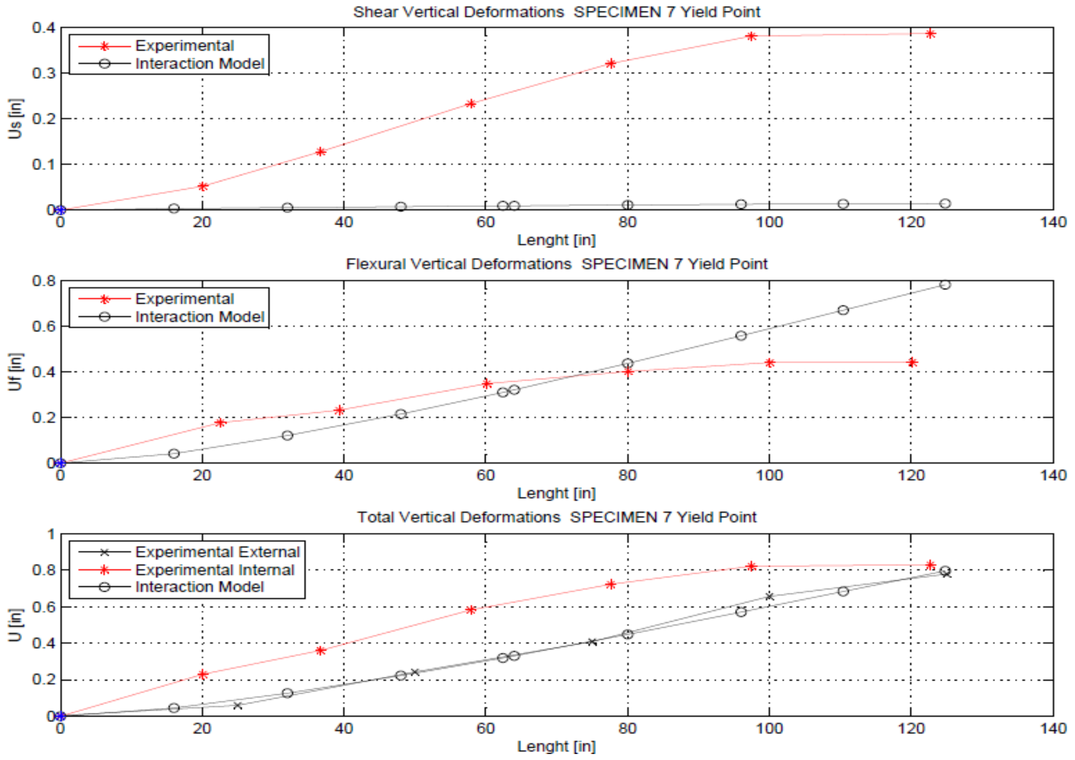

Figure 5.20: Experimental and analytical deflection profiles for Specimen 7 at Yield Point (end of the initial elastic stretch of the Load-Displacement curve) of the upward pull. The fixed end is shown with a blue asterisk. (Analytical refers to the Interaction Model). Drift level 0.62%.

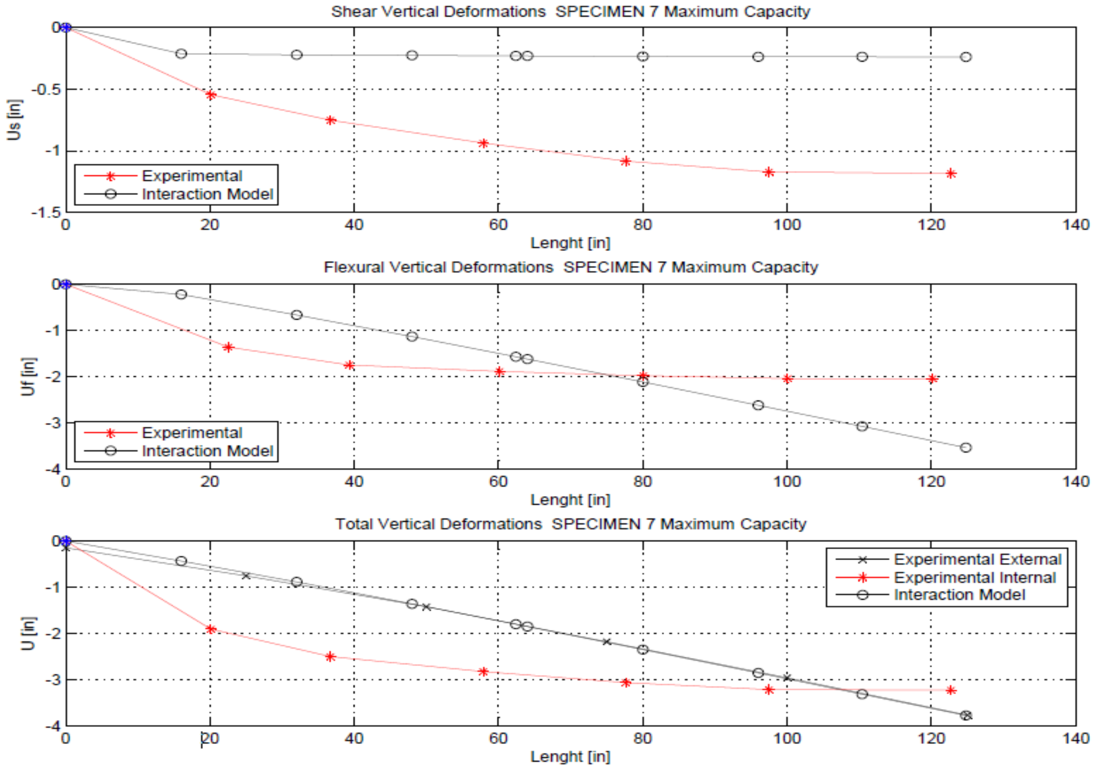

Figure 5.21: Experimental and analytical deflection profiles for Specimen 7 at Maximum Capacity level of the downward push. The fixed end is shown with a blue asterisk. (Analytical refers to the Interaction Model). Drift level 3.02%.

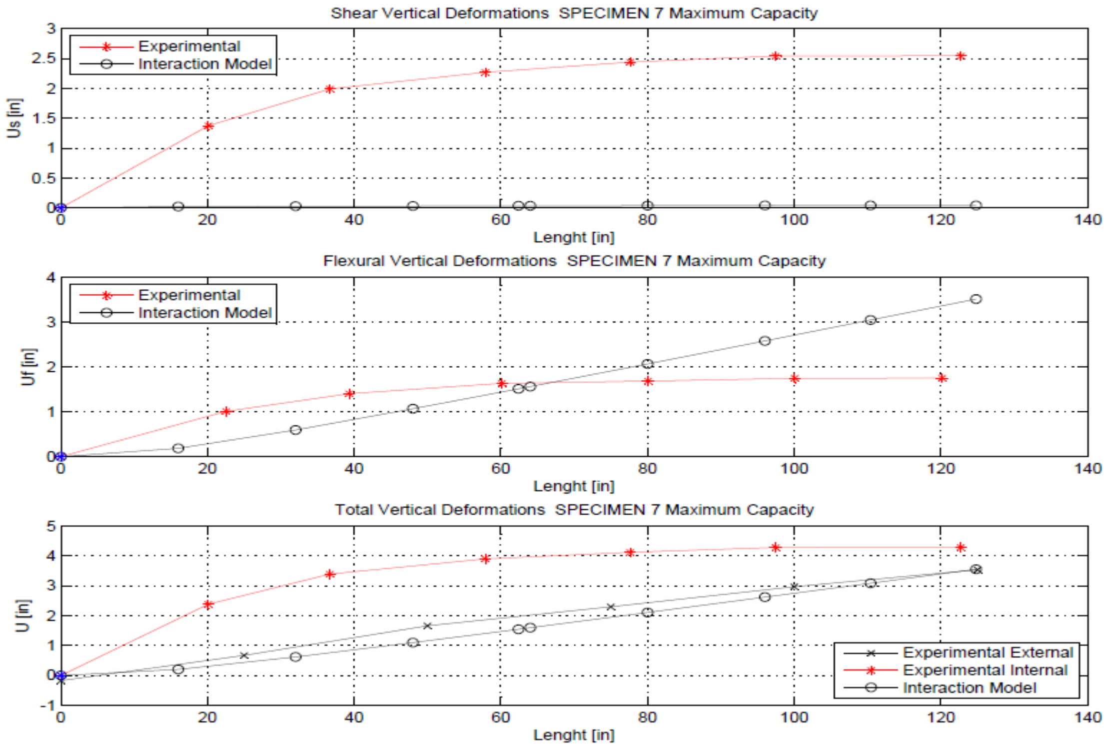

Figure 5.22: Experimental and analytical deflection profiles for Specimen 7 at Maximum Capacity level of the upward pull. The fixed end is shown with a blue asterisk. (Analytical refers to the Interaction Model). Drift level 2.84%.

5.1.4. Failure Mode

Some notions of the present analysis are mentioned in Section 5.1.3. In this section the analysis is concise.

Specimen 1

The failure mode is not accurately represented for Specimen 1 (the only specimen which fails at the opening). Experimental results describe quantitatively a failure at the levels where the opening is located, caused mainly by shear deformations. Visually, the situation is confirmed by Figures 3.14 and 3.15. The interaction model predicts failure at the beam/block interface.

Further assumptions are made for this specimen, analyzed in Section 5.2, in order to predict a more accurate response.

Specimen 2

Failure occurs at the beam/block interface for Specimen 2, with similar contributions and accumulation of shear and flexural deformations. Concrete cracking and buckling of reinforcing bars can be seen in Figures 3.16 and 3.17 at the levels closer to the reaction block.

The interaction model predicts high flexural deformations, but increasing linearly along the specimen, and a concentration of shear displacements in the element closest to the beam/block interface, but with lower magnitudes.

In the case of Specimen 2, the failure mode is half accurately predicted, as the accumulation of flexural deformations in the first element is not appreciated.

The opening remains undamaged analytically and experimentally.

Specimen 6

The failure of Specimen 6 occurs at the beam/block interface, with contributions of both flexural and shear displacements, accumulating in the first two levels. The flexural contribution is higher than the shear contribution. The situation is similar to the one described for Specimen 2. Figure 3.18 shows the failure of Specimen 6, in accordance with the description made here.

Analytical shear deformations are accumulated in the first two elements, but the magnitude of those deformations is significantly lower than the expected ones. The analytical flexural deformations exceed, in considerable amount, the ones expected when comparing them to the experimental results. The accumulation of flexural deformations in the levels closer to the beam/block interface is not predicted, as the flexural deformations increase almost linearly through the entire length of the specimen.

The opening remains undamaged analytically and experimentally, the same as Specimen 2.

Specimen 7

The failure of Specimen 7 is appreciable in Figures 3.20 and 3.21, showing a plastic hinge at the beam/block interface (deformations are expected in the levels closer to the interface).

Experimentally, the accumulation of deformations in the first two levels is significant for both the shear and flexural deformations, with similar contributions in the downwards direction and higher shear contribution in the upwards direction.

The analytical results behave similar to Specimens 2 and 6, as the shear deformations are accumulated in the first levels and the flexural deformations increase almost linearly through their lengths. The analytical flexural deformations are significantly higher when compared to the experimental results, as a potential result of the lack of instrumentation in the stretch closer to the reaction block, as it was mentioned in Section 5.1.3. The analytical shear deformations behave well qualitatively, but with lower magnitudes than the experimental shear deformations.

5.2. Results with alternative discretization

The alternative specimen discretization detailed in Section 4.4 was proposed with the intention of “translating” the failure of Specimen 1 from the beam/block interface to the opening.

Figure 5.23 shows the difference in the load-displacement response of Specimen 1 between the first proposed element discretization and the alternative discretization detailed in Section 4.4.

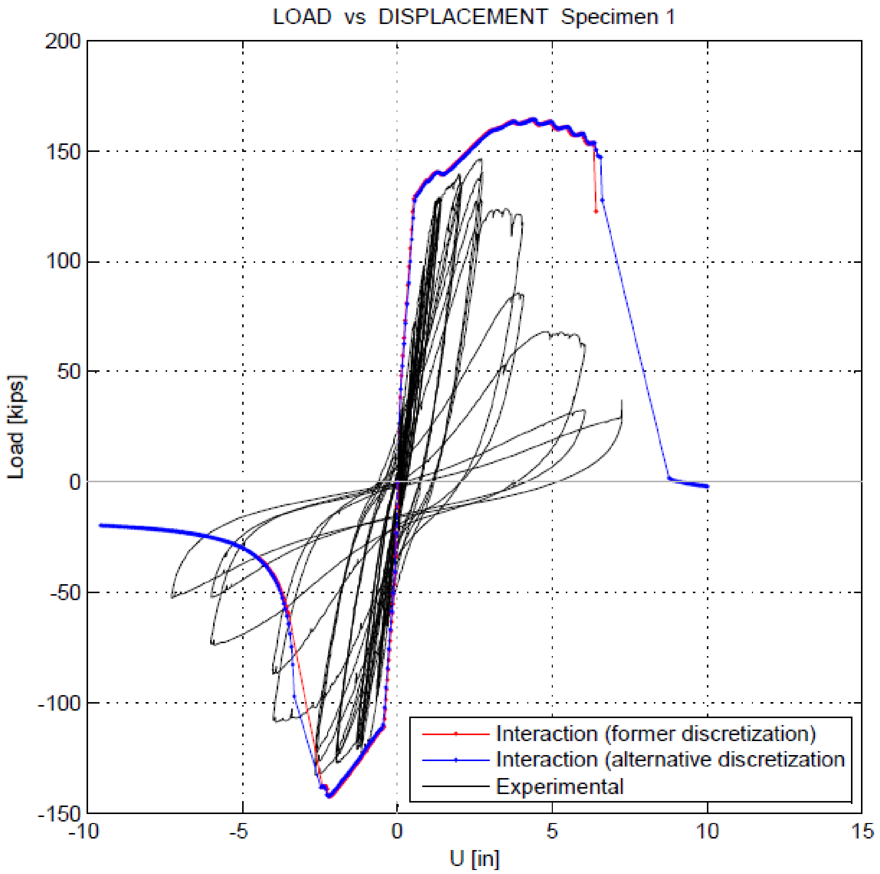

Figure 5.23: Difference in load-displacement response with the first discretization and the alternative discretization.

The load-displacement response is barely affected with the variation. Figures 5.24 and 5.25 show the deformation profiles of Specimen 1 with the alternative discretization at certain incremental load magnitudes. The intention is to predict the failure at the opening. In Figures 5.24 and 5.25 the upper and lower stretches at the center, are the deflection profiles of the elements that compose the opening (an upper portion and a lower portion of elements), that are translated to their respective centroids.

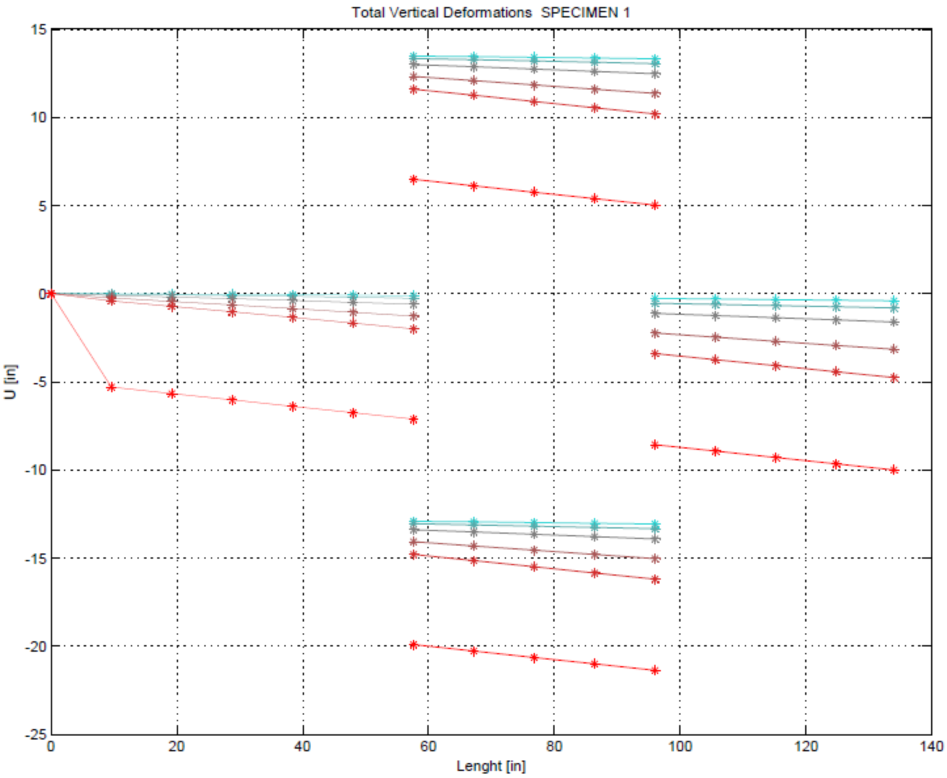

Figure 5.24: Total vertical deformations of Specimen 1 for the downward push with the alternative discretization.

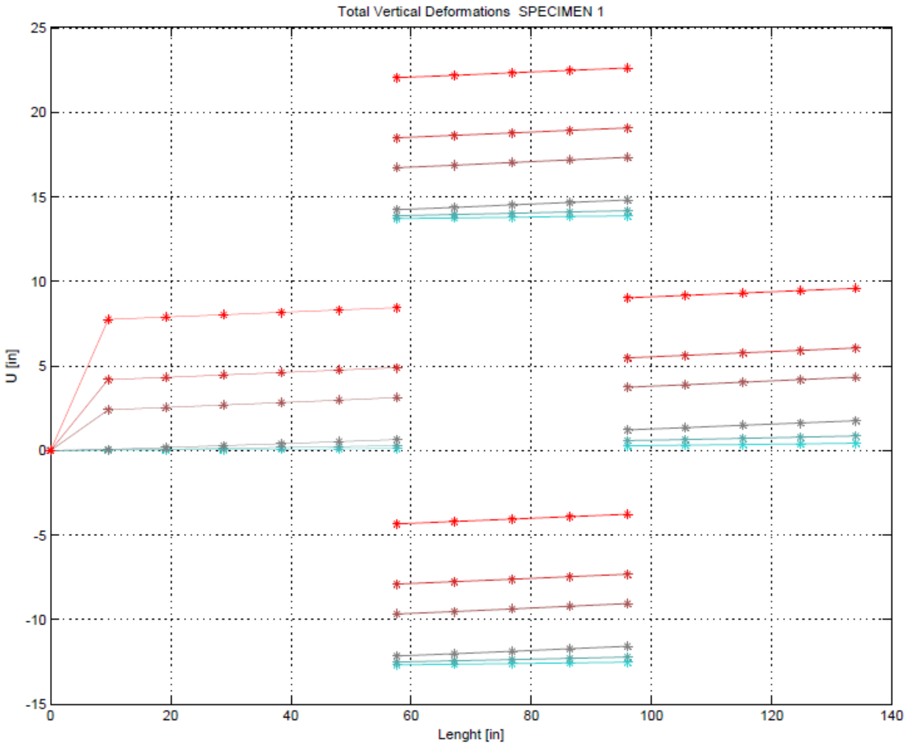

Figure 5.25: Total vertical deformations of Specimen 1 for the upward pull with the alternative discretization.

The intention to predict the failure at the opening is not fulfilled, as the deformations are concentrated in the first element (the element closest to the beam/block interface). That indicates that the failure is still predicted at the interface with the reaction block (same failure as the other specimens).

A more drastic variation is introduced, in order to force the modeled specimen to fail at the opening. This assumption consists in reducing the compressive strength of the concrete (f_C') and the yield strength (f_y) of the reinforcing bars for the elements that compose the opening.

This last variation was trialed several times, until the failure was located at the opening for Specimen 1. The results indicated that when the strengths were simultaneously reduced, it was necessary to reduce f_C' and f_y by at least 50% each in order to predict a failure at the opening. When reducing the yield strength only, it was necessary to reduce 70% of it in order to locate the failure at the opening. The failure was predicted in the downwards direction (as Figures 5.28 and 5.29 show respectively), which is the direction in which the failure occurs, according to the experimental response.

It is important to clarify that the variation of the lower strengths is not sufficient by itself. It requires the configuration given by the alternative beam discretization to accurately predict the failure at the opening. Even in the case when the yield strength of the reinforcing steel was reduced in 70%, the original discretization presents problems in order to converge and return a reasonable response.

Figures 5.26 and 5.27 show the difference between the original model, with the original discretization (without reduction in material strengths), and with the assumptions made in this section (alternative discretization and lower material strengths). The load displacement prediction notoriously improves in the downwards direction for both cases, and shows similar results in the upwards direction for the case where both material strengths are reduced.

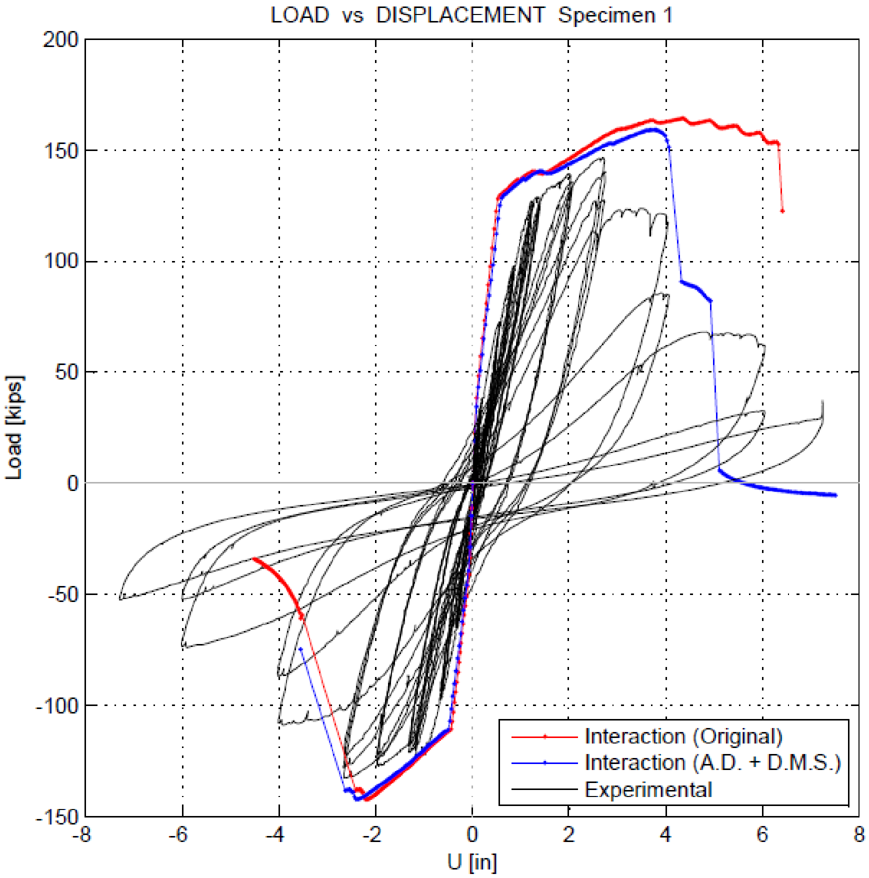

Figure 5.26: Load-displacement response, comparing the original interaction model formulation, and incorporating an alternative discretization with a decrease of the material strengths. Specimen 1. A. D. + D. M. S. stands for "Alternative Discretization + Decreasing Material Strengths”. 50% Reduction of f’c. 50% Reduction of fy.

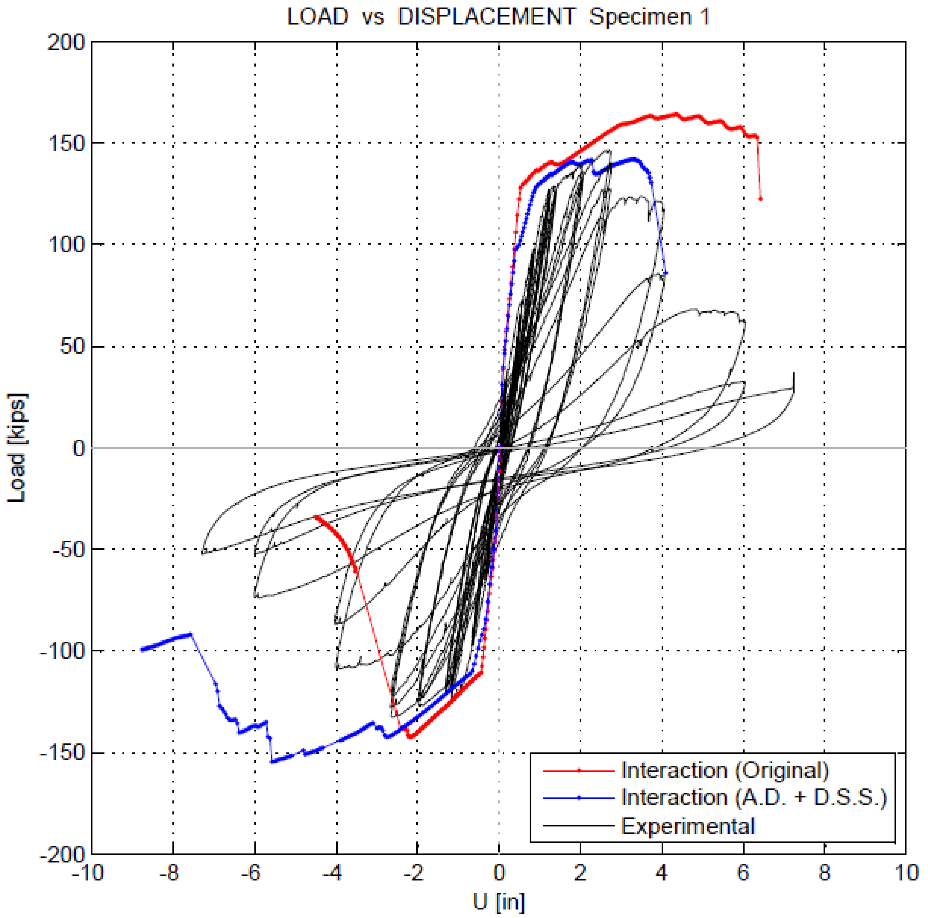

Figure 5.27: Load-displacement response, comparing the original interaction model formulation, and incorporating an alternative discretization with a decrease of the material strengths. Specimen 1. A. D. + D. S. S. stands for "Alternative Discretization + Decreasing Steel Strength". 70% Reduction of fy.

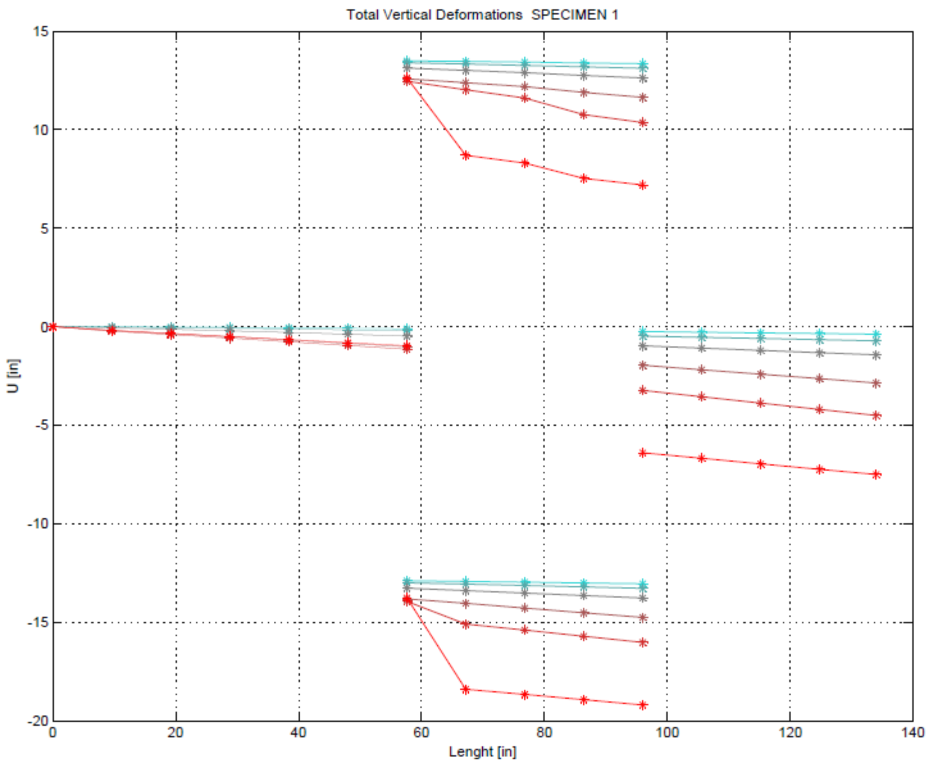

Figure 5.28: Failure at the opening using alternative beam discretization and lower strengths for both materials. Downward push for Specimen 1.

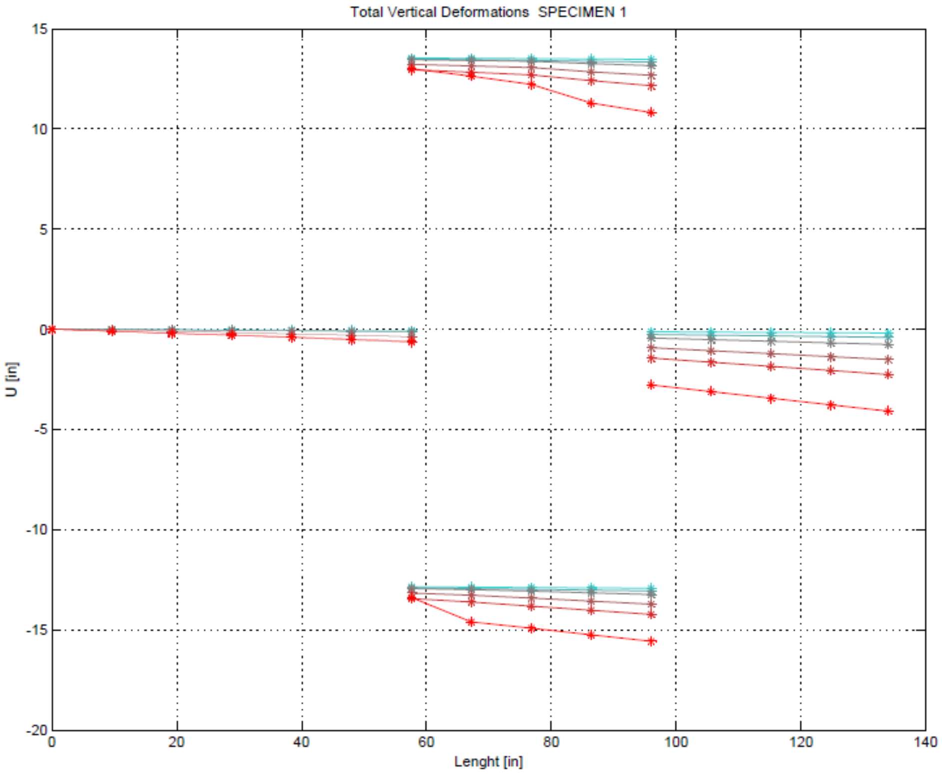

Figure 5.29: Failure at the opening using alternative beam discretization and lower strengths for the reinforcing steel. Downward push for Specimen 1.

The analytical load-displacement response resembles more the experimental case with the variations proposed in this section. These assumptions of lower material strengths seek to find a possible cause to the failure at the opening, as it would not be unlikely that the casting of the concrete presented difficulties because of the formwork at the opening or because of the reinforcing steel in that area, whom might have presented difficulties for the vibration, resulting in a concrete with lower strength at the opening levels. Other possible option, perhaps even more acceptable than the previous, would be that the adherence of the reinforcing bars was deficient or insufficient at the level of the opening, causing the failure at that zone. The assumption of 50% of the yield strength while the development length is reached (made in Section 4.3.4) might not have been sufficient in order to analytically represent the specimen, and a greater reduction of F_y (as the one supposed in this section) could solve the problem. Specimen 1 showed a response which differs significantly to that of the other specimens.

Figures 5.28 and 5.29 show the accumulation of displacements in the first element of the opening. The overall accumulation of damage in one particular element (with the interaction model) is expected (as in Figure 5.28 and in the lower stretch of Figure 5.29), as the model seeks to concentrate the damage in one particular element at the beginning of considerable displacements.

It is necessary to clarify that the last assumptions (lower material strengths: for both concrete and steel in the first case [1] and only for the steel in the second case [2]) were also tested on the other specimens with opening: Specimens 2 and 6. For the first one [1], both specimens analytically failed at the opening when decreasing the material strengths by 50% each, as it happened with Specimen 1. Since none of these specimens failed at the opening during the tests, the first assumption loses credibility as a hypothetic reason for the location of the failure in Specimen 1. Unless the presence of lower concrete compressive strength coupled with similar (in quantity) lower yield strength at the opening levels was a random error made in Specimen 1 or, Specimens 2 and 6 presented lower materials strengths at their openings and were still able to conserve the opening intact. For the second case [2], Specimen 6 analytically failed at the opening when decreasing the yield strength by 60% and Specimen 2 presented difficulties to complete the iterations. Similar to the first case, since Specimen 6 fails at the opening with the second assumption, it lessens the probability that a lower yield strength at the levels with opening was the reason for Specimen 1 to fail at that zone. With the distinct possibility that Specimen 6 was able to remain undamaged at the opening even with poor adherence for the reinforcing bars at the opening levels. Another variation tested, was to assign lower yield strength along the entire specimens. The results with this assumption showed that the failure was still located at the beam-block interface for all of the specimens.

Following with the results of cases [1] and [2] on Specimen 1. With the failure located at the opening, the question should be if the failure mode is accurately predicted. Figures 5.30 and 5.31 contain the shear and flexure deformations independently for Specimen 1, in the cases when the failure is located at the opening. Figure 5.30 indicates a failure at the opening due to shear deformations, as it is expected when the experimental results of Specimen 1 are considered. Figures 3.14 and 3.15 show the damage and the experimental deflection profiles in Figures 5.8 and 5.9 show the accumulation of shear deformations at the levels that compose the opening. Figure 5.31 also indicates failure at the opening due to shear deformations, with the difference that in the upper stretch of the opening, the deformations are accumulated in the third element (not in the first as in case [1]).

The moment/curvature diagrams of the elements that analytically accumulate the damage are shown in Figures D.9 and D.11 (up to initial degradation) and the Shear stress-strain responses for the same elements are shown in Figures D.10 and D.12 (up to initial degradation). These figures refer to elements 9 and 13 of Figure A.26 for case [1], the first elements at the opening, and the ones that accumulate the damage when the failure is located at the opening. For case [2], elements 11 and 13 are relevant, as element 11 is the one that accumulates the damage in this case in the upper stretch (for the lower stretch, the first element accumulates the damage as with case [1]). In particular, shear deformations tend to increase even beyond the initiation of degradation, whereas the curvature at a certain level starts unloading.

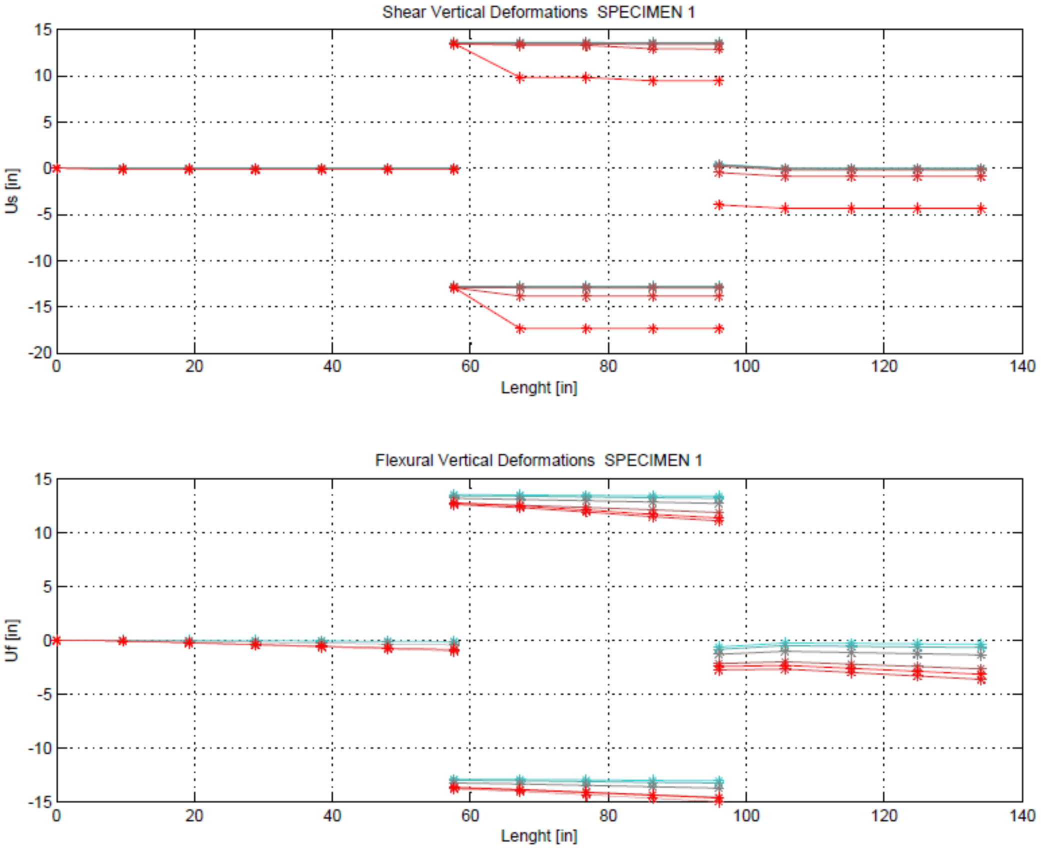

Figure 5.30: Analytical shear and flexural deformations at certain levels of loading when both material strengths are decreased and the failure is located at the opening. Specimen 1.

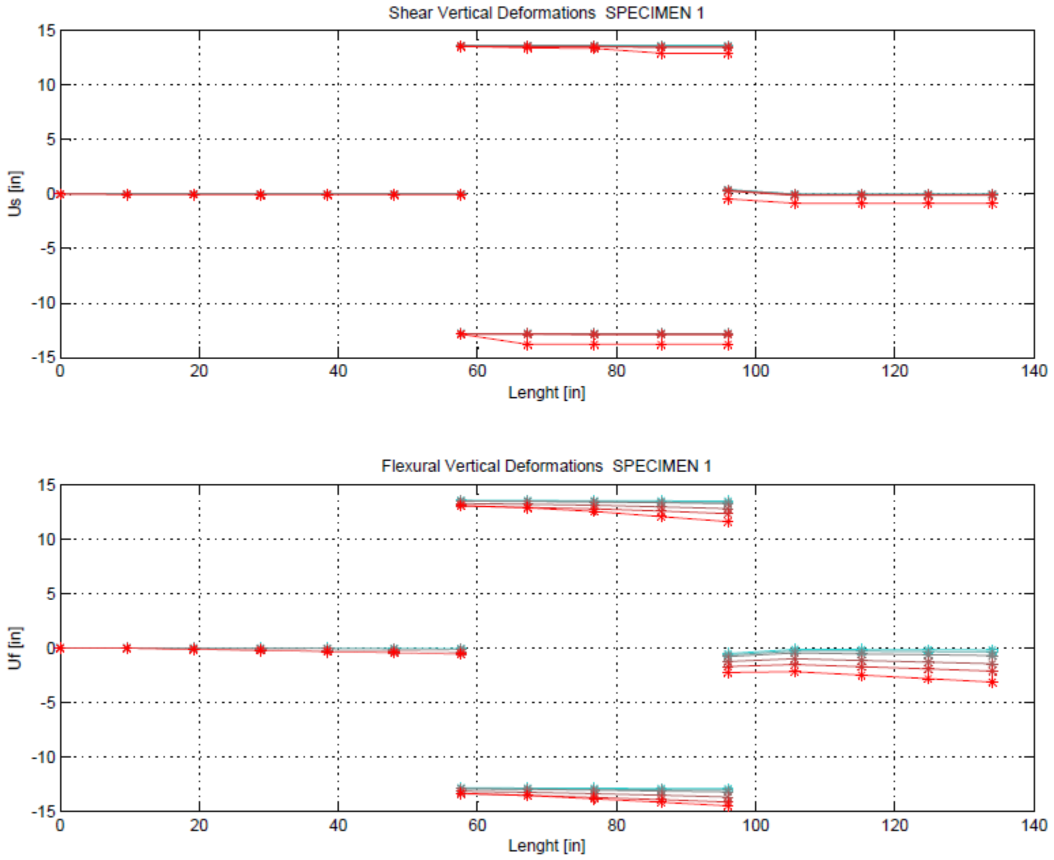

Figure 5.31: Analytical shear and flexural deformations at certain levels of loading when the strength of the reinforcing steel is decreased and the failure is located at the opening. Specimen 1.

5.3. Constraint variation at the loaded end

An unexpected concern arose when the analysis of the deflection profiles of the specimens was made (in Section 5.1.3). Some appreciable shear deformations appeared at the levels where the openings were located for all the specimens, including 2 and 6, for whom the failure did not occur at the opening. The presence of these deformations gives indication of a potential double curvature (in contrast with the cantilever specimen that was modeled).

The reason for this behavior of double curvature would be explained with a potential constraint in the rotation of the loaded end. The load application system, which is anchored to the specimens during the tests, might have restrained the rotation (totally or partially).

A simple procedure was made in order to study how the model would compare with the experimental results if the rotation was restricted at the loaded end. Two different restrictions for the rotation were introduced to the models: (1) zero end rotation (total restriction) and (2) calibrated rotational spring at the loaded end (partial restriction).

The idea is to observe how the model with restricted end rotation compares with both the model with non-restricted end rotation and with the experimental results. If the model with restricted end rotation improves the original results (i.e.: gives a better approach to the experimental results than the model with non-restricted end rotation), a recommendation for futures studies with similar load application conditions would be made, following the better approach.

The parameters that are used to compare the results are: the load displacement curves and the deflection profiles.

For the rotational spring, the calibration is made leaving the rotational stiffness that gives the best load displacement response (the best approximation to the experimental result).

It should be reminded that the original results (with non-restricted end rotation) exist for both the original and the alternative discretizations (available in Sections 4.1 and 4.4 respectively).

The results for each specimen are presented through Sections 5.3.1 to 5.3.4.

5.3.1. Specimen 1

5.3.1.1. Load-displacement curves for Specimen 1 with late variations

Figures 5.32 and 5.33 show the load displacement curves for Specimen 1.

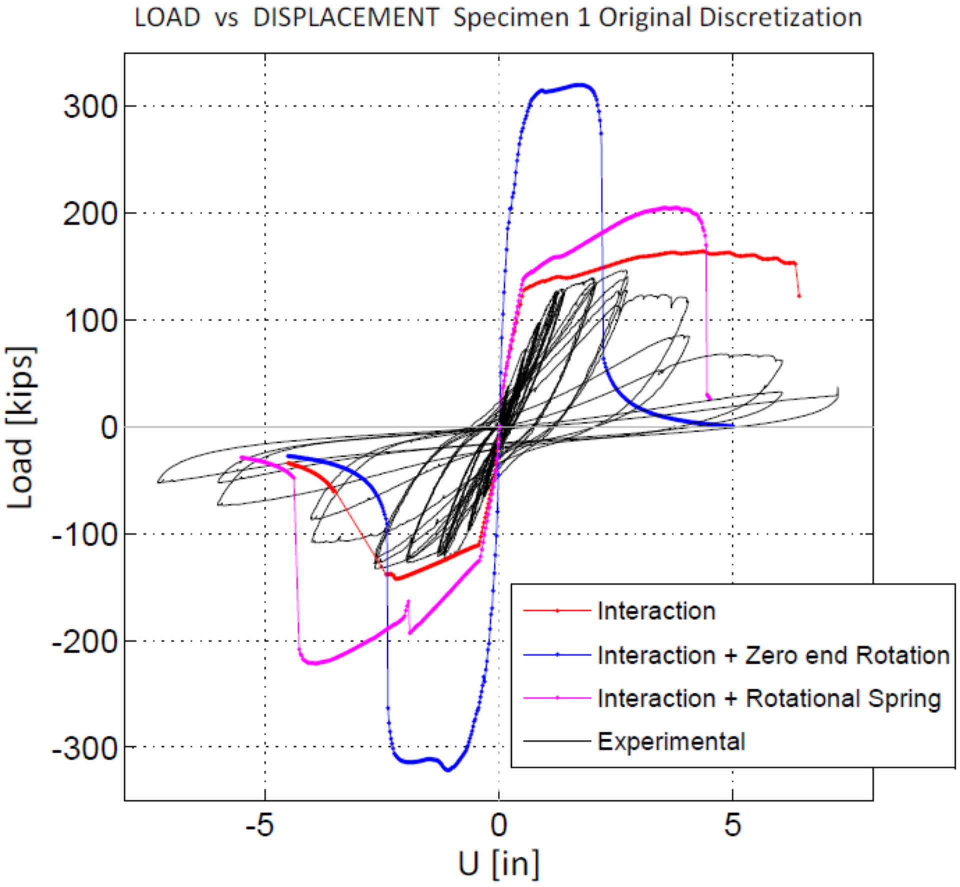

Figure 5.32: Load displacement response for Specimen 1. Comparison. Original discretization.

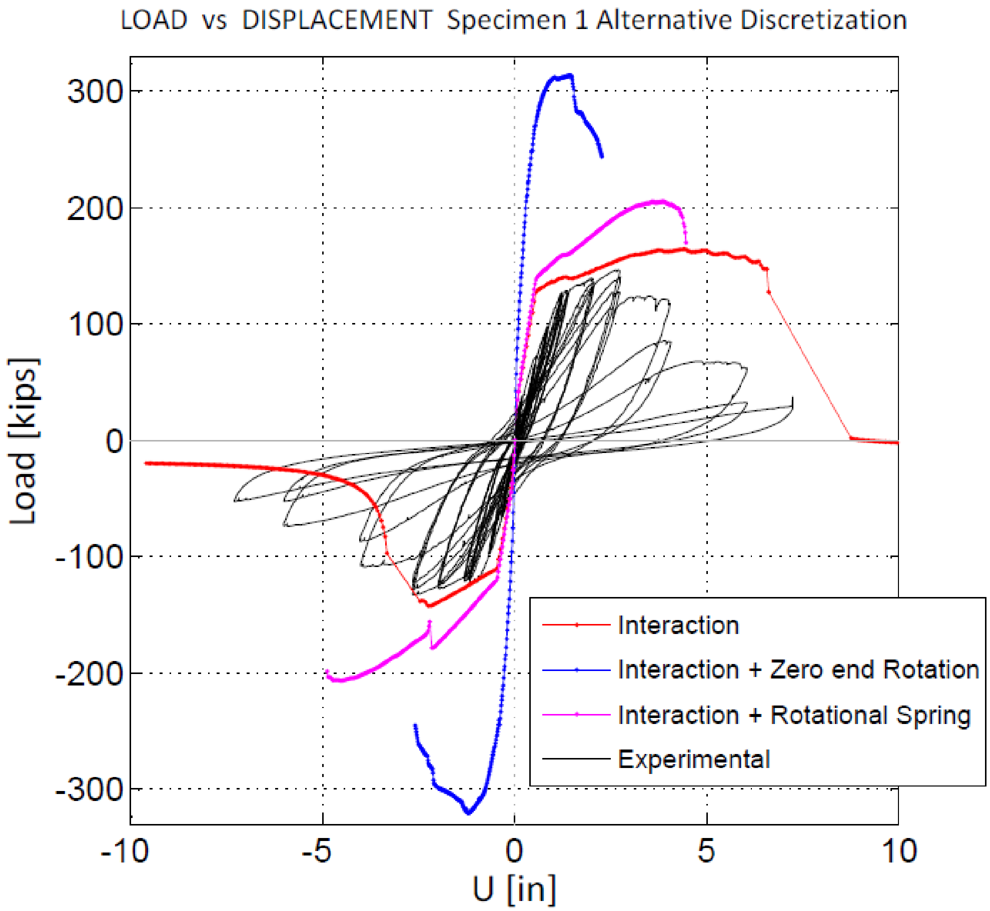

Figure 5.33: Load displacement response for Specimen 1. Comparison. Alternative discretization.

It is evident that the load carrying capacity is exaggeratedly overestimated by the interaction model when the rotation is fully restricted at the loaded end (by more than 100%). For the partial restriction of the rotation (with rotational spring at the loaded end), the capacity is also overestimated, but in a more acceptable range (40 to 67%).

The degradation is better represented with the partial restriction of the rotation, when compared to both the total restriction of the rotation and the original interaction model approach with non-restricted end rotation.

5.3.1.2. Deflection profiles for Specimen 1 with late variations

The deflection profiles at the displacement of experimental maximum capacity were analyzed. The curves can be seen in Appendix E, Figures E.1 to E.4.

Overall, the case with total restriction of the rotation at the loaded end approaches the experimental results better than the original interaction model (with non-restricted rotation at the loaded end) and the case with partial restriction for the rotation. The magnitudes of both the shear and the flexural deformations are better estimated with the fully restrained rotation.

The concentration of flexural deformations at certain levels (at the first level) is not well predicted by the different variations of the model.

For the alternative discretization, the concentration of shear deformations in the levels of the opening is accurately predicted with the model with zero end rotation, producing a better approach of the total deformations.

The upward pull of the alternative discretization is presented in Figure 5.34 (Figure E.4) as an example of the improvements that the model with zero end rotation produces in the deflection profiles. It should be observed, in particular, the concentration of shear deformations in the levels that compose the opening.

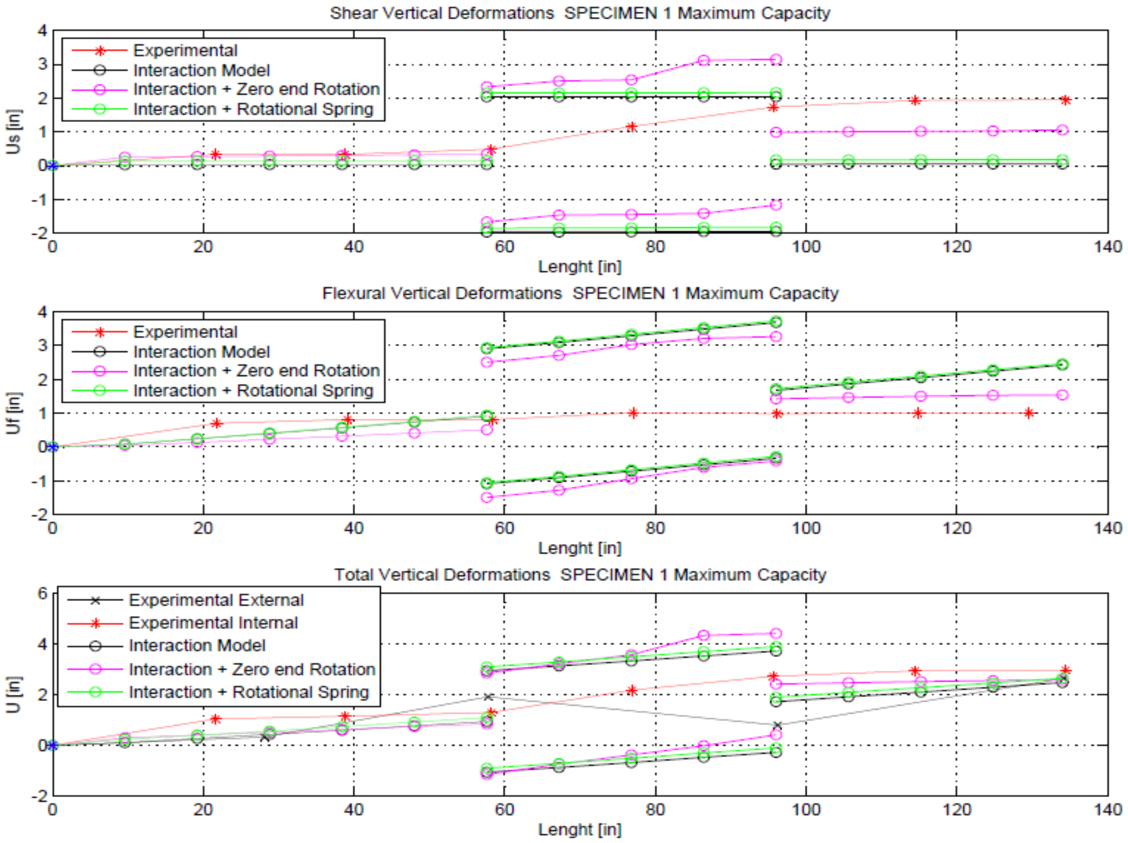

Figure 5.34: Deflection Profiles for Specimen 1. Altern. Discret. Comparison with late variations. Upwards.

5.3.2. Specimen 2

5.3.2.1. Load-displacement curves for Specimen 2 with late variations

The load displacement responses are shown in Figures 5.35 and 5.36.

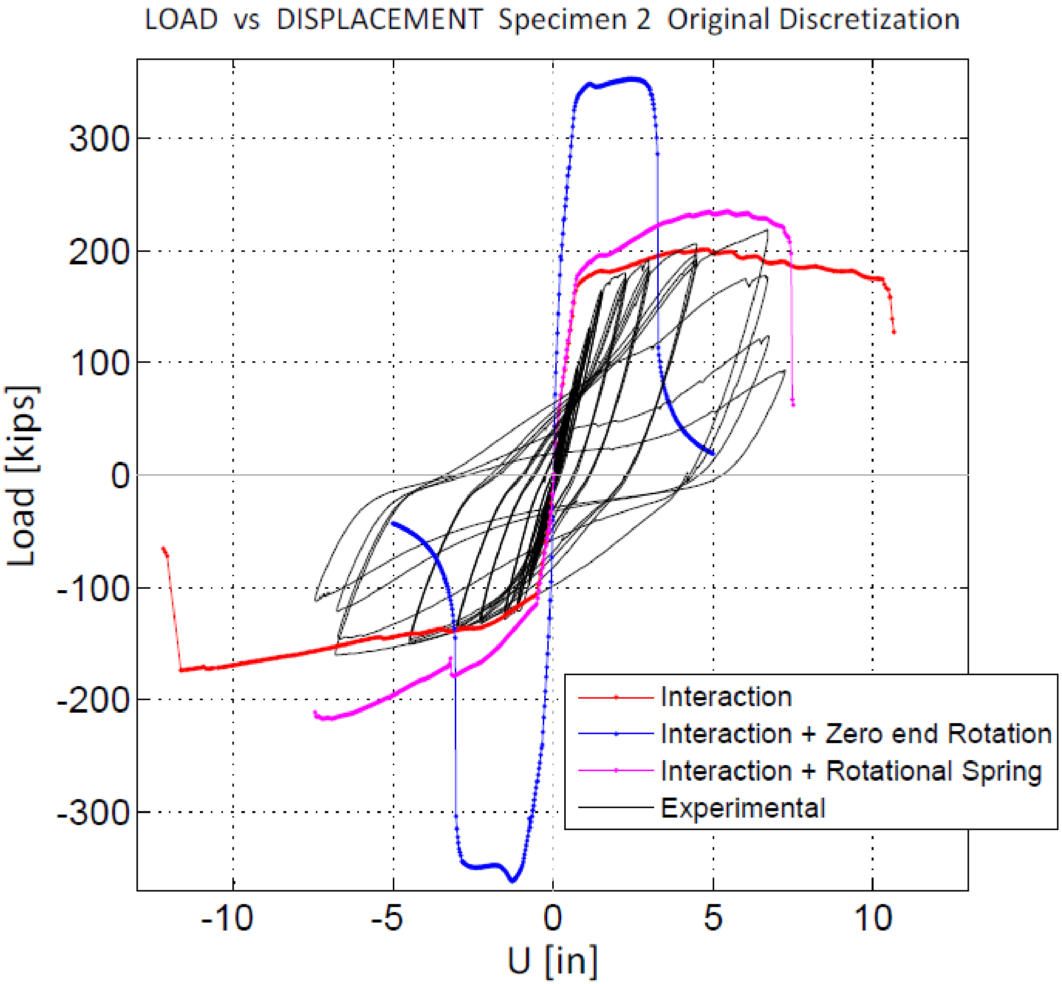

Figure 5.35: Load displacement response for Specimen 2. Comparison. Original discretization.

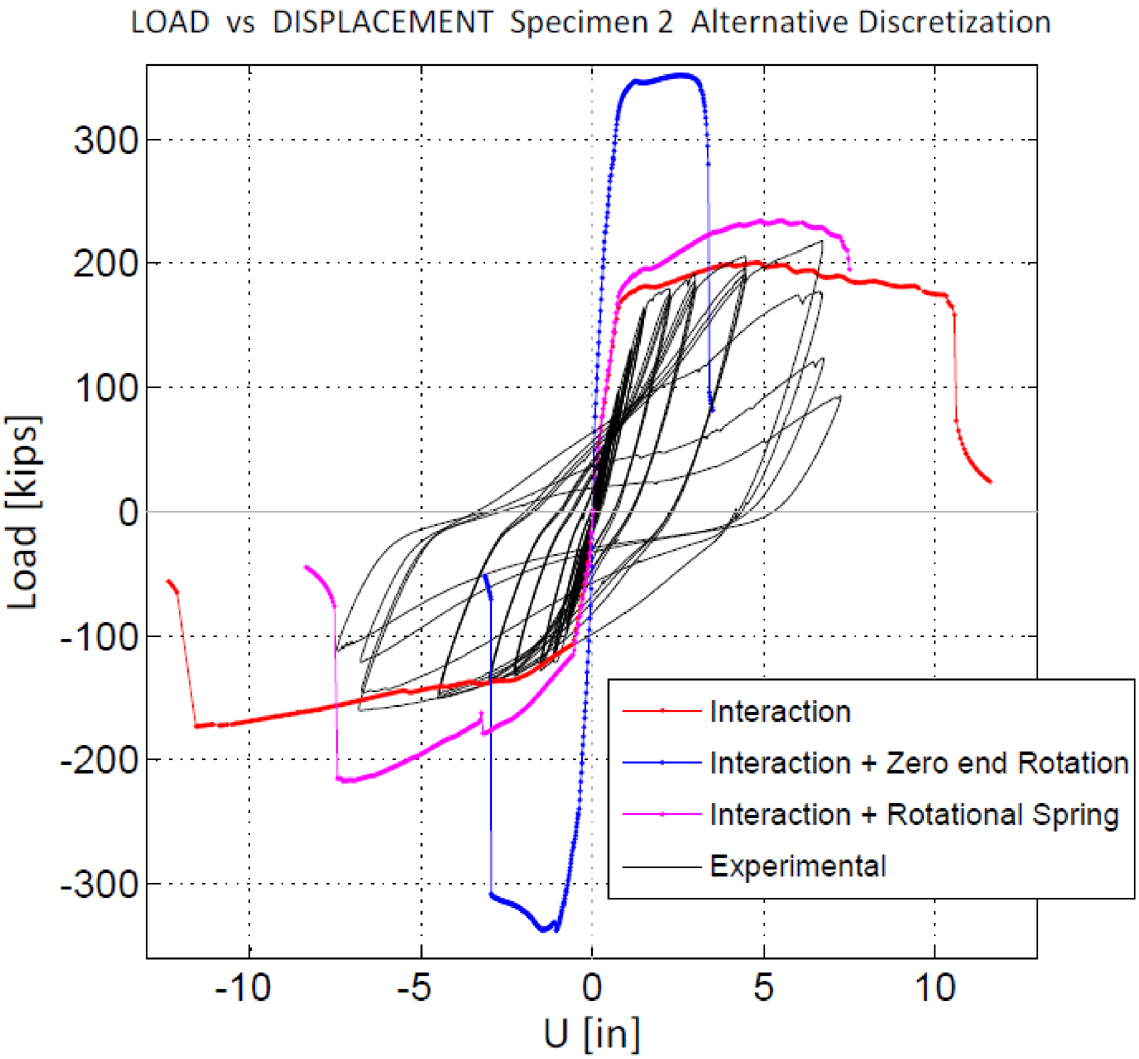

Figure 5.36: Load displacement response for Specimen 2. Comparison. Alternative discretization.

The load displacement curves for Specimen 2 behave equally to those of Specimen 1. The fully restricted rotation at the loaded end produces exaggerated load carrying capacity, while the partially restricted rotation improves the degradation (compared to the original interaction model), coupled with an overestimated but much more reasonable capacity (just 8% overestimation for the downwards direction and 35% for the upwards direction).

5.3.2.2. Deflection profiles for Specimen 2 with late variations

Similar to Specimen 1, the model with zero end rotation produces the best approach with the experimental results in the deflection curves, compared to the original interaction model and the model with partially restricted rotation. The deflection curves are available in Appendix E, Figures E.5 to E.8. The model with zero end rotation overall better estimates the independent shear and flexural deformations, and also better predicts the concentration of shear deformations in certain levels.

With the original discretization, the concentration of shear deformations in the first level is accurately predicted, but it neglects the accumulation of some shear deformations in the levels of the opening.

The flexural deformations are deficiently estimated, as the damage accumulation in the first level is not captured by the model variations and the magnitude of the flexural deformations is not satisfyingly predicted.

For the total deformations, the combination of original discretization and zero end rotation produces the best results, especially because of the concentration of deformations in the first level. In order to justify the previous asseveration, Figure 5.37 (Figure E.7) shows the upward pull for Specimen 2 with the original discretization approach.

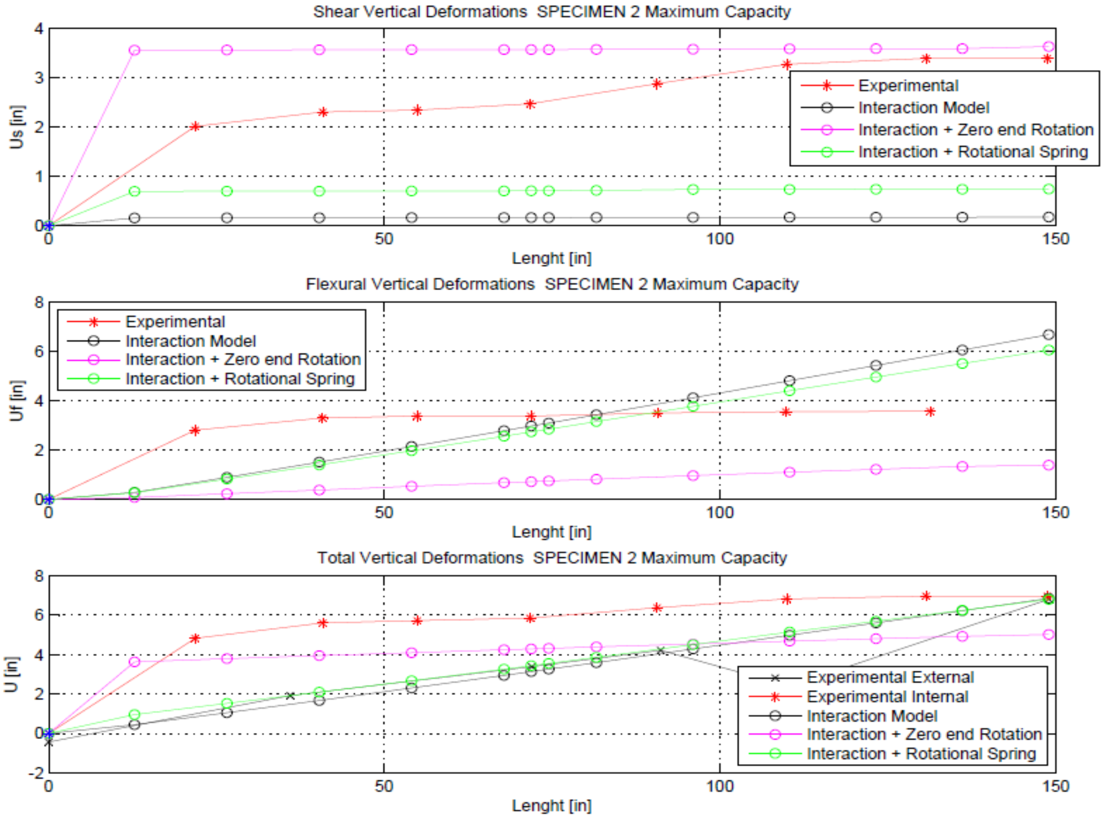

Figure 5.37: Deflection Profiles for Specimen 2. Origin. Discret. Comparison with late variations. Upwards.

5.3.3. Specimen 6

5.3.3.1. Load-displacement curves for Specimen 6 with late variations

Figures 5.38 and 5.39 show the load displacement curves for Specimen 6.

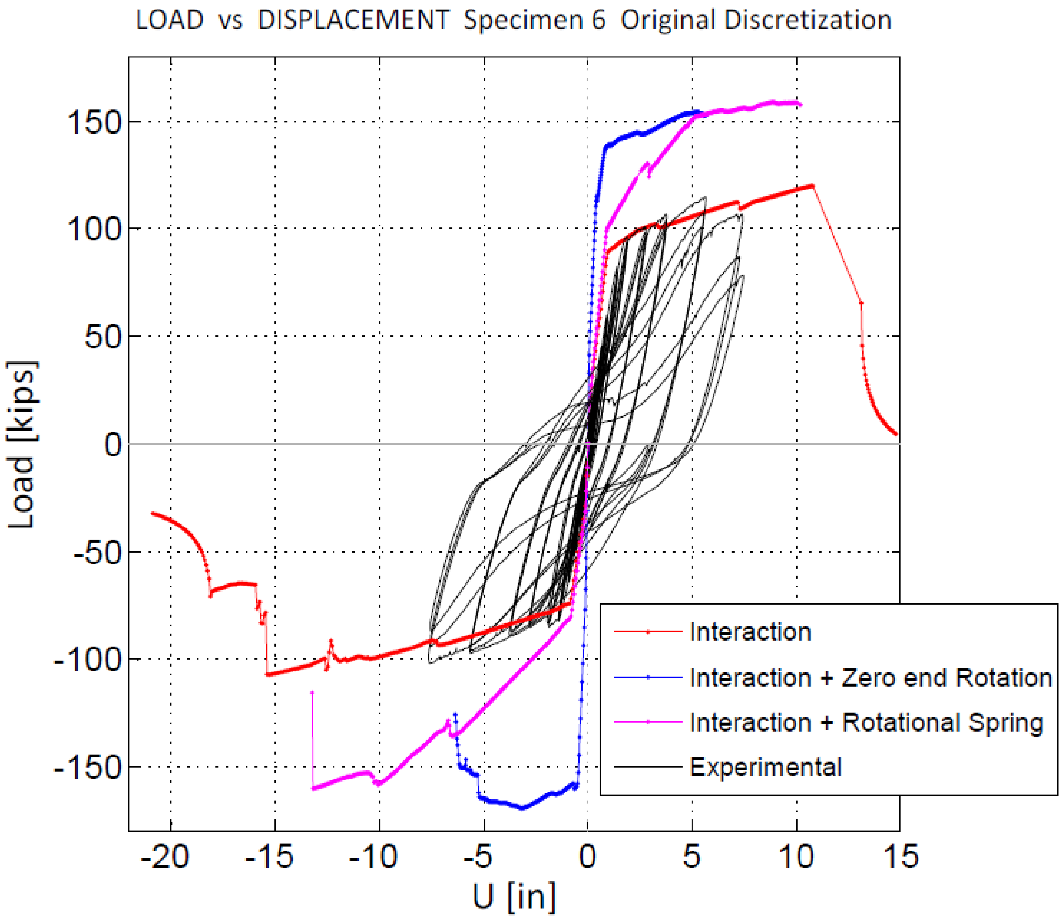

Figure 5.38: Load displacement response for Specimen 6. Comparison. Original discretization.

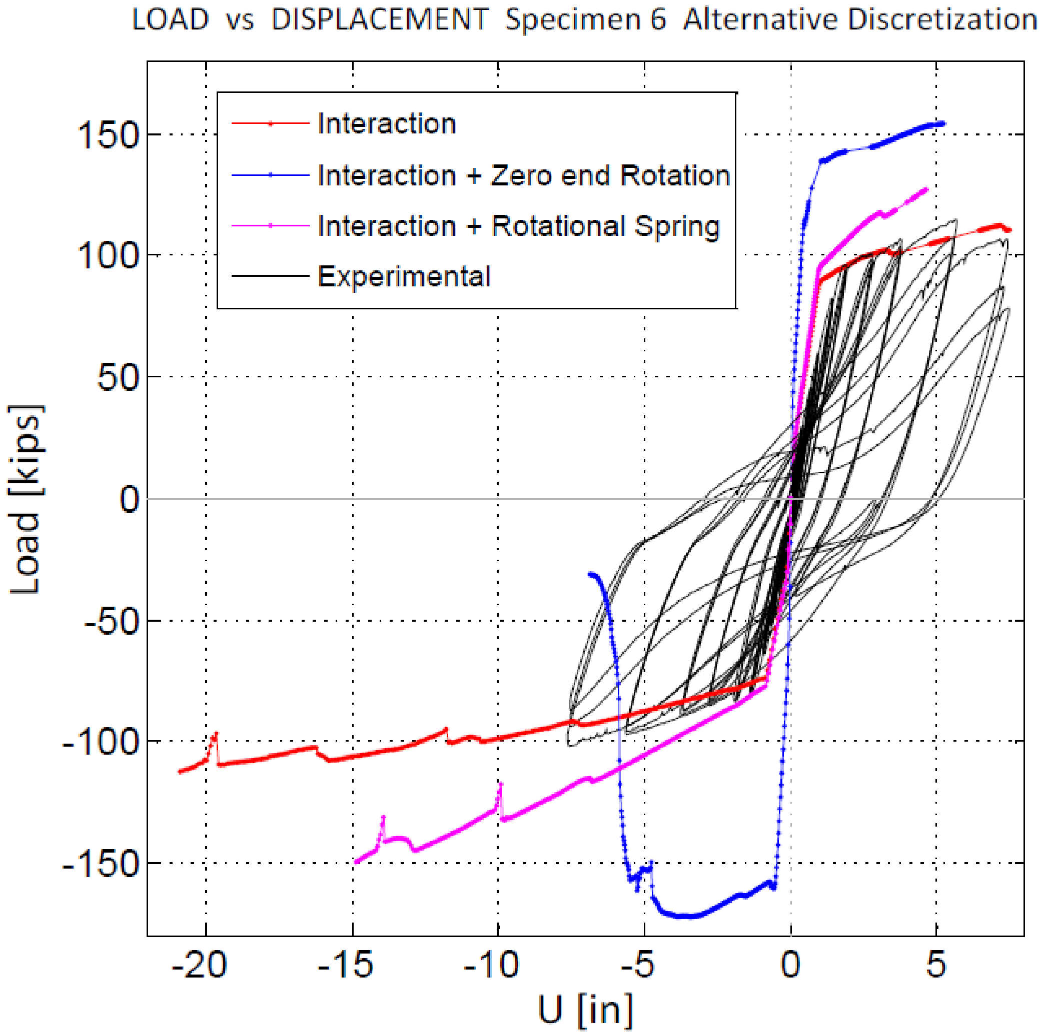

Figure 5.39: Load displacement response for Specimen 6. Comparison. Alternative discretization.

Specimen 6 presented some difficulties in order to finish the iteration process for some variations of the interaction model. Overall, Specimen 6 behaves similarly to Specimens 1 and 2, with the fully restricted end rotation returning the highest capacities (but not exaggerated in this case, 35 to 69% overestimation).

About the degradation, it is not entirely clear if the partial restriction of the rotation at the loaded end gives a better approach, because of the problems mentioned before.

5.3.3.2. Deflection profiles for Specimen 6 with late variations

Figures E.9 to E.12 of Appendix E show the deflection profiles for Specimen 6.

All the variations of the model fail to predict the accumulation of flexural deformations in the first two levels.

The shear deformation magnitudes are underestimated by all the model variations, with the exception of the upward pull of the alternative discretization, but it gives a correct magnitude with inaccurate prediction of the localization of damage.

For the total displacements, no improvement was found with either variation of the model, since the concentration of deformations in the first two levels is still not being predicted.

Figure 5.40 (Figure E.12) is presented, in order to show that no significant improvement is made with the latest variations. In particular, important discrepancies in the localization of damage are observed. The problems that this specimen presented in order to finish the iterations during the simulations (mentioned in Section 5.3.3.1) might be a reason for the lack of improvement.

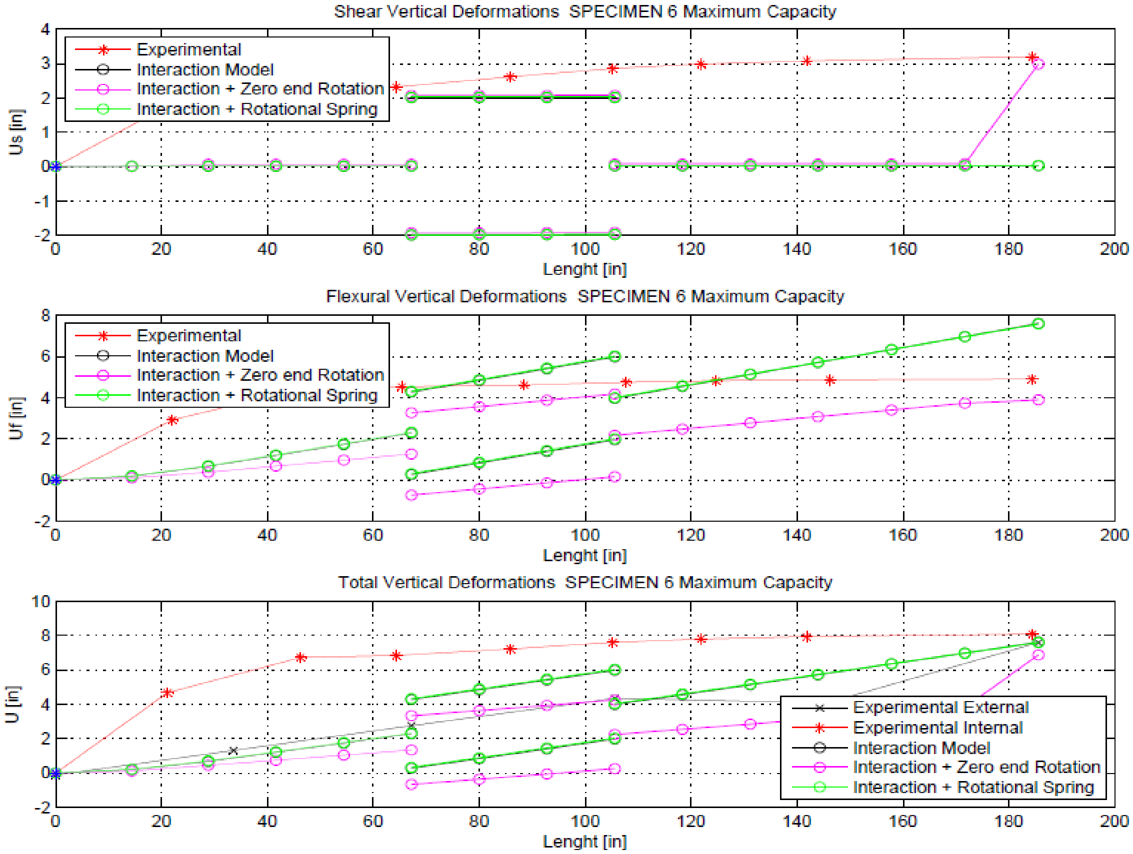

Figure 5.40: Deflection Profiles for Specimen 6. Altern. Discret. Comparison with late variations. Upwards.

5.3.4. Specimen 7

5.3.4.1. Load-displacement curves for Specimen 7 with late variations

The load displacement curve is shown in Figure 5.41.

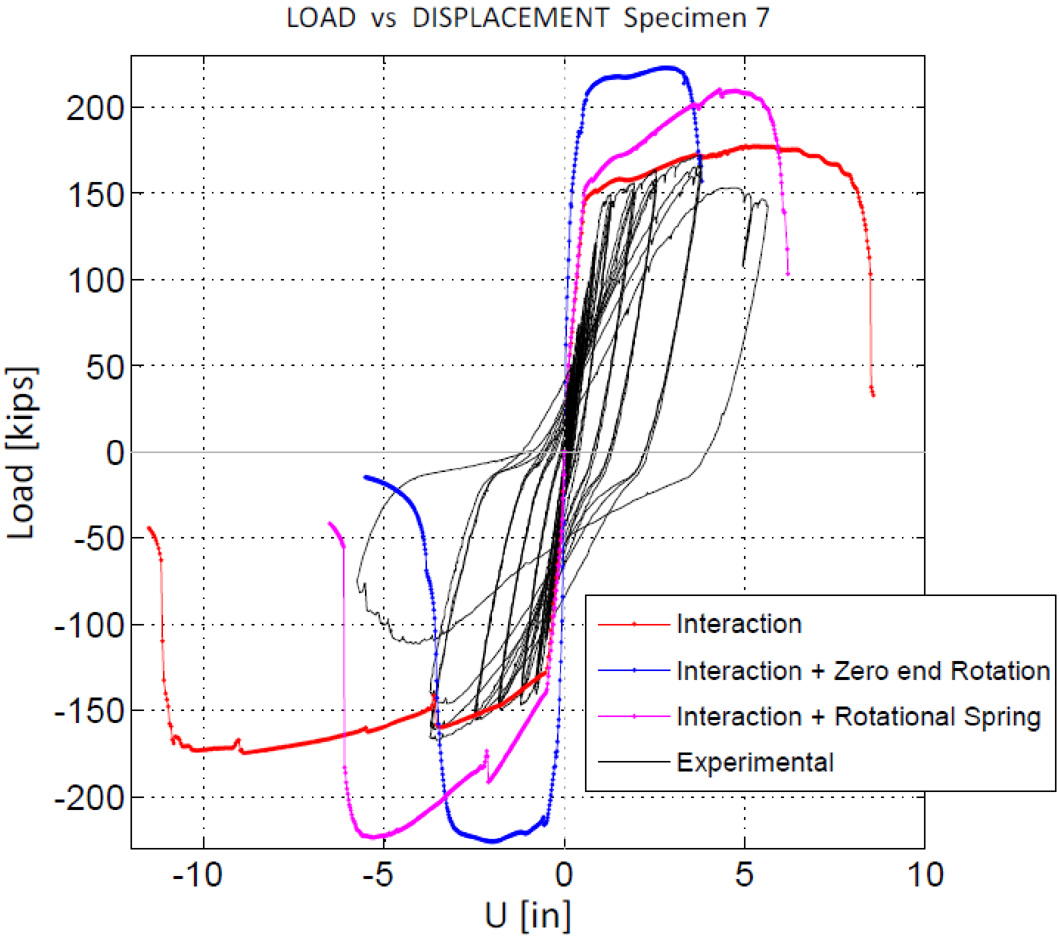

Figure 5.41: Load displacement response for Specimen 7. Comparison.

Specimen 7 is the one without opening, hence, only the original discretization applies for it.

Both cases (full and partial restriction of the rotation at the loaded end) present similar results in capacity, which is overestimated (in the range of 22 to 35% higher), with a slight better approach given by the rotational spring at the loaded end).

The degradation is better represented with both new variations (total and partial restriction of the rotation at the loaded end) than with the original interaction model (no restriction for the rotation).

5.3.4.2. Deflection profiles for Specimen 7 with late variations

The magnitudes of the shear deformations are underestimated by the interaction model with non-restricted and with partially restricted end rotation (as Figures E.13 and E.14 of Appendix E can justify). The model with zero end rotation (fully restricted rotation) estimates the magnitude more accurately, but concentrates the damage in the last level, contrary to the experimental results, that accumulate the damage in the first levels.

In the case of the flexural deformations, the magnitude is well predicted with the zero end rotation approach, but the concentration of deformations in the first levels is not predicted.

The total deformations profile is inaccurately estimated by the analytical model variations, because of its inability to predict the accumulation of damage in the first levels. Figure 5.42 (Figure E.13) shows the downward push of Specimen 7 in order to justify the analysis made in this section.

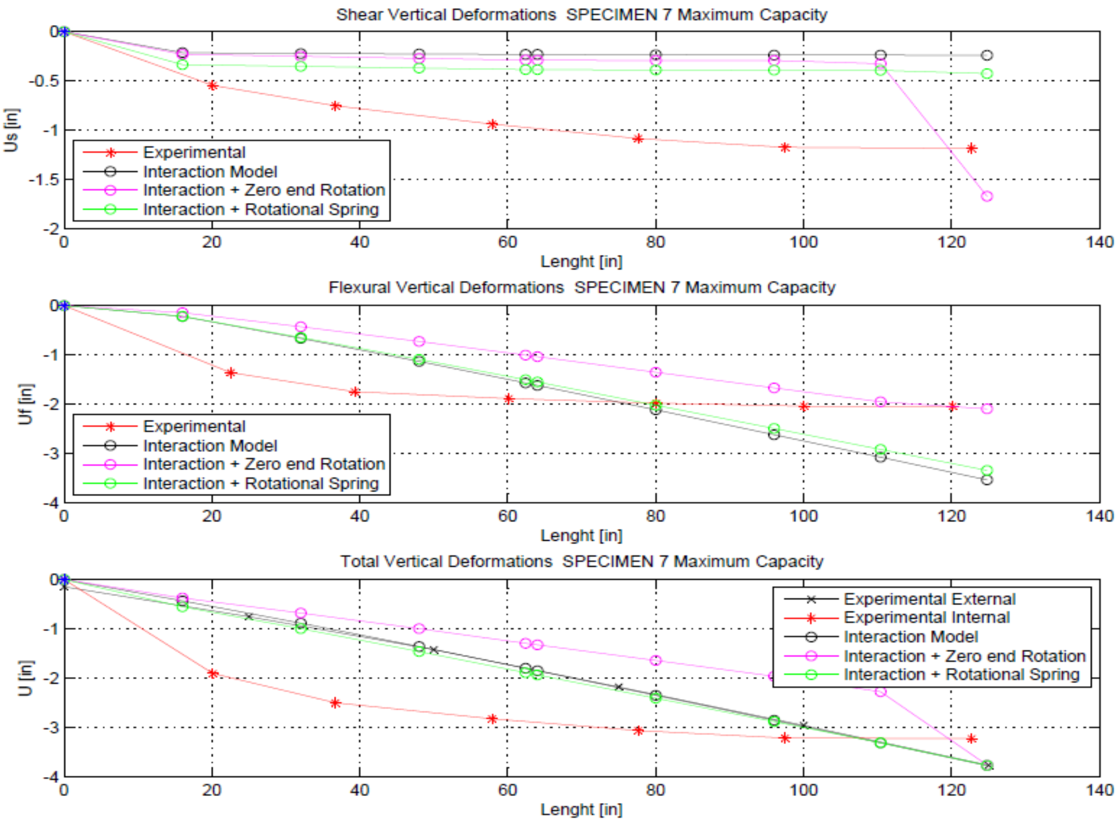

Figure 5.42: Deflection Profiles for Specimen 7. Comparison with late variations. Downwards.

In general, the analysis made in Section 5.3 indicates that the interaction model with partial restriction of the rotation at the loaded end (rotational spring) gives a better approach than the model with total restriction of the rotation (zero end rotation) with regard to the load-displacement curves. It represents a better approach in terms of maximum capacity and degradation. The degradation is better represented with the rotational spring even when compared with the original interaction model with non-restricted end rotation. The capacity is still better estimated by the original model, which supports the case that the prediction of capacity is the best quality of the interaction model so far.

In the case of the deflection curves, the results are different. The zero end rotation approach gives a better estimation overall, in terms of concentration of damage at certain levels and in the magnitude of the independent shear and flexural deformations. And this is valid when compared to both the rotational spring approach and with the original approach, making it impossible to fully dismiss the zero end rotation approach.

The estimation of the initial stiffness is not improved with the latest variations, which can be noted directly from the load-displacement curves.

CHAPTER 6. Summary and Conclusions

An analytical model that combines the shear and flexure responses, proposed by Massone et al. (2006), was studied. The challenge was to adapt the shear-flexure interaction model for its use in cantilever reinforced concrete beams with transverse rectangular openings at the center of their length. The openings were found in three of a total of four modeled specimens. Each opening crosses the horizontal transverse direction of their respective specimen. The analytical responses were compared with experimental results, from studies conducted by Lemnitzer et al. (2013). The specimens where built as replicas of special moment frame beams, and their cross section had the appearance of a T shaped beam, due to the presence of a top slab in each one of them.

A flexural model, unable to account for the shear contribution, was used as a base for the more complex interaction model. The results with the former were similar to the results given by the interaction model in terms of global response (load-displacement curve), but it was unable to reach a degradation zone (when the load-carrying ability ceases due to the damage). The limitations exhibited by the flexural model support the importance of the development and improvement of a model that can take into account the coupled shear and flexure responses.

In order to incorporate an opening to the elements using the shear-interaction model, the chosen approach was to assign a negligible area to the fibers in an element that composes an opening, with the intention that those fibers do not contribute to the resistance of the element.

In general, the analytical response was better predicted for the upwards direction (pulling the tip of a specimen upwards), except for ductility, which was overestimated in greater amount in that direction. The initial stiffness was around 100% higher for the analytical response (compared to the experimental response) in the downwards direction for all of the specimens. In the upwards direction, overall, the results are at least around 20-30% more accurately estimated than in the downwards direction, with the exception of Specimen 7, where the initial stiffness was almost predicted upwards (just 8% overestimation), and with the exception of Specimen 1, that estimated the initial stiffness with the same inaccuracy in both directions. Specimen 7 was the only specimen without an opening, somewhat minimizing the importance of having predicted the mentioned stiffness, as the objective was to predict the behavior of beams with openings. In the upwards direction, the reinforcing steel ratio involved was lower than in the downwards direction, and the top slab contributes a little more concrete mass for the compressive resistance of the upper portion. The ductility was higher in the upwards direction as consequence of the lower reinforcing ratio and perhaps, in a smaller extent, due to the presence of the top slab in the upper portion.

Ductility presented a major discrepancy between the analytical and the experimental results, with the interaction model proving to represent too ductile responses, especially in the upwards direction. The maximum capacities and degradation zones were often estimated at twice the displacement of the experimental response. In ductility, the only specimen that was adequately predicted was Specimen 1 in the upwards directions, reaching maximum capacity at 1.6% drift, compared to the 2.0% experimental drift and reaching the degradation zone at 1.8% drift, similar to the 2.0% experimental drift.

The maximum capacities predicted were found in acceptable ranges: around 10% higher prediction for Specimen 1 in both directions, about 8% lower in the downwards direction and 8% higher in the upwards direction for Specimen 2, around 5% higher for Specimen 6 in both directions and just about 4% higher for Specimen 7 in both directions. Specimen 2 reached the highest maximum capacity with 218 [kips] in the downwards direction, as it was expected, being the heaviest reinforced specimen. In the upwards direction, Specimen 7 reached the maximum capacity at 167 [kips] (about 4% higher than Specimen 2). Overall the maximum capacity was accurately predicted using the shear-flexure interaction model, most likely being the better quality found for the model in this entire study.

The load-displacement results of the interaction model resemble the experimental results at great scale, but not in detail. The interaction model, with the first assumptions made (up to Section 4.3.4), proves to be too ductile in order to completely resemble the experimental curves.

Continuing with the global response, the estimated deflection profiles differ significantly from the experimental results. In general, the shear displacements are underestimated by the interaction model, often predicting the accumulation of shear damage in certain locations accurately, but estimating lower magnitudes for those displacements. Some noticeable experimental shear deformations were observed in the levels that compose the openings (which were not analytically predicted), warning about a possible double curvature beam behavior. This point is addressed a few paragraphs later, discussing the latest variations made for the model.

The flexural displacements tend to be overestimated in both directions. Contrary to the shear displacements, the accumulation of the flexural displacements or flexural damage in certain elements is not accurately estimated, since the analytical flexural displacements increase almost linearly through the length of each specimen. The overestimation of the flexural deformations can be attributed partly to the lack of instrumentation in the first gap between the reaction block and the first end of the horizontal LVDTs. The inability to predict the accumulation of flexural damage in the first levels cannot be justified by the same condition.

The overestimation of the flexural displacements mentioned in the previous paragraph is responsible for the undesirable high ductility predicted by the interaction model.

The experimental deflection profiles present some deficiencies in those captured and estimated via external instrumentation, because the shapes of the profiles are not that of a continuous cantilever beam, with the exception of Specimen 7 and Specimen 6, whose deflection profiles shapes via external instrumentation are acceptable. Regardless of the previous analysis, at least the displacement at the tip of each specimen, estimated using external instrumentation, shows satisfying results.

Discrepancies were found in the tip displacement estimated as the accumulation of shear and flexure deformations along the entire specimens via internal instrumentation, when compared to the tip displacement estimated using external instrumentation (which is trustful). The “externally estimated” tip displacement is around 30% higher for all specimens, compared to the internal cumulative displacement. Although the estimated shear and flexure displacements (using internal instrumentation) are quite acceptable for the levels in between the beam/block interface and the tip of the beam, their accumulation up to the tip fails to be captured completely. A possible reason for this, could be the gap left between the reaction block and the first ends of the LVDTs, mentioned a few paragraphs before. That gap may be presenting considerable rotation or displacements that could not be captured during the tests.

The failure mode of Specimen 1 is not accurately represented with the first common formulation of the interaction model. Experimentally, Specimen 1 fails at the opening (develops a plastic hinge at the levels that compose the opening) and the interaction model predicts failure at the beam/block interface. A variation for the beam discretization and the assumption of a considerable decrease in the material strengths was necessary to implement in order to enable the prediction of the failure at the opening for Specimen 1, and it was only possible in the downwards direction. The alternative discretization showed little improvement in the global response (load-displacement curves), but it is an acceptable approach for modeling reinforced concrete elements with openings, since it did not worsen the results either. It is a reasonable approach, since it does not force the specimen to follow the Bernoulli hypothesis for the elements that compose the opening, which are formed by two independent sections, that were forced to work as one section using the original discretization. The alternative discretization was implemented for the rest of the specimens, but the load-displacement curves were not included in this study, as the results were barely different from those obtained with the first approach. The assumption of lower material strengths is somewhat too drastic (50% of f_c' and 50% of f_y for the elements that compose the opening or, just 30% of f_y over the same elements) to be the cause of the experimental failure of Specimen 1 at the opening, considering the rigorous procedures followed during the construction of the specimens, but it was the one assumption (together with the alternative discretization) that enabled the accurate prediction of the location of the failure. The lack of adherence for the reinforcing bars in the elements that compose the opening would be the most likely explanation.

The assumptions of: self-weight load, rotational spring at the beam/block interface and the consideration of half of the yield strength of reinforcing bars while the development length is reached, all contribute to better approach the experimental conditions of the specimens.

The latest proposed variations (zero end rotation and rotational spring at the loaded end) gave significant improvements independently. The zero end rotation assumption improved the deflection curves in magnitudes and in the ability to locate damage concentration at certain levels of the specimens. The rotational spring approach improved the degradation of the load-displacement curves. Neither approach showed satisfactory results at predicting the capacity or at correcting the initial stiffness. The fact that the improvements were not given by just one of the latest variations, the recommendation of one of them for futures studies is not that direct, especially since both variations worsened the results of the best quality of the original model so far (the prediction of capacity). Both variations should be tested to represent this loading condition, always taking into account not to worsen the capacity results.

As final comments, it can be mentioned that the shear-flexure interaction model predicts accurately the maximum capacity of cantilever beams with and without openings. The failure mode of the tested specimens is approached significantly accurately, but with some improvements to be made: like the prediction of the accumulation of flexural damage at certain levels or a desirable lesser underestimation of the magnitudes of the shear displacements. An alternative beam discretization can improve both the global response and the local response of beams with openings. The alternative discretization is highly recommended for future studies that focus on the prediction of the behavior of reinforced concrete elements with openings. The estimated ductility is a major issue when the objective is to accurately predict the displacements at the beginning of the degradation zone for cantilever beams with openings, since they are significantly overestimated.

REFERENCES

1. ACI (American Concrete Institute) Committee 318. 2011. Building Code Requirements for Structural Concrete (ACI 318-11) and Commentary (ACI 318R- 11). Farmington Hills, MI: ACI.
2. Aykac B., Aykac S., Kalkan I., Dundar B., Can H., 2014. Flexural Behavior and Strength of Reinforced Concrete Beams with Multiple Transverse Openings. ACI Struct. J.; 111: 267-278.
3. Belarbi A., Hsu TTC., Constitutive laws of concrete in tension and reinforcing bars stiffened by concrete. ACI Struct. J. 1994; 91 (4):465–474.
4. Chai W., Lemnitzer A., Erickson T., Herrera L., 2013, “Cyclic Behavior of SMRF RC Beams with and without openings – Phase 1”, A report on the experimental testing program conducted under Grant No. 130726.
5. Galleguillos T., “Modeling of SFRC Beams”, thesis, Department of Civil Engineering, University of Chile; 2010. [in Spanish].
6. Gotschlich N., “Modeling of RC beams with pre-stressed cables with different shear span-to-depth ratio”, thesis, Deparment of Civil Engineering, University of Chile; 2011. 81 p. [in Spanish].
7. Massone L.M., Strength prediction of squat structural walls via calibration of a shear–flexure interaction model. Eng Struct 2010; 32 (4): 922–32.
8. Massone L.M., Galleguillos T.A., Kang Thomas H.-K., Kim Woosuk, 2012, “Shear-flexure coupling behavior of steel fiber-reinforced concrete beams”, ACI Structural Journal 2012; 109-S37: 435-444.
9. Massone L.M., Gotschlich N.J., Kang Thomas H.-K., Hong S-G, 2013, “Shear-flexural interaction for pre-stressed self-consolidating concrete beams”, *Engineering Structures*, 56:1464-1473.
10. Massone L.M., Orakcal K., Wallace J.W., Shear–flexure interaction for structuralwalls.SP-236. ACI special publication—Deformation capacity and shear strength of reinforced concrete members under cyclic loading. 2006. p.127–50.
11. Massone L.M., Orackal K., Wallace J.W., “Modeling of squat structural walls controlled by shear”. ACI Structural Journal 2009; 106 (5): 646-655.
12. Massone L.M., Wallace J.W., “Load-Deformation Responses of Slender Reinforced Concrete Walls”, ACI Structural Journal, V. 101, No. 1, Jan.-Feb. 2004, pp. 103-113.
13. Menegotto M., Pinto E., Method of analysis for cyclically loaded reinforced concrete plane frames including changes in geometry and non-elastic behavior of elements under combined normal force and bending. In: Proceedings, IABSE symposium, Lisbon, Portugal; 1973.
14. Petrangeli M., Pinto P.E., Ciampi V., Fiber element for cyclic bending and shear of RC structures. I: Theory. J Eng Mech 1999; 125 (9): 994–1001.

15. Saatcioglu M., Razvi S., “Strength and Ductility of Confined Concrete”. Journal of Structural Engineering, 118 (6), 1590-1607. 1992.
16. Thorenfeldt, E., Tomaszewicz, A., and Jensen, J.J. 1987. Mechanical properties of high strength concrete and application in design. Proceedings of the Symposium on Utilization of High Strength Concrete, Tapir, Trondheim, Norway, pp. 149-159.
17. Vecchio F.J., Collins M.P., The modified compression-field theory for reinforced concrete elements subjected to shear. ACI J 1986; 83 (2):219–31.

APPENDIX

Appendix A.

A.1. Complemental Figures

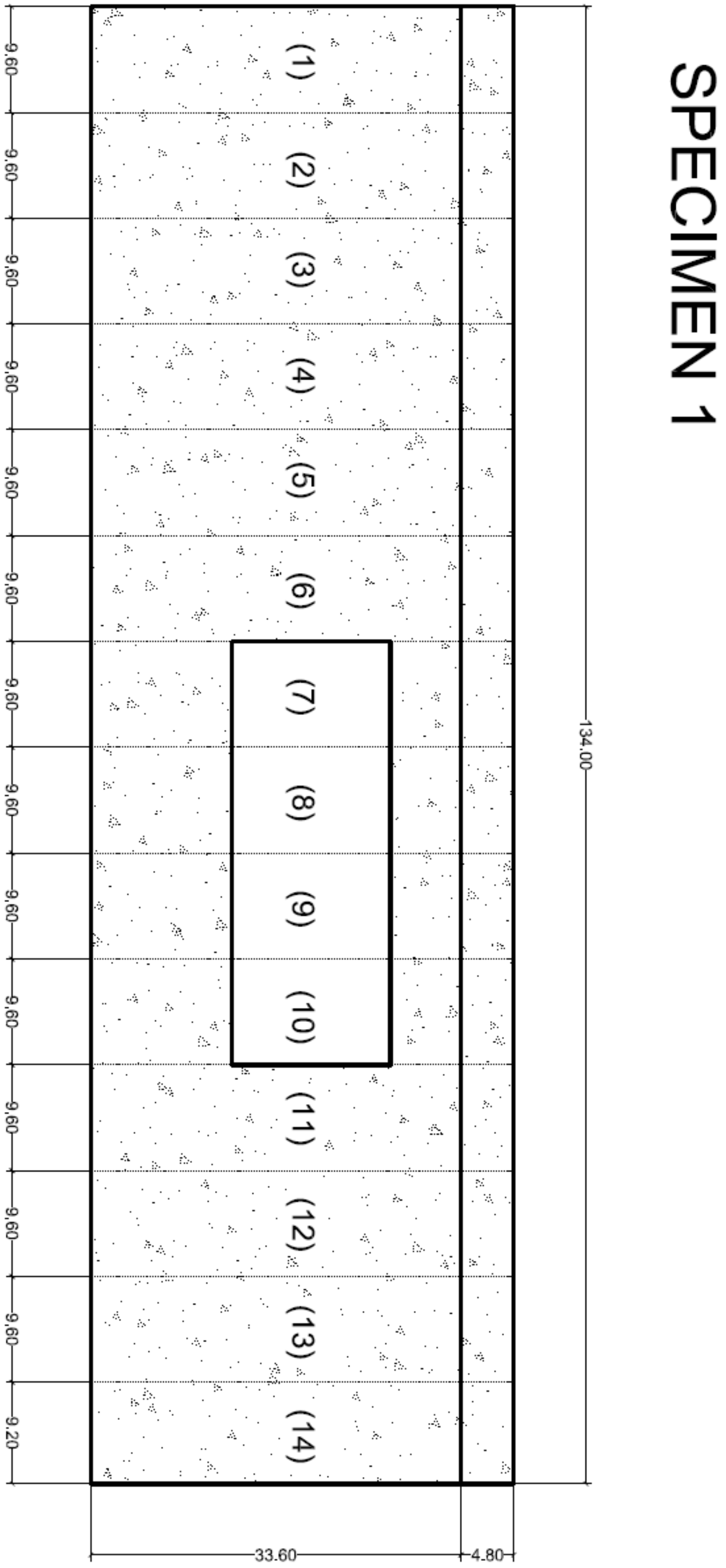

Figure A.1: Element Discretization for Specimen 1. Dimensions in inches.

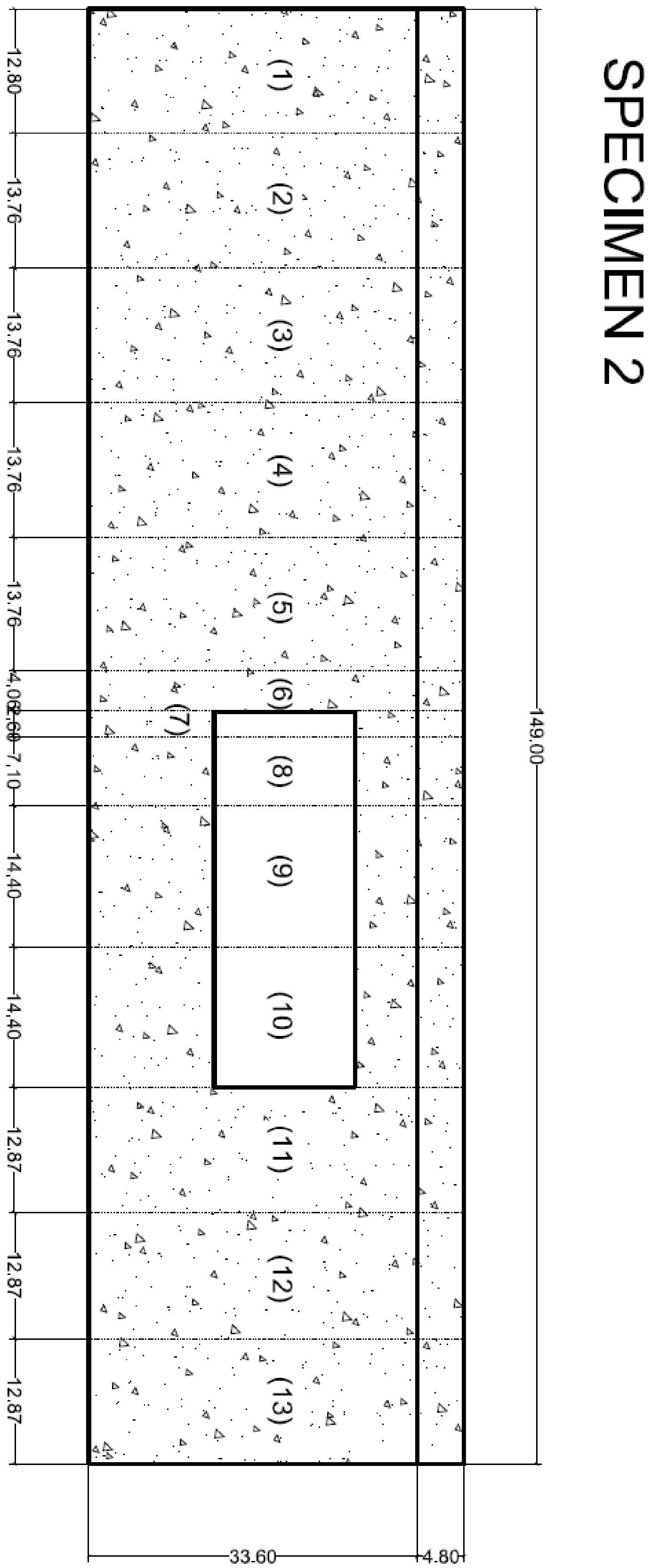

Figure A.2: Element Discretization for Specimen 2. Dimensions in inches.

Figure A.3: Element Discretization for Specimen 6. Dimensions in inches.

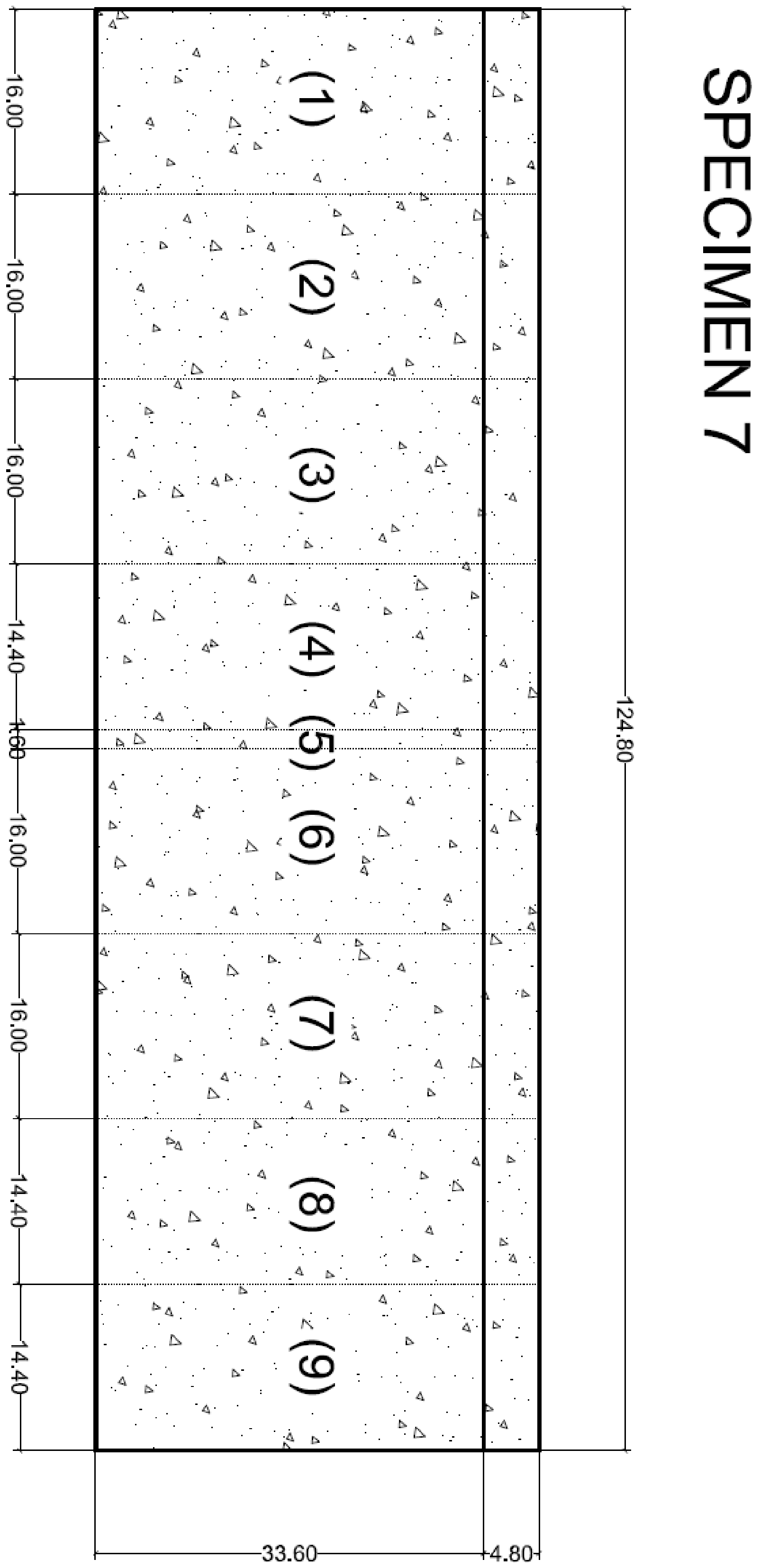

Figure A.4: Element Discretization for Specimen 7. Dimensions in inches.

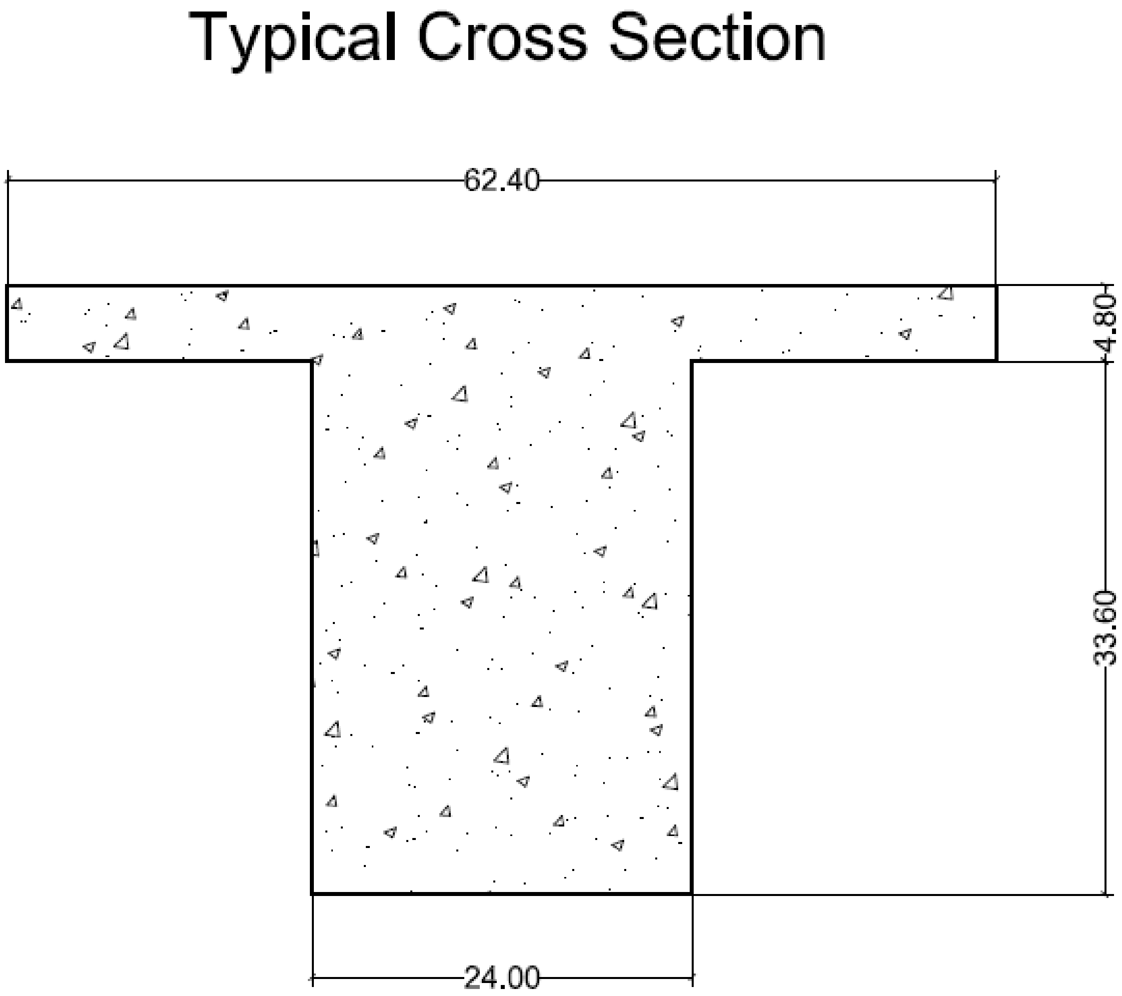

Figure A.5: Typical Cross Section. Dimensions in inches.

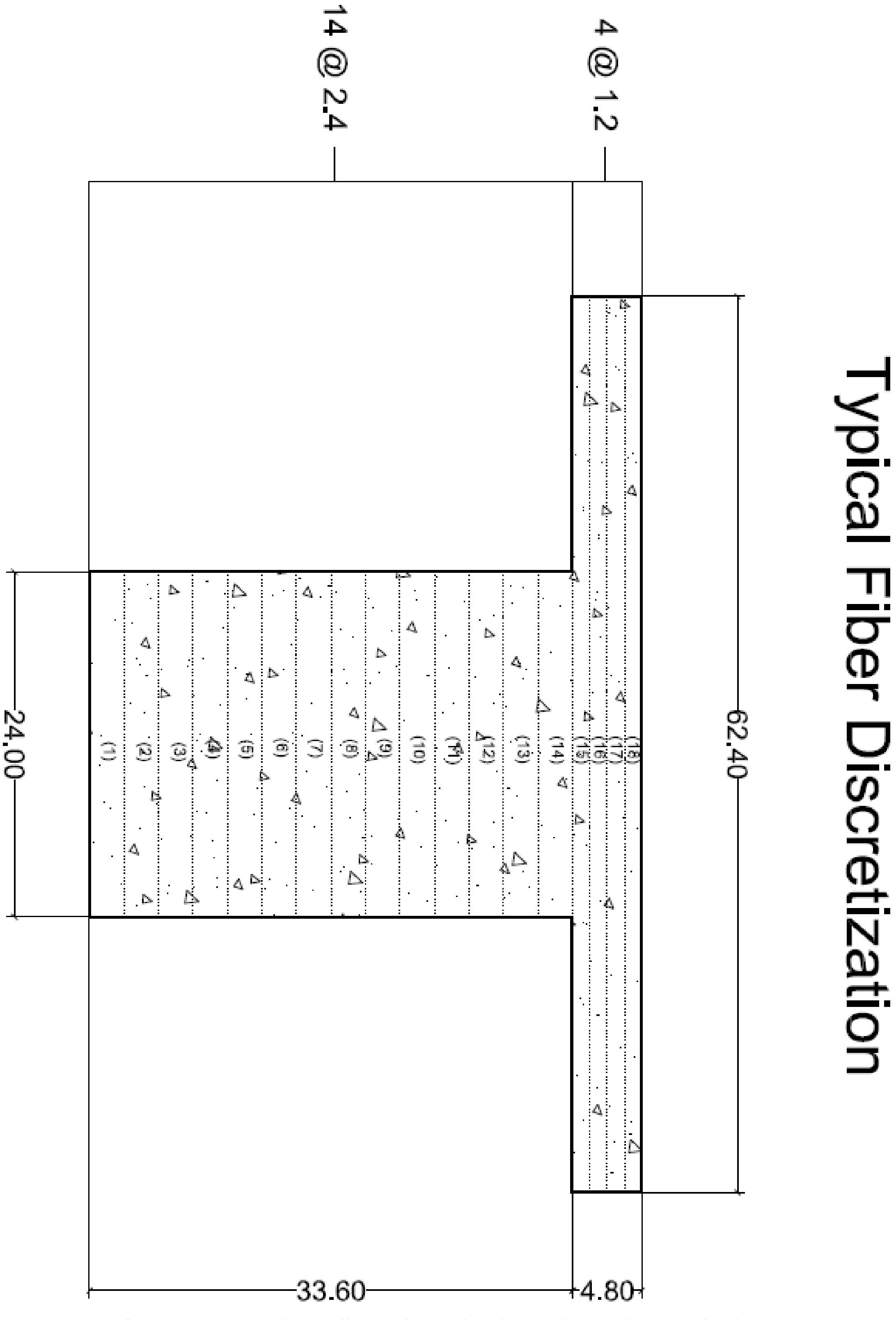

Figure A.6: Typical Fiber Discretization. Dimensions in inches.

A.2. Cross sections description

A.2.1. Cross sections descriptions for Specimen 1

Six different cross sections can be found in **Specimen 1** (in order of appearance from fixed end to loaded end):

- Section 1 (Figure A.7) extends for the first $9.6\ [inches]$ and is related to Element (1) (from this point, Elements refer to Figure A.1).
- Section 2 (Figure A.8) extends in the range $9.6'' < L < 57.6''$ and is related to Elements (2) to (6).
- Section 5 (Figure A.9) extends in the range $57.6'' < L < 76.8''$ (exactly the first half of the opening) and is related to Elements (7) and (8). It may be noted that Section 5 corresponds to Section 2 but with the emergence of the opening.
- Section 3 (Figure A.10) is located between $L = 76.8''$ and $L = 86.4''$ and is related to Element (9) alone.
- Section 6 (Figure A.11) completes the opening ($86.4'' < L < 96.0''$) and is related to Element (10).
- The last one, Section 4 (Figure A.12) is found for the remainder of the length ($96.0'' < L < 134.0''$) and is related to Elements (11) to (14), with the exception of Element (14), which is modeled without flanges, because the presence of the load application system interferes with them in the built specimens that are modeled.

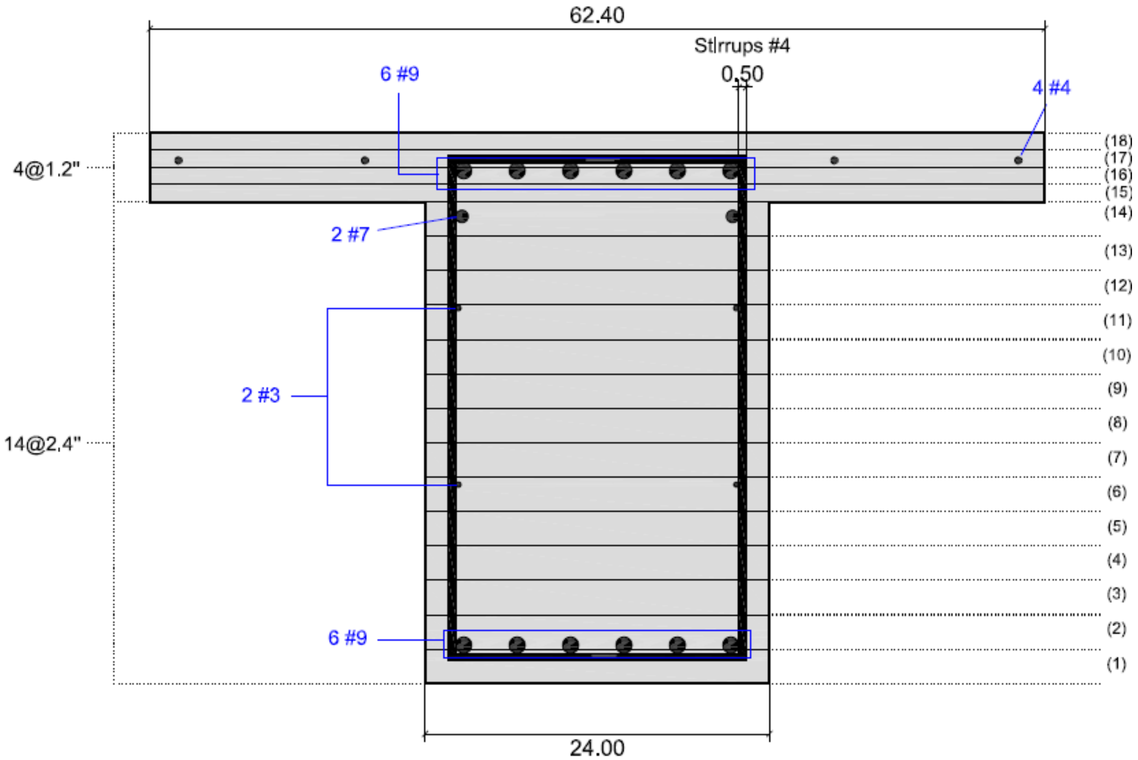

Figure A.7: Cross section 1 for Specimen 1. Dimensions in inches.

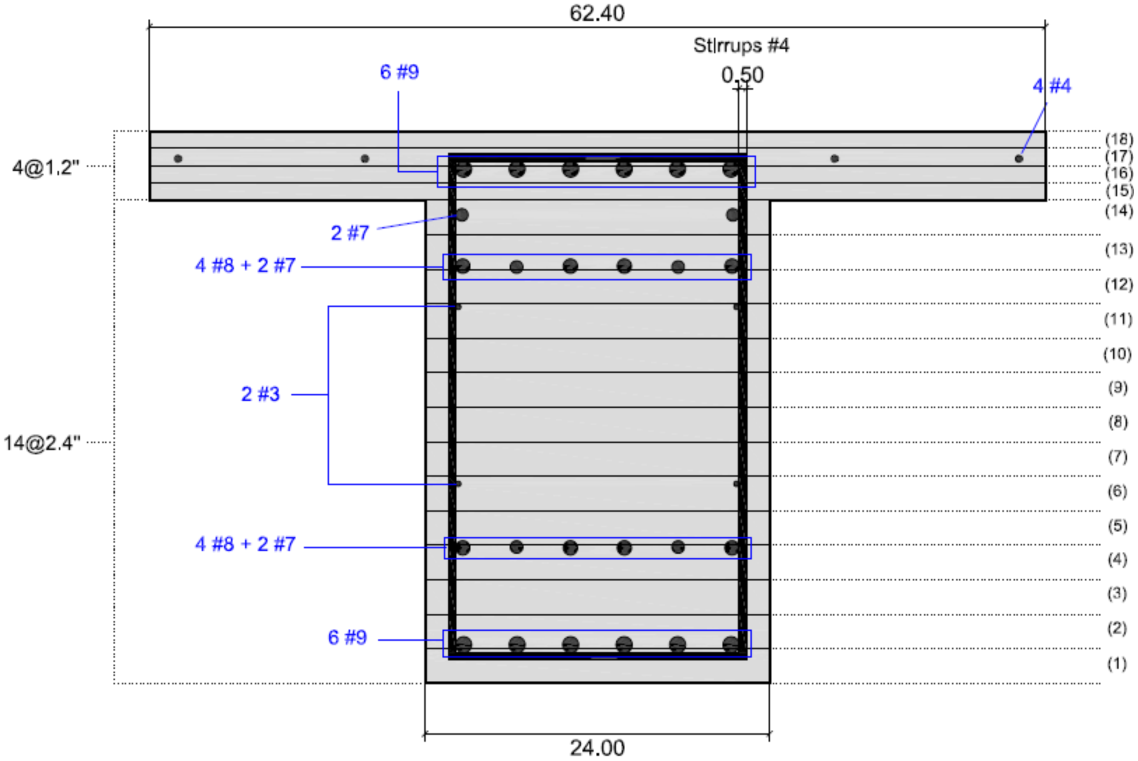

Figure A.8: Cross section 2 for Specimen 1. Dimensions in inches.

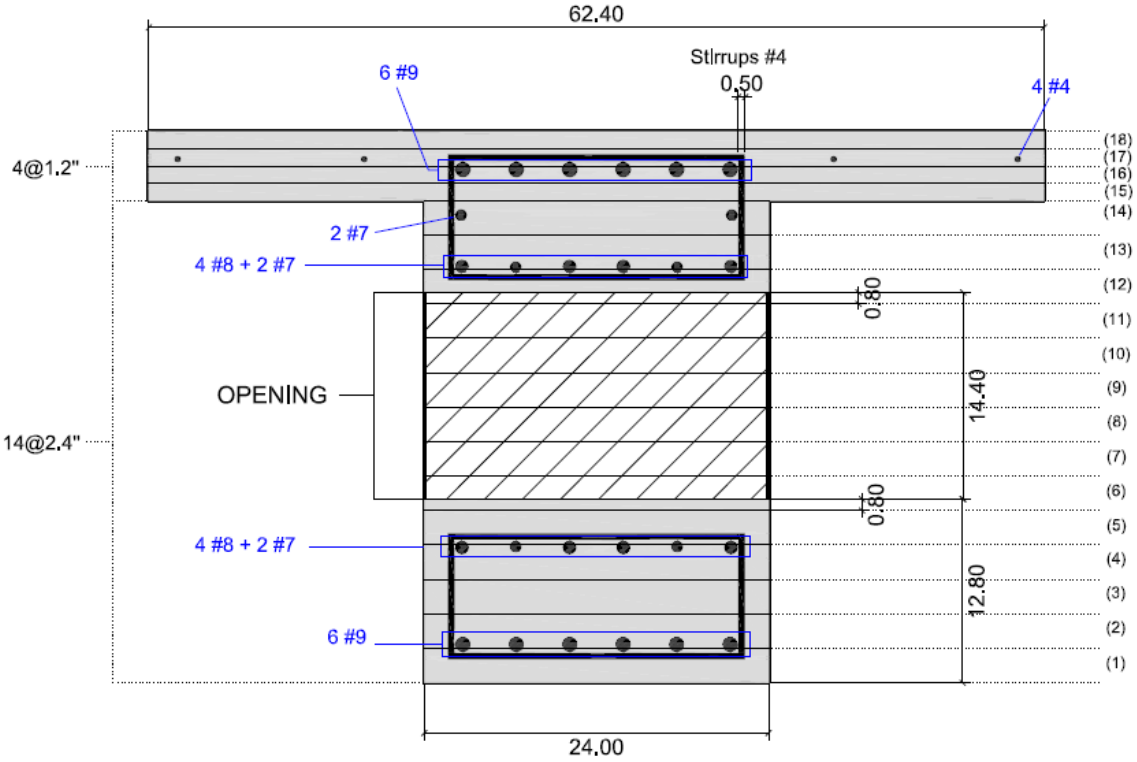

Figure A.9: Cross section 5 for Specimen 1. Dimensions in inches.

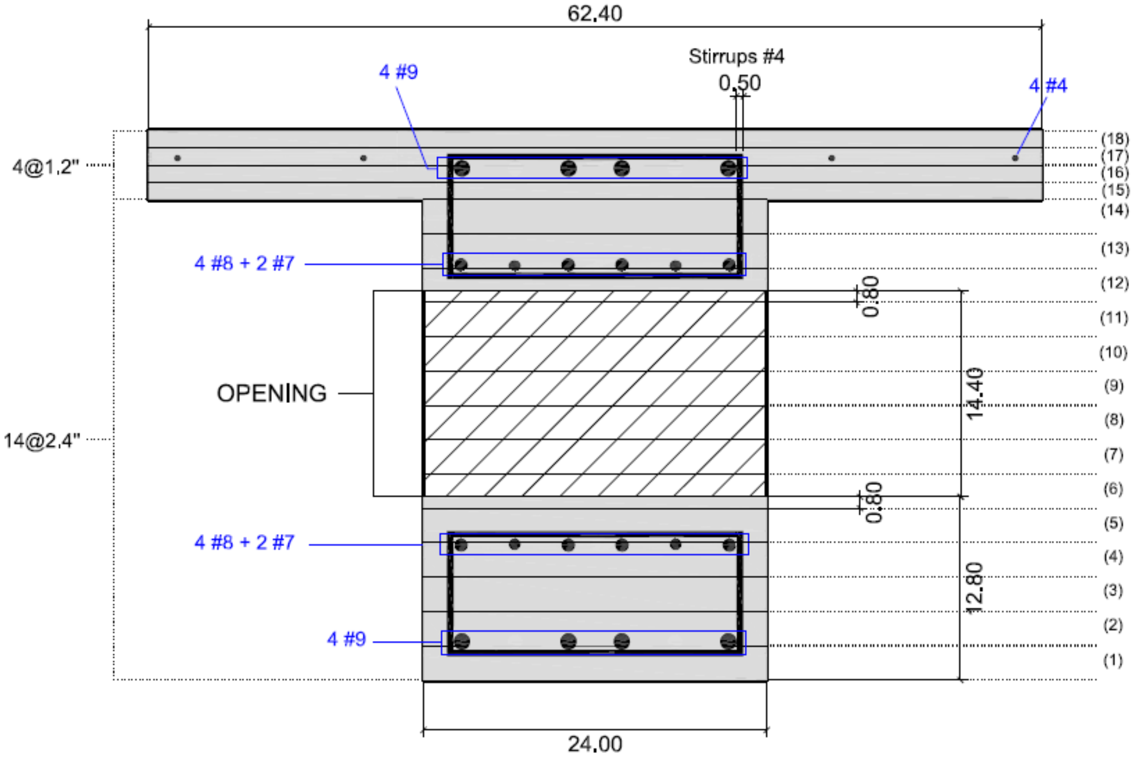

Figure A.10: Cross section 3 for Specimen 1. Dimensions in inches.

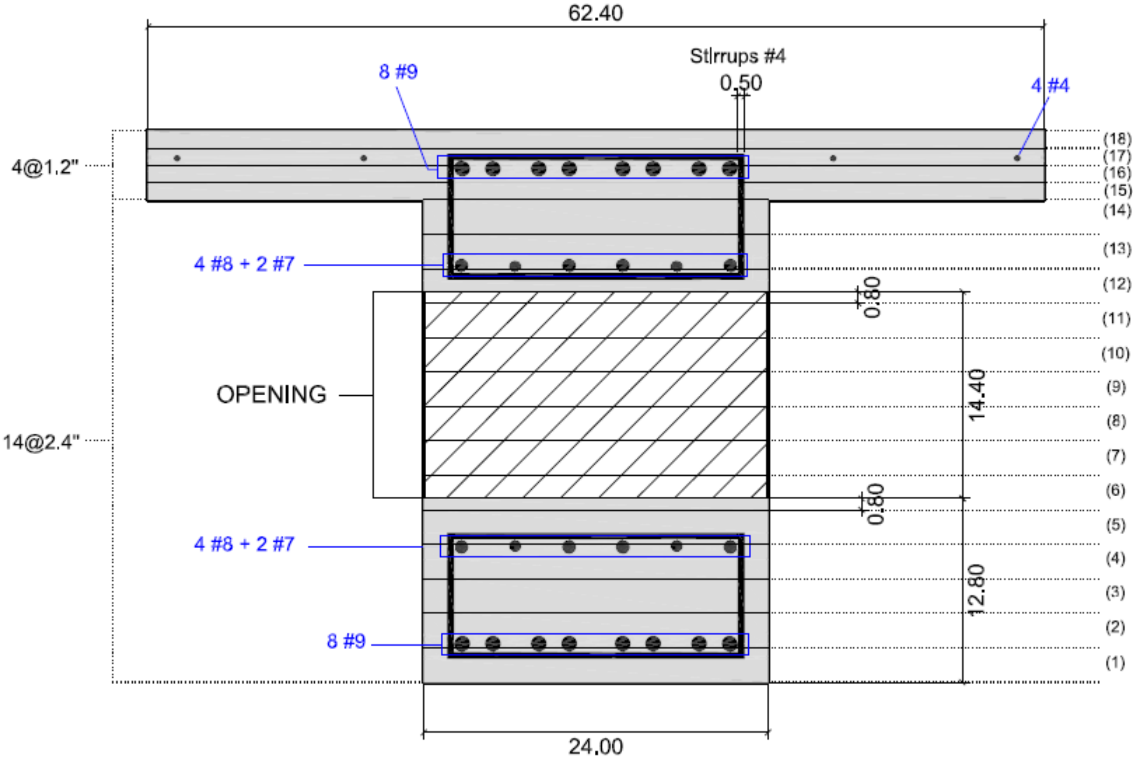

Figure A.11: Cross section 6 for Specimen 1. Dimensions in inches.

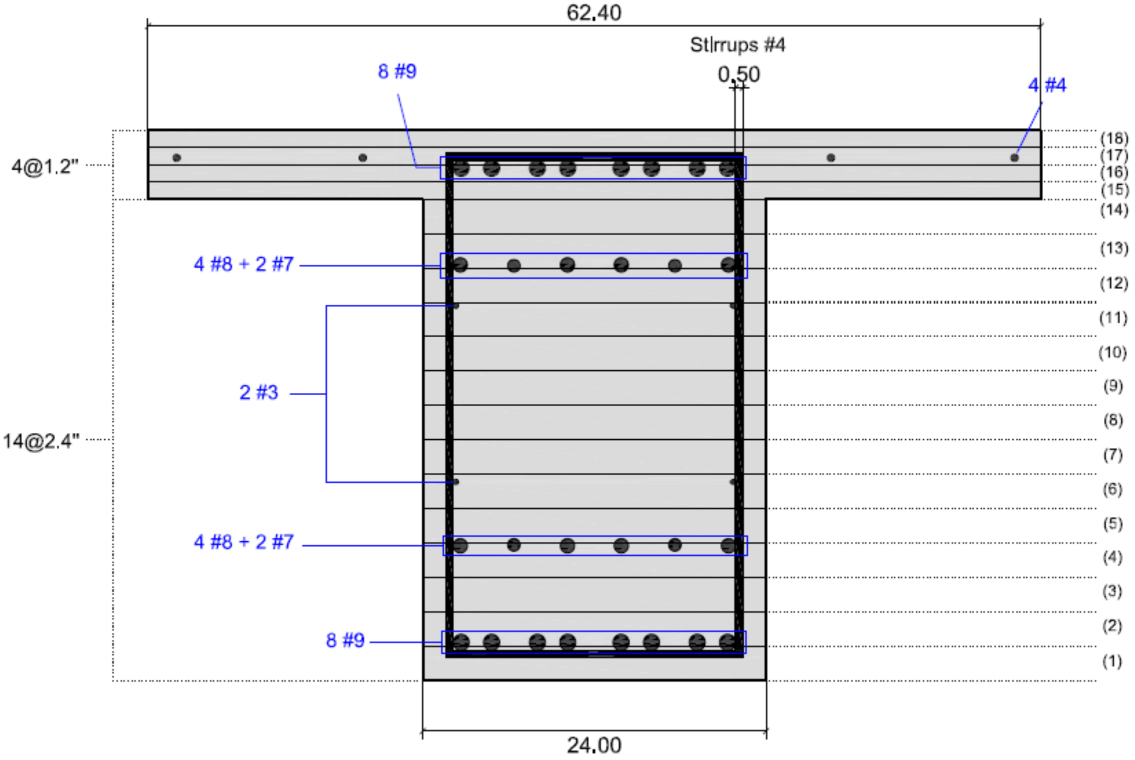

Figure A.12: Cross section 4 for Specimen 1. Dimensions in inches.

Table A.1: Tributary areas for Specimen 1.

Fiber #	Section 1			Section 2			Section 5			Section 3			Section 6			Section 4		
	Area [in^2]			Area [in^2]			Area [in^2]			Area [in^2]			Area [in^2]			Area [in^2]		
	Unconfined	Confined	Steel	Unconfined	Confined	Steel	Unconfined	Confined	Steel	Unconfined	Confined	Steel	Unconfined	Confined	Steel	Unconfined	Confined	Steel
Fiber 1	46.96875	9.50165	1.1296	46.96875	9.50165	1.13	46.96875	9.50165	1.13	46.96875	9.87815	0.7531	46.96875	9.12515	1.506	46.96875	9.12515	1.506
Fiber 2	9	43.7655	4.8345	9	43.7655	4.835	9	43.7655	4.835	9	45.377	3.223	9	42.154	6.446	9	42.154	6.446
Fiber 3	9	48.6	0	9	48.6	0	9	48.6	0	9	48.6	0	9	48.6	0	9	48.6	0
Fiber 4	9	48.6	0	9	45.5478	3.052	9	45.5478	3.052	9	45.5478	3.0522	9	45.5478	3.052	9	45.5478	3.052
Fiber 5	9	48.6	0	9	47.308	1.292	28.2	47.308	1.292	9	47.308	1.292	28.2	47.308	1.292	9	47.308	1.292
Fiber 6	9	48.3791	0.2209	9	48.3791	0.221	0	0	0	9	48.3791	0.2209	0	0	0	9	48.3791	0.221
Fiber 7	9	48.6	0	9	48.6	0	0	0	0	9	48.6	0	0	0	0	9	48.6	0
Fiber 8	9	48.6	0	9	48.6	0	0	0	0	9	48.6	0	0	0	0	9	48.6	0
Fiber 9	9	48.6	0	9	48.6	0	0	0	0	9	48.6	0	0	0	0	9	48.6	0
Fiber 10	9	48.6	0	9	48.6	0	0	0	0	9	48.6	0	0	0	0	9	48.6	0
Fiber 11	9	48.3791	0.2209	9	48.3791	0.221	0	0	0	9	48.3791	0.2209	0	0	0	9	48.3791	0.221
Fiber 12	9	48.6	0	9	47.5088	1.091	9	28.3088	1.091	9	47.5088	1.0912	9	28.3088	1.091	9	47.5088	1.091
Fiber 13	9	48.6	0	9	45.347	3.253	9	45.347	3.253	9	45.347	3.253	9	45.347	3.253	9	45.347	3.253
Fiber 14	9	47.3974	1.2026	9	47.3974	1.203	9	47.3974	1.203	9	48.6	0	9	48.6	0	9	48.6	0
Fiber 15	50.58	24.3	0	50.58	24.3	0	50.58	24.3	0	50.58	24.3	0	50.58	24.3	0	50.58	24.3	0
Fiber 16	50.58	19.7638	4.5362	50.58	19.7638	4.536	50.58	19.7638	4.536	50.58	21.2759	3.0241	50.58	18.2517	6.048	50.58	18.2517	6.048
Fiber 17	62.4509	10.2158	2.2133	62.4509	10.2158	2.213	62.4509	10.2158	2.213	62.4509	10.6917	1.7374	62.4509	9.7398	2.689	62.4509	9.7398	2.689
Fiber 18	74.88	0	0	74.88	0	0	74.88	0	0	74.88	0	0	74.88	0	0	74.88	0	0

A.2.2. Cross sections descriptions for Specimen 2

Specimen 2 has five different cross sections through its length (same order used as when presenting the sections for Specimen 1):

- Section 1 (Figure A.13) extends for the first $12.8\ [inches]$ and is related to Element (1) (as seen on Figure A.2 for all Elements from this point and on).
- Section 2 (Figure A.14) is located in the range $12.8'' < L < 71.9''$ and is related to Elements (2) to (6).
- Section 5 (Figure A.15) extends between $L = 71.9''$ and $L = 81.6''$. It is related to Elements (7) and (8).
- Section 3 (Figure A.16) is found in the range $81.6'' < L < 110.4''$ and is related to Elements (9) and (10).
- Finally, Section 4 (Figure A.17) extends for the remaining of the specimen ($110.4'' < L < 149.0''$), forming the Elements (11) to (13). As with S1, the last Element is modeled without flanges.

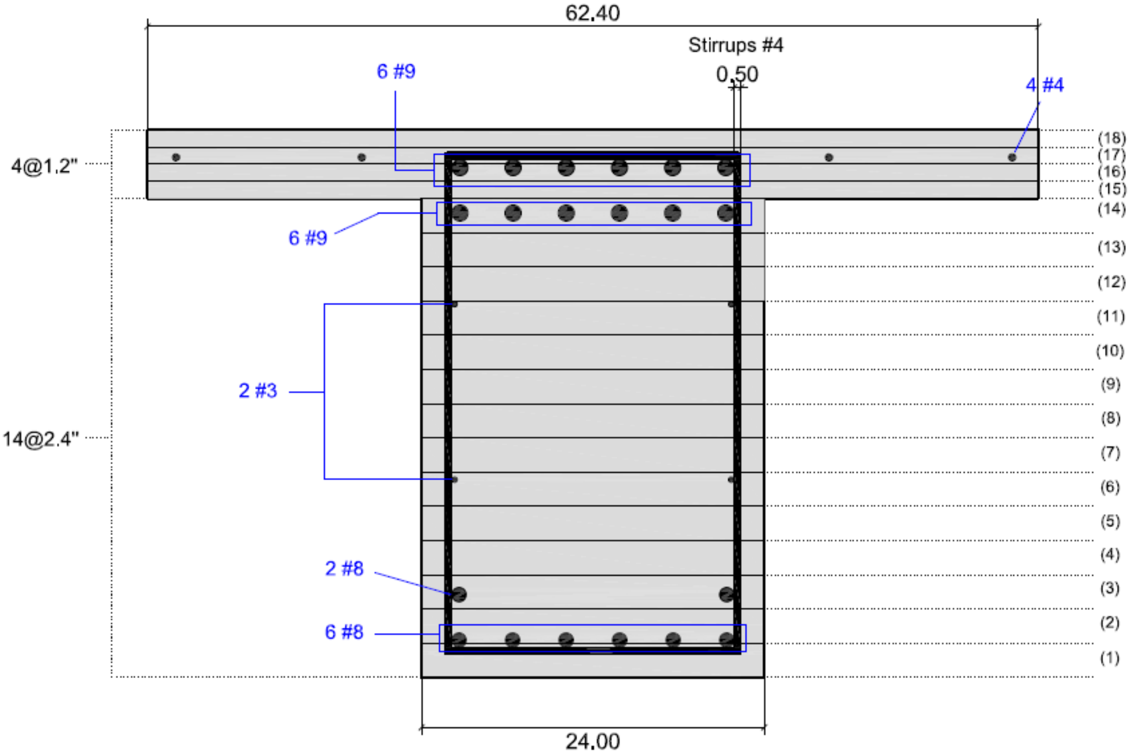

Figure A.13: Cross section 1 for Specimen 2. Dimensions in inches.

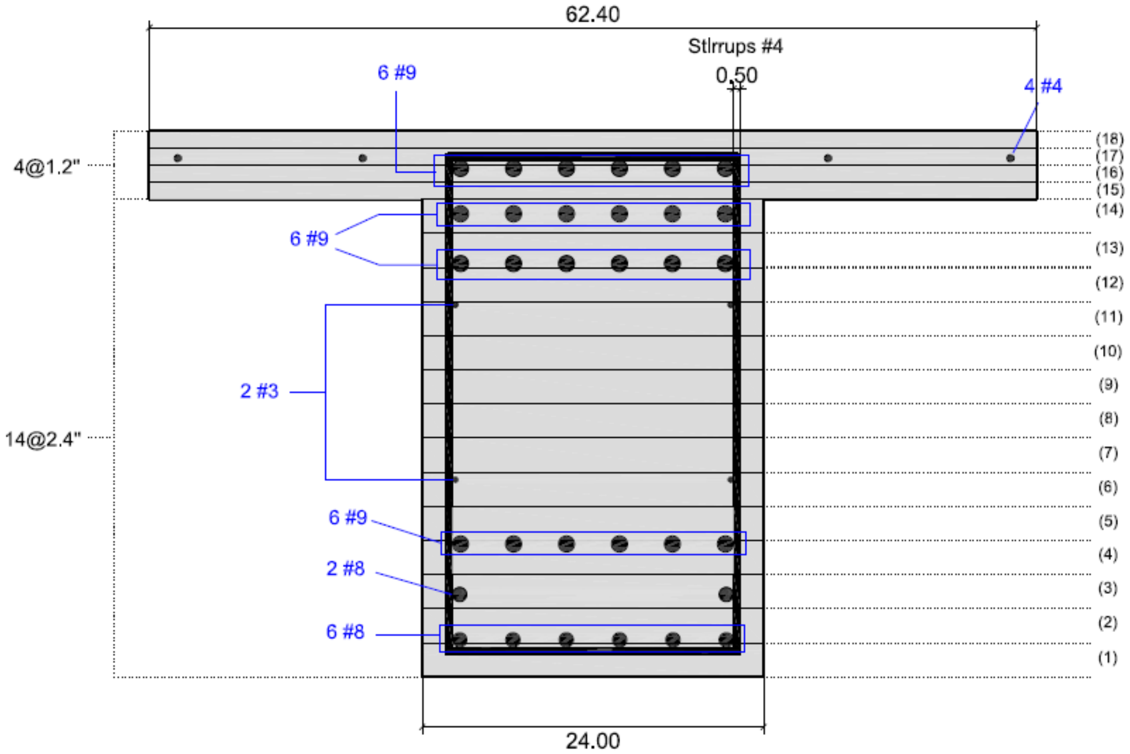

Figure A.14: Cross section 2 for Specimen 2. Dimensions in inches.

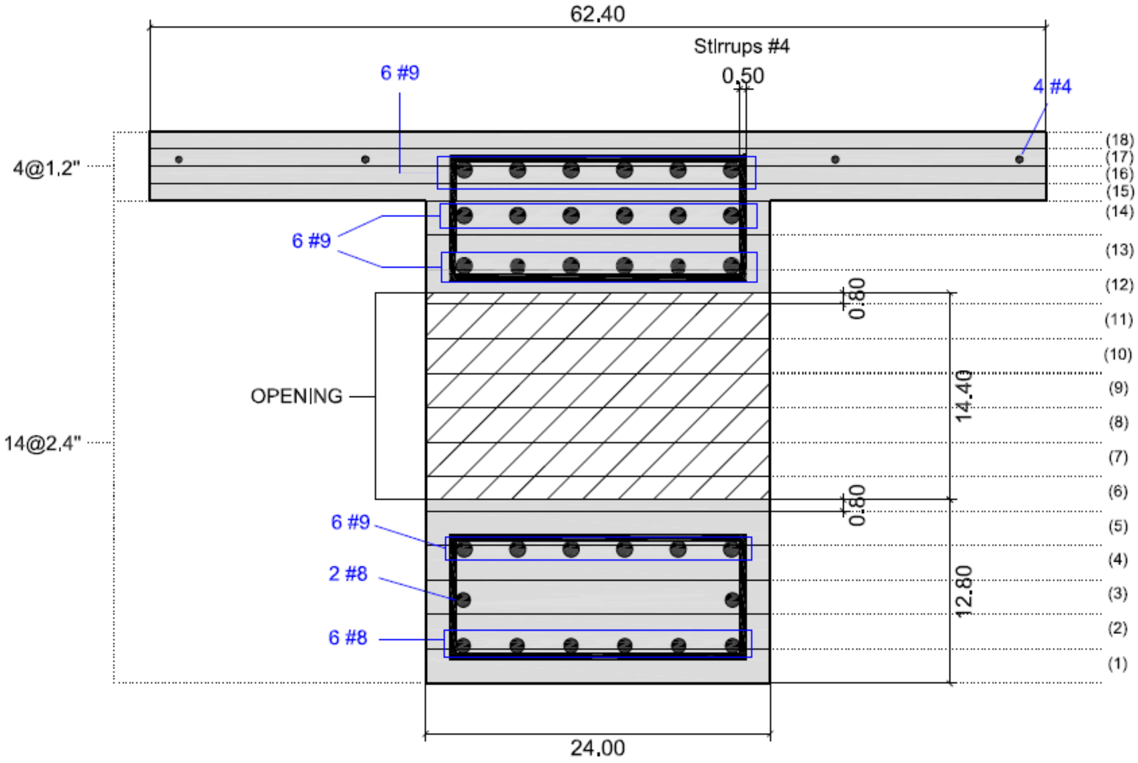

Figure A.15: Cross section 5 for Specimen 2. Dimensions in inches.

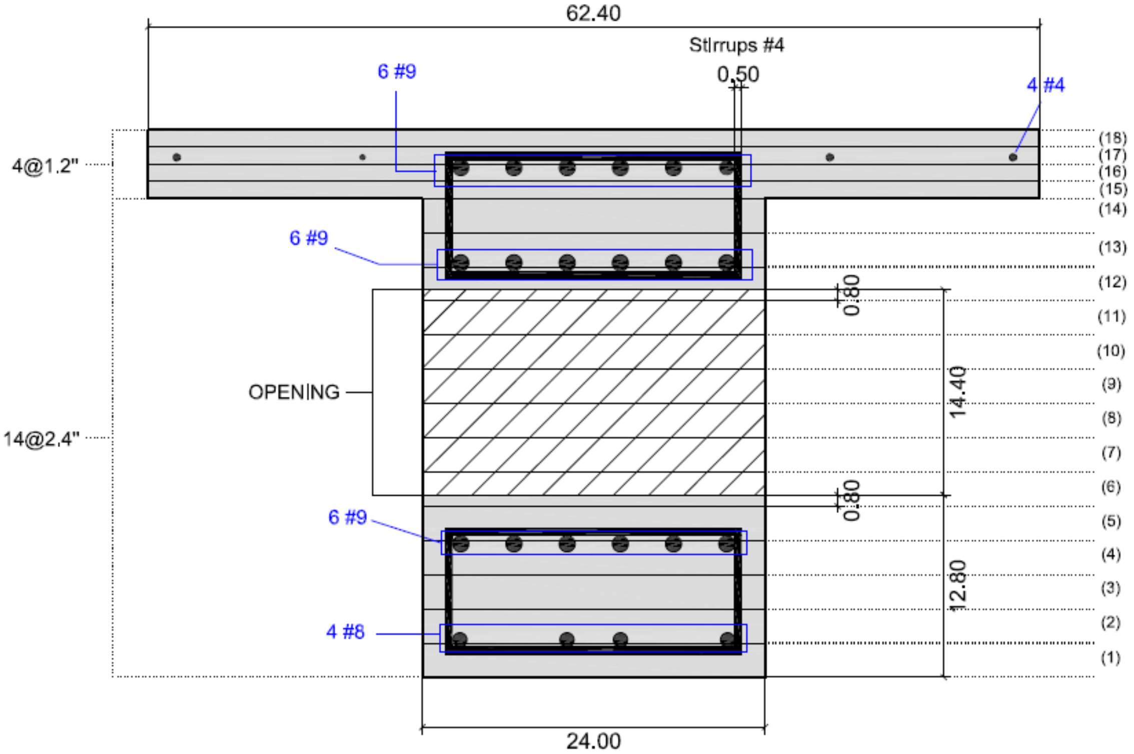

Figure A.16: Cross section 3 for Specimen 2. Dimensions in inches.

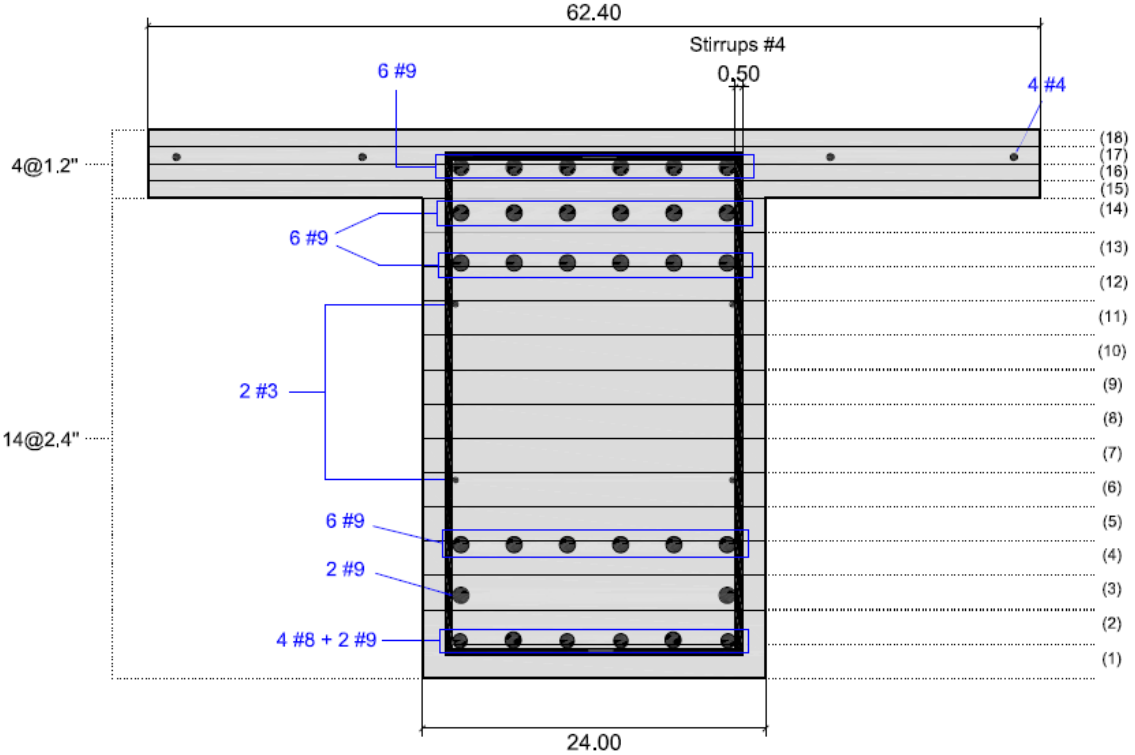

Figure A.17: Cross section 4 for Specimen 2. Dimensions in inches.

Table A.2: Tributary areas for Specimen 2.

Fiber #	Section 1			Section 2			Section 5			Section 3			Section 4		
	Area [in2]			Area [in2]			Area [in2]			Area [in2]			Area [in2]		
	Unconfined	Confined	Steel	Unconfined	Confined	Steel	Unconfined	Confined	Steel	Unconfined	Confined	Steel	Unconfined	Confined	Steel
Fiber 1	46.96875	9.57795	1.0533	46.96875	9.57795	1.0533	46.96875	9.57795	1.0533	46.96875	9.92905	0.702	46.96875	9.55255	1.0787
Fiber 2	9	44.9409	3.6591	9	44.9409	3.6591	9	44.9409	3.6591	9	46.1606	2.439	9	44.5491	4.0509
Fiber 3	9	47.0292	1.5708	9	47.0292	1.5708	9	47.0292	1.5708	9	48.6	0	9	46.612	1.988
Fiber 4	9	48.6	0	9	44.0638	4.5362	9	44.0638	4.5362	9	44.0638	4.536	9	44.0638	4.5362
Fiber 5	9	48.6	0	9	47.1721	1.4279	28.2	47.1721	1.4279	9	47.1721	1.428	9	47.1721	1.4279
Fiber 6	9	48.3791	0.2209	9	48.3791	0.2209	0	0	0	9	48.3791	0.221	9	48.3791	0.2209
Fiber 7	9	48.6	0	9	48.6	0	0	0	0	9	48.6	0	9	48.6	0
Fiber 8	9	48.6	0	9	48.6	0	0	0	0	9	48.6	0	9	48.6	0
Fiber 9	9	48.6	0	9	48.6	0	0	0	0	9	48.6	0	9	48.6	0
Fiber 10	9	48.6	0	9	48.6	0	0	0	0	9	48.6	0	9	48.6	0
Fiber 11	9	48.3791	0.2209	9	48.3791	0.2209	0	0	0	9	48.3791	0.221	9	48.3791	0.2209
Fiber 12	9	48.6	0	9	47.3973	1.2027	9	28.1973	1.2027	9	47.3973	1.203	9	47.3973	1.2027
Fiber 13	9	48.6	0	9	43.8385	4.7615	9	43.8385	4.7615	9	43.8385	4.762	9	43.8385	4.7615
Fiber 14	9	42.6359	5.9641	9	42.6359	5.9641	9	42.6359	5.9641	9	48.6	0	9	42.6359	5.9641
Fiber 15	50.58	24.3	0	50.58	24.3	0	50.58	24.3	0	50.58	24.3	0	50.58	24.3	0
Fiber 16	50.58	19.7638	4.5362	50.58	19.7638	4.5362	50.58	19.7638	4.5362	50.58	19.7638	4.536	50.58	19.7638	4.5362
Fiber 17	62.4509	10.2158	2.2133	62.4509	10.2158	2.2133	62.4509	10.2158	2.2133	62.4509	10.2158	2.213	62.4509	10.2158	2.2133
Fiber 18	74.88	0	0	74.88	0	0	74.88	0	0	74.88	0	0	74.88	0	0

A.2.3. Cross sections descriptions for Specimen 6

As with Specimen 2, **Specimen 6** is formed by five different cross sections along its length (presented following the same order rule previously used: from fixed end to loaded end):

- Section 1 (Figure A.18) extends for the first $28.8\ [inches]$ and is related to Elements (1) and (2) (Elements refer to Figure A.3 for this part).
- Section 2 (Figure A.19) is found in the range $28.8'' < L < 67.2''$. It is related to Elements (3), (4) and (5).
- Section 5 (Figure A.20) rules the entire length of the opening, from $L = 67.2''$ to $L = 105.6''$, and is related to Elements (6), (7) and (8).
- Section 3 (Figure A.21) is located in the range $105.6'' < L < 144.0''$. Elements (9), (10) and (11) conform this interval.
- Section 4 (Figure A.22) extends for the remaining of the specimen ($144.0'' < L < 185.6''$), relating to Elements (12), (13) and (14) (No flanges for the last Element).

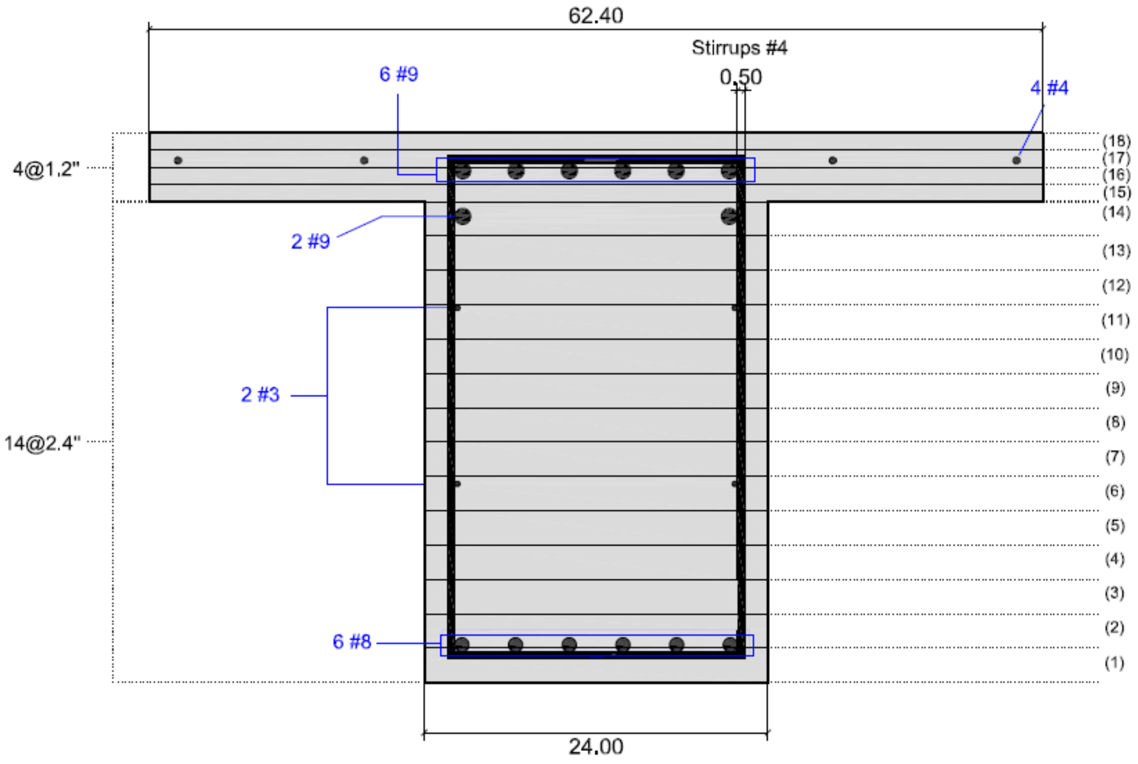

Figure A.18: Cross section 1 for Specimen 6. Dimensions in inches.

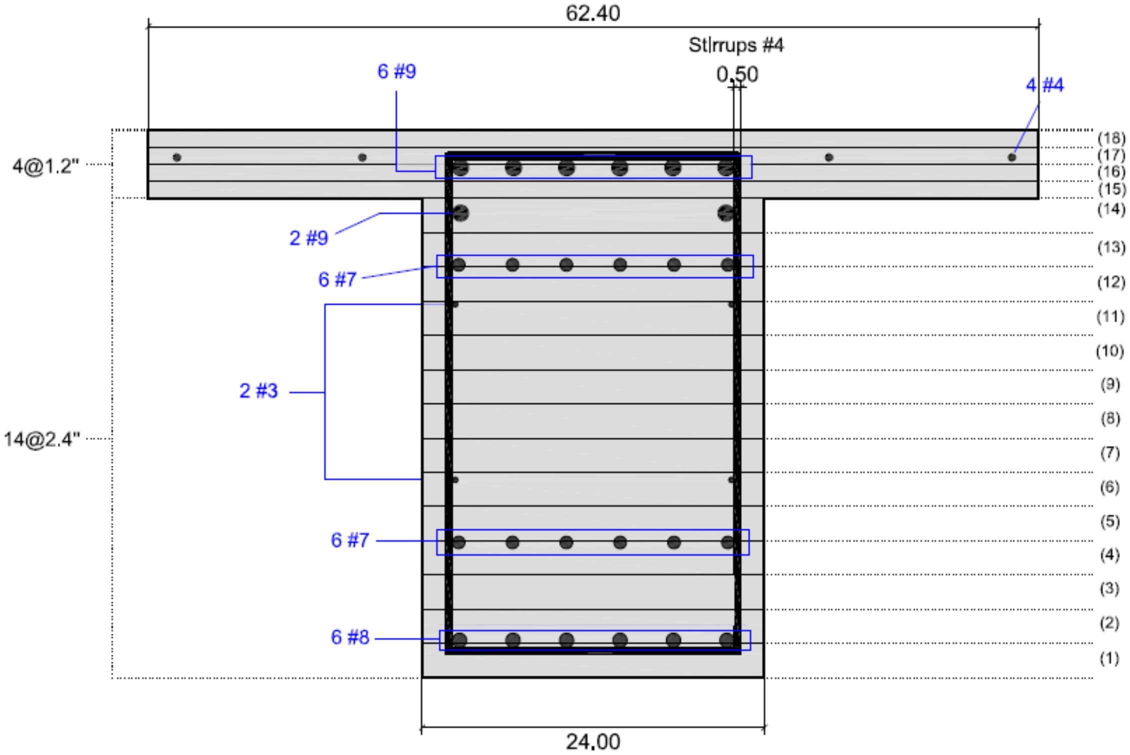

Figure A.19: Cross section 2 for Specimen 6. Dimensions in inches.

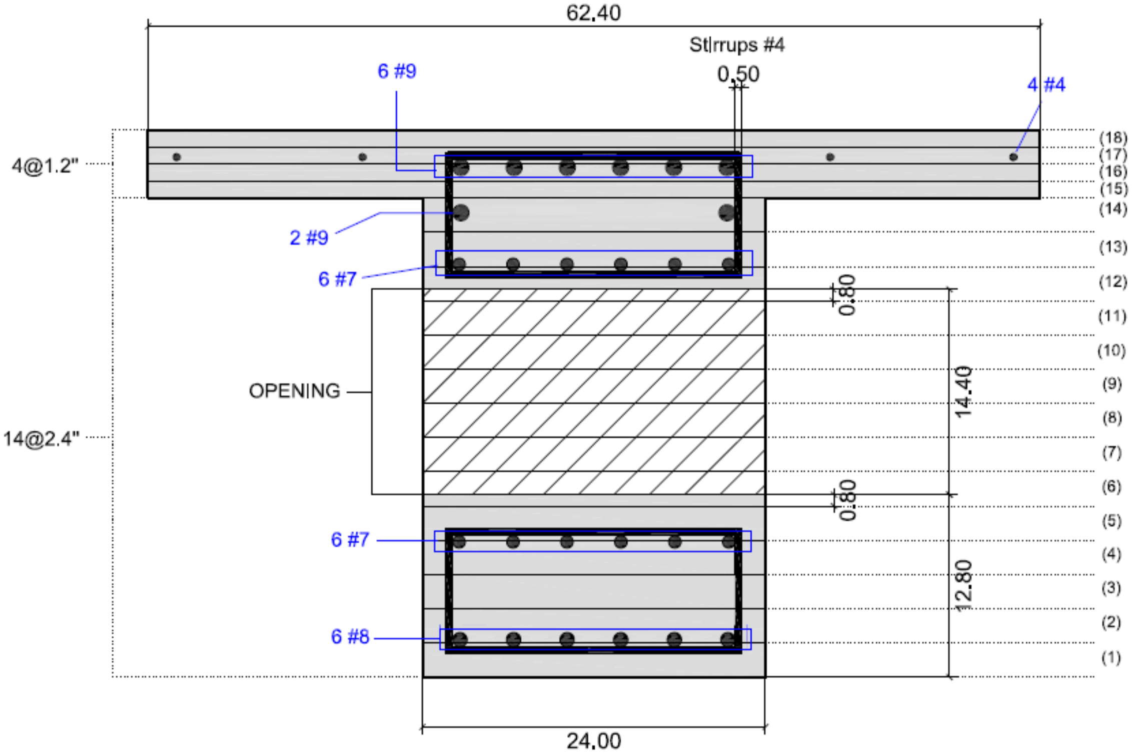

Figure A.20: Cross section 5 for Specimen 6. Dimensions in inches.

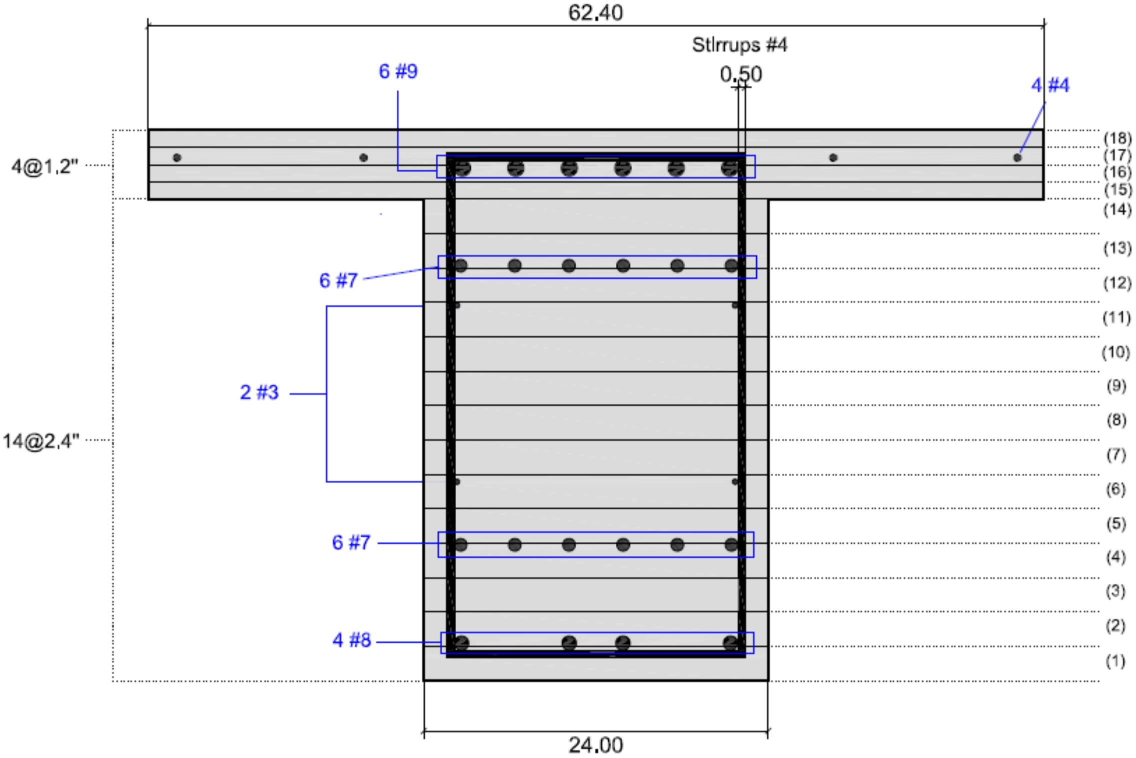

Figure A.21: Cross section 3 for Specimen 6. Dimensions in inches.

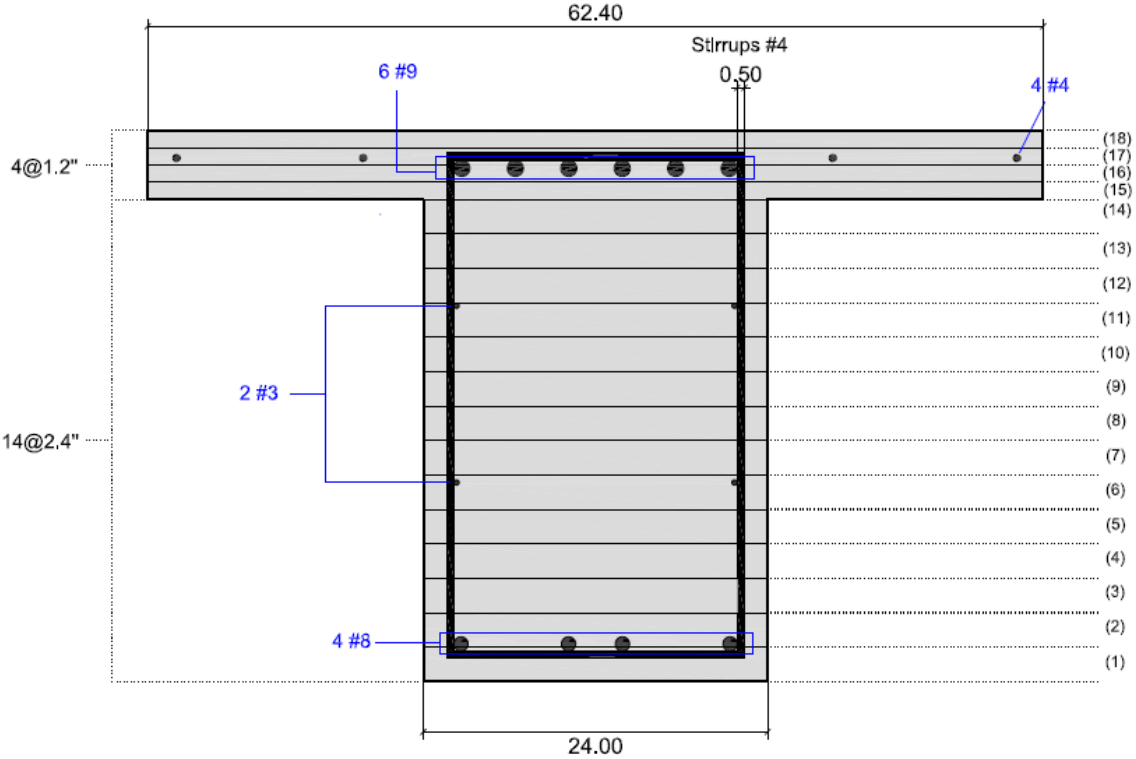

Figure A.22: Cross section 4 for Specimen 6. Dimensions in inches.

Table A.3: Tributary areas for Specimen 6.

Fiber #	Section 1			Section 2			Section 5			Section 3			Section 4		
	Area [in^2]			Area [in^2]			Area [in^2]			Area [in^2]			Area [in^2]		
	Unconfined	Confined	Steel	Unconfined	Confined	Steel	Unconfined	Confined	Steel	Unconfined	Confined	Steel	Unconfined	Confined	Steel
Fiber 1	46.96875	9.57795	1.0533	46.96875	9.57795	1.0533	46.96875	9.57795	1.0533	46.96875	9.92905	0.7022	46.96875	9.92905	0.7022
Fiber 2	9	44.9409	3.6591	9	44.9409	3.6591	9	44.9409	3.6591	9	46.1606	2.4394	9	46.1606	2.4394
Fiber 3	9	48.6	0	9	48.6	0	9	48.6	0	9	48.6	0	9	48.6	0
Fiber 4	9	48.6	0	9	46.212	2.388	9	46.212	2.388	9	46.212	2.388	9	48.6	0
Fiber 5	9	48.6	0	9	47.3801	1.2199	28.2	47.3801	1.2199	9	47.3801	1.2199	9	48.6	0
Fiber 6	9	48.3791	0.2209	9	48.3791	0.2209	0	0	0	9	48.3791	0.2209	9	48.3791	0.2209
Fiber 7	9	48.6	0	9	48.6	0	0	0	0	9	48.6	0	9	48.6	0
Fiber 8	9	48.6	0	9	48.6	0	0	0	0	9	48.6	0	9	48.6	0
Fiber 9	9	48.6	0	9	48.6	0	0	0	0	9	48.6	0	9	48.6	0
Fiber 10	9	48.6	0	9	48.6	0	0	0	0	9	48.6	0	9	48.6	0
Fiber 11	9	48.3791	0.2209	9	48.3791	0.2209	0	0	0	9	48.3791	0.2209	9	48.3791	0.2209
Fiber 12	9	48.6	0	9	46.0243	2.5757	9	26.8243	2.5757	9	46.0243	2.5757	9	48.6	0
Fiber 13	9	48.6	0	9	47.5678	1.0322	9	47.5678	1.0322	9	47.5678	1.0322	9	48.6	0
Fiber 14	9	47.3974	1.2026	9	47.3974	1.2026	9	47.3974	1.2026	9	48.6	0	9	48.6	0
Fiber 15	50.58	24.3	0	50.58	24.3	0	50.58	24.3	0	50.58	24.3	0	50.58	24.3	0
Fiber 16	50.58	19.7638	4.5362	50.58	19.7638	4.5362	50.58	19.7638	4.5362	50.58	19.7638	4.5362	50.58	19.7638	4.5362
Fiber 17	62.4509	10.2158	2.2133	62.4509	10.2158	2.2133	62.4509	10.2158	2.2133	62.4509	10.2158	2.2133	62.4509	10.2158	2.2133
Fiber 18	74.88	0	0	74.88	0	0	74.88	0	0	74.88	0	0	74.88	0	0

A.2.4. Cross sections descriptions for Specimen 7

Only two different cross sections can be found in **Specimen 7**:

- Section 1 (Figure A.23) extends for the first $96.0\,[inches]$, and it is related to Elements (1) to (7) (Elements as seen in Figure A.4).
- Section 2 (Figure A.24) completes the length of the specimen ($96.0'' < L < 124.8''$). It is related to Elements (8) and (9) (Elements from Figure A.4), and as described for the other specimens. The last Element is modeled without flanges.

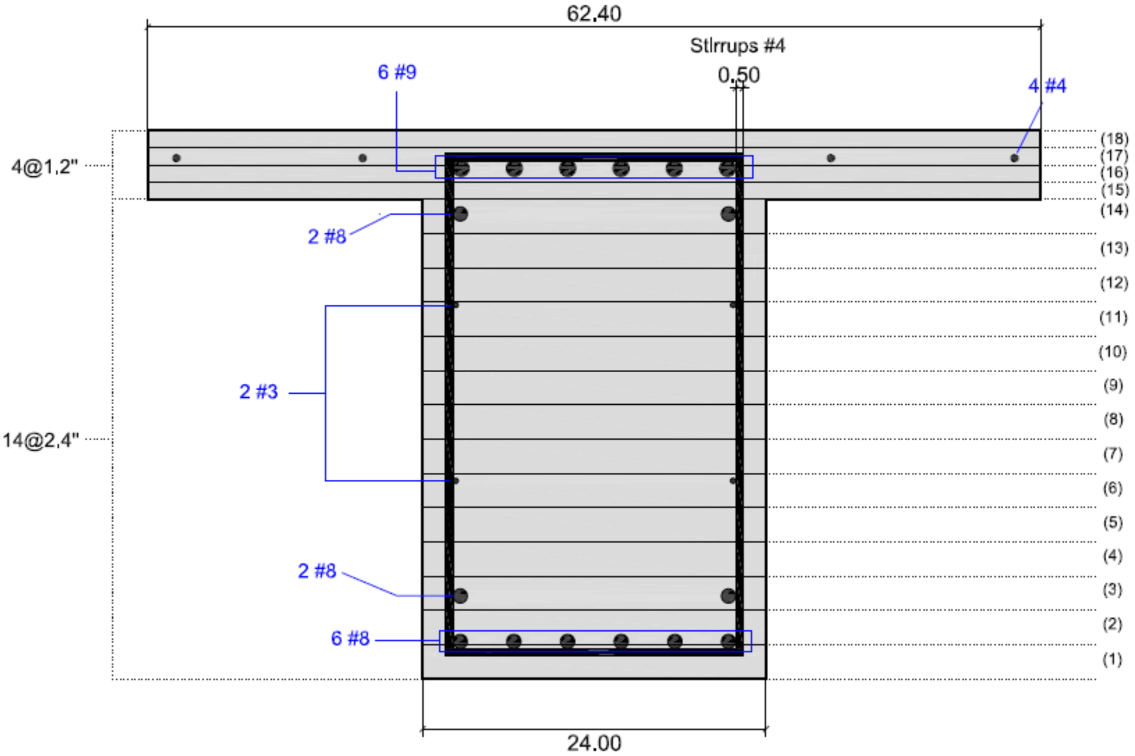

Figure A.23: Cross section 1 for Specimen 7. Dimensions in inches.

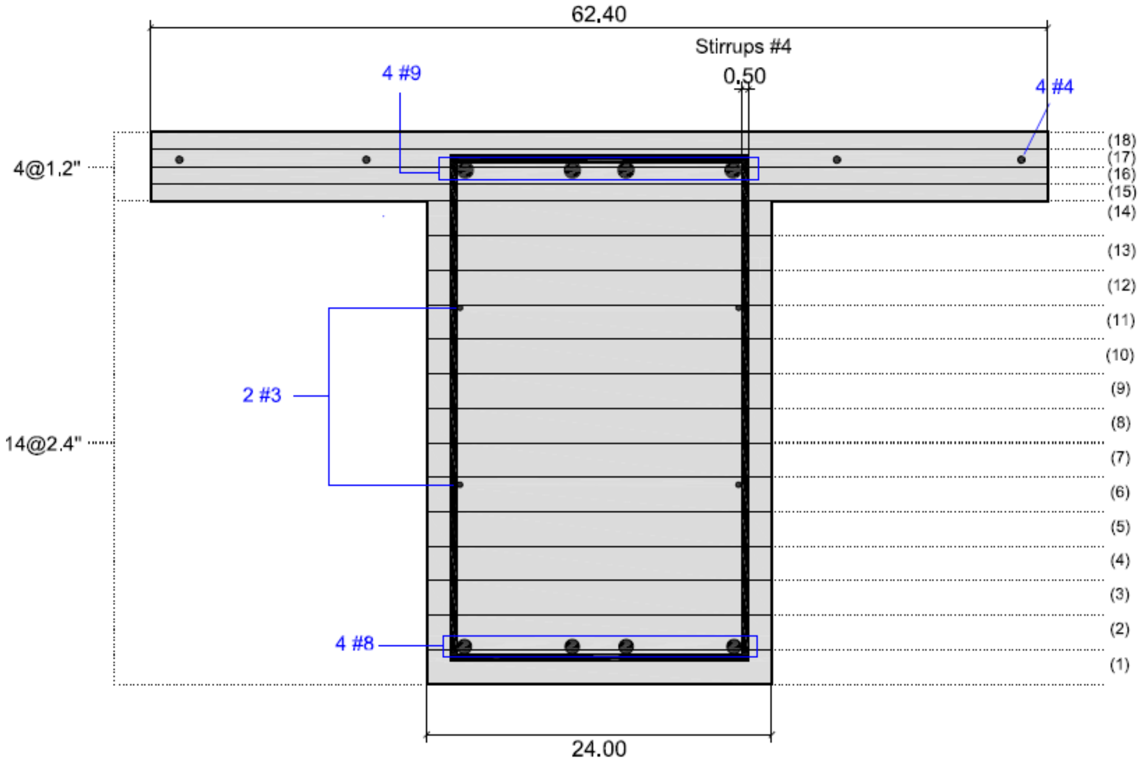

Figure A.24: Cross section 2 for Specimen 7. Dimensions in inches.

Table A.4: Tributary areas for Specimen 7.

Fiber #	Section 1			Section 2		
	Area [in^2]			Area [in^2]		
	Unconfined	Confined	Steel	Unconfined	Confined	Steel
Fiber 1	46,9688	9,5783	1,053	46,9688	9,9293	0,702
Fiber 2	9	44,9406	3,6594	9	46,1604	2,4396
Fiber 3	9	47,0292	1,5708	9	48,6	0
Fiber 4	9	48,6	0	9	48,6	0
Fiber 5	9	48,6	0	9	48,6	0
Fiber 6	9	48,3791	0,2209	9	48,3791	0,2209
Fiber 7	9	48,6	0	9	48,6	0
Fiber 8	9	48,6	0	9	48,6	0
Fiber 9	9	48,6	0	9	48,6	0
Fiber 10	9	48,6	0	9	48,6	0
Fiber 11	9	48,3791	0,2209	9	48,3791	0,2209
Fiber 12	9	48,6	0	9	48,6	0
Fiber 13	9	48,6	0	9	48,6	0
Fiber 14	9	47,0292	1,5708	9	48,6	0
Fiber 15	50,58	24,3	0	50,58	24,3	0
Fiber 16	50,58	19,764	4,536	50,58	21,276	3,024
Fiber 17	62,4509	10,2164	2,2128	62,4509	10,6922	1,737
Fiber 18	74,88	0	0	74,88	0	0

Table A.5: Transverse Reinforcement Assignment.

Specimen 1

Spacing	Range		N° of Stirrups	N° of Elements		Elements involved	Stirrups/Element	Transverse Area/Element [in^2]
	L_1 [in]	L_2 [in]						
4.75"	0	86.3	18	9	(9.6" in Length)	(1) to (9)	2	0.7854
3.25"	86.3	134	16	5	(≈9.6" in Length)	(10) to (14)	3.2	1.2566

Specimen 2

Spacing	Range		N° of Stirrups	N° of Elements		Elements involved	Stirrups/Element	Transverse Area/Element [in^2]
	L_1 [in]	L_2 [in]						
4.75"	0	67.84	15	5	(≈13.568" in Length)	(1) to (5)	3	1.1781
	67.84	71.9	1	1	(4.06" in Length)	(6)	1	0.3927
3.25"	71.9	81.6	-	2	Custom	(7) and (8)	Custom	0.7854
	81.6	149	21	5	(≈13.482" in Length)	(9) to (13)	4.2	1.6493

Specimen 6

Spacing	Range		N° of Stirrups	N° of Elements		Elements involved	Stirrups/Element	Transverse Area/Element [in^2]
	L_1 [in]	L_2 [in]						
4.75"	0	67.2	14	5	(≈13.44" in Length)	(1) to (5)	2.8	1.0996
4.5"	67.2	105.5	8	3	(12.8" in Length)	(6) to (7)	2.67	1.0485
8.75"	105.6	185.6	9	6	(≈13.33" in Length)	(9) to (14)	1.5	0.5891

Specimen 7

Spacing	Range		N° of Stirrups	N° of Elements		Elements involved	Stirrups/Element	Transverse Area/Element [in^2]
	L_1 [in]	L_2 [in]						
4.75"	0	62.4	13.6	4	(16" in Length)	(1) to (4)	3.4	1.3352
	62.4	64	-	1	(1.6" in Length)	(5)	Custom	1.3352
	64	80	-	1	(16" in Length)	(6)	Custom	1.3352
	80	96	2	1	(16" in Length)	(7)	2	0.7854
6.5"	96	124.8	5	2	(14.4" in Length)	(8) and (9)	2.5	0.9817

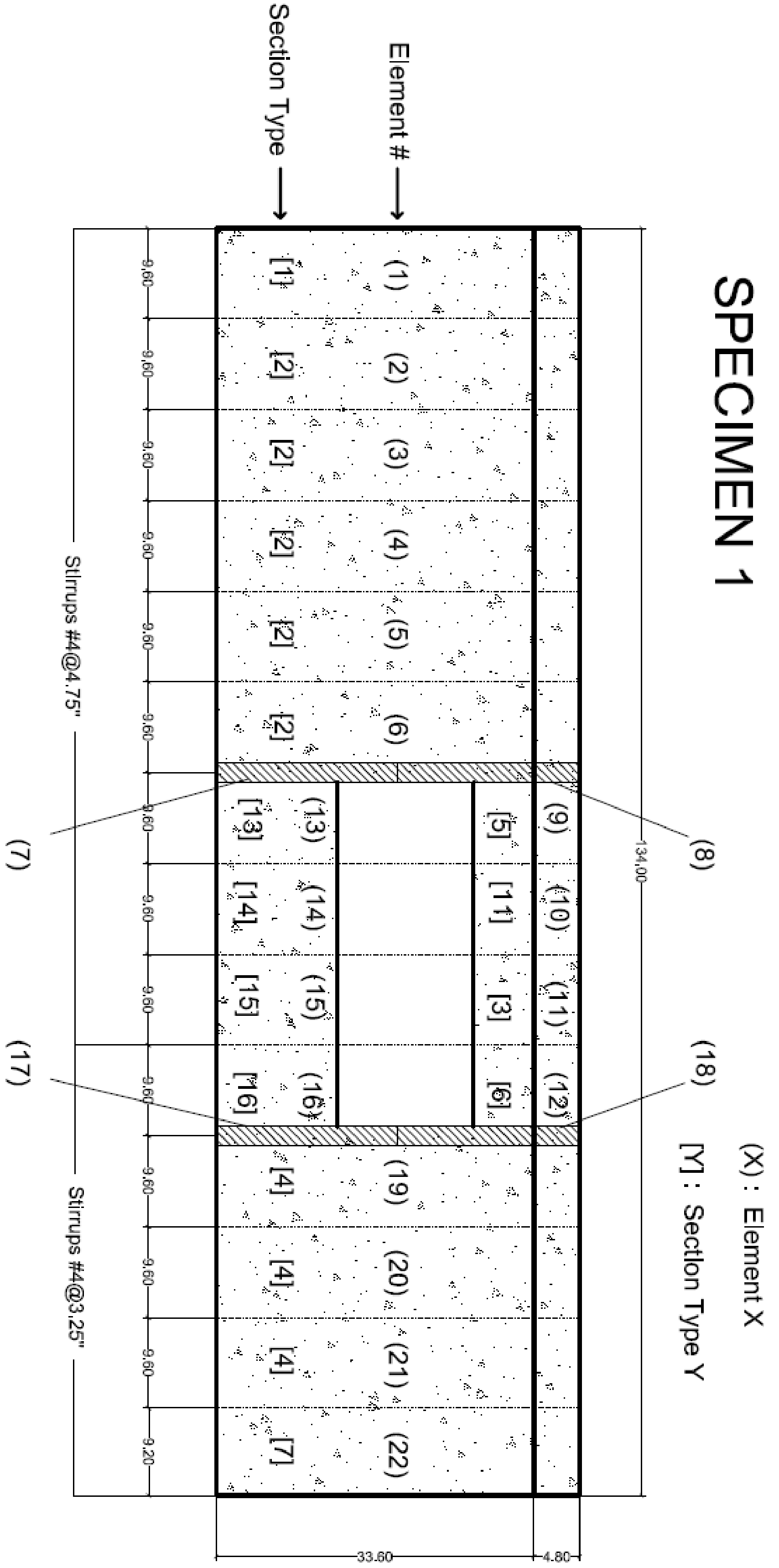

Figure A.25: Specimen 1 with alternative discretization. Dimensions in inches.

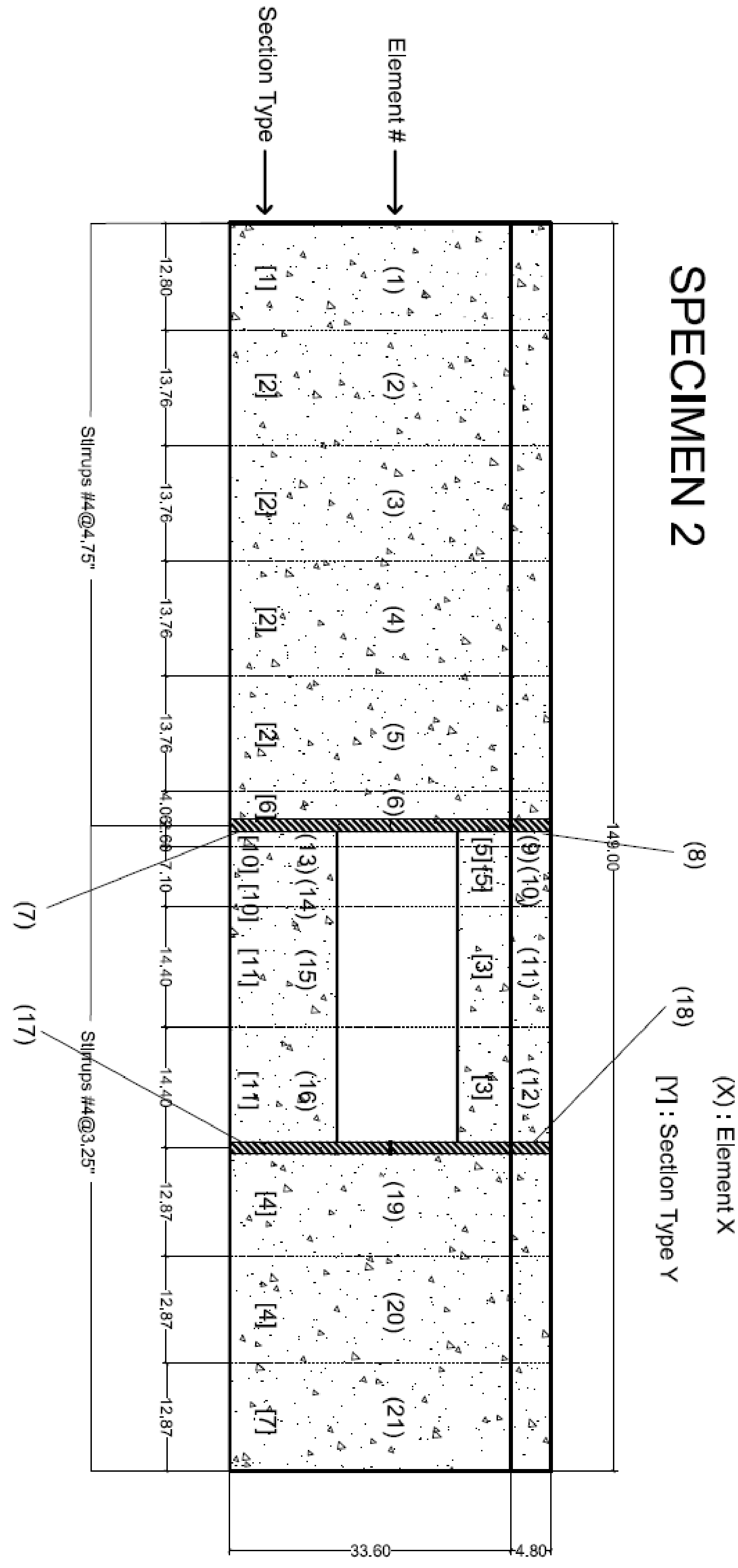

Figure A.26: Specimen 2 with alternative discretization. Dimensions in inches.

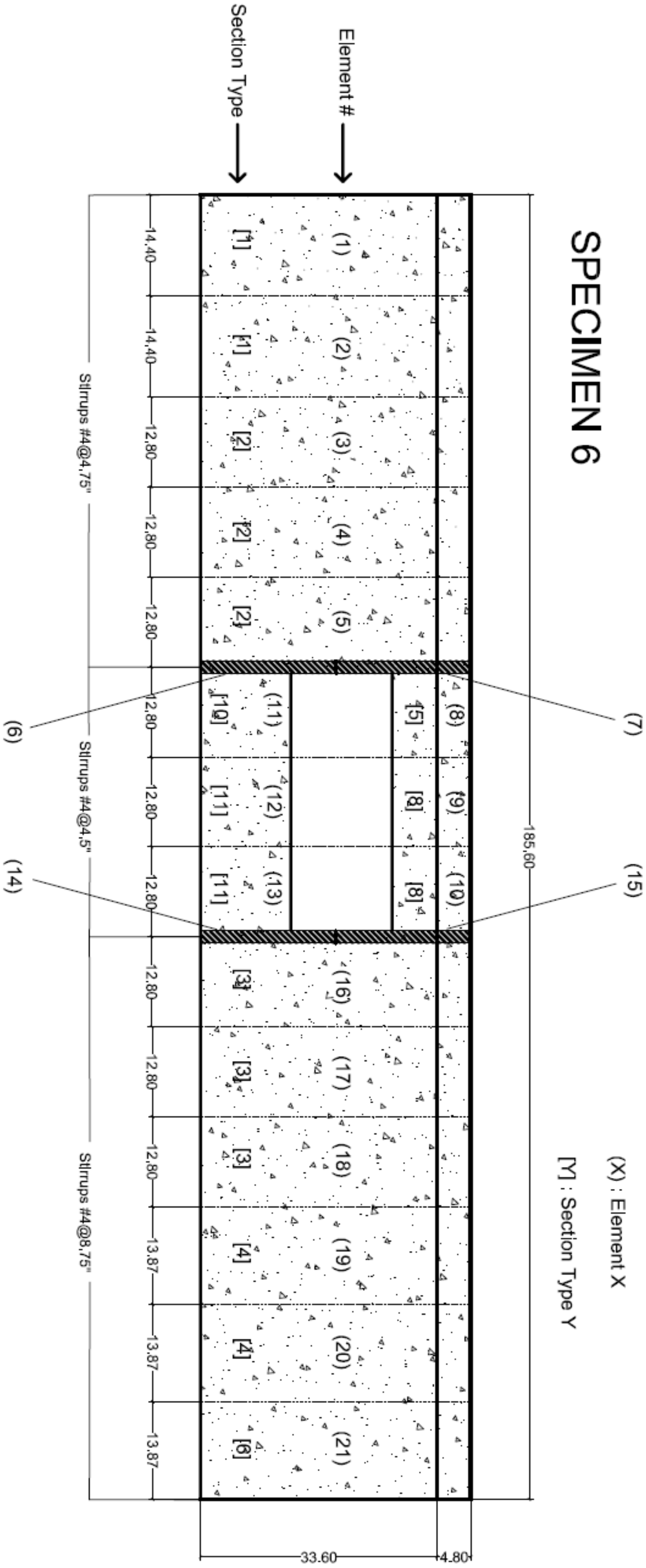

Figure A.27: Specimen 6 with alternative discretization. Dimensions in inches.

Appendix B.

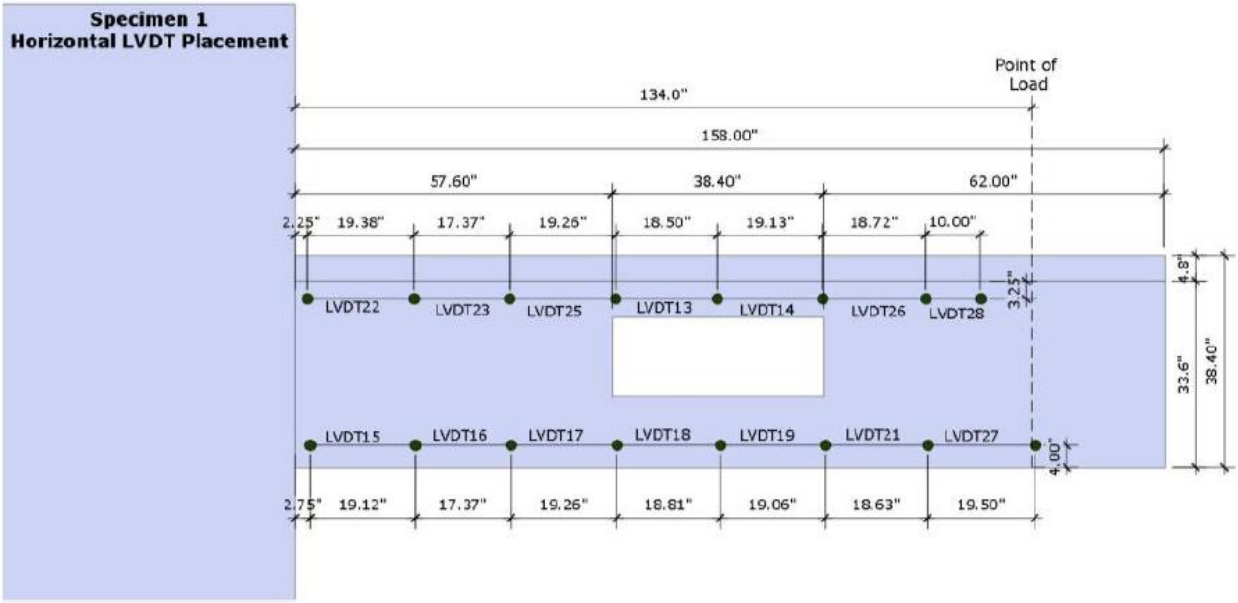

Figure B.1: Layout of horizontal LVDTs on Specimen 1 (Lemnitzer et al., 2013).

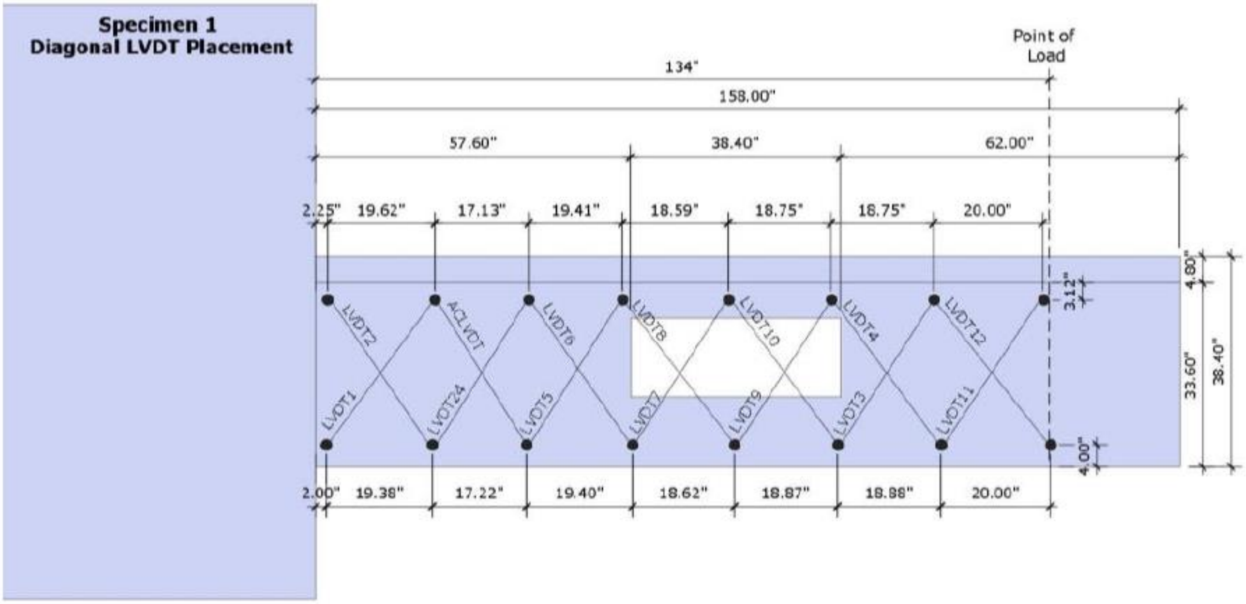

Figure B.2: Layout of diagonal LVDTs on Specimen 1 (Lemnitzer et al., 2013).

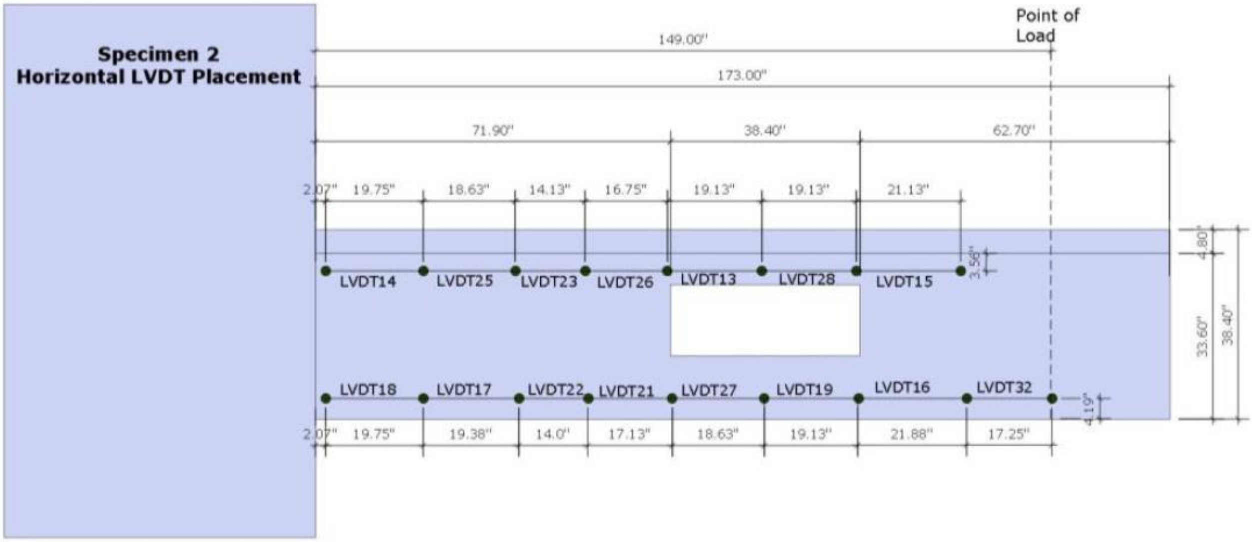

Figure B.3: Layout of horizontal LVDTs on Specimen 2 (Lemnitzer et al., 2013).

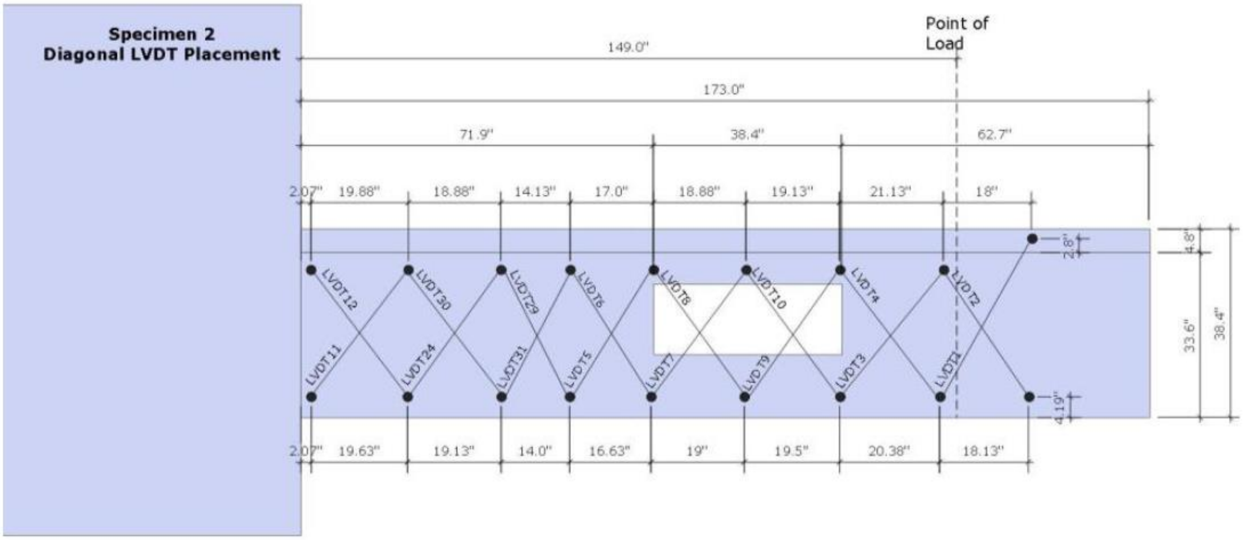

Figure B.4: Layout of diagonal LVDTs on Specimen 2 (Lemnitzer et al., 2013).

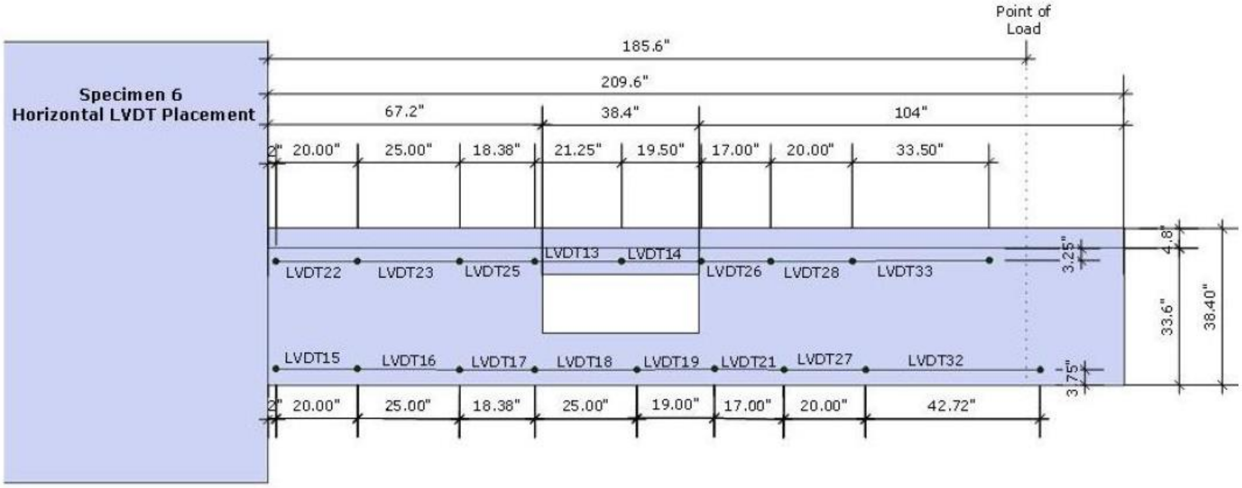

Figure B.5: Layout of horizontal LVDTs on Specimen 6 (Lemnitzer et al., 2013).

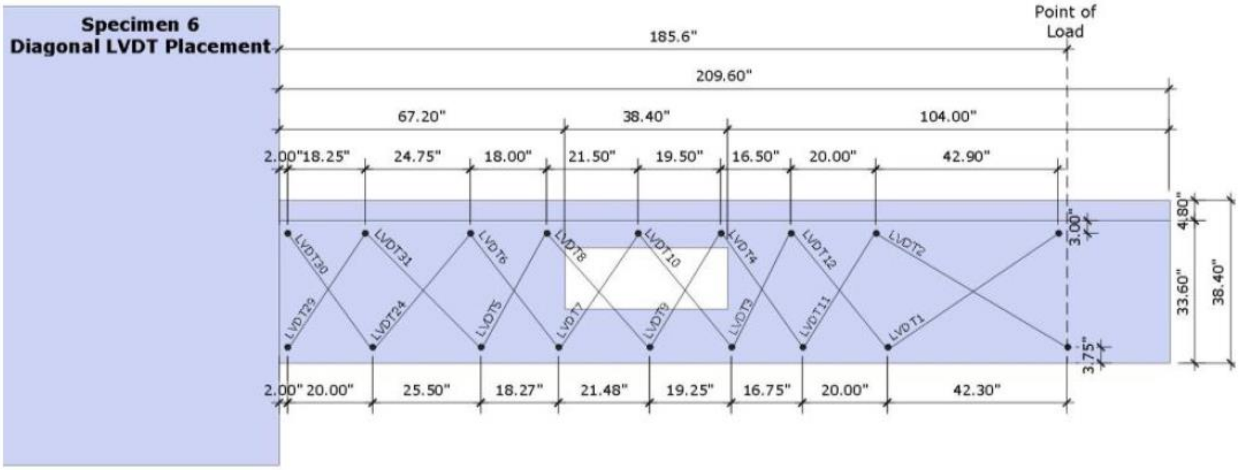

Figure B.6: Layout of diagonal LVDTs on Specimen 6 (Lemnitzer et al., 2013).

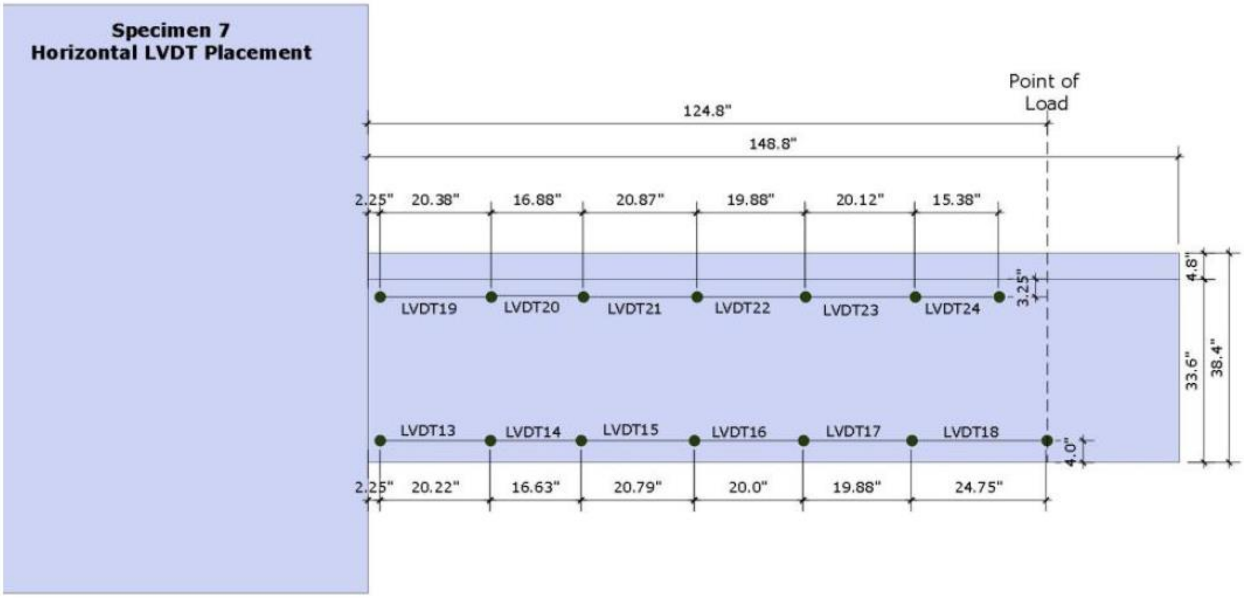

Figure B.7: Layout of horizontal LVDTs on Specimen 7 (Lemnitzer et al., 2013).

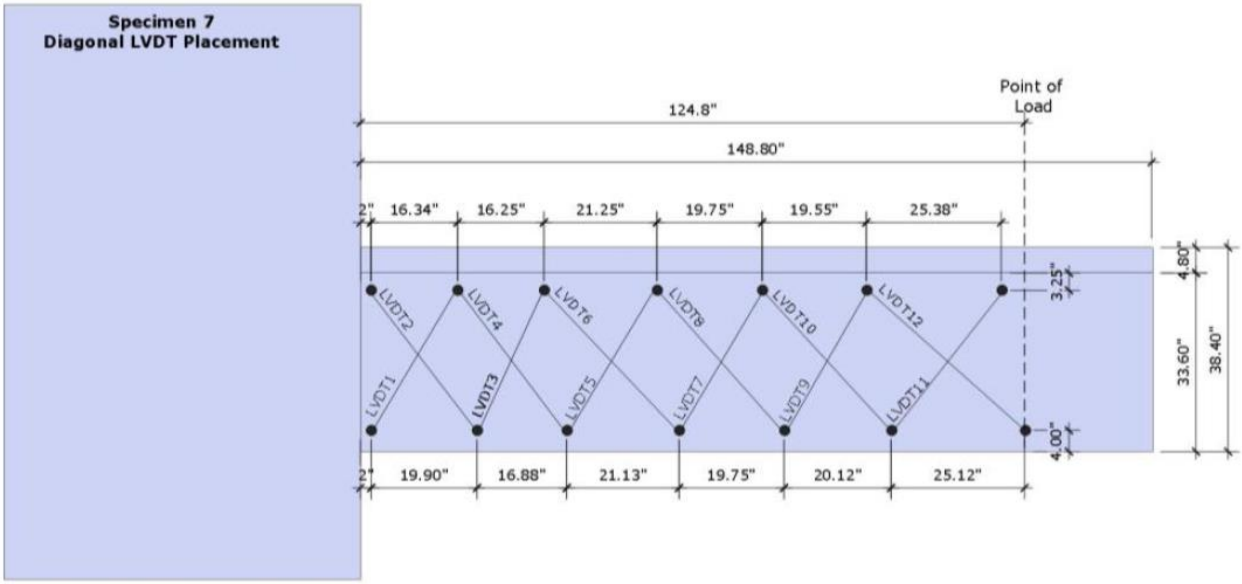

Figure B.8: Layout of diagonal LVDTs on Specimen 7 (Lemnitzer et al., 2013).

Appendix C.

Table C.1: Cross section dimensions.

Typical Cross Section	
Bf [in]	62.4
tf [in]	4.8
Bw [in]	24
hw [in]	33.6
Area [in²]	1105.92
Area [cm²]	**7134.953**

Table C.2: Self-weight loads applied on the specimens.

Parameters	**Specimen 1**	**Specimen 2**	**Specimen 6**	**Specimen 7**
L [in]	134	149	185.6	124.8
L [cm]	340.36	378.46	471.424	316.992
Area (Cross Section) [cm²]	7134.953	7134.953	7134.953	7134.953
Volume [cm³]	2210979.22	2482820.93	3146114.7	2261723.02
Volume [m³]	2.211	2.483	3.146	2.262
Concrete Unit Weight [Ton/m³]	2.5	2.5	2.5	2.5
Specimen Weight [Ton]	5.527	6.207	7.865	5.654
Specimen Weight [lb]	12185.013	13684.164	17339.448	12465.001
Specimen Weight [kips]	**12.185**	**13.684**	**17.339**	**12.465**

Table C.3: Parameters of materials.

		Specimen 1	Specimen 2	Specimen 6	Specimen 7
Unconfined Concrete	**f'_c [ksi]**	7.7	7.6	7.83	7
	f'_c [Mpa]	53.09	52.4	53.986	48.263
	n	3.923	3.882	3.976	3.639
	k	1.526	1.515	1.541	1.448

		Specimen 1		Specimen 2		Specimen 6			Specimen 7	
Confined Concrete		Section 1	Section 2	Section 1	Section 2	Section 1	Section 2	Section 3	Section 1	Section 2
	f'_{cc} [ksi]	8.485	8.776	8.298	8.557	8.528	8.560	8.251	7.785	7.605
	f'_{cc} [Mpa]	58.505	60.510	57.215	58.998	58.801	59.022	56.886	53.676	52.435
	n	2.0032	1.8653	1.7850	1.6694	1.7804	1.7641	1.9479	2.0359	2.1318
	k	1	1	1	1	1	1	1	1	1
	n	1.9343		1.7272		1.8308			2.0839	
	k	1		1		1			1	

		Specimen 1	Specimen 2	Specimen 6	Specimen 7
Concrete in Tension	**f_{cr} [ksi]**	0.3291	0.3269	0.3318	0.3138
	ε_{cr}	0.00008	0.00008	0.00008	0.00008
	b	0.4	0.4	0.4	0.4

		Specimen 1	Specimen 2	Specimen 6	Specimen 7
Steel	ρ	0.02084	0.02836	0.02051	0.013604
	B	0.01560	0.011350	0.016053	0.02225
	R_o	25	25	25	25

Appendix D.

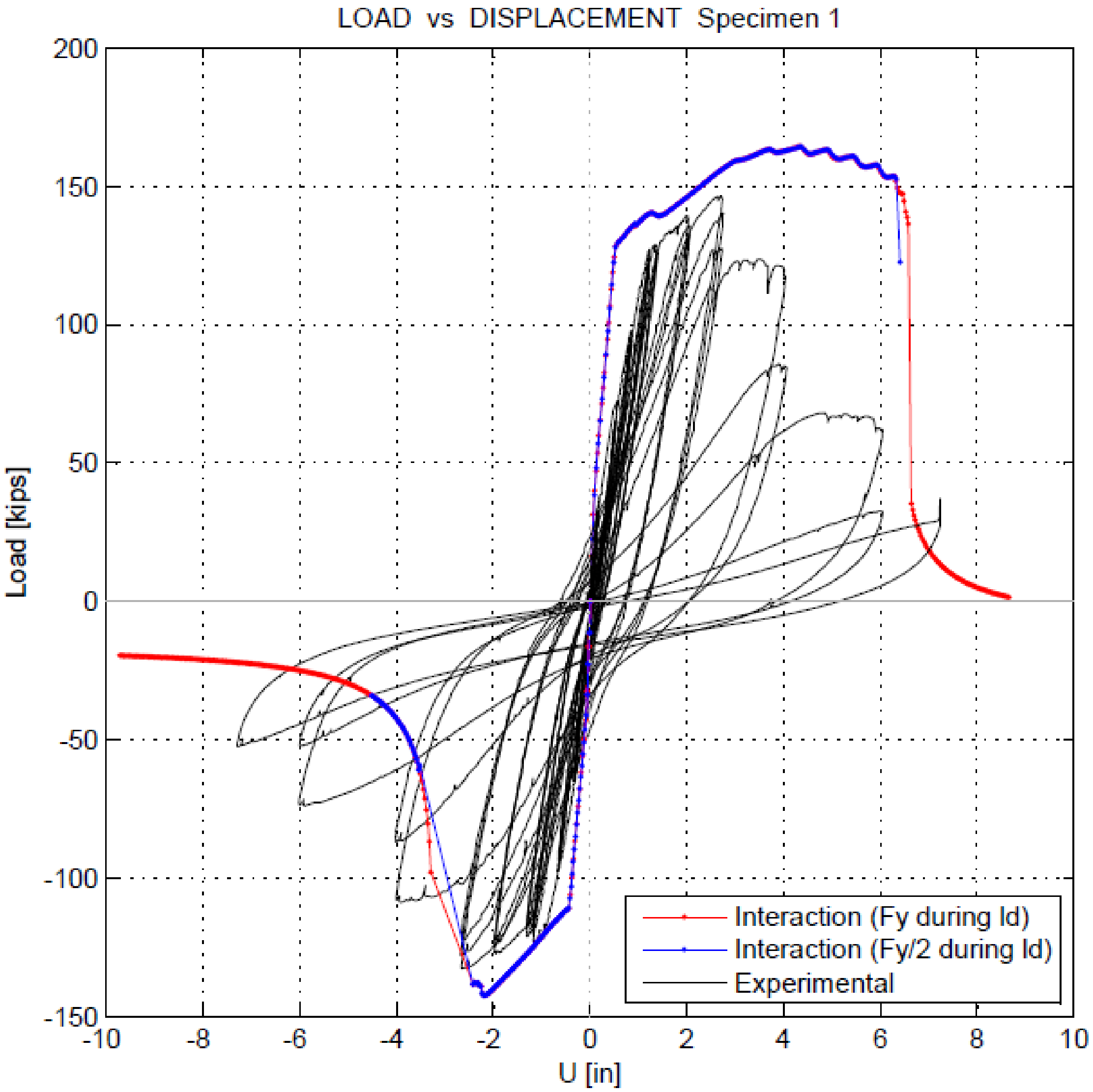

Figure D.1: Load-Displacement response comparison for Specimen 1 before and after considering de the assumption made in Section 4.3.4.

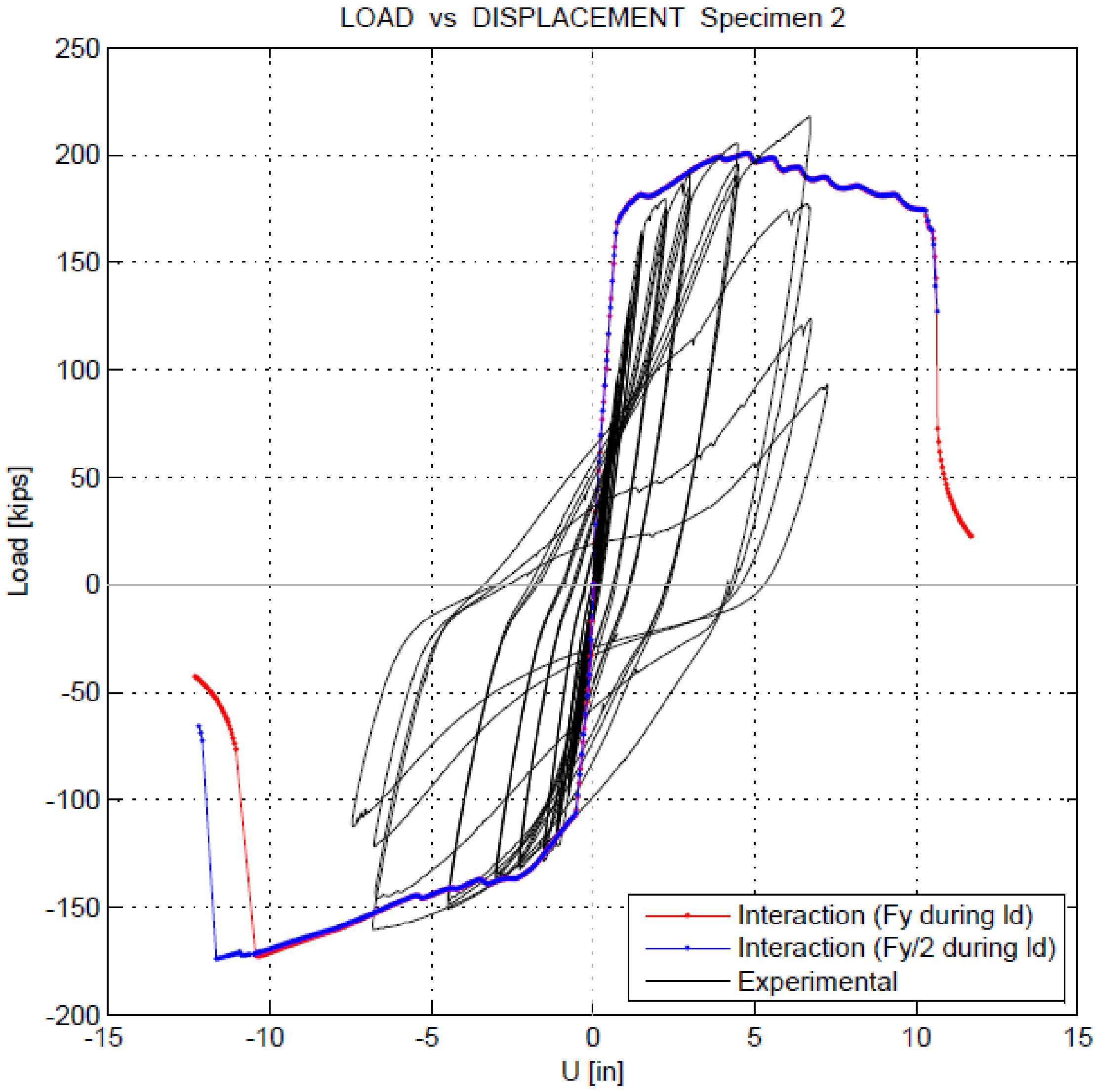

Figure D.2: Load-Displacement response comparison for Specimen 2 before and after considering de the assumption made in Section 4.3.4.

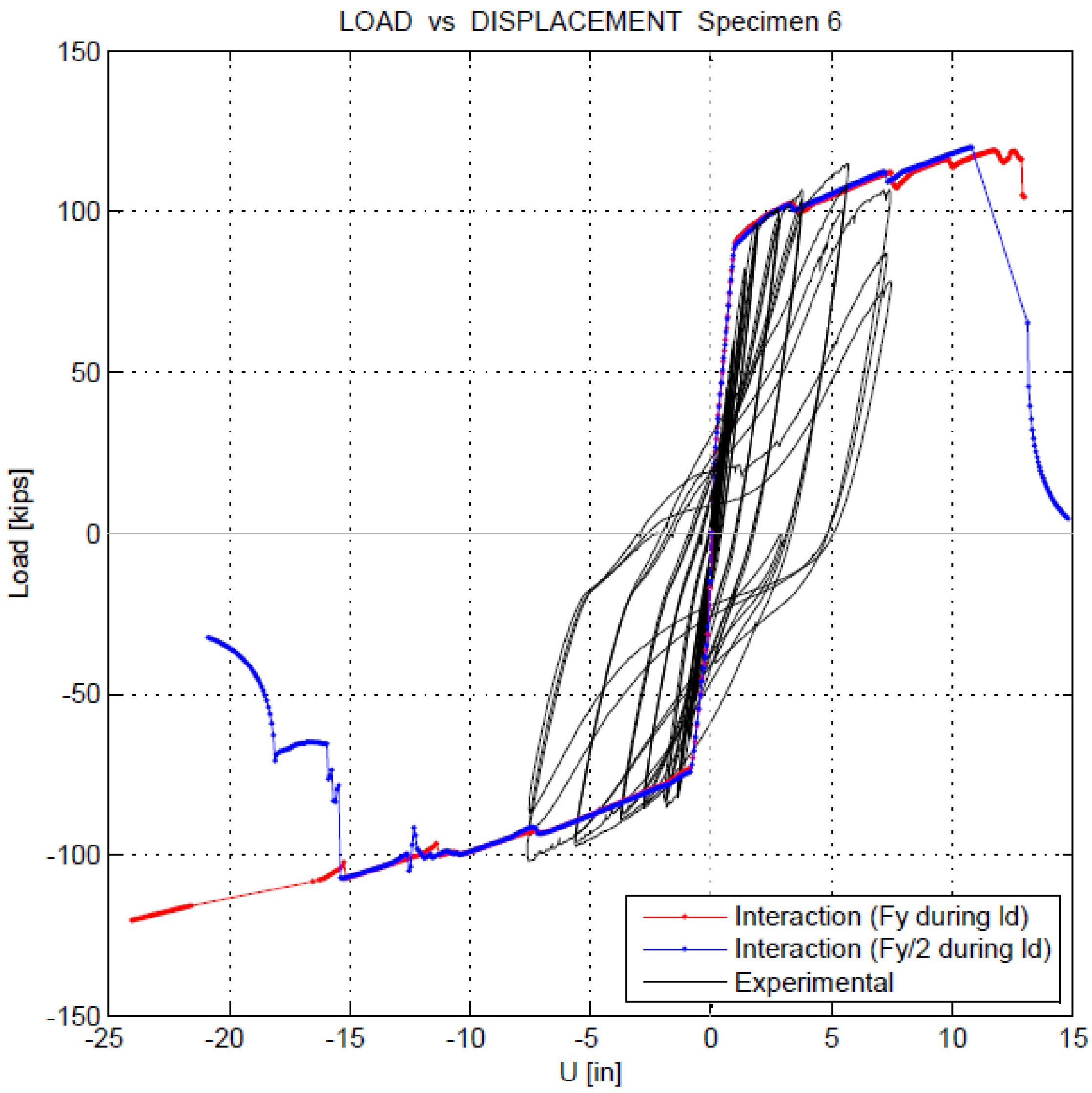

Figure D.3: Load-Displacement response comparison for Specimen 6 before and after considering de the assumption made in Section 4.3.4.

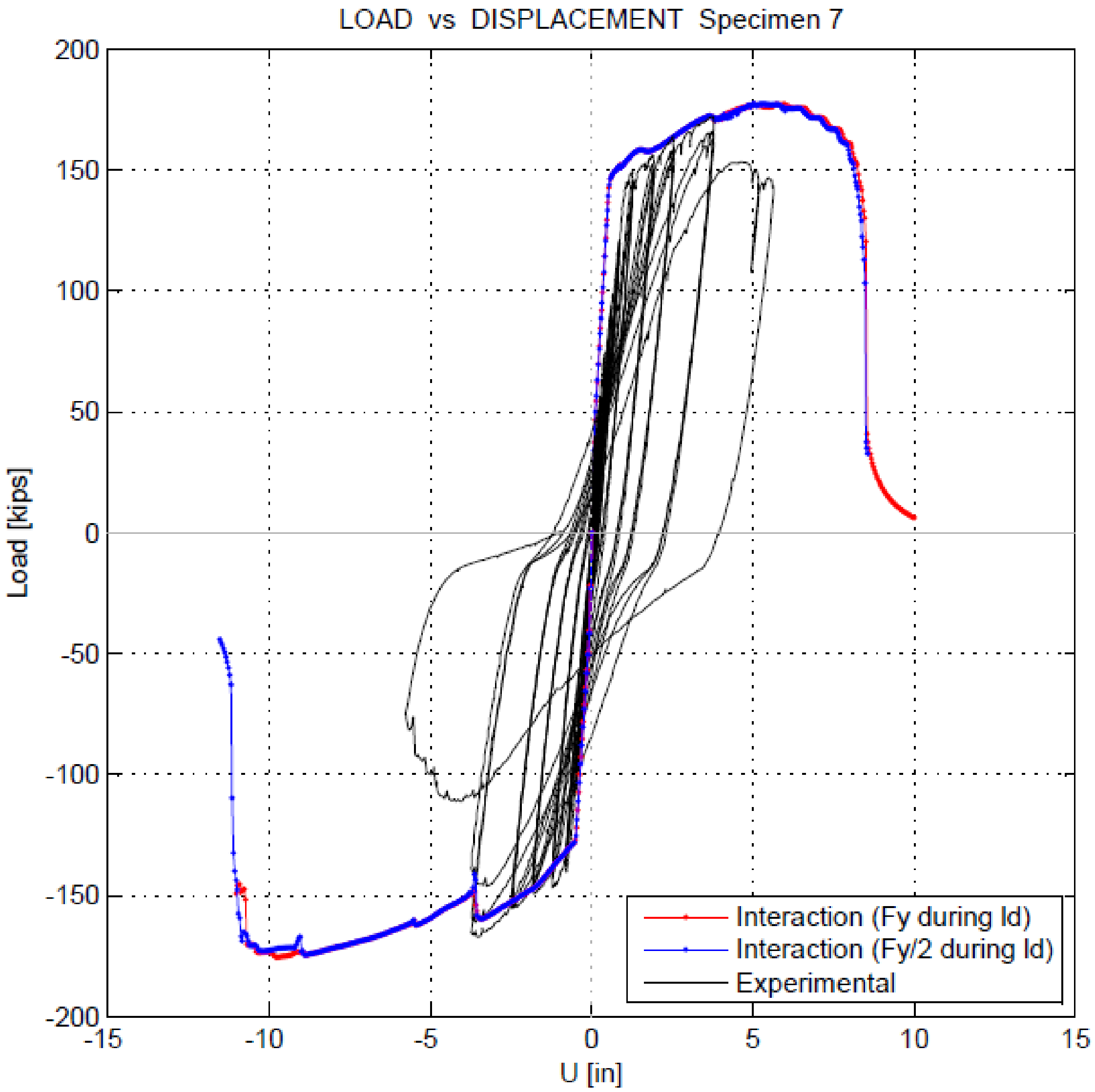

Figure D.4: Load-Displacement response comparison for Specimen 7 before and after considering de the assumption made in Section 4.3.4.

Table D.1: Maximum capacity results comparison.

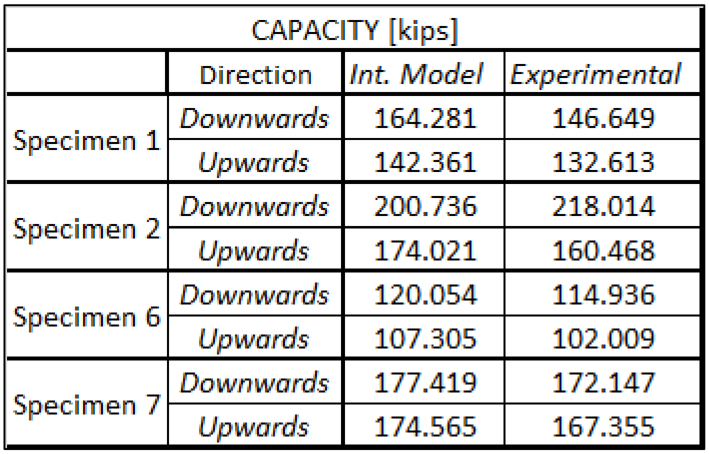

CAPACITY [kips]			
	Direction	*Int. Model*	*Experimental*
Specimen 1	*Downwards*	164.281	146.649
	Upwards	142.361	132.613
Specimen 2	*Downwards*	200.736	218.014
	Upwards	174.021	160.468
Specimen 6	*Downwards*	120.054	114.936
	Upwards	107.305	102.009
Specimen 7	*Downwards*	177.419	172.147
	Upwards	174.565	167.355

Table D.2: Initial stiffness comparison.

		INITIAL STIFFNESS								
		Yield Strength [ksi]			Yield Displacement [in]			**Initial Stiffness [kips/in]**		
	Direction	*F. Model*	*I. Model*	*Exp.*	*F. Model*	*I. Model*	*Exp.*	*F. Model*	*I. Model*	*Exp.*
Specimen 1	*Downwards*	123.683	122.561	127.216	0.4748	0.4886	1.2233	260.495	250.841	103.994
	Upwards	110.066	107.363	123.929	0.4239	0.4177	1.1561	259.651	257.034	107.2
Specimen 2	*Downwards*	159.265	163.732	164.596	0.6601	0.7125	1.5089	241.274	229.799	109.08
	Upwards	101.541	106.066	121.617	0.4876	0.5344	1.1092	208.247	198.477	109.64
Specimen 6	*Downwards*	85.343	86.437	94.671	0.8786	0.9121	1.7471	97.135	94.766	54.187
	Upwards	70.370	71.9286	82.310	0.7687	0.802	1.3932	91.544	89.687	59.08
Specimen 7	*Downwards*	137.116	139.325	141.414	0.4875	0.5213	1.0152	281.264	267.265	139.3
	Upwards	124.703	125.342	101.740	0.4719	0.4899	0.428	264.257	255.852	237.71

Table D.3: Displacements and Drifts at maximum capacity.

			Interaction Model			*Experimental*		
	Length [in]	Direction	Max. Capacity [kips]	Disp. [in]	Drift	Max. Capacity [kips]	Disp. [in]	Drift
Specimen 1	134	*Downwards*	164.281	4.329	3.2%	146.649	2.692	2.0%
		Upwards	142.361	2.195	1.6%	132.613	2.639	2.0%
Specimen 2	149	*Downwards*	200.736	4.749	3.2%	218.014	6.702	4.5%
		Upwards	174.021	11.661	7.8%	160.468	6.807	4.6%
Specimen 6	185.6	*Downwards*	120.054	10.759	5.8%	114.936	5.629	3.0%
		Upwards	107.305	15.328	8.3%	102.009	7.601	4.1%
Specimen 7	124.8	*Downwards*	177.419	5.057	4.1%	172.147	3.767	3.0%
		Upwards	174.565	8.885	7.1%	167.355	3.539	2.8%

Table D.4: Loads, displacements and drifts comparison at the beginning of degradation.

			Interaction Model			*Experimental*		
	Length [in]	Direction	Degradation Load [kips]	Disp. [in]	Drift	Degradation Load [kips]	Disp. [in]	Drift
Specimen 1	134	*Downwards*	152.65	6.329	4.7%	145.274	2.735	2.0%
		Upwards	138.395	2.420	1.8%	132.484	2.665	2.0%
Specimen 2	149	*Downwards*	174.228	10.307	6.9%	217.163	6.718	4.5%
		Upwards	174.021	11.661	7.8%	159.068	6.817	4.6%
Specimen 6	185.6	*Downwards*	119.961	10.808	5.8%	106.930	7.404	4.0%
		Upwards	107.201	15.397	8.3%	100.323	7.640	4.1%
Specimen 7	124.8	*Downwards*	103.235	8.479	6.8%	142.19	5.647	4.5%
		Upwards	166.952	10.878	8.7%	138.501	3.734	3.0%

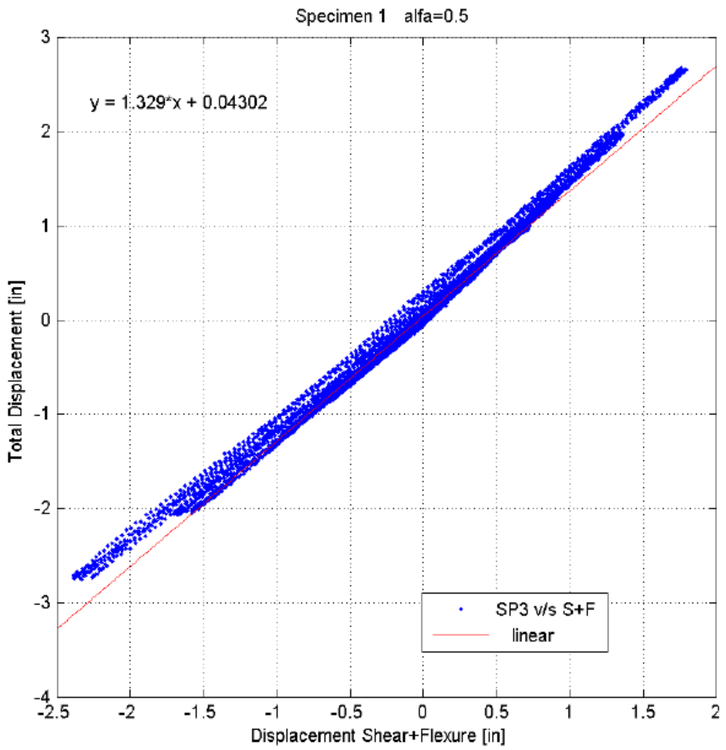

Figure D.5: Scatter of Total Displacement vs Estimated Shear+Flexure Displacement for Specimen 1. Each displacement is estimated at the load application point.

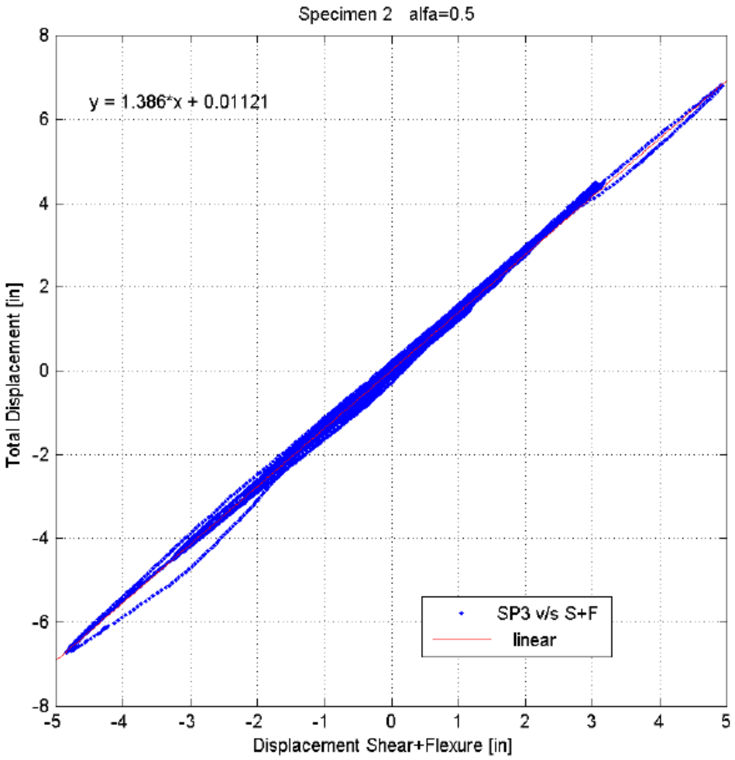

Figure D.6: Scatter of Total Displacement vs Estimated Shear+Flexure Displacement for Specimen 2. Each displacement is estimated at the load application point.

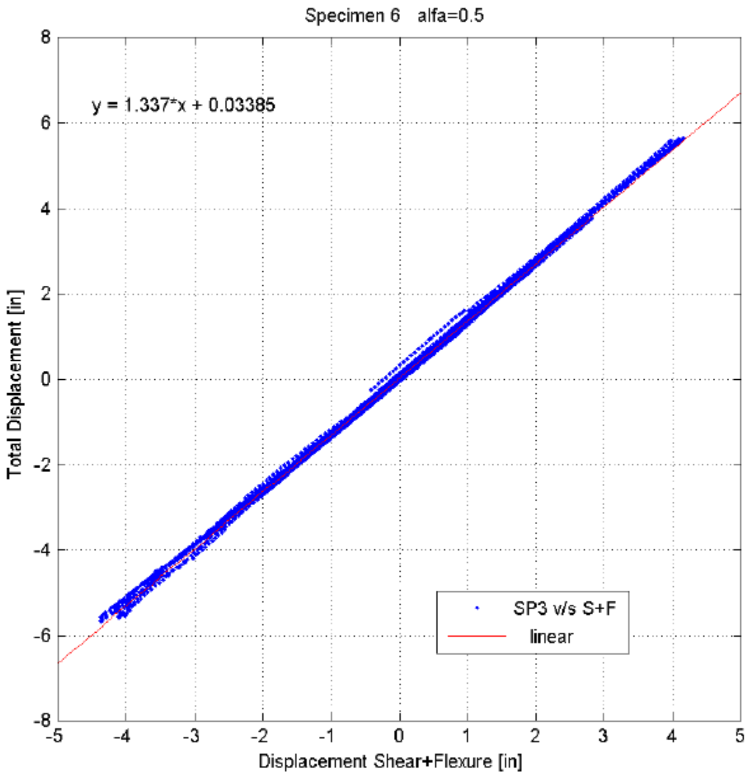

Figure D.7: Scatter of Total Displacement vs Estimated Shear+Flexure Displacement for Specimen 6. Each displacement is estimated at the load application point.

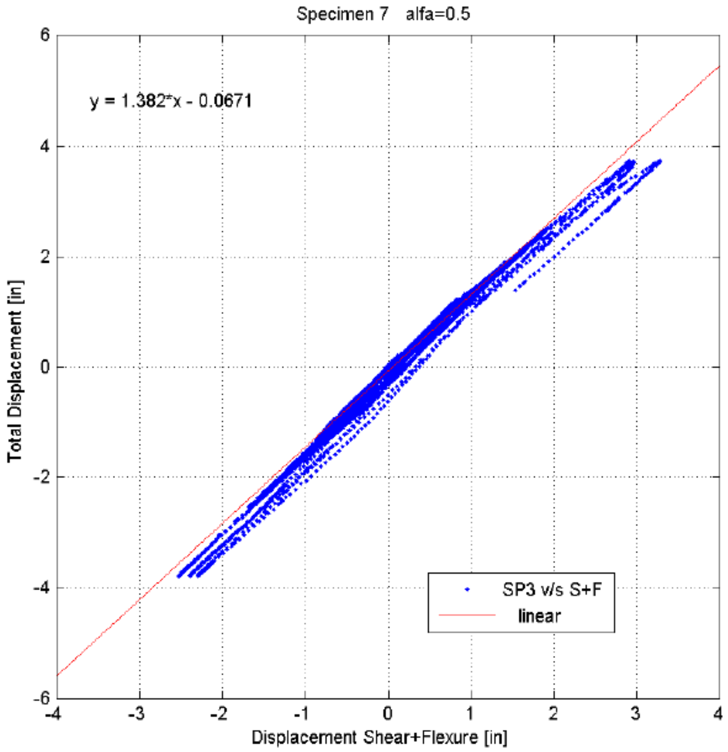

Figure D.8: Scatter of Total Displacement vs Estimated Shear+Flexure Displacement for Specimen 7. Each displacement is estimated at the load application point.

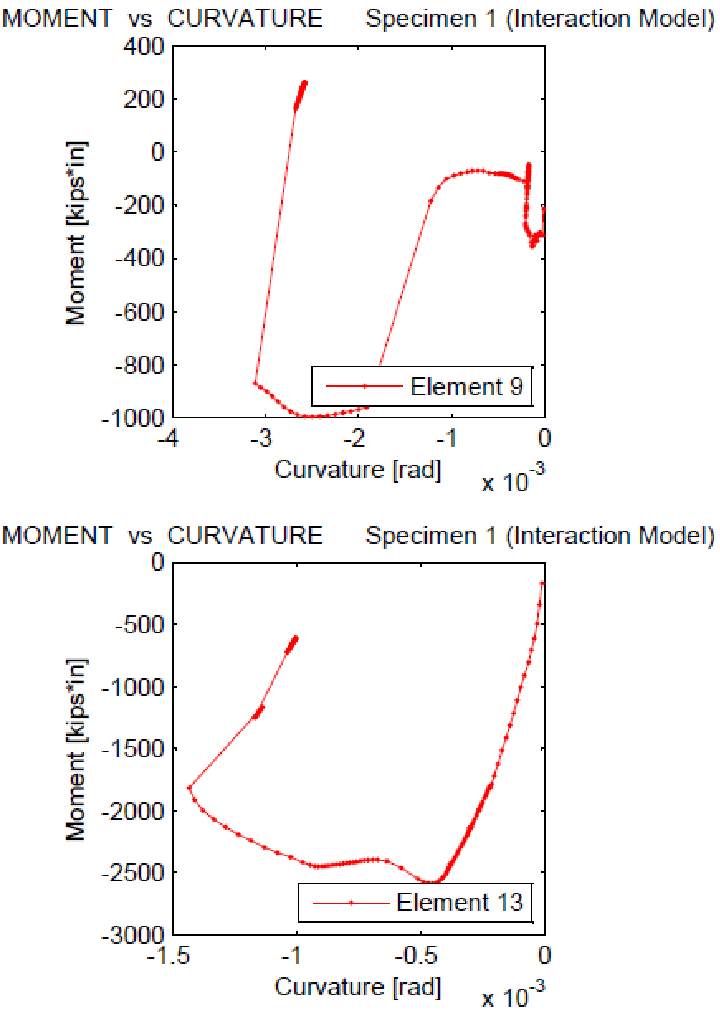

Figure D.9: Moment-curvature responses of elements that accumulate the damage when the failure is located at the opening (Lower strengths for both materials). Specimen 1.

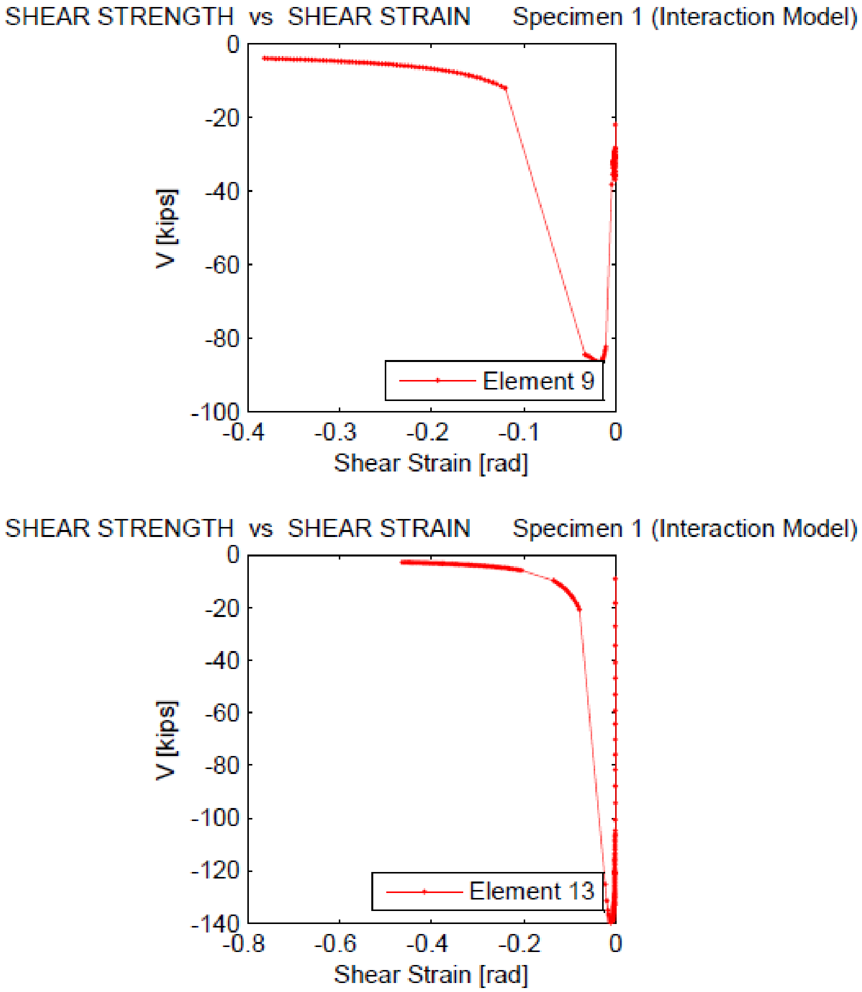

Figure D.10: Shear stress-strain responses of elements that accumulate the damage when the failure is located at the opening (Lower strengths for both materials). Specimen 1.

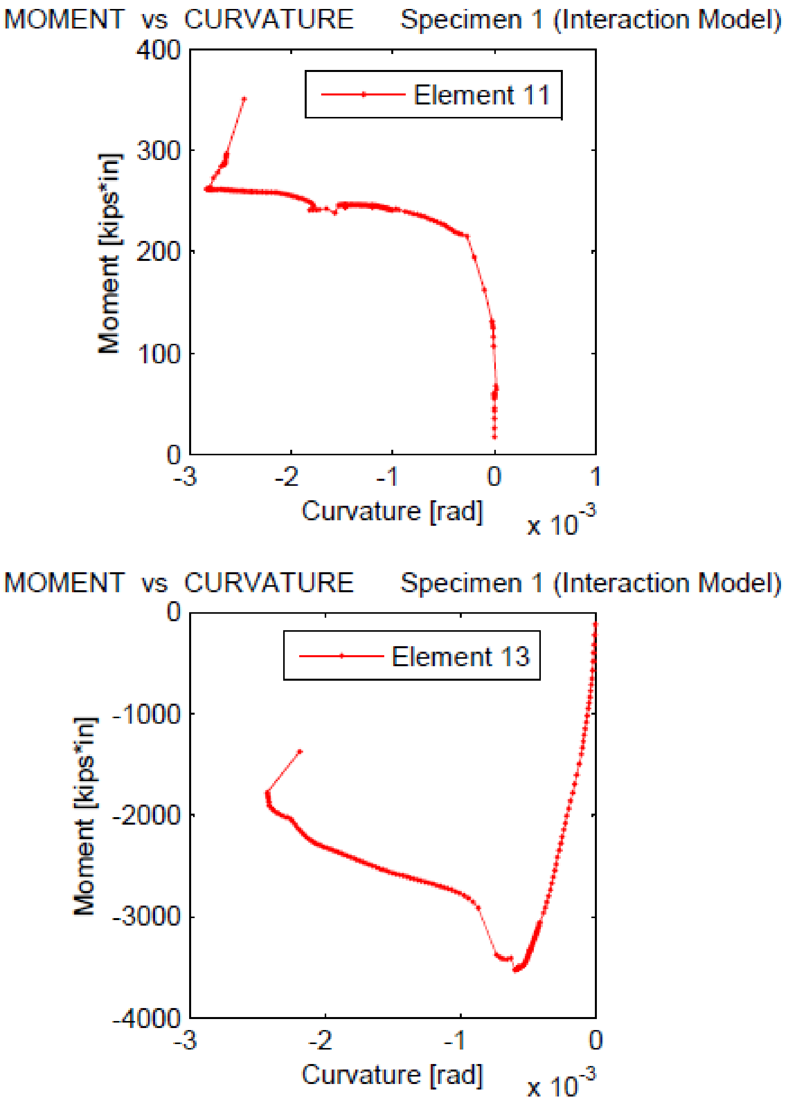

Figure D.11: Moment-curvature responses of elements that accumulate the damage when the failure is located at the opening (Lower strength for the reinforcing steel). Specimen 1.

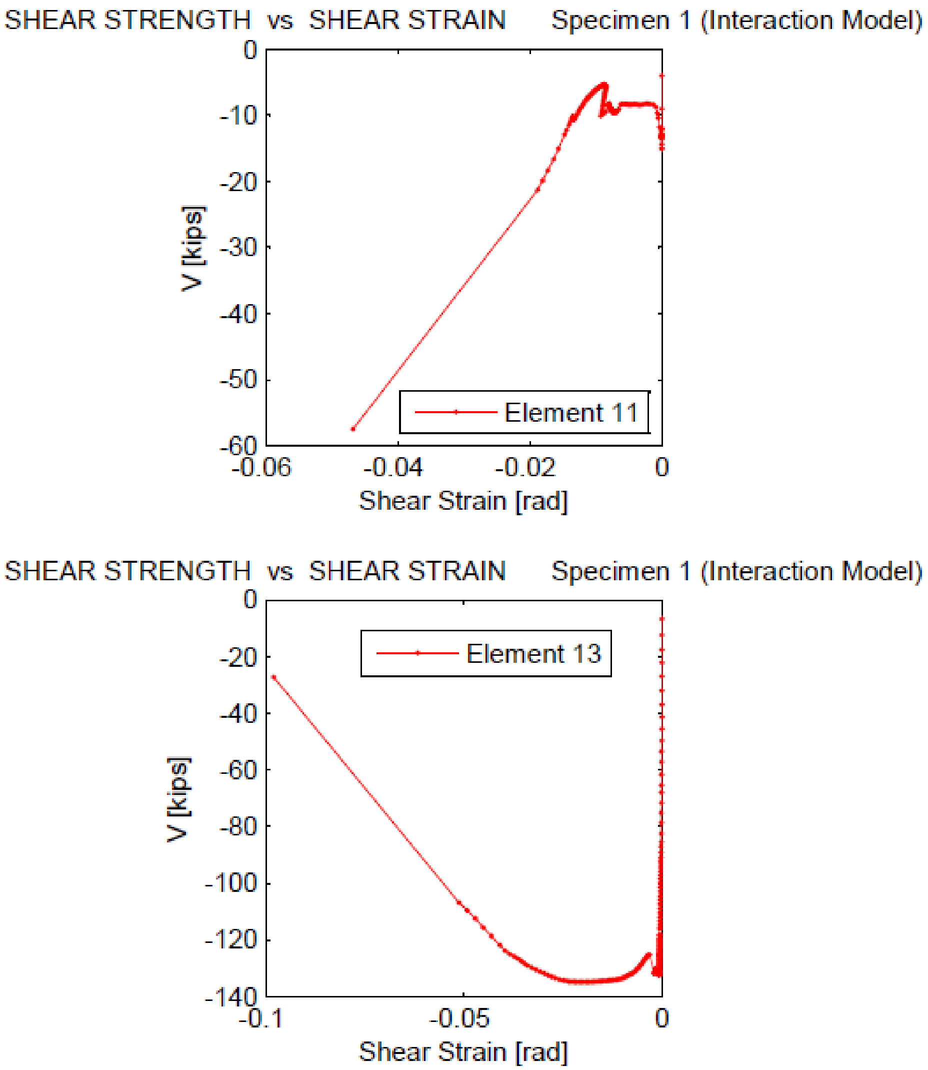

Figure D.12: Shear stress-strain responses of elements that accumulate the damage when the failure is located at the opening (Lower strength for the reinforcing steel). Specimen 1.

Appendix E.

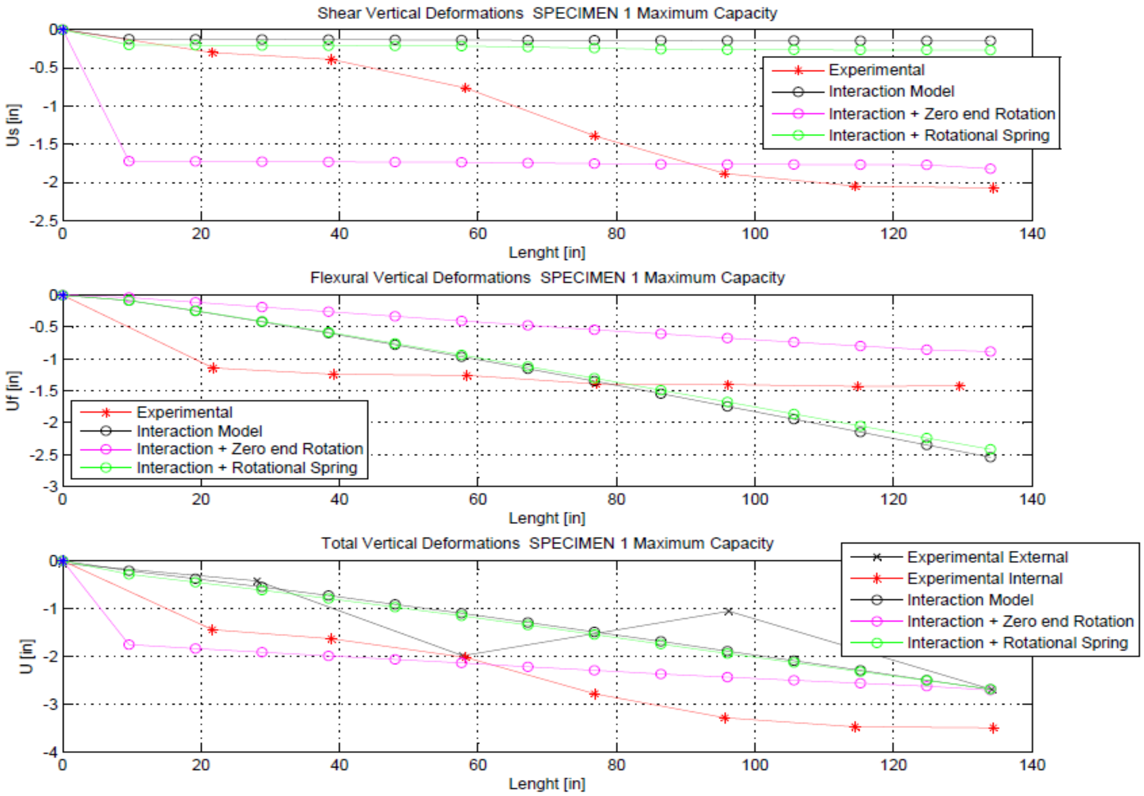

Figure E.1: Deflection Profiles for Specimen 1. Origin. Discret. Comparison with late variations. Downwards.

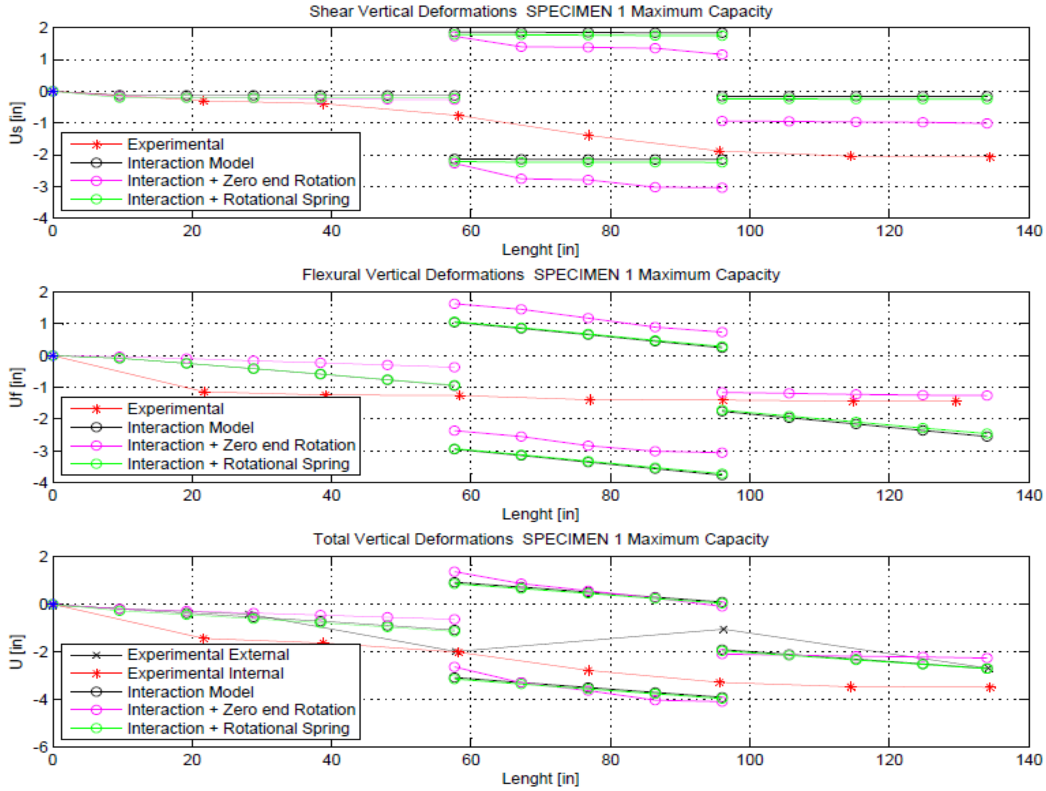

Figure E.2: Deflection Profiles for Specimen 1. Altern. Discret. Comparison with late variations. Downwards.

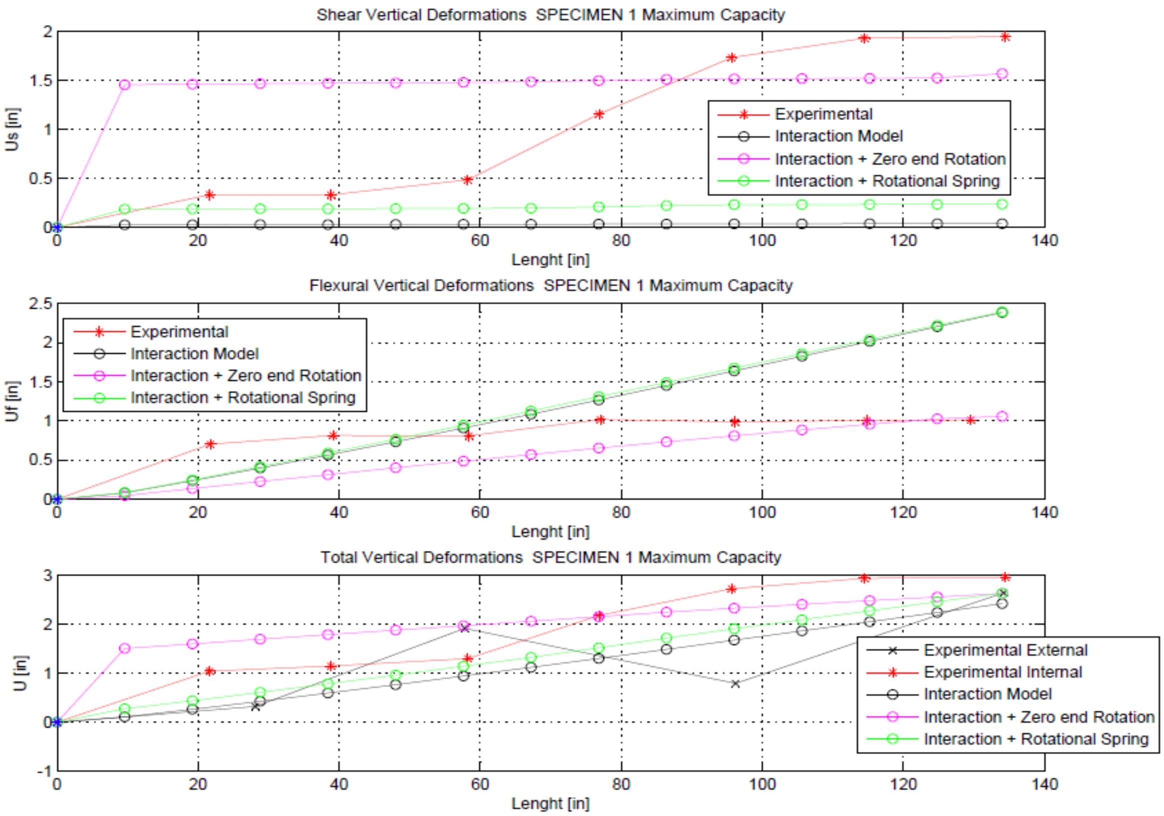

Figure E.3: Deflection Profiles for Specimen 1. Original Discret. Comparison with late variations. Upwards.

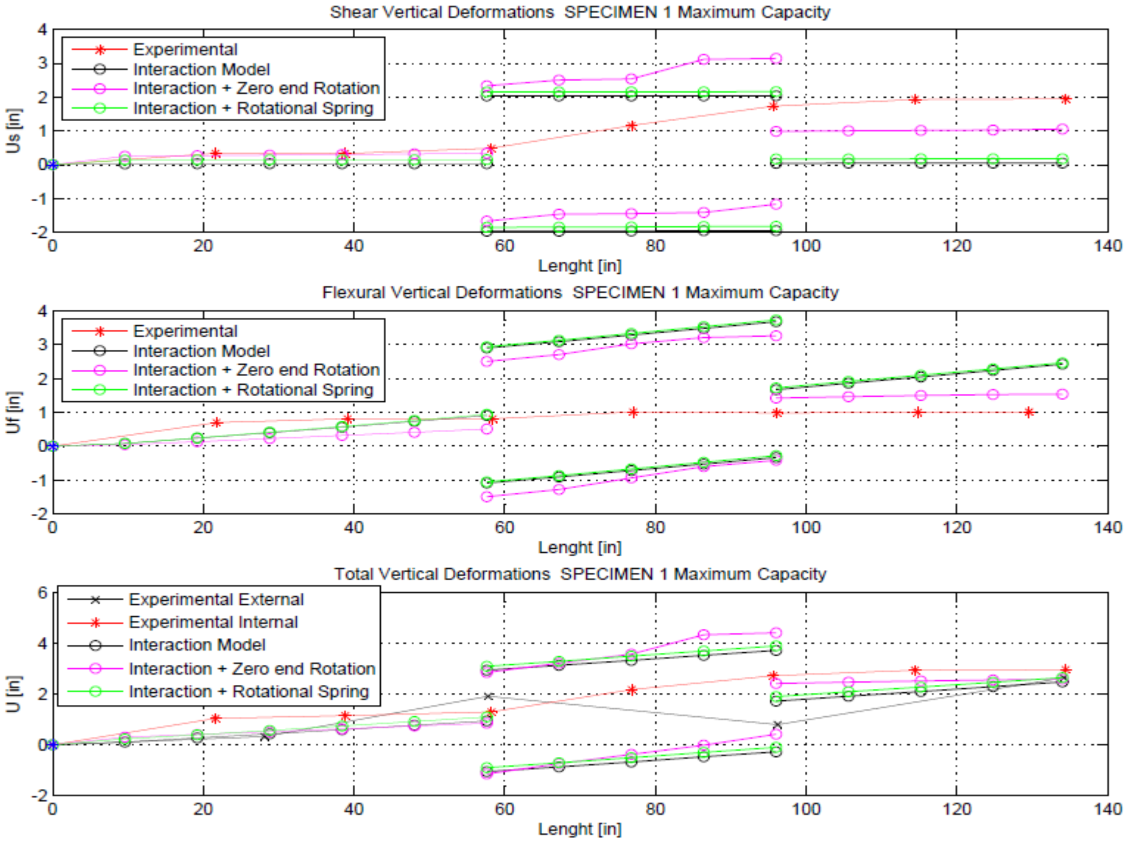

Figure E.4: Deflection Profiles for Specimen 1. Altern. Discret. Comparison with late variations. Upwards.

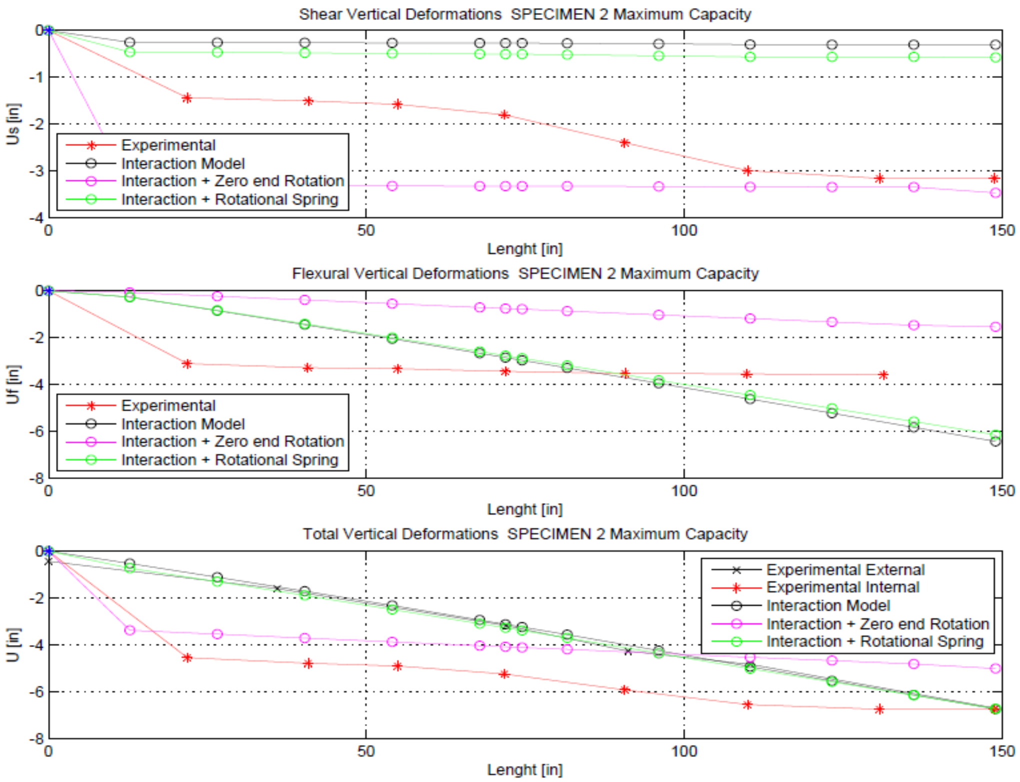

Figure E.5: Deflection Profiles for Specimen 2. Origin. Discret. Comparison with late variations. Downwards.

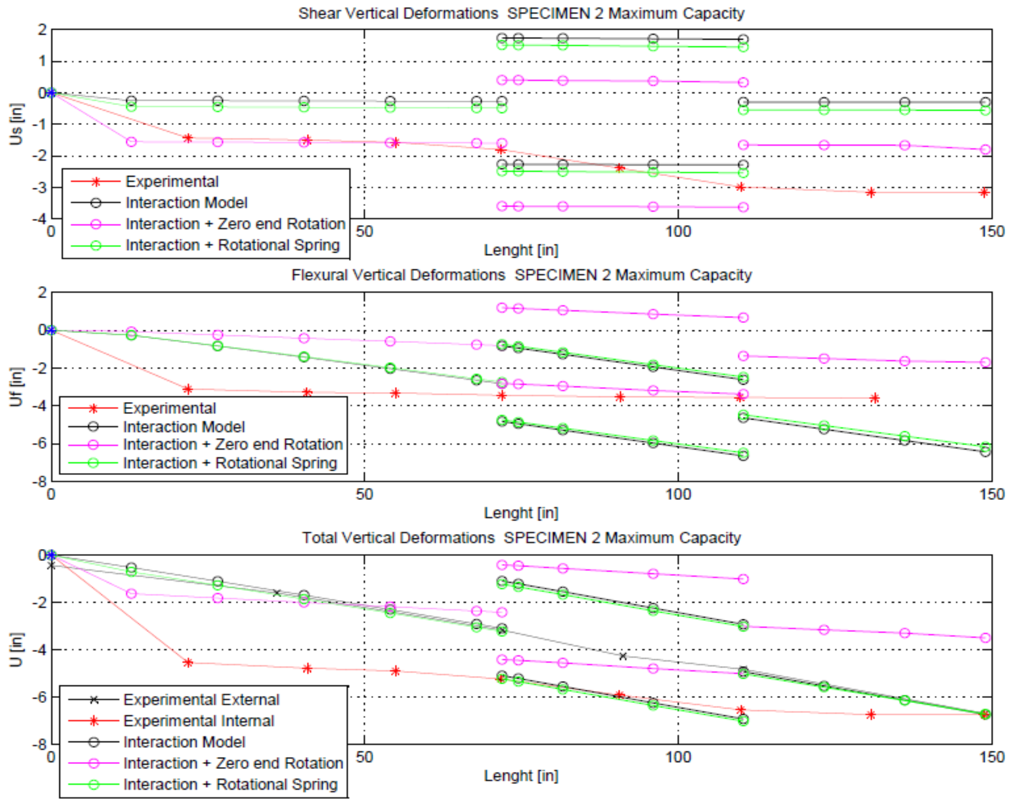

Figure E.6: Deflection Profiles for Specimen 2. Altern. Discret. Comparison with late variations. Downwards.

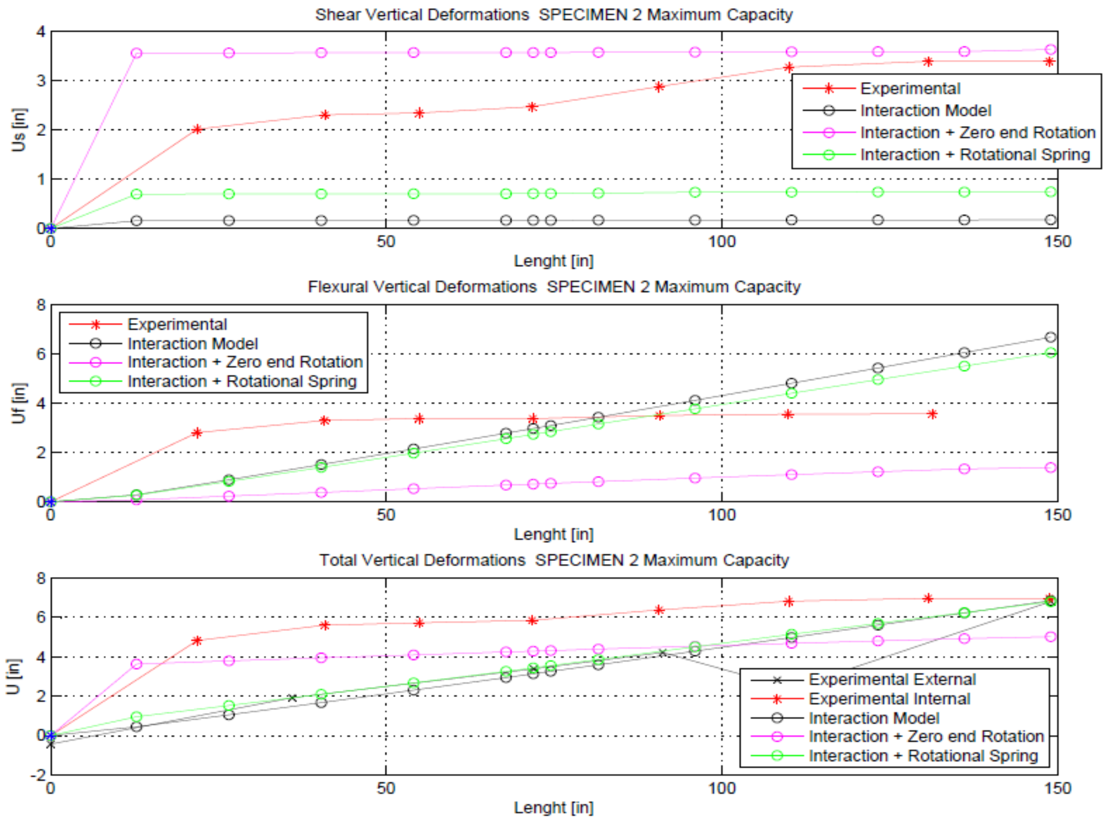

Figure E.7: Deflection Profiles for Specimen 2. Origin. Discret. Comparison with late variations. Upwards.

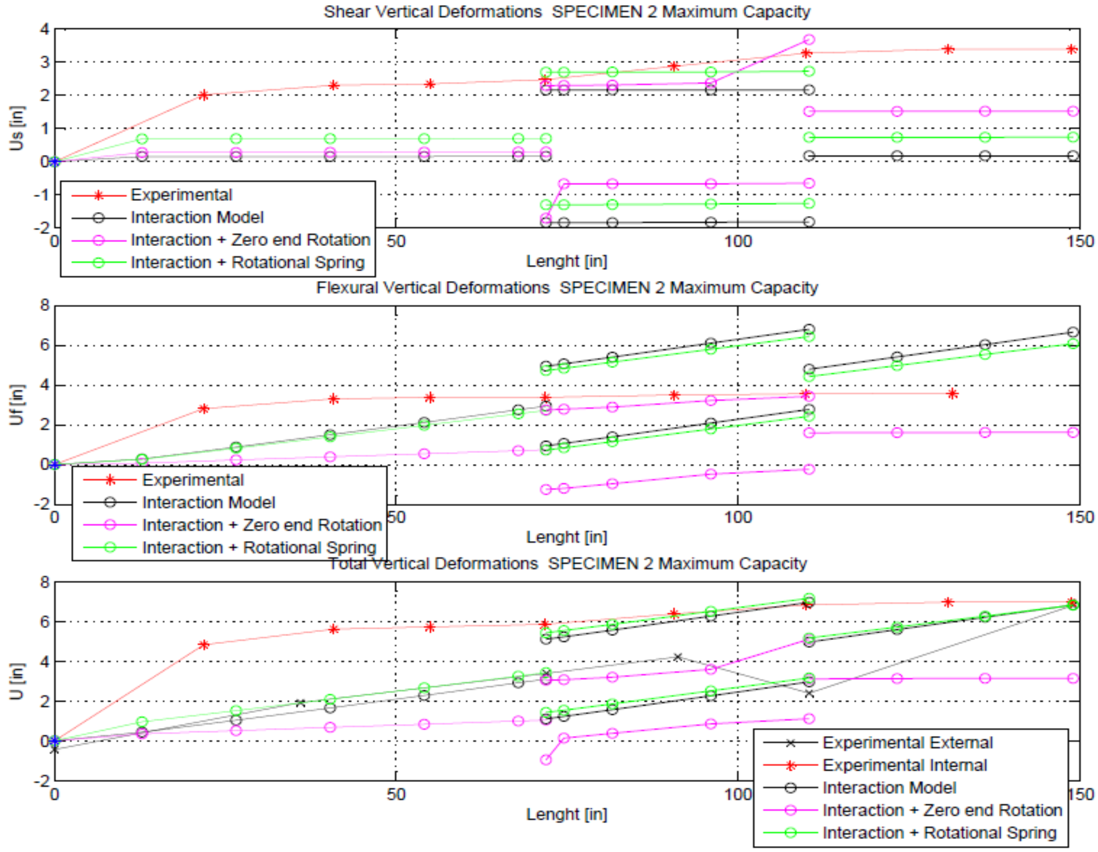

Figure E.8: Deflection Profiles for Specimen 2. Altern. Discret. Comparison with late variations. Upwards.

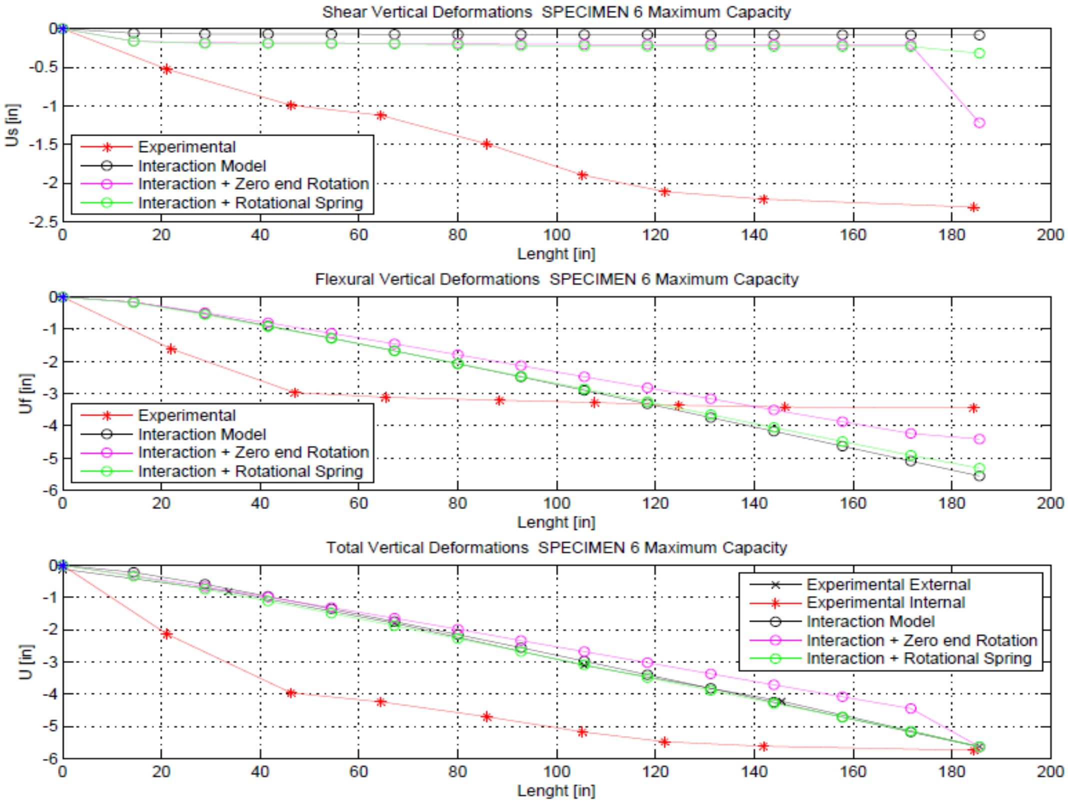

Figure E.9: Deflection Profiles for Specimen 6. Origin. Discret. Comparison with late variations. Downwards.

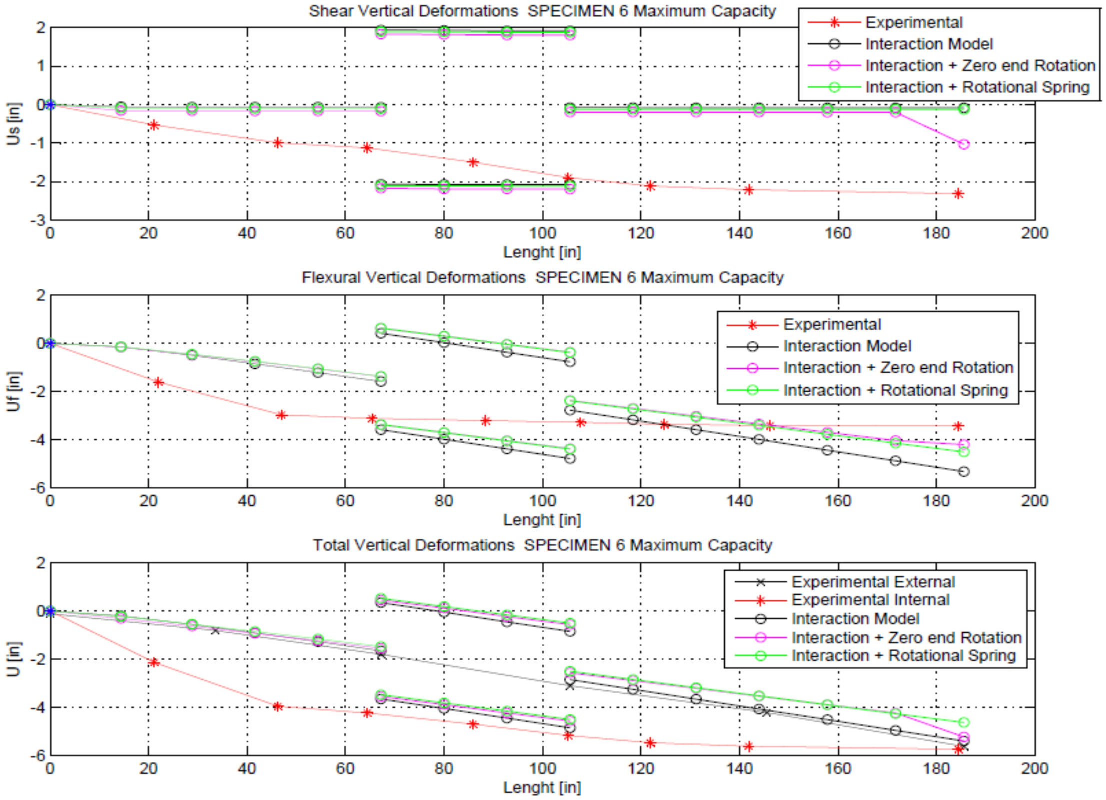

Figure E.10: Deflection Profiles for Specimen 6. Altern. Discret. Comparison with late variations. Downwards.

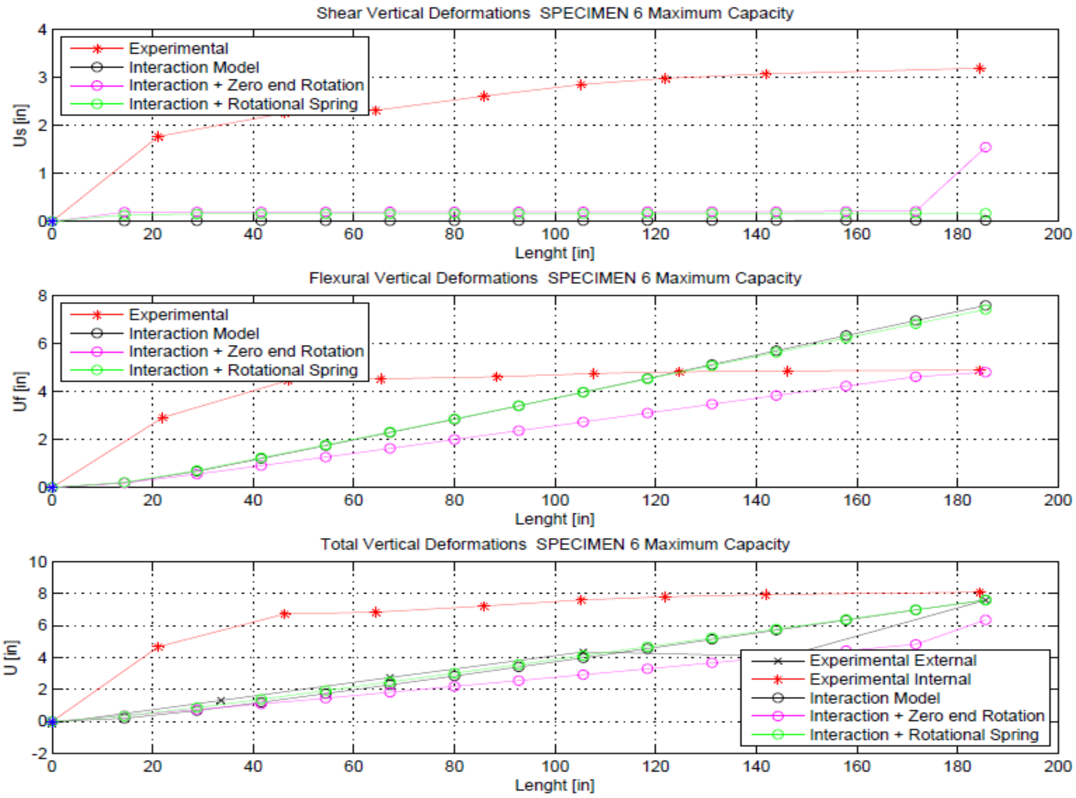

Figure E.11: Deflection Profiles for Specimen 6. Origin. Discret. Comparison with late variations. Upwards.

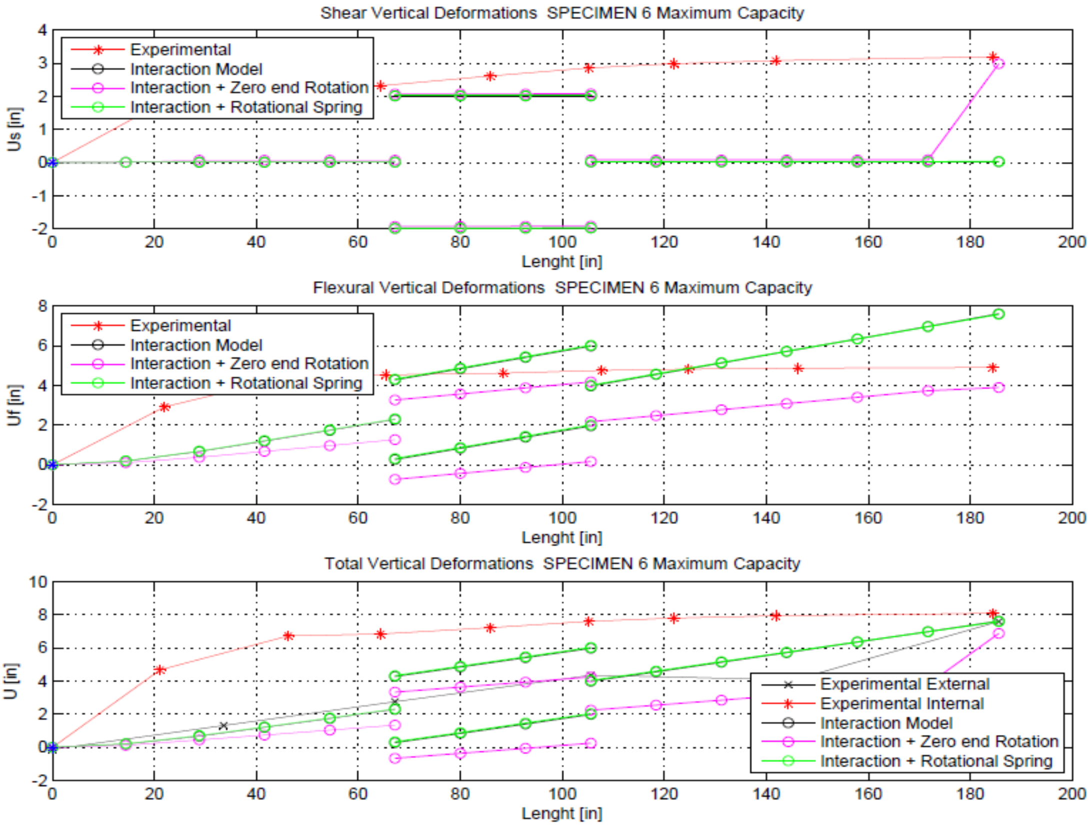

Figure E.12: Deflection Profiles for Specimen 6. Altern. Discret. Comparison with late variations. Upwards.

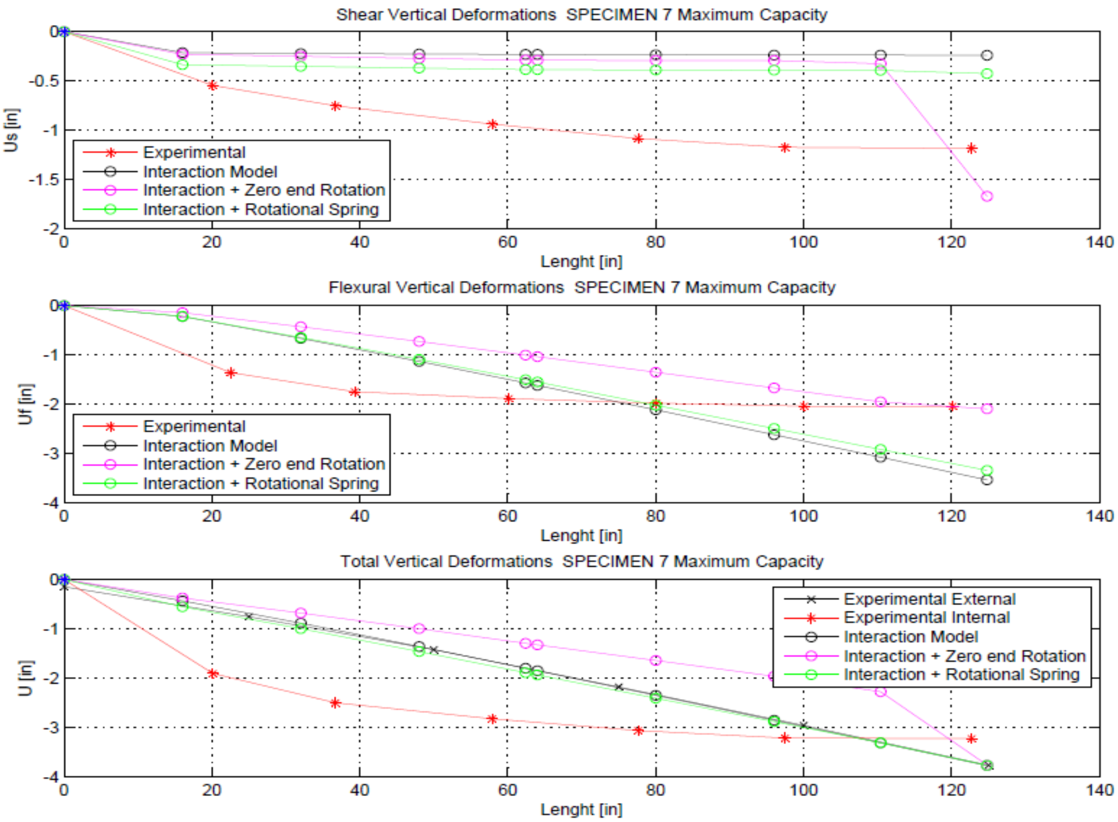

Figure E.13: Deflection Profiles for Specimen 7. Comparison with late variations. Downwards.

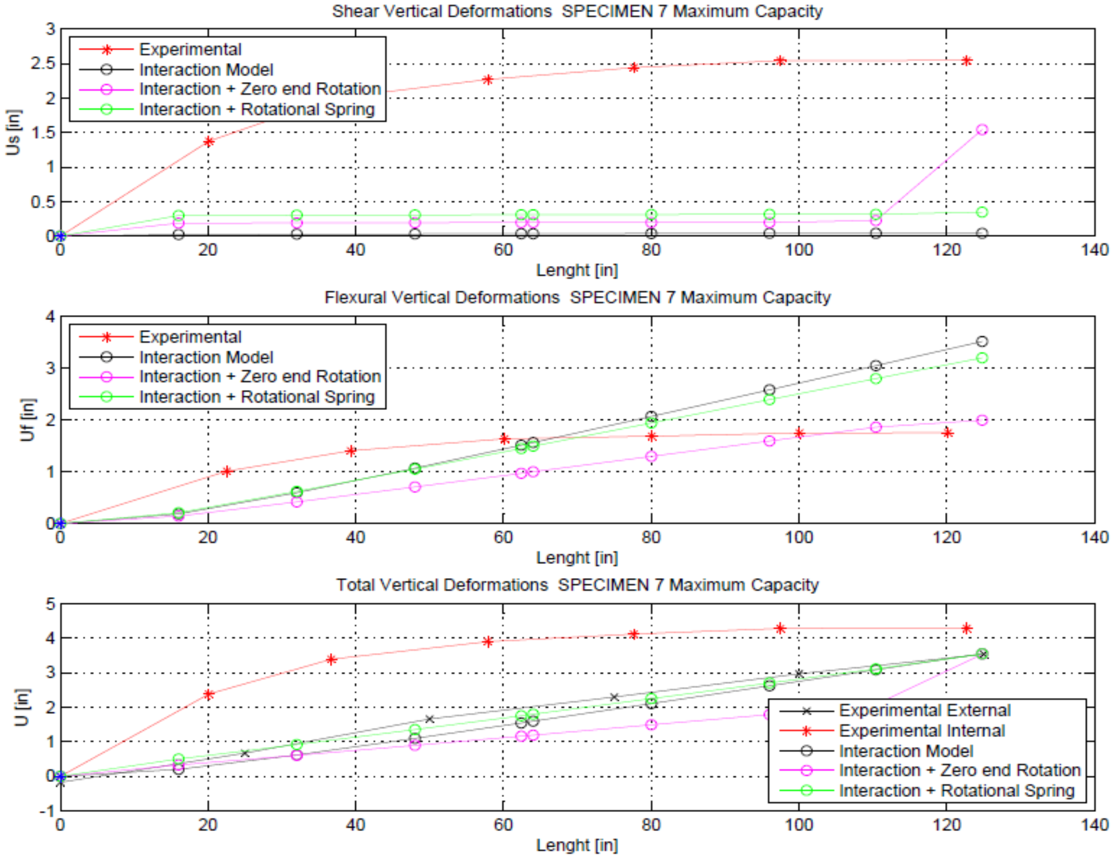

Figure E.14: Deflection Profiles for Specimen 7. Comparison with late variations. Upwards.